(1)

Studies on the electromagnetic moments of proton drip line nuclei ^{9}C and ^{13}O

Minoru Tanigaki

Abstract

The electromagnetic moments of proton drip-line nuclei ^{9}C ($I^{\pi} = 3/2^{-}$, $T_{1/2}$ = 127 ms) and ^{13}O ($I^{\pi} = 3/2^{-}$, $T_{1/2}$ = 8.6 ms) have been determined to study the structure of nuclei far from the stability line. The magnetic moments of ^{9}C and ^{13}O, and the quadrupole moment of ^{13}O have been determined for the first time by use of β-NMR technique.

The present experiment was performed at RIKEN Ring Cyclotron. The polarized nuclear beam were produced through the projectile fragmentation of intermediate-energy heavy ion beams. The β-NMR technique was applied for the present measurements.

The 70*A* MeV ^{12}C beam from RIKEN Ring Cyclotron was used to bombard the C target and the produced ^{9}C nuclei were separated from the various fragments by use of the RIPS (Riken Projectile Fragment Separator). The polarization was obtained by selecting an emission-angle span and also a momentum range of the ejected ^{9}C nuclei from the target. For the detection of the β-NMR of the separated ^{9}C nuclei, they were implanted into a Pt catcher cooled down to 30 K. The magnetic moment of ^{9}C was determined to be $|\mu(^{9}\mathrm{C})| = 1.3914 \pm 0.0005\ \mu_{\mathrm{N}}$.

The ^{13}O nuclei were also produced using the same technique as for ^{9}C. In this case the primary beam of 135*A* MeV ^{16}O was used to bombard a Be target. For the detection of the β-NMR of the separated ^{13}O nuclei, they were implanted into a Pt catcher and a MgO crystal. Using the known chemical shifts of O in the MgO crystal, the magnetic moment of ^{13}O was determined to be $|\mu(^{13}\mathrm{O})| = 1.3891 \pm 0.0003\ \mu_{\mathrm{N}}$. By taking into account the diamagnetic and paramagnetic corrections, the Knight shift of ^{13}O in a Pt metal was determined to be $+(4.23 \pm 0.14) \times 10^{-3}$. This result was consistent with the value calculated from the Korringa-relation and the observed spin-lattice relaxation time $T_1 = 9.7^{+2.6}_{-1.7}$ ms.

The quadrupole coupling constant of ^{13}O in TiO_2 (c // H_0) was measured by detecting β-NQR in which the AFP method was used for the determination of the $Q(^{13}\mathrm{O})$ value. For the identification of the implantation site of ^{13}O in the TiO_2 crystal, β-NQR of short-lived ^{19}O($I^{\pi} = 5/2^{+}$, $T_{1/2}$ = 27.0 s) was detected,

which is another O isotope suitable for determining the final sites of the implanted O ions in TiO_2 by detecting β-NMR. It was found from this β-NQR study, that the site of the present ^{13}O corresponding to the observed β-NQR peak was from those ^{13}O in an interstitial site in TiO_2. Using the spectra of ^{19}O and ^{13}O in the interstitial site, the ratio of the quadrupole moment of ^{19}O and ^{13}O was determined. Where the quadrupole moment of ^{19}O was given from the ratio of the two coupling constants of ^{19}O and stable isotope ^{17}O in the substitutional site of O in TiO_2, and the known $Q(^{17}O)$ value of the ^{17}O. Thus the values of $|Q(^{13}O)|$ and $|Q(^{19}O)|$ have been determined to be 11.0 ± 1.6 mb and 3.6 ± 0.5 mb, respectively. Presently obtained $Q(^{19}O)$ is consistent with the previous result obtained by Matsumoto et al.

The present quadrupole moments were compared with the theoretical predictions. The present $\mu(^{9}C)$ value is far different from the shell model prediction (-1.59 μ_N) calculated by the OXBASH with Cohen-Kurath model and CKPOT as the two-body effective interaction parameters, where g-factors of free nucleons were used. On the other hand, $\mu(^{9}Li)$, which is the mirror nucleus of ^{9}C, and the present $\mu(^{13}O)$ are successfully reproduced by the shell model calculation with the same conditions. The spin expectation value of ^{9}C - ^{9}Li pair was also extracted from their magnetic moments by assuming g-factors of free nucleons for the bound nucleon. The value $\langle\sigma\rangle = 1.44$ was obtained, which is far larger than that from the shell model calculation, $\langle\sigma\rangle = 1.07$ with the effective g-factors for the bound nucleons determined experimentally from the doubly closed shell ±1 nucleon nuclei around A=16. Advanced shell model calculation including higher order configuration mixing and more reliable relativistic correction is urged to clarify the present anomaly and renormalizaton of g-factors.

The predicted $Q(^{13}O)$ value, by OXBASH with Cohen-Kurath model and the effective charge of nucleons ($e_p^{eff} = 1.3e$ and $e_n^{eff} = 0.5e$) was +16 mb. The shell model calculation performed preliminary by Kitagawa, in which the potential depth was adjusted to reproduce the one proton separation energy, was not only sucessfully reproduced the discrepancy of the OXBASH calculation of $Q(^{13}O)$, but showed the overall agreement with the experimentally determined quadrupole moments of p-shell nuclei. From the wave function of ^{13}O obtained in

his calculation, the spatially extension of the proton density distribution and the enhancement of the proton root mean square radius were also given. Therefore, the existence of the proton halo in ^{13}O is strongly suggested.

Contents

Acknowledgments

It is a pleasure and an honor for the author to express his gratitude to all who have helped to make the present work successful:

Professor T. Minamisono for his proposing the present study, giving the continuous guidance and the discussions during the present study.

Professor Y. Nojiri for his constant collaboration, discussions and encouragement.
Associated Professor K. Matsuta for his constant guidance, collaboration and the discussions.
Research Associate M. Fukuda for his constant collaboration, discussions and encouragement.

Chief Scientist I. Tanihata and Senior Scientist T. Kobayashi at RIKEN for their management on the experiments in RIKEN and discussions.
Dr. S. Fukuda for his advice on the calculation of electromagnetic moments and his participation on the β-NMR measurements at RIKEN.
Dr. S. Momota, Dr. K. Yoshida, Dr. A. Ozawa and Dr. T. Suzuki for their participation on the β-NMR measurements at RIKEN and discussions.

Mr. M. Fujimaki and Mr. H. Kumagai for their technical supports on the experiment at RIKEN.

Dr. J.R. Alonso, Dr. G.F. Krebs and Dr. T.J.M. Symons for their supports and discussions.

Dr. H. Kitagawa and Professor H. Sagawa for the discussion and the shell model calculations on the nuclei in p-shell region.

Associated Professor S. Takeda for the managements of FT-NMR measurements

and the discussions on analysis of FT-NMR spectra.
Associated Professor S. Miyajima for kindly offering the equipment for high resolution FT-NMR at IMS and the discussions on FT-NMR measurements.

Mr. M. Yoshida for the management of the synthesis of the crystal of ^{17}O enriched TiO_2.
Mr. Y. Murayama and Mr. Y. Kano at Earth Seiyaku co. ltd. for their synthesis of the crystal of ^{17}O enriched TiO_2.

Professor H. Akai for discussing and calculating the hyperfine interactions of light impurities in metals.

Mr. Y. Takahashi for his constant technical supports and developments on the equipment, especially on Van de Graaff accelerator, and for his encouragement.

Mr. M. Sakamoto, Mr. H. Iwata and T. Mizuta for their technical support and encouragements.
Mr. K. Onishi for his support on computing.

Dr. T. Ohtsubo and Dr. M. Mihara for their participation in the experiments and the discussions.

K. Sato for the KKR calculation of the hyperfine interactions of O in TiO_2 and his participation on the β-NMR measurements at RIKEN.
T. Miyake, T. Onishi, M. Sasaki, Dr. T. Yamaguchi, A. Harada, T. Fukao, Y. Matsumoto and K. Minamisono for their participation on the β-NMR measurements at RIKEN.

Dr. T. Izumikawa and Y. Maruyama for their supports in the experiments at Van de Graaff facility.

Mr. M. Nakazato for his discussions and encouragement.

Ms. K. Ohsawa for her business managements.

My parents for their continous supports and encouragements.
Ms. Y. Takata for her continuous support and encouragement.

Last, not the least, Professor K. Nagashima, Professor T. Kishimoto and
Associate Professor T. Sato for their encouragements.

1. Introduction

The nuclear structure studies on the nuclei far from the stability line have been one of the interesting topics in the forefront of nuclear physics. Since the last nucleon is loosely bound for these drip-line nuclei and since the numbers of proton and neutron are very much different, their structures are expected to be different from those around the stable line. Their loosely bound valence nucleons may be responsible for the halo structure in those nuclei, and thus the interactions of nucleons at such low nucleon density region should be different from those in tightly bound nuclei. It is clear that the recent developments on the radioactive beam technique have made possible to provide us with those large T_z nuclei near neutron and proton drip-lines for the experimental study.

Many interesting features have already been disclosed for such light nuclei in the drip-line region. For example, the halo structure, one of the significant feature, has been found on the neutron drip-line nuclei such as ^{11}Li, ^{11}Be and ^{14}Be from the measurement of the interaction cross section at high energy (~800*A* MeV) by Sugimoto and Tanihata at LBL [1].

In the proton drip-line side, it was believed that a proton halo in proton rich nucleus was suppressed by the existence of repulsive Coulomb force and centrifugal force in the nucleus. The interaction cross section measurement at 800*A* MeV by Tanihata et al. [1] showed no signals of proton halo, i.e., no vivid enhancement of interaction cross section was observed.

Since the cross section measurements at high energy employed by Tanihata are designed mainly to observe the total matter distributions and since such a suppressed proton halo would be only a small fraction of the total matter distributions, their result did not simply deny the existence of halo-like structure in proton drip-line nuclei. As a matter of fact, Minamisono pointed out the possibility for the detection of proton halo through the electric quadrupole moment. Namely, as long as the core of a nucleus is spherical, the quadrupole moment dominantly reflects the angular and radial distributions of valence protons. Especially in the case of ^{8}B, it is expected that the proton distribution swells out radially in this nucleus because one proton separation energy of ^{8}B is as

small as ~ 0.14 MeV while that of one neutron separation energy is as large as ~ 13 MeV. Minamisono et al. measured the quadrupole moment of ^{8}B [2-4] and found its quadrupole moment twice as large as compared with the result predicted by the conventional shell model calculation. From the good agreement of the experimental result with the shell model calculation in which the parameters of the Woods-Saxon potential were adjusted to reproduce the one proton separation energy, they concluded the existence of halo structure in ^{8}B [2, 3]. Following their work, many theoretical and experimental studies are employed to extend their study and to understand the structure of the proton drip-line nuclei, especially on ^{8}B. Another approach to confirm the halo structure is now in progress by Osaka group. They measured interaction cross sections of light proton drip-line nuclei at ~ 40*A* MeV, which is much lower energy compared with the previous work done by Tanihata [1]. In this energy region, the contribution of proton halo to the interaction cross section is expected to be enhanced because of the larger nucleon-nucleon interaction cross section at this energy region.

Halo structure means that the valence nucleons move around in an extended radial space with low matter density space compared with those for the usual nuclei, in which all nucleons are deeply bound. Therefore, the *g*-factors of the last nucleon is expected to be modified because the limitation of the meson cloud distribution to the last nucleon or the interactions of nucleons in low matter density region should be different from those in around the stable line. Furthermore, we have to confirm if the understanding of the shell structures, well established in the stable and ones near the stable lines, holds for the ones far from the stability lines.

For the clear understanding of nuclear structures and the interactions of nucleons in low matter density of these exotic nuclei, it is very important to study their electromagnetic moments which reflect the angular momenta of the valence nucleons inside the nuclei. For the isospin doublet nuclei with $T = 1/2$, Sugimoto elegantly showed that the spin expectation values could be deduced from the magnetic moments of a mirror pair [5].

The same procedure of analyses applied to drip-line nuclei must be

important for the understanding of their structures. Regardless of their importance, the electromagnetic moments have been measured on the nuclei around the $N = Z$ line on the nuclear chart, as shown in Fig. 1-1. In particular, however, none of the electromagnetic moments of the nuclei with T_z = -3/2 nuclei have been studied because of the difficulty of the production of and creation of polarization in such unstable nuclei far from the stability line, while those of neutron rich nuclei have been relatively studied well.

Only the projectile fragmentation process in high energy heavy ion collision is the practical way to produce the nuclei far from the stability line, i.e., the nuclei even with nuclear lifetime shorter than one μs. Tanihata et al. Successfully developed the technique to measure interaction cross sections of such unstable nuclides with various stable target nuclides at Lawrence Berkeley Laboratory [1]. Their method was to employ the unstable beams directly, i.e., during the flight of the unstable nuclei, for the measurement. People in Osaka group kept working on the unstable beam to apply it for wider interdisciplinary regions nuclear science and other sciences. They utilized the technique to study the property of obtained nuclei after implanted in matters. They developed a projectile fragment separator at LBL and succeeded to obtain the secondary beam of such nuclei [6, 7]. Furthermore, Matsuta et al. succeeded to obtain the polarized nuclear beam via the projectile fragmentation process by selecting the momentum and angle of the ejected nuclei at intermediate energy as high as 106*A* MeV at LBL [8]. Asahi et al. found the polarized nuclear beam can be also obtained in the relatively lower energy region of 40*A* MeV [9]. Their results mean the β-NMR technique can be applied to the selected nuclides for the electromagnetic moments measurements. Recently, following the success of Osaka group at LBL, high intensity and high quality radioactive beam of drip-line nuclei become available at some facilities such as RIPS (RIken Projectile Fragment Separator) at RIKEN. RIPS is well known as a very powerful tool to reach the nuclei far from the stability line and many studies on these nuclei have been employed with this facility. Another example is shown at the National Institute of Radiological Sciences (NIRS), where Kanazawa et al. have constructed a new secondary beam separator.

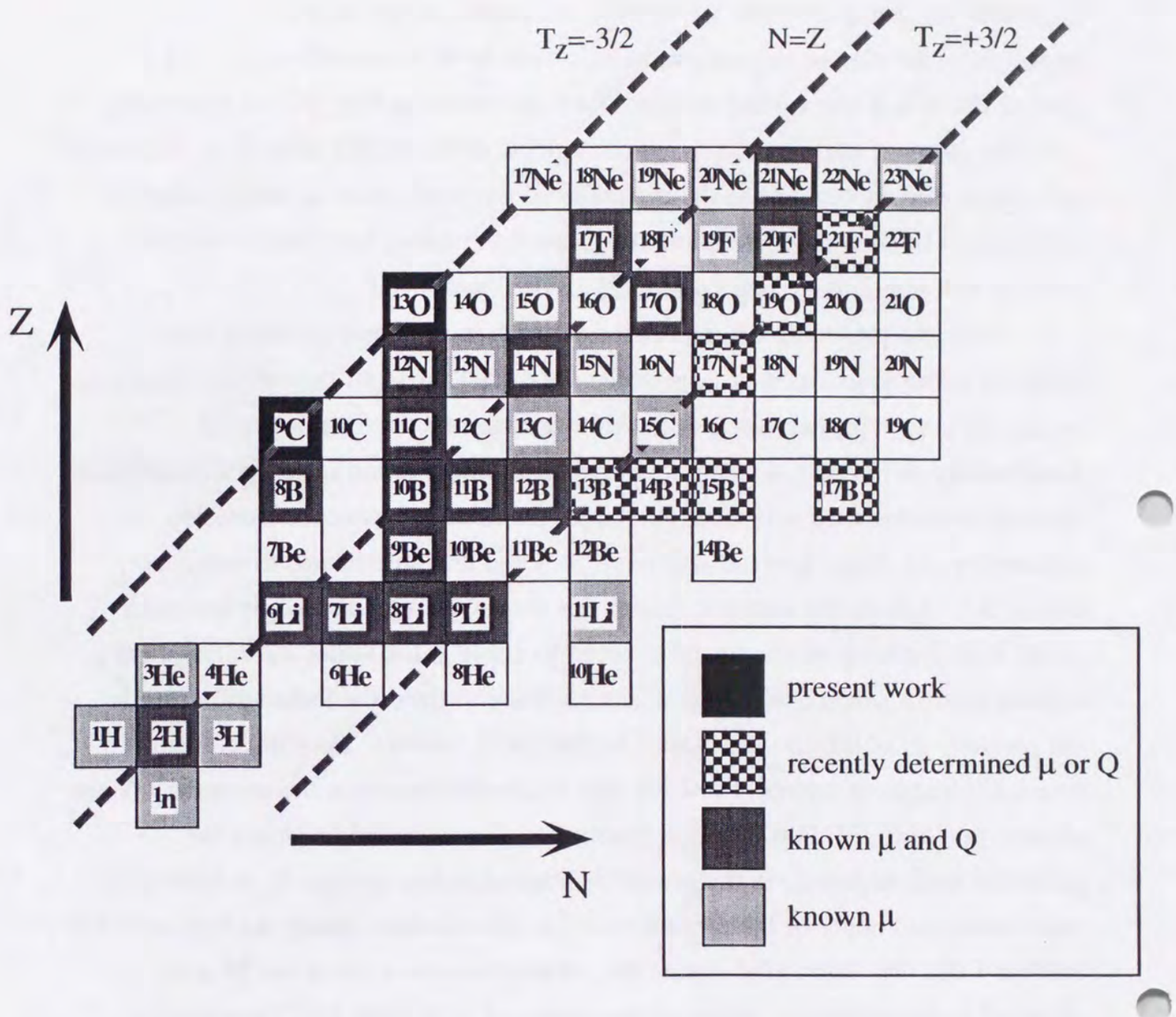

Fig. 1-1. Electromagnetic moments of light nuclei. None of the electromagnetic moments of T_z= -3/2 nuclei were known before the present work.

The β-NMR technique, starting from the pioneering work of the magnetic moment measurement of ^{17}F by Sugimoto [10], has been applied and proven to be a very effective method for the determination of electromagnetic moments of many unstable nuclei. This is a kind of NMR technique in which the NMR resonance is monitored by the asymmetric β-ray distribution from the polarized short-lived β-emitting nuclei implanted in an implantation medium.

The key concept of β-NMR technique is that the nuclear polarization is maintained in an implanted medium after the implantation process. Minamisono found that the implanted nuclei sat in some well defined sites of the crystal which were far from the defects produced by the ion itself at low temperature [11]. In other words, the nuclei sat in a perfect crystal unit cell regardless of their large kinetic energies in the implantation.

Under the influence of an additional electric field gradient q to the strong external magnetic field, the resonance line of a nuclide with spin $I \geq 1$ split into $2I$ lines due to its quadrupole interaction with the q. Although the electric quadrupole coupling can be obtained from the interval of these resonance lines, this effect also causes the reduction of the sensitivity of the NMR detection because the only one of $2I$ lines can be manipulated as long as the conventional β-NMR technique is applied. To overcome this disadvantage, a newly modified β-NMR, the beta nuclear quadrupole resonance (β-NQR) technique has been developed by Minamisono et al [12]. In this technique, all resonance lines are manipulated simultaneously and the magnitude of β-ray asymmetry change in the resonance detection is as large as that without the electric quadrupole interaction, regardless of its spin I. Therefore, full manipulation of the polarization of nuclei with large spin I has become possible and the required beam time for the measurement is drastically reduced to ~ 1/250 for the case of $I = 3/2$, compared with the case detected by the conventional technique, which was used in the measurement of $Q(^{17}\mathrm{F})$.

In the detection of β-NMR, the knowledge on hyperfine interactions between nuclei and implantation media is required. The nuclei we study are implanted in the media and they feel crystalline electromagnetic fields produced in the media. It should be noted that the local electromagnetic fields produced in

the crystal can be too strong to produce artificially. Our group noticed the importance to utilize such hyperfine fields for various studies and we have studied such interactions since we started the β-NMR measurements. Now, we have a huge compilation of the experimental and theoretical knowledge of the hyperfine interactions between the nucleus and electrons in a variety of implantation media such as metals, semiconductors, ionic crystals or even liquid helium. With these knowledge, suitable substances for high precision measurements of the electromagnetic moment can be chosen as the implantation medium and one can evaluate the magnitude of magnetic shielding factor or the electric field gradient where the nucleus is caught in. Since the quadrupole moment of ^{13}O has been derived from the quadrupole coupling constant in a TiO_2 crystal, the Fourier Transformed NMR (FT-NMR) measurement of the stable isotope ^{17}O in TiO_2 for the determination of the electric field gradient at O site in TiO_2 is employed in the present study.

This systematic study will provide important information for the structures and the matter distributions, such as halo structure, of proton drip-line nuclei or the renormalization effects on the *g*-factors of valence nucleon caused by the nucleon-nucleon interactions in low matter density region. This study is expected to clarify the peculiarity of these exotic nuclei.

We combined the radioactive beam technique with the β-NMR technique to obtain a new powerful method for the study on nuclear spectroscopy. We obtained the proton drip-line nuclei through the projectile fragmentation process. The projectile fragmentation separator was used for selecting the nuclei and for the momentum selection obtaining the polarized beam. The polarization was kept in a well defined site inside the crystal under a strong magnetic field. We are able to perform systematic studies for the electromagnetic moments of proton drip-line nuclei.

In this paper, the measurements of magnetic moments of ^{9}C and ^{13}O, and the quadrupole moment of ^{13}O are reported. β-NQR measurement of ^{19}O in TiO_2 for the study of the implantation sites of O in TiO_2 is also introduced, where the quadrupole moment of ^{19}O is determined again with the result of the present study. Using those magnetic moments combined with those of their

mirror partners, the nuclear structure and possible renormalization of g-factors inside the drip-line nucleus is discussed. With the shell model calculation paying attention to the binding energy by Kitagawa, the possibility of the halo structure in ^{13}O is discussed. The FT-NMR measurement of the stable isotope ^{17}O in TiO_2 also reported in the appendix.

2. Electromagnetic moments of a nucleus

2.1. Magnetic moment

2.1.1. Single particle model

Any nuclei with spin I = 1/2 or higher have magnetic moments $\vec{\mu}$, the vector sum of contributions from orbital motion and the spin of nucleon inside the nucleus.

According to the single particle model, all properties are represented by the last nucleon and the rest of nucleons form a core of 0^+ state. The magnetic moment μ_S is determined by the inherent magnetic moment and the orbit of the last nucleon as follows.

$$\mu_S = g_s \langle s_z \rangle + g_l \langle l_z \rangle \quad \text{in } \mu_N, \text{ and}$$
$$I = \langle s_z \rangle + \langle l_z \rangle \qquad (2\text{-}1)$$

where I is the total spin of the nucleus, g_s and g_l denote the spin and orbital g-factors, $\langle s_z \rangle$ and $\langle l_z \rangle$ are the expectation values of spin and orbital angular momenta for the last nucleon, respectively. g_s = 5.585 (-3.826) and g_l = 1 (0), which are values for free nucleons, are used for the last proton (neutron). Under the single particle model, I is equal to the total angular momentum j of the last nucleon.

In this single particle model, depending on the total angular momentum of the last nucleon which is either $j = l + 1/2$ or $l - 1/2$, $\langle s_z \rangle$ is written as follows in a quantum mechanics treatment,

$$\langle s_z \rangle = \frac{j(j+1)+s(s+1)-l(l+1)}{2j(j+1)} \cdot j = \begin{cases} \frac{1}{2} & \text{for } j = l + \frac{1}{2} \\ -\frac{2l-1}{2(2l+1)} & \text{for } j = l - \frac{1}{2} \end{cases} \qquad (2\text{-}2)$$

Therefore, the magnetic moment μ_s is given as,

$$\mu_S = \begin{cases} \frac{1}{2} g_s + g_l l & \text{for } j = l + 1/2 \\ g_s \frac{2l-1}{2(2l+1)} + g_l \frac{l(2l-1)}{(2l+1)} & \text{for } j = l - 1/2. \end{cases} \qquad (2\text{-}3)$$

The values given by the equations are called Schmidt values. In Fig. 2-1 the Schmidt value are compared with the experimental values. As shown, almost all of the experimental result are distributed between the Schmidt lines for proton (neutron) in $j = l + 1/2$ and $j = l - 1/2$ states and the measured values lie closer to each line for their single particle states than the other line in all cases. Therefore, the Schmidt value qualitatively explains the experimental magnetic moment.

2.1.2. Sum moments of mirror nuclei

The nuclei are not simply described by the single particle model because the core itself is no longer "hard". This means the core can be excited and the wave function of the real nucleus is the mixture of several states. Despite this complication, isospin symmetry gives us quite useful information because the strong force, which governs the interactions between nucleons, is charge independent and, therefore, the nuclear structures are identical between the mirror pairs.

Once the magnetic moments of mirror pairs are determined, $\langle s_z \rangle$ and $\langle l_z \rangle$ can be extracted assuming mirror symmetry of the nuclear structure. By introducing the isospin operator τ_3, the operators for choosing the proton and neutron can be written as $(1 \pm \tau_3)/2$, respectively. So, the magnetic moment of a nucleus can be written as

$$\mu = \langle j,j | \sum_i \left[\frac{(1-\tau_3^{(i)})}{2} \left(g_l^{(p)} l_z^{(i)} + g_s^{(p)} s_z^{(i)} \right) + \frac{(1+\tau_3^{(i)})}{2} \left(g_l^{(n)} l_z^{(i)} + g_s^{(n)} s_z^{(i)} \right) \right] | j,j \rangle .$$

(2-4)

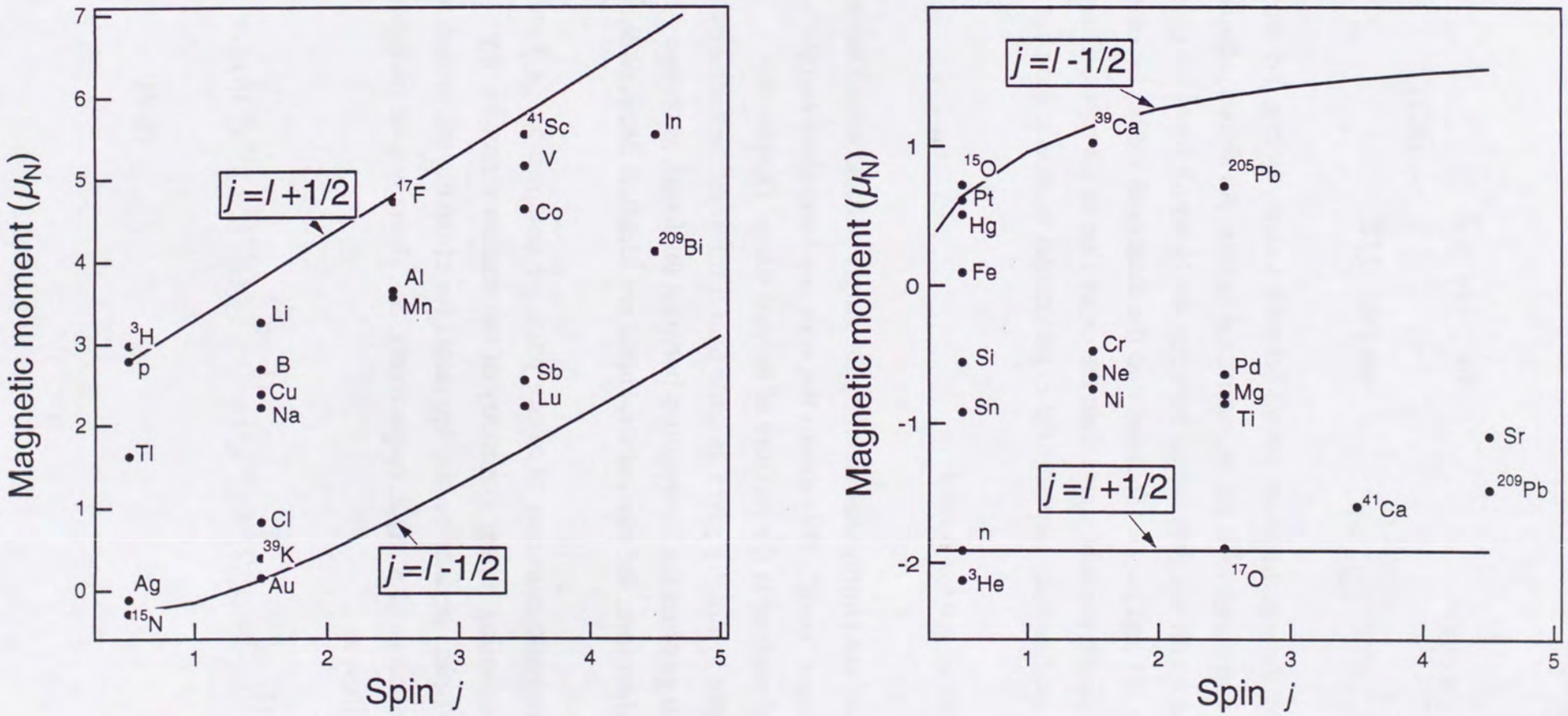

Fig. 2-1. Magnetic moments of proton-odd and neutron-odd nuclei. The solid lines in the graphs are the Schmidt values. Almost all magnetic moments lie between Schmidt lines. The magnetic moments of LS doubly closed shell ±1 nucleon nuclei are very close to Schmidt values, while *jj* closed shell ±1 nucleon nuclei, such as ^{209}Bi, are far from Schmidt lines.

The sum of i is taken for all nucleons. The notations l and s denote the angular momenta for orbital and spin, p and n for proton and neutron, respectively.

Then, the isoscalar moment $\mu^{(0)}$, which is defined as a half of the sum moment of the mirror pair and is conserved under the isospin inversion, is written as

$$\mu^{(0)}=\frac{1}{2}\left(\mu\left(T_z=+T\right)+\mu\left(T_z=-T\right)\right)$$
$$=\left(\frac{\left(g_l^{(p)}+g_l^{(n)}\right)}{2}\left\langle\sum_i l_z^{(i)}\right\rangle+\frac{\left(g_s^{(p)}+g_s^{(n)}\right)}{2}\left\langle\sum_i s_z^{(i)}\right\rangle\right)\equiv g_l^{(0)}\left\langle l_z\right\rangle+g_s^{(0)}\left\langle s_z\right\rangle. \tag{2-5}$$

Combining Eq. 2-5 with the relation $I=\langle l_z\rangle+\langle s_z\rangle$, expectation values $\langle l_z\rangle$ and $\langle s_z\rangle$ are obtained separately as

$$\langle s_z\rangle=\frac{2\left(\mu^{(0)}-g_l^{(0)}I\right)}{g_s^{(0)}-g_l^{(0)}},\qquad \langle l_z\rangle=I-\langle s_z\rangle. \tag{2-6}$$

The isovector moment, which is defined as the subtraction of mirror moments and is changing its sign by the isospin inversion, is written as,

$$\mu^{(1)}=\frac{1}{2}\left(\mu\left(T_z=+T\right)-\mu\left(T_z=-T\right)\right)$$
$$=\left(\frac{\left(g_l^{(p)}-g_l^{(n)}\right)}{2}\left\langle\sum_i \tau_3 l_z^{(i)}\right\rangle+\frac{\left(g_s^{(p)}-g_s^{(n)}\right)}{2}\left\langle\sum_i \tau_3 s_z^{(i)}\right\rangle\right)\equiv g_l^{(1)}\left\langle\tau_3 l_z\right\rangle+g_s^{(1)}\left\langle\tau_3 s_z\right\rangle, \tag{2-7}$$

where τ_3 is the isospin operator. In this case, simple discussion like in the case of isoscalar moment is not so easy because the equation $\langle\tau_3 l_z\rangle+\langle\tau_3 s_z\rangle=\pm I$ does not necessarily hold.

2.2. Corrections to the Schmidt values

Followings are the main reasons responsible for the deviation of the measured magnetic moments from the Schmidt values.

2.2.1. Configuration mixing

The deviations between the Schmidt lines and experimental results have following trends:

(i) The deviation becomes larger as the mass number of nucleus becomes larger.

(ii) The measured magnetic moments of doubly closed shell ±1 nucleon nuclei show good agreements with the Schmidt value. The agreement becomes better if the core is LS doubly closed shell such as ^{16}O or ^{40}Ca compared with the case of *jj* closed shell such as ^{208}Pb.

(iii) The measured magnetic moments are always close to Schmidt value for $I^{\pi} = 1/2^{-}$ nuclei.

These trends can be explained by introducing the configuration mixing. If the closed core which is filled up to $j = l + 1/2$ and the last nucleon is in $j = l - 1/2$ orbit, the core can be easily excited to one-particle-one-hole state due to the spin-dependent components in the nuclear force, $V_{\sigma}(r_{12})(\vec{\sigma}_1 \cdot \vec{\sigma}_2)$. Therefore, the wave function of the nucleus is easily mixed with the one for $j = l - 1/2$ state.

According to Bohr and Mottelson [13], the degree of correction for the configuration mixing can be estimated with the first order perturbation theory as

$$\delta g \approx -\frac{4\langle V_\sigma \rangle}{\Delta} \sum_m \langle j=l+1/2,\ m|\mu_z|j=l-1/2,m\rangle \langle j=l-1/2,\ m|\sigma_z|j=l+1/2,m\rangle$$

$$= -\frac{2\langle V_\sigma \rangle}{3\Delta}(g_s - g_l)\langle j=l-1/2||\mu_z||j=l+1/2\rangle^2$$

$$= -\frac{8}{3}\frac{\langle V_\sigma \rangle}{\Delta}\frac{2l(l+1)}{2l+1}(g_s - g_l), \qquad (2\text{-}8)$$

where $\langle V_\sigma \rangle$ is the magnitude of the spin-dependent field, Δ is the energy gap between $j = l + 1/2$ and $j = l - 1/2$ states.

Advanced shell model calculation codes including this configuration mixing effect are available. In these calculation codes, the configuration mixing effects are calculated with the realistic potential and interactions between nucleons.

OXBASH [14], which is one of the most popular shell-model calculation codes, is developed by the Oxford, Buenos Aires and MSU groups. This code gives matrix elements of

i) 1- and 2- particle parentage amplitudes
ii) 1- and 2- body transition densities
iii) direct overlaps of two wave functions, and
iv) cluster overlaps involving three wave functions.

The outline of the calculation procedure is as follows. An *m*-scheme Slater determinant basis for a particular number of particles and a particular parity for total I_z and T_z is produced from the given single particle states. Restrictions can be made in both individual *I*-orbits and major shells. Then the basis states with good spin and isospin are produced by a projection technique.

The Hamiltonian matrix is produced from above basis states, single particle energies and two-body matrix elements. The two-body matrix elements are already responsible for the configuration mixing. These parameters are phenomenologically determined so that the calculated results reproduces the experimental data for the objective model space. For example, several parameter sets such as CKPOT given by Cohen and Kurath [15] are available in 1p model

space, where ^{9}C and ^{13}O are included. The eigenstates and eigenvectors of this Hamiltonian are then obtained to calculate parentage amplitudes and one- or two-body transition densities. i) ~ iv) are calculated from these obtained amplitudes and densities.

Observable values such as electromagnetic moments are obtained from i) ~ iv) with additional calculation codes given with the OXBASH.

In the pioneering work of Sugimoto, $\langle\sigma\rangle \equiv 2\langle s_z\rangle$ for $T = 0$, 1/2 and 1 for mirror pairs up to $A = 41$ were deduced from the magnetic moments of mirror nuclei via Eq. 2-6 under the assumption that the g-factors of the nucleons inside the nucleus is not renormalized. $\langle\sigma\rangle$ derived from the present magnetic moments in the same manner as Sugimoto are shown in Fig. 2-2. The value of $\langle\sigma\rangle$ gradually reduces to 0 as the nucleus goes far from the doubly closed shell such as ^{16}O or ^{40}Ca. The comparison of $\langle\sigma\rangle$ extracted from the experimentally determined magnetic moments and from the shell model calculations [14, 16] is also shown in this figure. Their results well reproduce the trends of $\langle\sigma\rangle$ extracted by Sugimoto.

2.2.2 Mesonic exchange current

The anomalous g-factors of nucleons in free space are understood as the result of the meson cloud around the nucleon. Since this meson cloud is expected to be blocked with others inside the nucleus, the g-factors of nucleons should be changed. This effect is understood as the exchange of mesons for the propagation of nuclear force between nucleons and the main reason for the deviation of the magnetic moments of ^{3}H and ^{3}He to outside the Schmidt lines.

The magnetic moment operator can be written as

$$\vec{\mu} = \vec{\mu}_{\text{free}} + \vec{\mu}_{\text{ex}}$$
$$\vec{\mu}_{\text{free}} = \sum_i \left(g_l^{(0)} \vec{l} + g_s^{(0)} \vec{s} + g_l^{(1)} \vec{\tau l} + g_s^{(1)} \vec{\tau s} \right), \qquad (2\text{-}9)$$

where the isoscalar and isovector g-factors in $\vec{\mu}_{\text{free}}$ are $g_l^{(0)} = g_l^{(1)} = 0.5$, $g_s^{(0)} = 0.88$ and $g_s^{(1)} = 4.71$, which are for free nucleons. $\vec{\mu}_{\text{ex}}$ is the two-body exchange

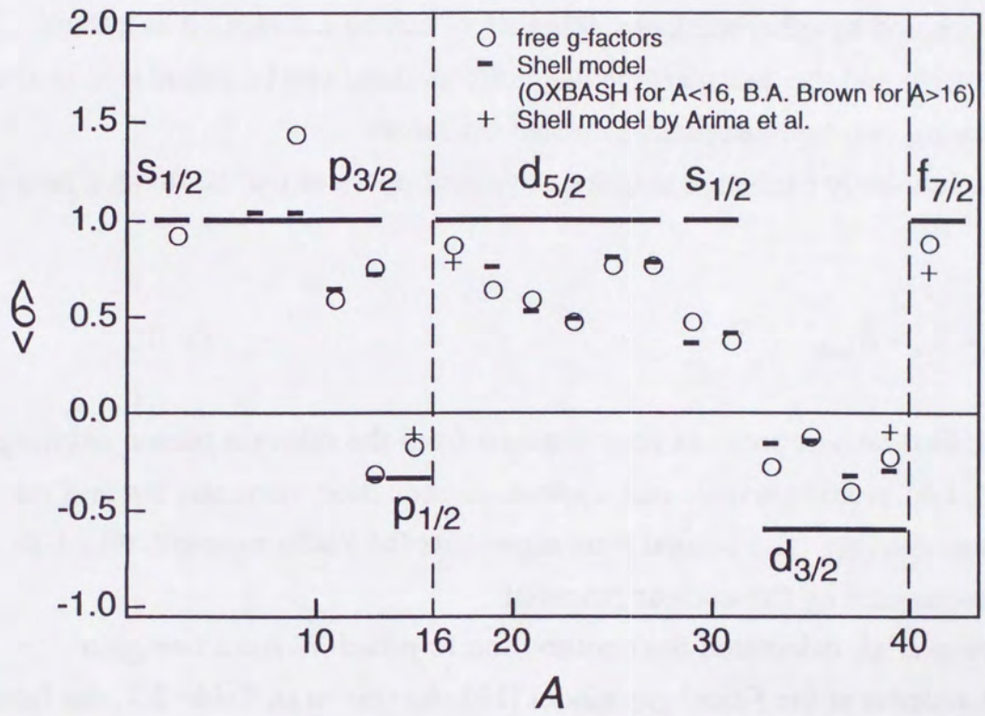

Fig. 2-2. Spin expectation values of mirror pairs up to $A = 41$. OXBASH calculation was performed in the p-model space with CKPOT as effective interaction. Theoretical results for $A > 16$ are calculated by Brown and Wildenthal [16]. In the shell model calculation by Arima [18] for doubly closed shell ± 1 nucleon nuclei, contributions from the second order configration mixing and the mesonic exchange currents are taken into account.

magnetic moment operator. The deviation from the magnetic moment from its single particle value is written as the matrix element between perturbed nuclear states.

According to Miyazawa [17], contribution of one pion exchange process describes the virtual meson cloud around a nucleon when the nucleon is put into medium because the nucleon is prohibited from making transitions to states already occupied by other nucleons. This effect can be interpreted as a Pauli blocking effect and the quasiparticle magnetic moment can be introduced instead of considering two-body exchange current operators.

The two-body exchange magnetic moment operator can be divided into two parts as,

$$\vec{\mu}_{ex} = \vec{\mu}_{int} + \vec{\mu}_{Sachs} \qquad (2\text{-}10)$$

The first term represents contributions from the relevant meson exchange processes, i.e., pionic current, pair current, Δ-excitation currents, $\omega\pi$ and $\rho\pi$ dissociation currents. The second term represents the Sachs moment, which is mainly determined by the nuclear potential.

Arima et al. calculated the contribution to g-factors from one pion exchange process in the Fermi gas model [18]. As shown in Table 2-1, the first term mainly affects the spin g-factors and Sachs moment only affects on the orbital part of isovector g-factor. They mentioned that the contribution of Δ-hole excitation is very large and that the degree of contribution very strongly depends on the Fermi momentum, while other contributions do not crucially depend on it.

2.2.3 Tensor correlation

There still remains the finite discrepancies between the experimental results and theoretical calculations although the first order configuration mixing satisfactory explain the most part of these deviations. For example, the first order configuration mixing should vanish in the magnetic moments of LS doubly closed shell ± 1 nucleon nuclei, but observed deviation is not zero. Mavromatis, Zamick

Table 2-1. Contribution to g-factors from one pion exchange process in Fermi gas model [18].

	δg_l	δg_s
Isovector		
Pair + pionic	0	0.108
Δ Excitation	0	-0.655
$\omega\pi$ Current	0	-0.104
Sachs moment	0.099	0
Sum	0.099	-0.650
Isoscalar		
$\rho\pi$ Current	0	-0.024

and Brown [19], and quite independently Ichimura and Yazaki [20] employed calculations in which the second order calculations and meson exchange currents were taken into account, but they obtained only very small second-order corrections. Shimizu, Ichimura and Arima recalculated the same effect, but paid attention to the intermediate states with the higher excited states up to $12\hbar\omega$ and tensor correlations. They found the necessity of the tensor correlations for the explanation of the quenching of the spin expectation values.

The correction of the present tensor correlation is described by adding the term $g_P[Y_2 \otimes \vec{s}]$ to the M1 operators [18]

$$\mu = g_s \langle s_z \rangle + g_l \langle l_z \rangle + g_P [Y_2 \otimes \vec{s}] \qquad (2\text{-}11)$$

where g_p is the spin tensor g-factor.

2.2.4. Relativistic effect

Since the velocity of the nucleon inside the nucleus is about one tenth of the light speed, the motion of a nucleon inside the nucleus should be treated relativistically using the Dirac equation for the detailed discussion of nuclear

magnetic moments. This effect is calculated by Ohtsubo et al. for the simple case [21], i.e., the square well potential of which depth is adjusted so as to give the experimental separation energy of the nucleon. Their results up to $A = 43$ is shown in Fig. 2-3. In their calculation, they mentioned that the relativistic correction depended on total angular momentum j, but not the orbital angular momentum l.

2.3. Quadrupole moment

The electric quadrupole moment is a measure of the extent to which the nuclear charge distribution deviates from spherical symmetry. The moment is defined as

$$Q=\langle I,M=I|Q_{\mathrm{op}}|I,M=I\rangle, \tag{2-12}$$

where the quadrupole moment operator is given as

$$eQ_{\mathrm{op}}=\int \rho_e(\vec{r})r^2\left(3\cos^2\theta-1\right)dv, \tag{2-13}$$

in terms of the charge density $\rho_e(\vec{r})$ in the nucleus.

In the shell model description, for a single proton in an orbit (nlj), one obtains

$$\begin{aligned} Q&=\langle j,m=j|r^2\left(3\cos^2\theta-1\right)|j,m=j\rangle \\ &=-\frac{2j-1}{2j+2}\langle r^2\rangle \end{aligned} \tag{2-14}$$

where the radial average is given as,

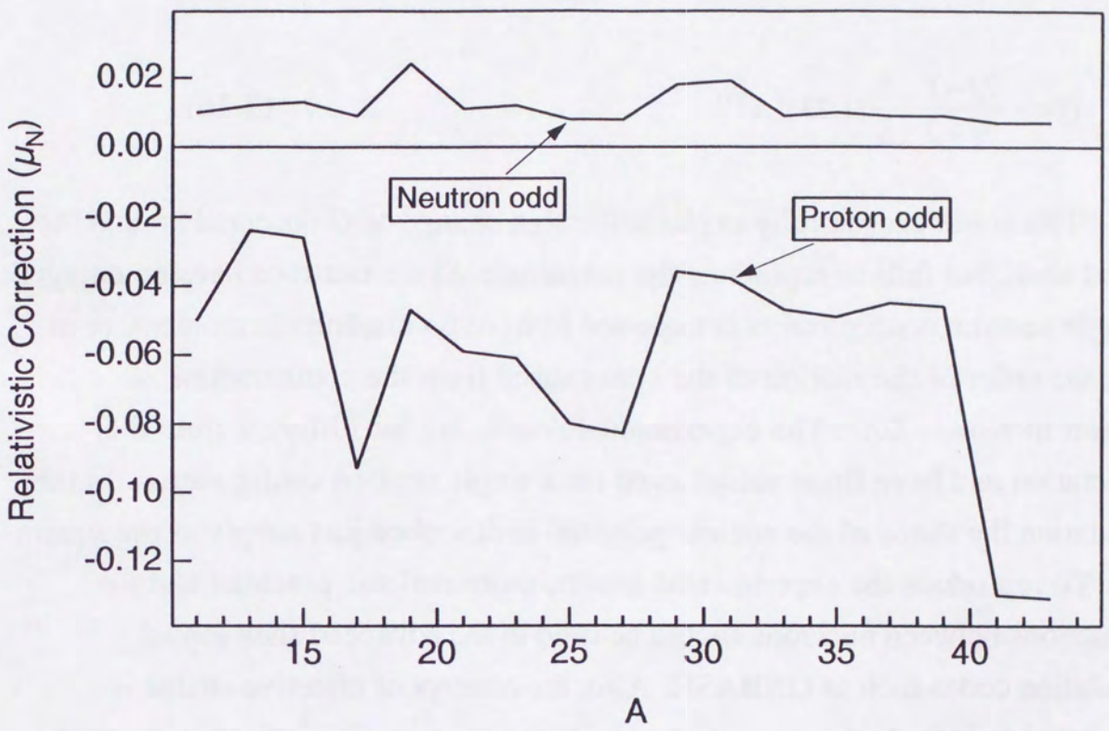

Fig. 2-3. Relativistic correction to the nuclear magnetic moment calculated by Ohtsubo et al [21]. The square well potential of which depth was adjusted to reproduce the experimental separation energy was used in this calculation.

$$\langle r^2 \rangle = \int_0^\infty r^4 \left(R_{nlj}(r)\right)^2 \mathrm{d}r. \qquad (2\text{-}15)$$

Here, $R_{nlj}(r)$ is the radial wave function. By taking the rough estimation of radius R of a mass A nucleus $R = 1.25A^{1/3}$ as $R_{nlj}(r)$ for the estimation of Q,

$$Q = -\frac{2j-1}{2j+2} \cdot \frac{3}{5} (1.25)^2 A^{2/3} \qquad (2\text{-}16)$$

This result successfully explains the sign change of Q observed around the closed shell, but fails to reproduce the magnitude. Since neutrons have no charge, a single neutron configuration is expected to have no quadrupole moment, or at most the order of the motion of the core caused from the counteraction of neutron motion, $\sim Z/A^2$. The experimental results are far different from this expectation and have finite values even for a single neutron configuration. In this calculation the shape of the nuclear potential is described just simply as the square well. To reproduce the experimental results, more realistic potential and the interactions between nucleons should be used in the advanced shell model calculation codes such as OXBASH. Also, the concept of effective charge is introduced to include the interactions inside the nucleus. This effective charge has been investigated in every nuclear shell region from the quadrupole moment and E2 transition probability. For $1p_{3/2}$ shell region, the effective charges were empirically estimated as $e_p^{eff} = 1.3e$ and $e_n^{eff} = 0.5e$.

The quadrupole moments of neutron-odd nuclei can be basically explained by these treatments. For example, the quadrupole moment of $^{11}_{6}C_5$ ($|Q_{exp}| = 34.3$ mb) is well accounted for by the value of +31.6 mb given from OXBASH[1] and the above effective charges, while it is expected to be 0 mb from the single particle model.

[1]The Cohen-Kurath model with CKPOT as the effective interaction was taken for the present OXBASH calculation.

3. Experimental principle

3.1. Nuclear magnetic resonance

A nucleus which has spin more than $I \geq 1/2$ interacts with external magnetic fields due to its magnetic moment. A free spin with an angular momentum $\vec{I}\hbar$ and a magnetic moment $\vec{\mu} = \gamma_N \hbar \vec{I}$ precesses around the axis which is parallel to the direction of the static magnetic field $\vec{H}_0$. This motion is written in the classical treatment as follows

$$\frac{d\vec{\mu}}{dt} = \gamma_N \vec{\mu} \times \vec{H}_0. \qquad (3\text{-}1)$$

When an additional magnetic field $\vec{H}_1$, which rotates at the angular frequency of $\vec{\omega}$, is applied perpendicular to $\vec{H}_0$, this equation includes the additional $\vec{H}_1$ term as,

$$\frac{d\vec{\mu}}{dt} = \gamma_N \vec{\mu} \times \left(\vec{H}_0 + \vec{H}_1\right). \qquad (3\text{-}2)$$

To make this equation simpler, motion of $\vec{\mu}$ is described in the frame which rotates at $\vec{\omega}_0$. Eq. 3-2 is rewritten as follows,

$$\frac{d\vec{\mu}}{dt} = \gamma_N \vec{\mu} \times \left\{\left(\vec{H}_0 + \frac{\vec{\omega}}{\gamma_N}\right) + \vec{H}_1\right\} \equiv \gamma_N \vec{\mu} \times \vec{H}_{\text{eff}}. \qquad (3\text{-}3)$$

This equation describes that $\vec{\mu}$ rotates around a static magnetic field $\vec{H}_{\text{eff}}$. One can find that $\vec{\mu}$ rotates around $\vec{H}_1$ if $\vec{\omega} = -\gamma_N \vec{H}_0$. This frequency is called "Larmor Frequency", $\vec{\omega}_L$. In this condition, the projection to z-axis of the spin becomes zero as seen in Fig. 3-1.

This phenomenon is also treated quantum mechanically. The Hamiltonian of a nuclear spin I with a magnetic moment of $\vec{\mu} = \gamma_N \hbar \vec{I}$ is written as

$$H_M = -\vec{\mu} \cdot \vec{H}_0 = -\gamma_N \hbar \vec{I} \cdot \vec{H}_0. \qquad (3\text{-}4)$$

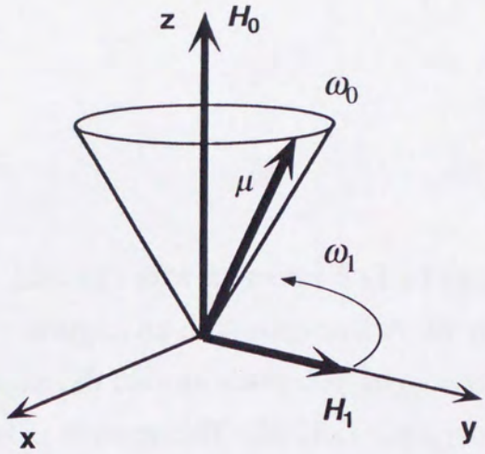

A spin is precessing around a strong magnetic field H_0 at the angular frequency ω_0. An additional weak rotating field $H_1(\omega_1)$ is applied to this system perpendicular to H_0.

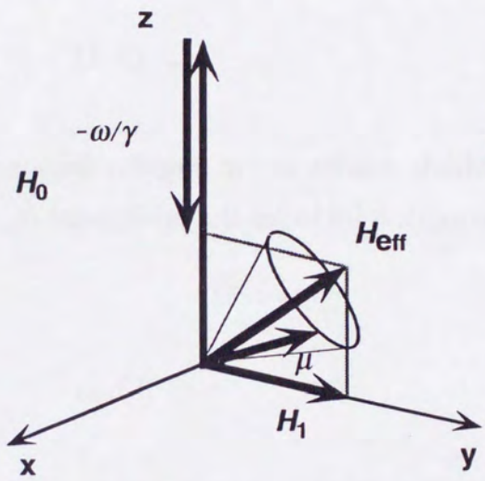

A spin is precessing around H_{eff} in the rotating frame fixed to H_1.

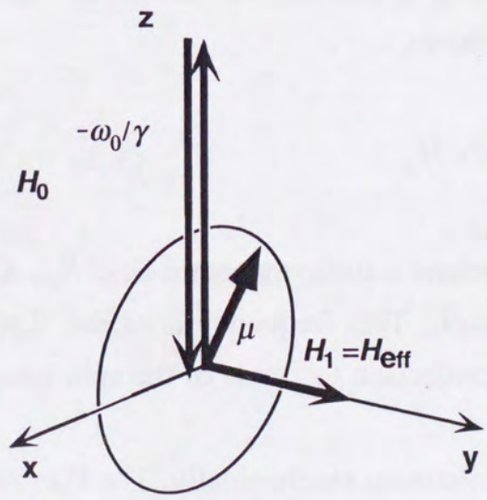

When $\omega_1=\omega_0$, H_{eff} is equal to H_1. Therefore the spin rotates around H_1 and the expectation value of the spin projection to z-axis becomes 0.

Fig. 3-1. Motion of a spin under the existence of a strong magnetic field (H_0) and an addtional RF field (H_1).

This Hamiltonian has $2I$ eigenstates and each state is characterized by magnetic quantum numbers $m = I, I-1, \ldots, -I$. The energy of each state is defined as

$$E_M(m) = -\gamma_N \hbar H_0 m. \qquad (3\text{-}5)$$

A transition between $|m-1\rangle$ and $|m\rangle$ can be induced by applying a photon which has energy corresponding to energy difference between these two states. This gap is equal to Larmor frequency under a pure magnetic interaction.

The definition of "Polarization" P of a spin ensemble is

$$P = \frac{\sum_m m p_m}{\sum_m p_m}, \qquad (3\text{-}6)$$

where m is the magnetic quantum number of the substate and p_m is the population of magnetic sublevel m. An RF field which is equal to the energy gap of neighboring states induces the transition between these states and the population of these states are interchanged as shown in Fig. 3-2. For the pure magnetic interaction case, all of the substates start transition simultaneously by applying an RF at Larmor frequency.

3.2. Depolarization:destruction of the polarization

Usually, the populations evolve to an equilibrium state while the RF is being applied. This is because of the existence of the local field, such as the dipolar field induced by surrounding nuclear magnetic moments as discussed in [22]. This equalization process is called the "depolarization", i.e., destruction of the polarization. If the RF of amplitude $H_1 = -\omega_1/\gamma$ is rotating at frequency ω in the plane perpendicular to H_0, the Hamiltonian with additional local field can be written as [22]

$$H = \hbar\omega_0 I_z + H_L + \hbar\omega_1 \left(I_x \cos\omega t + I_y \sin\omega t\right) \qquad (3\text{-}7)$$

where the ω_0 is the Larmor frequency and H_L is the Hamiltonian for the local

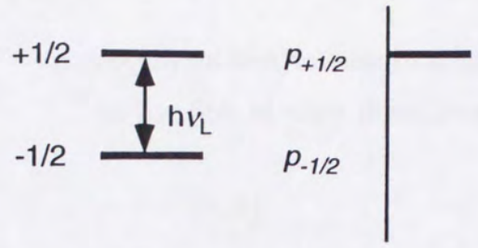

The energy levels of magnetic substates for spin I is split into $2I$ levels under the existence of a strong magnetic field. In the case of the present $I = 1/2$ system, the energy levels are splitted into two levels. For simplicity, only the +1/2 state is populated.

The transition between the magnetic substates of +1/2 and -1/2 occurs by applying the photon at the energy of $h\nu_L$.

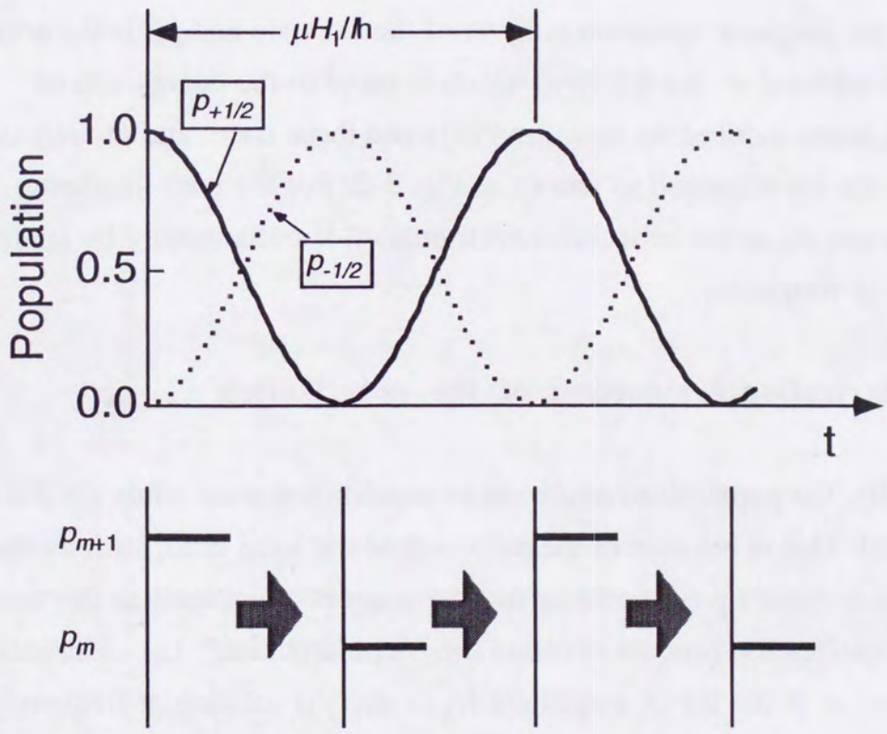

The populations of these two states are changing while applying photons to the system. The oscillation frequency of these population is $\mu H_1/\hbar$, which is equal to the rotating speed of spin around H_1 in the classical treatment.

Fig. 3-2. Quantum view of NMR for $I = 1/2$ system

field. In the rotating frame with angular frequency ω around H_0, the effective Hamiltonian is

$$\begin{aligned} H_{\text{eff}} &= \exp(i\omega I_z t) H \exp(-i\omega I_z t) - \hbar\omega I_z \\ &= \hbar\Delta I_z + H_L + \hbar\omega_1 I_x, \end{aligned} \tag{3-8}$$

where $\Delta = \omega_0 - \omega$.

If $\hbar\Delta$ is comparable to H_L, all terms are not negligible. This is a realistic estimation for the nucleus in a solid material, where the dipolar field induced by the surrounding nuclei is the order of 1 Oe. After the significant time duration, the system will evolve in the rotating frame to a state describable by a single spin temperature, that is by a density matrix of the form as

$$\sigma_{\text{R.F.}} = \exp(-\beta H_{\text{eff}}) / \text{Tr}\{\exp(-\beta H_{\text{eff}})\}$$

$$\therefore P_{\text{R.F.}} = \sum_m \frac{m \exp(-\beta E_{\text{eff}}(m))}{\text{Tr}\{\exp(-\beta E_{\text{eff}}(m))\}}, \tag{3-9}$$

where, $\sigma_{\text{R.F.}}$ and $P_{\text{R.F.}}$ are is the spin temperature and the polarization of the present system, $\beta = \frac{1}{k_B T}$ and $E_{\text{eff}}(m) = \langle m | H_{\text{eff}} | m \rangle$, respectively.
Since the differences of energy between neighboring eigenstates are at most the order of dipolar field, the differences of populations are negligibly small compared to the initial polarization (Fig. 3-3). The time constant for reaching equilibrium is of the order of $T_2 \approx \frac{\hbar}{H_L}$, typically the order of 100 μs ~ 1 ms [22].

3.3. Adiabatic fast passage (AFP) technique

As shown in Eq. 3-3, the nuclear magnetic moment precesses around the effective magnetic field $\vec{H}_{\text{eff}}$. If the angular velocity $\vec{\omega}$ of applied RF is swept over the resonance frequency at much slower speed than that of the precession of $\vec{\mu}$ around $\vec{H}_{\text{eff}}$, the magnetic moment is inverted as a result of the inversion of $\vec{H}_{\text{eff}}$ because $\vec{\mu}$ should stick to the motion of $\vec{H}_{\text{eff}}$ precessing around it. (Fig. 3-4). This is called adiabatic fast passage method (AFP) [23]. This technique has already

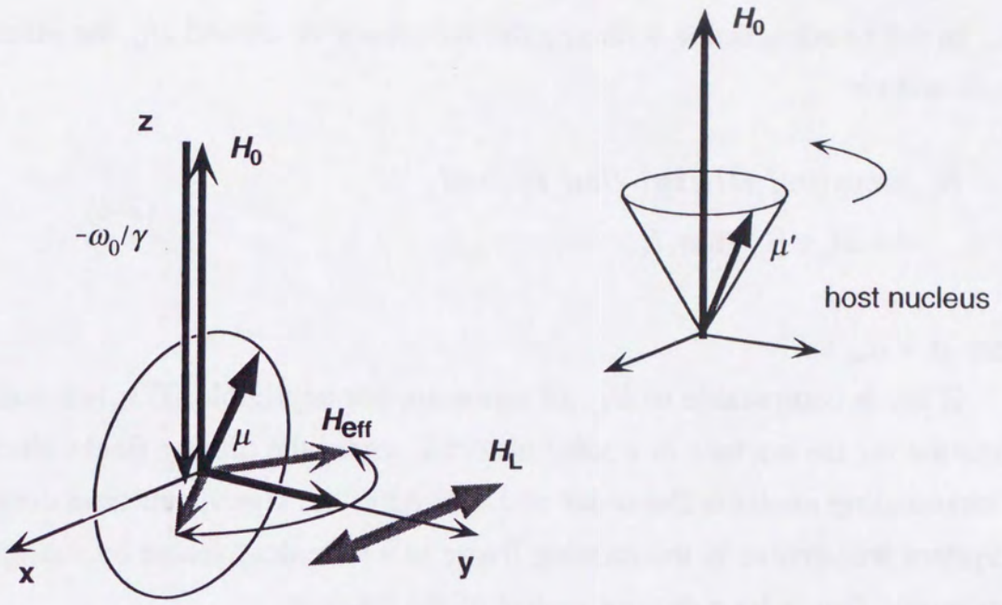

Due to the disturbance of the addtional dynamic dipolar field H_L, which is induced by the host nuclei , H_{eff} is no longer a good quantum axis.

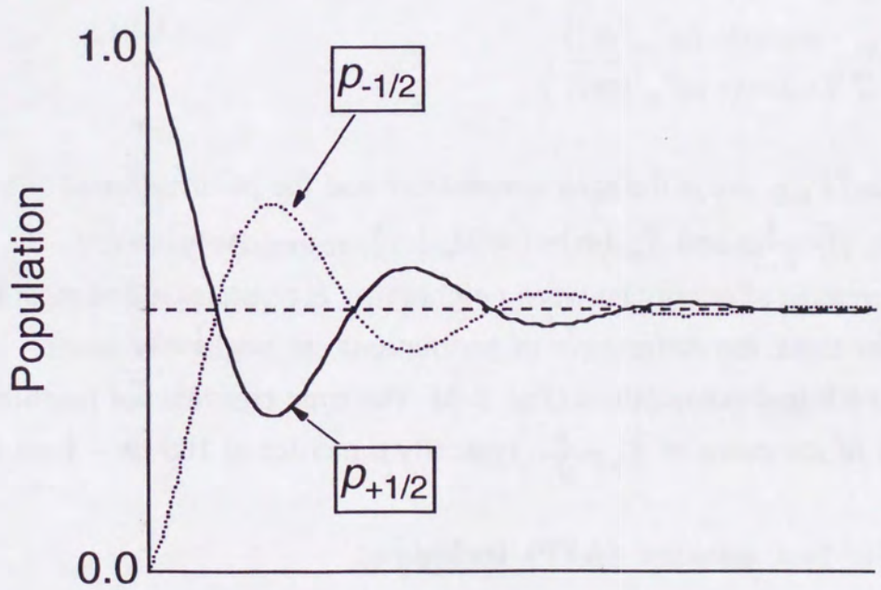

The populations of magentic substates evolve to a equibilium state due to the addtional dynamic dipolar field H_L. This is a typical oscllation of the populations for I = 1/2 system under the existence of H_L. Initially, only m = 1/2 state is populated.

Fig. 3-3. Depolarization Process

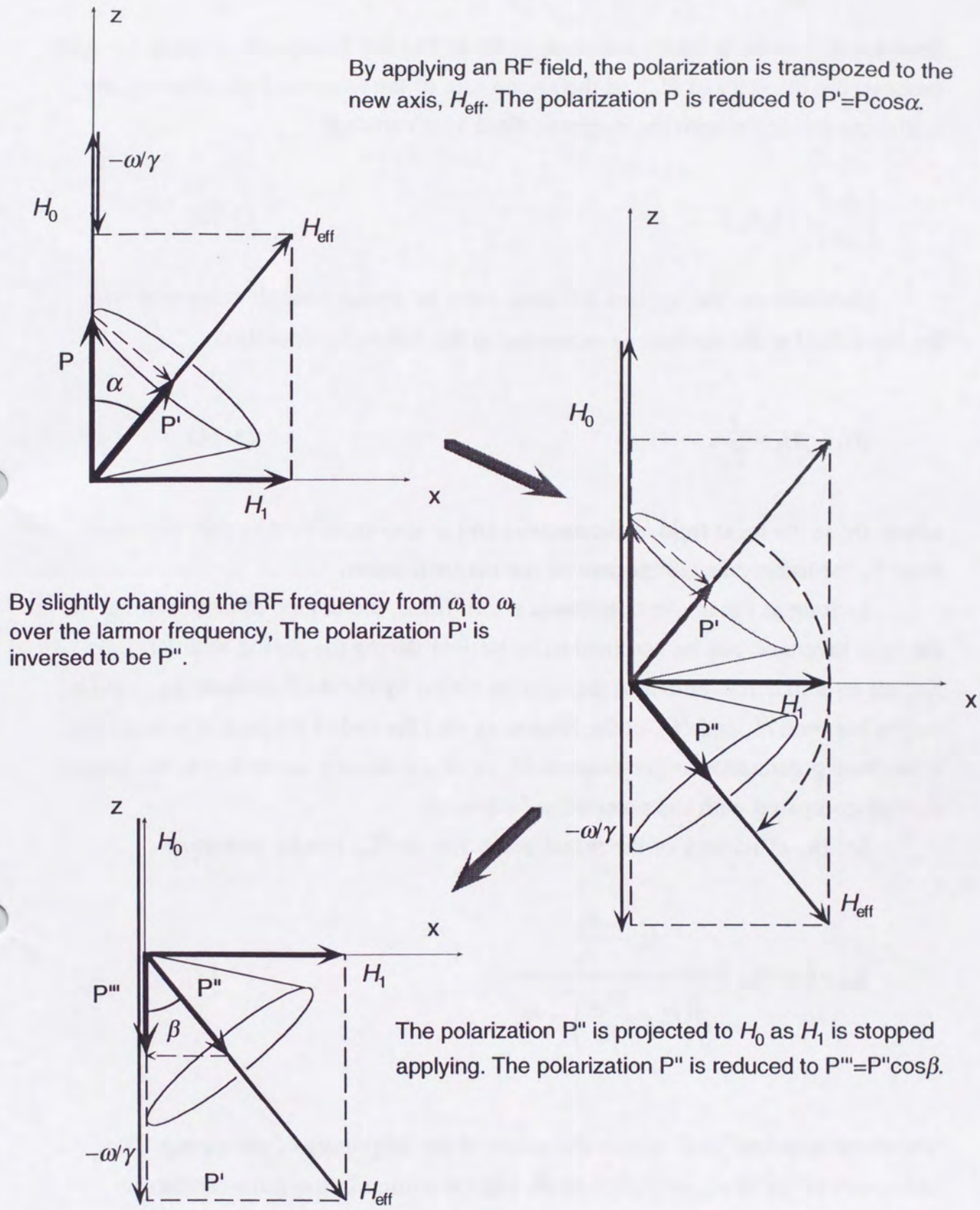

Fig. 3-4. Adiabatic Fast Passage process. The axis are fixed to the RF (H_1) rotating frame. The polarization is reduced by the projection to the new axis.

been applied to the β-NMR detection of ^{8}B in Pt [24]. In order to employ the AFP process, the intensity of $\vec{H}_1$ and the sweep rate of the frequency must satisfy the following condition with the magnetic field kept constant,

$$\left|\frac{d\omega}{dt}\right| \ll (\gamma_N H_1)^2. \tag{3-10}$$

Furthermore, the applied RF field must be strong enough compared with the local field at the nucleus as expressed in the following condition

$$\gamma H_1 \gg \gamma H_L \approx \frac{1}{T_2}. \tag{3-11}$$

where H_L is the local field at the nucleus and is also expressed by the relaxation time T_2 for transverse component of the magnetization.

As long as the above conditions are fulfilled, the degree of achievement of the spin inversion can be assumed to be perfect during the period with RF field. So, the overall achievement of the spin inversion by the AFP method depends on angles between $\vec{H}_0$ and $\vec{H}_{eff}$ at the beginning and the end of frequency sweep. This is because polarization is projected to $\vec{H}_0$ or $\vec{H}_{eff}$ at these periods due to the sudden change compared with the precession frequency.

So, the efficiency of the initial projection to $\vec{H}_{eff}$ can be written as

$$\varepsilon_{init} = \cos\alpha_{init} = \frac{H_0 - \dfrac{\omega_{init}}{\gamma_N}}{\sqrt{\left(H_0 - \dfrac{\omega_{init}}{\gamma_N}\right)^2 + H_1^2}} \tag{3-12}$$

where the notation "init" means the values at the beginning of the sweep. The efficiency of the final projection to $\vec{H}_0$ can be written in the same manner as

$$\varepsilon_{end} = \cos\alpha_{end} \frac{H_0 - \frac{\omega_{end}}{\gamma_N}}{\sqrt{\left(H_0 - \frac{\omega_{end}}{\gamma_N}\right)^2 + H_1^2}}. \qquad (3\text{-}13)$$

Finally, the achievement ε of the AFP process is given as

$$\varepsilon = \varepsilon_{init} \cdot \varepsilon_{end} = \frac{H_0 - \frac{\omega_{init}}{\gamma_N}}{\sqrt{\left(H_0 - \frac{\omega_{init}}{\gamma_N}\right)^2 + H_1^2}} \frac{H_0 - \frac{\omega_{end}}{\gamma_N}}{\sqrt{\left(H_0 - \frac{\omega_{end}}{\gamma_N}\right)^2 + H_1^2}}. \qquad (3\text{-}14)$$

From this equation, one can easily find that the degree of achievement ε becomes small with the narrow sweep range and the strong H_1. For the complete inversion of polarization, the amplitude of H_1 is set to small at the beginning, then increased to a suitable strength to ensure the condition Eq. 3-10 and 3-11, then decreased again to small as that of the beginning, as shown in Fig. 3-5.

3.4. Electric quadrupole interactions in a high magnetic field

Under a finite electric field gradient, the electric quadrupole interaction should be also considered for obtaining the Hamiltonian of a nuclear spin with a quadrupole moment. By defining the electric field gradient as

$$\frac{\partial^2 E}{\partial i^2} = V_{ii}$$

$$eq = V_{ZZ},$$

$$\left(\eta = \frac{V_{XX} - V_{YY}}{V_{ZZ}},\ |V_{ZZ}| \geq |V_{YY}| \geq |V_{XX}|\right), \qquad (3\text{-}15)$$

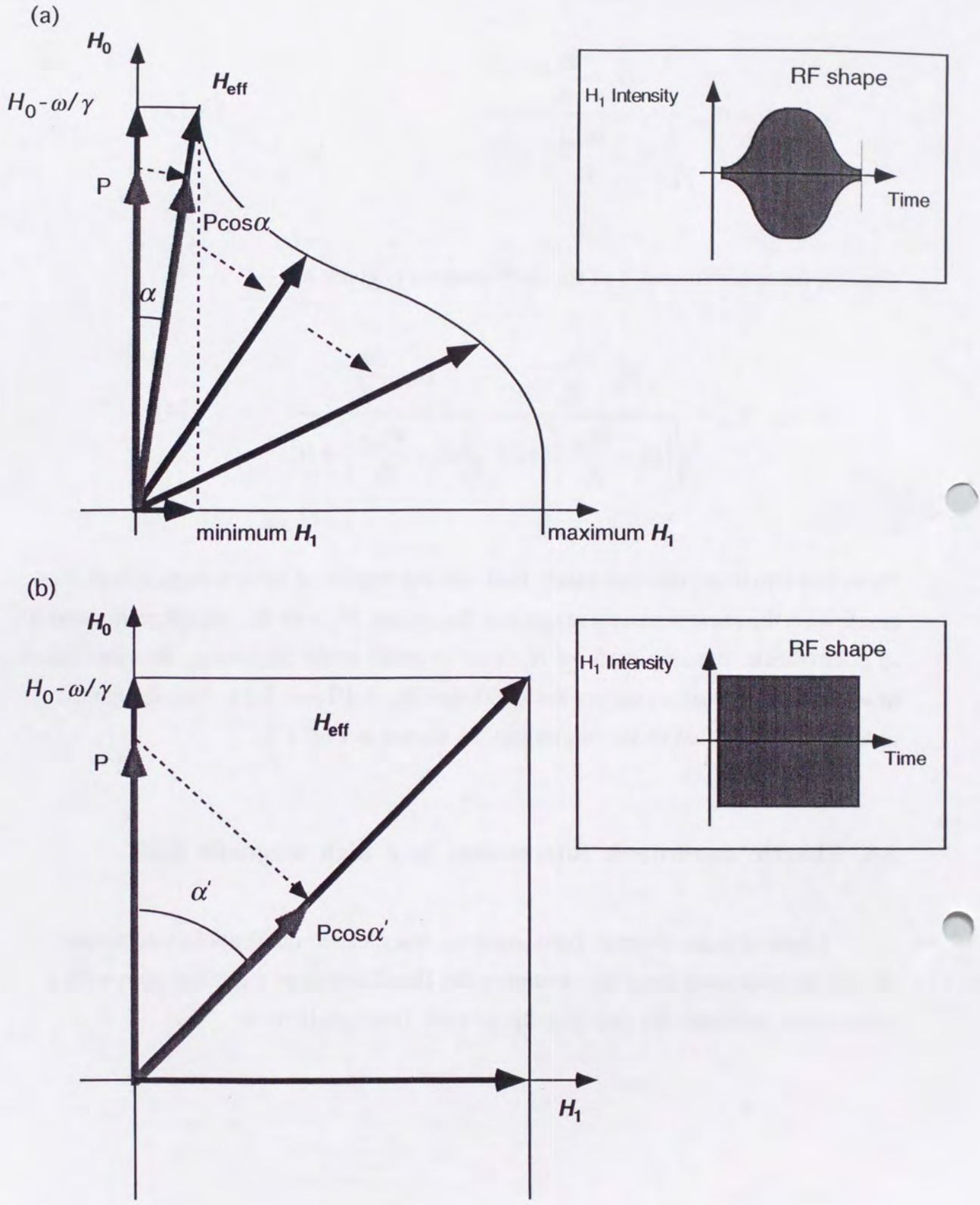

Fig. 3-5. Effect of RF amplitude modulation (AM) for AFP manipulation. The axis are fixed to the RF rotating frame. The appropriate AM improves the efficiency of spin manipulation because the reduction at the initial transpose of polarization to H_{eff} can be small (a) compared to the RF without AM (b).

the Hamiltonian of a nuclear spin with a quadrupole moment can be written as follows

$$H=-\gamma\hbar\vec{I}\cdot\vec{H}_0+\frac{e^2qQ}{4I(2I-1)}[3I_z^2-I(I+1)+\frac{1}{2}\eta(I_+^2+I_-^2)]. \qquad (3\text{-}16)$$

Here, the X, Y, Z axes are the principal axes of the symmetrical tensor $V_{ij}=\frac{\partial^2 E}{\partial i\,\partial j}$. Q is the quadrupole moment of the nuclear spin I. $I_\pm$ are the ascending and descending operators along the defined z-axis. If the Zeeman coupling is much stronger than the quadrupole coupling, the z-axis of this system should be chosen parallel to $\vec{H}_0$. Then this Hamiltonian is rewritten as follows using the polar angle as shown in Fig. 3-6.

$$\begin{aligned}
H &= H_M+H_Q \\
H_M &= -\mu H_0 I_z \\
H_Q &= \frac{e^2qQ}{12I(2I-1)}\left[\frac{1}{2}\left(3\cos^2\theta-1+\eta\sin^2\theta\cos2\phi\right)\{3I_z^2-I(I+1)\}\right. \\
&\quad +\left(\frac{3}{4}\sin2\theta-\frac{\eta}{4}\sin2\theta\cos2\phi+i\frac{\eta}{2}\sin\theta\sin2\phi\right)(I_+I_z+I_zI_+) \\
&\quad +\left(\frac{3}{4}\sin2\theta-\frac{\eta}{4}\sin2\theta\cos2\phi-i\frac{\eta}{2}\sin\theta\sin2\phi\right)(I_-I_z+I_zI_-) \\
&\quad +\left(\frac{3}{4}\sin^2\theta-\frac{\eta}{4}(\cos^2\theta+1)\cos2\phi-i\frac{\eta}{2}\cos\theta\sin2\phi\right)I_+^2 \\
&\quad \left.+\left(\frac{3}{4}\sin^2\theta-\frac{\eta}{4}(\cos^2\theta+1)\cos2\phi+i\frac{\eta}{2}\cos\theta\sin2\phi\right)I_-^2\right]
\end{aligned} \qquad (3\text{-}17)$$

Under a strong magnetic field limit, this equation can be treated as a perturbation. The energy of the eigenstates can be written as

$$E_m=E_m^{(0)}+E_m^{(1)}+E_m^{(2)}+\cdots, \qquad (3\text{-}18)$$

where $E_m^{(i)}$ represents the contribution to the energy from the perturbation of

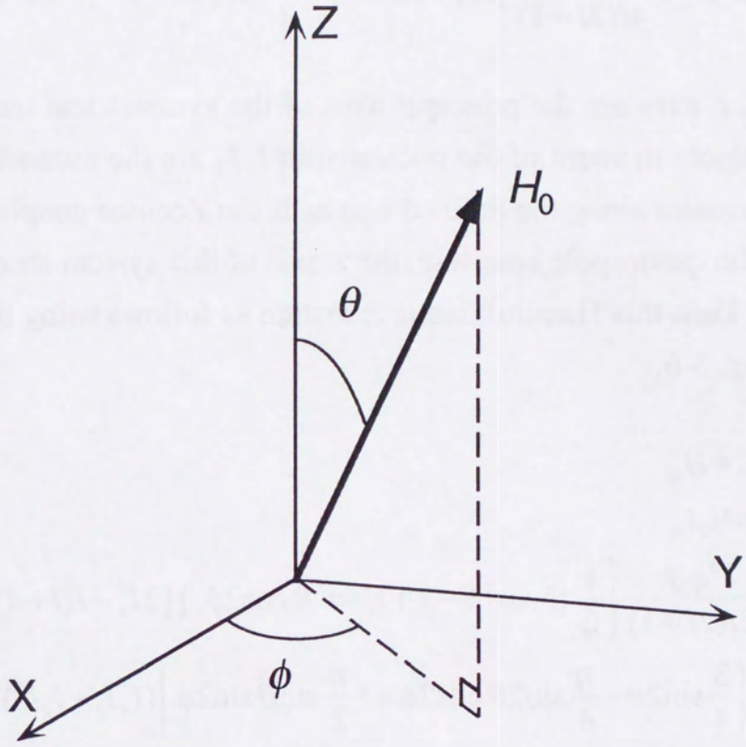

Fig. 3-6. Definition of the polar angle.

order i.

The first term is from the magnetic interaction corresponding to Eq. 3-5. The second term, $E_m^{(1)}$, is the contribution from the first order perturbation given as

$$E_m^{(1)} = \langle m | H_Q | m \rangle = \frac{h\nu_Q}{4} \left(3\cos^2\theta - 1 + \eta \sin^2\theta \cos 2\phi\right) \left\{ m^2 - \frac{I(I+1)}{3} \right\}, \tag{3-19}$$

where $\nu_Q = \frac{3eqQ}{2I(2I-1)h}$.

According to the second order perturbation calculation, $E_m^{(2)}$ is given as,

$$\begin{aligned} E_m^{(2)} = -\left(\frac{h\nu_Q^2}{12\nu_L}\right)\left(\frac{m}{24}\right) \{ & [3\sin 2\theta - \eta(\sin 2\theta \cos 2\phi + i2\sin\theta \sin 2\phi)] \\ & \times [3\sin 2\theta - \eta(\sin 2\theta \cos 2\phi - i2\sin\theta \sin 2\phi)][8m^2 - 4I(I+1)+1] \\ & - \{3\sin^2\theta + \eta[(1+\cos^2\theta)\cos 2\phi + i2\cos\theta \sin 2\phi]\} \\ & \times \{3\sin^2\theta + \eta[(1+\cos^2\theta)\cos 2\phi - i2\cos\theta \sin 2\phi]\}[2m^2 - 2I(I+1)+1]\} \end{aligned} \tag{3-20}$$

The transition frequency between the magnetic substates m and m-1 is given as

$$\nu_m = \frac{E_{m-1} - E_m}{h}. \tag{3-21}$$

The contribution from the magnetic interaction is described as,

$$\nu_m^{(0)} = \nu_L. \tag{3-22}$$

The contribution from the first order perturbation is given as,

$$\nu_m^{(1)} = -\frac{\nu_Q}{2}\left(3\cos^2\theta - 1 + \eta \sin^2\theta \cos 2\phi\right)\left(m - \frac{1}{2}\right). \tag{3-23}$$

The contribution from the second order perturbation is as

$$\nu_m^{(2)} = -\left(\frac{h\nu_Q^2}{12\nu_L}\right)\{[3\sin 2\theta - \eta(\sin 2\theta\cos 2\phi + 2i\sin\theta\sin 2\phi)]$$
$$\times[3\sin 2\theta - \eta(\sin 2\theta\cos 2\phi - 2i\sin\theta\sin 2\phi)]\left[m(m-1) - \frac{I(I+1)}{6} + \frac{3}{8}\right]$$
$$-\{3\sin^2\theta + \eta[(1+\cos^2\theta)\cos 2\phi + 2i\cos\theta\sin 2\phi]\}$$
$$\times\{3\sin^2\theta + \eta[(1+\cos^2\theta)\cos 2\phi - 2i\cos\theta\sin 2\phi]\}\left[\frac{m(m-1)}{4} - \frac{I(I+1)}{12} + \frac{1}{8}\right]\Big\}. \quad (3\text{-}24)$$

The contribution from the first order perturbation gives the symmetric distribution of the $2I$ NMR lines around the Larmor frequency. In the case of I = 3/2 nuclei, such as ^{9}C or ^{13}O, three resonance lines are observed. The second order perturbation gives the frequency shift of the same direction. These contributions are schematically shown in Fig. 3-7.

In the actual extraction of the resonance frequencies, energy eigenstates are calculated exactly by the matrix diagonalization, which gives the very close value with the second order perturbation calculation in the present strong field limit.

3.5. β-NMR

The conventional β-NMR technique is suitable for detecting NMR of short-lived β-emitting nuclei. This technique is consisted of essentially 4 parts: (1) production of the polarized short-lived β-emitting nuclei, (2) implantation of the nuclei and maintaining the polarization, (3) manipulation of the polarization by applying RF magnetic field and (4) detection of the polarization through β-ray asymmetry change.

3.5.1. Production of the polarized short-lived β-emitting nuclei

For the production of polarized short-lived β-emitting nuclei, the recoil angle selection on low energy nuclear reactions have been used for long time. Recently, polarized nuclei can be obtained by selecting the angle and the

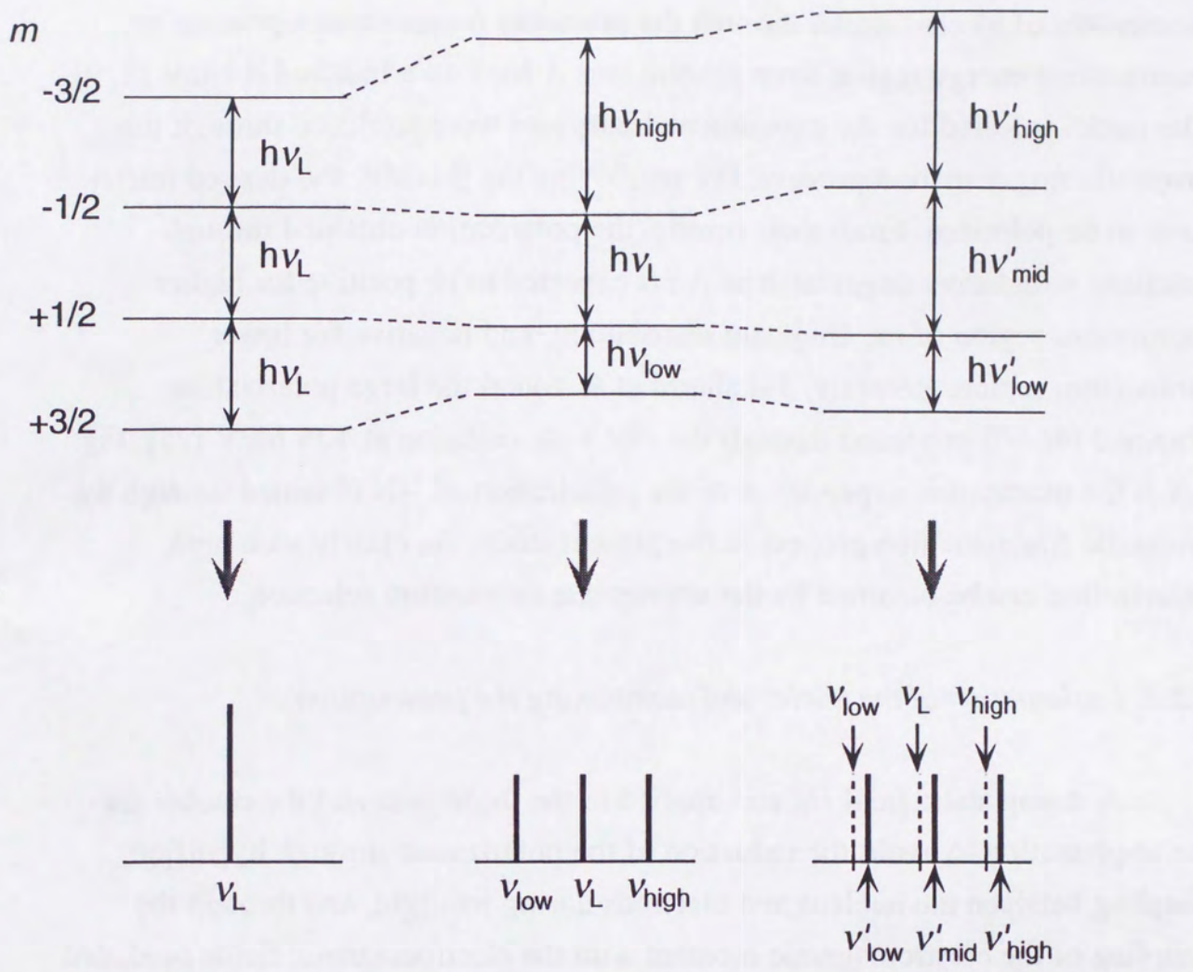

Fig. 3-7. Energy levels of magnetic substates and observed resonance lines for spin $I = 3/2$ under the existence of an electric field gradient.

momentum of ejected nuclei through the projectile fragmentation process at intermediate energy region from several tens *A* MeV to a hundred *A* MeV [8, 9]. The nuclei selected for the experimental purposes were produced through the projectile fragmentation process. For employing the β-NMR, the desired nuclei have to be polarized. From their results, the polarization obtained through reactions with heavy target such as Au is expected to be positive for higher momentum region of the fragment distribution, and negative for lower momentum region. Recently, Takahashi et al. found the large polarization obtained for ^{12}B produced through the ^{14}N + Be collision at 40*A* MeV [25]. Fig. 3-8 is the momentum dependence of the polarization of ^{12}N obtained through the projectile fragmentation process in the present study. As clearly seen here, polarization can be obtained by the appropriate momentum selection.

3.5.2. Implantation of the nuclei and maintaining the polarization

A strong static field H_0 was applied to the flight path and the catcher for the implantation to avoid the reduction of the polarization through hyperfine coupling between the nucleus and electrons during its flight, and through the coupling of the electromagnetic moment with the electromagnetic fields produced by the radiation damages during the implantation process and after stopped in a well defined crystallographic locations. Since the nuclei produced from the projectile fragmentation process around a hundred *A* MeV is obtained as mostly fully stripped ions, the reduction of polarization is negligible. For the case of ^{9}C and for the magnetic moment measurement of ^{13}O, H_0 = 4 kOe was applied. For the case of ^{13}O in TiO_2 for the quadrupole moment measurement, H_0 = 8 kOe was applied to maintain the polarization. In the present experiment, the final energy degrader was put in the same magnetic field applied to the catcher to ensure decoupling after slowing down of the nuclei below ~20*A* MeV. It is noted that the static field is also employed to perform the NMR detection, i.e., imperative for the spin manipulation.

The implantation media were also chosen carefully for the long spin-lattice relaxation time. The crystal which has defects inside is not suitable for the present

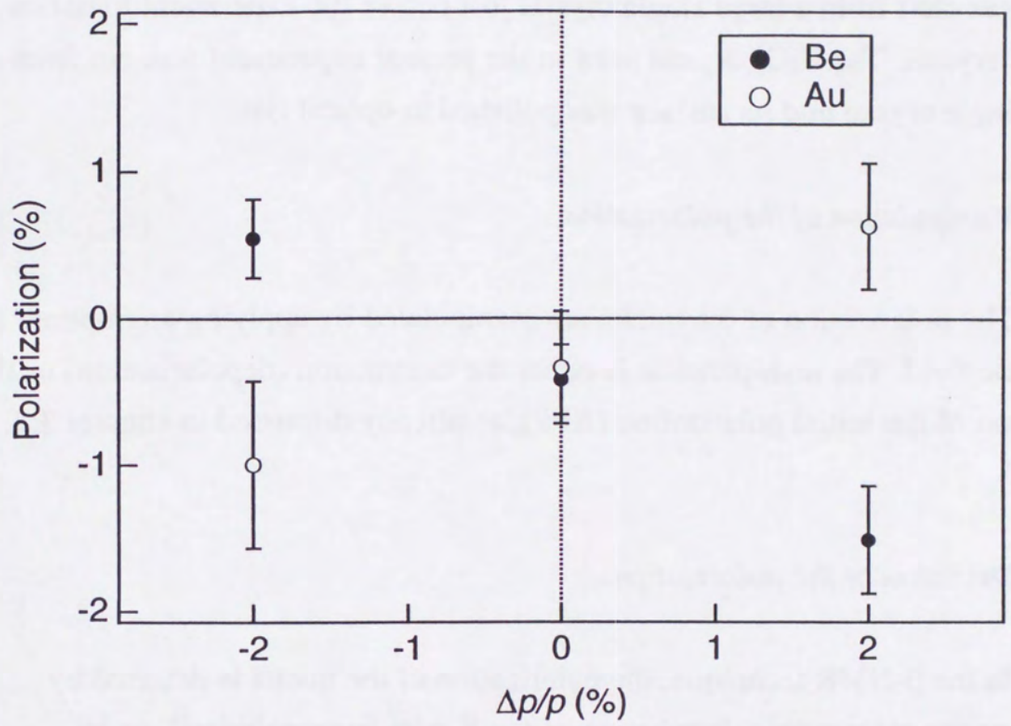

Fig. 3-8. Momentum dependence of the polarization of ^{12}N measured by β-NMR. Incident beam was ^{16}O at 135 *A* MeV. β-ray asymmetry change is propotional to the obtained polarization.

study. This is because both ^{9}C and ^{13}O have quadrupole moments, their polarization would be destroyed through the quadrupole coupling with the electric field gradient caused by the defects in the implantation media. The implantation medium for ^{9}C was polycrystalline Pt foil which was annealed to eliminate defects. A plate of MgO and one of TiO_2 single crystal were used for ^{13}O. This MgO was cleft from a large single crystal just before the experiment to obtain the perfect crystal. The TiO_2 crystal used in the present experiment was cut from a large single crystal and its surface was polished to optical flat.

3.5.3. Manipulation of the polarization

The polarization of the nuclei are manipulated by applying appropriate RF magnetic field. The manipulation is either the destruction (depolarization) or the inversion of the initial polarization (AFP), as already discussed in chapter 3.2. and 3.3.

3.5.4. Detection of the polarization

In the β-NMR technique, the polarization of the nuclei is detected by detecting the asymmetric distribution of the β-rays from polarized nuclei. Polarization change caused by NMR is observed as the change in the β-ray asymmetry.

Based on the parity violating weak interaction, the angular distribution of the β-ray emitted from polarized nuclei is written as follows;

$$W(\varphi)=1+AP\frac{v}{c}\cos\varphi, \qquad (3\text{-}25)$$

where A and P are the asymmetry parameter and the polarization of the nuclei, respectively. v and c are the velocities of the emitted β-ray and light, respectively. φ is the angle between the emitted β-ray and the polarization axis. v/c for both ^{9}C and ^{13}O become almost equal to 1 in the present cases because the maximum β-ray energies for ^{9}C and ^{13}O are 15.5 MeV and 16.7 MeV, respectively.

The asymmetry parameter is given from the weak interaction theory as [26]

$$A = \pm \lambda_{II'} \frac{|C_A|^2 |\int \sigma|^2}{|C_v|^2 |\int 1|^2 + |C_A|^2 |\int \sigma|^2} - 2\delta_{II'} \sqrt{\frac{I}{I+1}} \frac{C_A C_V \int \sigma \int 1}{|C_v|^2 |\int 1|^2 + |C_A|^2 |\int \sigma|^2}, \tag{3-26}$$

where the upper and lower sign denote β^+ and β^- decay, respectively. I and I' are the nuclear spin of initial and final state. The coefficient $\lambda_{II'}$ is

$$\begin{aligned} \lambda_{II'} &= 1 && \text{for } I' = I - 1 \\ &\frac{1}{I+1} && \text{for } I' = I \\ &\frac{-I}{I+1} && \text{for } I' = I + 1. \end{aligned} \tag{3-27}$$

$\int \mathbf{1}$ is the Fermi matrix element, C_V is the Fermi coupling constant, $\int \sigma$ is the Gamow-Teller matrix element and C_A is the Gamow-Teller coupling constant. Based on the decay scheme of ^9C and ^{13}O shown in Fig. 3-9, asymmetry parameters for these β-decays are predicted to be $A(^9C) = +0.2 \sim +0.3$, $A(^{13}O) = \sim +0.9$, respectively.

(a) Depolarization method

The simplest manipulation of the polarization is the "depolarization", equalizing the populations of two magnetic sublevels. The depolarization can be achieved by applying RF at Larmor frequency to the spin ensemble as discussed above of this chapter.

Typical time sequence of this method is shown in Fig. 3-10, where two cycles, with spin polarization is kept as it is produced and with the polarization destroyed by RF, are repeated. The ratio R_{off}, i.e., the counting rate ratio of the upper and lower counters without any spin manipulation, is written as

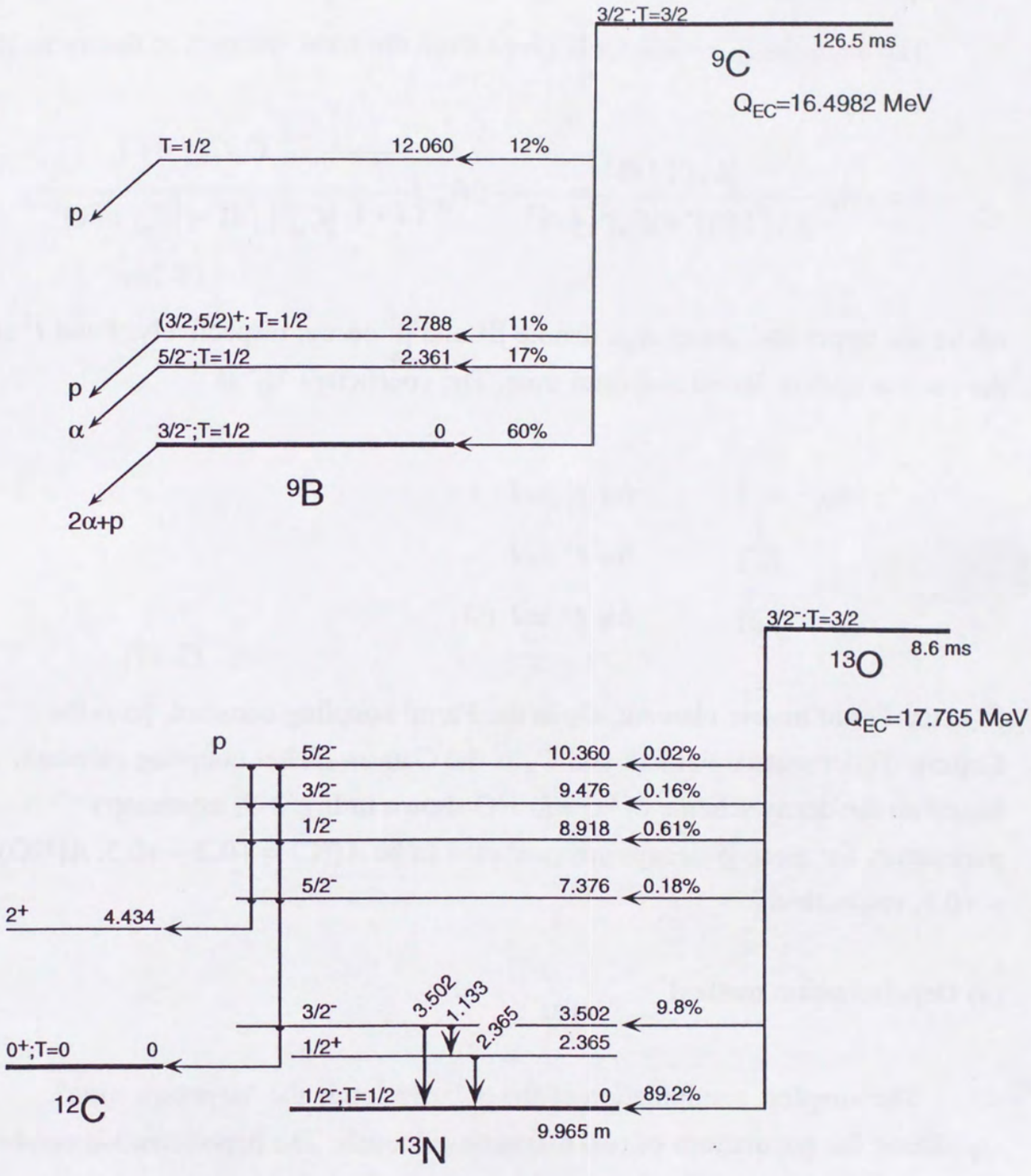

Fig. 3-9. Decay scheme of ^{9}C and ^{13}O.

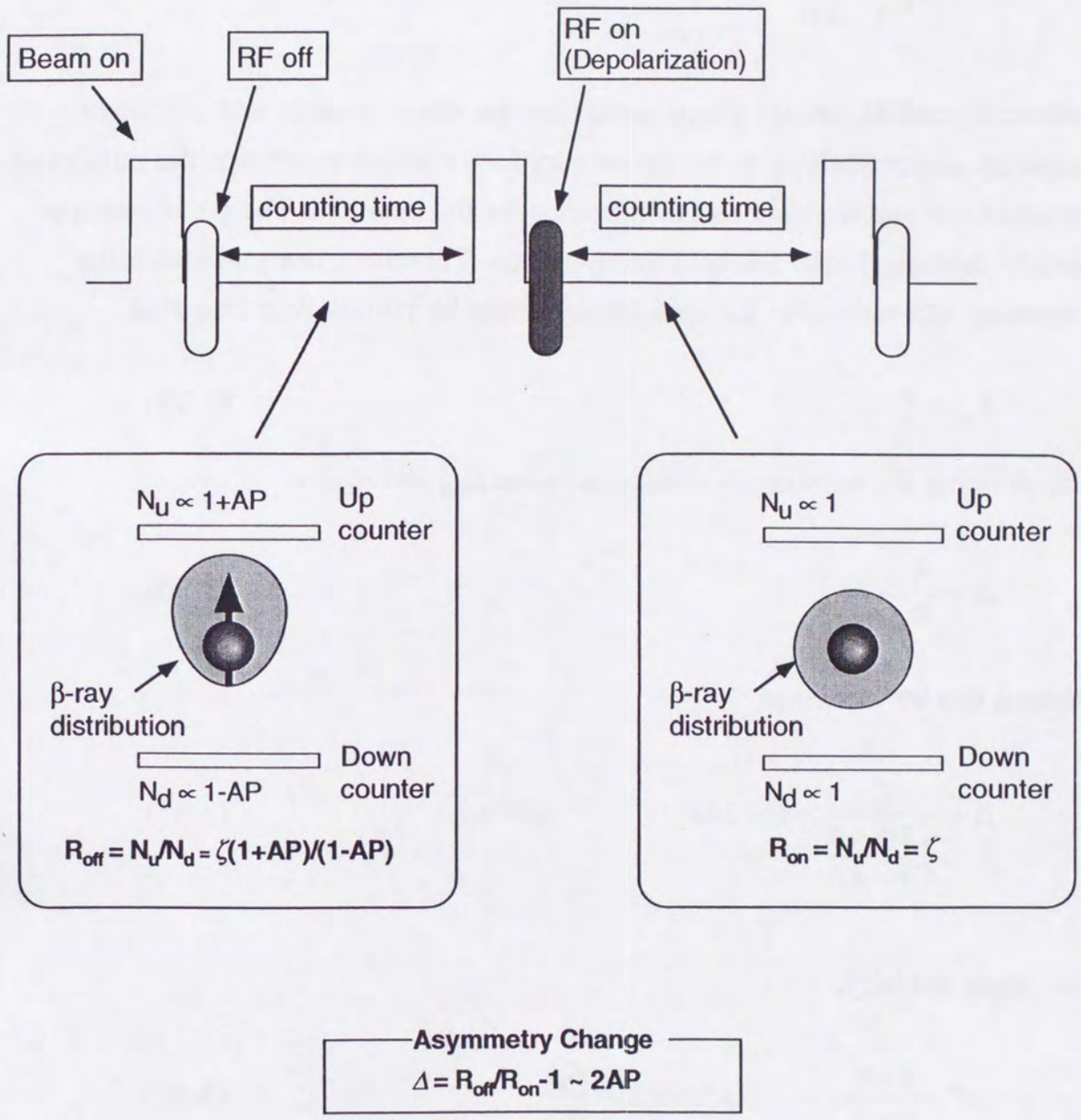

Fig. 3-10. Sequence for depolarization method in β-NMR. β-ray asymmetry change on resonance is detected by the asymmetry of β-ray counts at upper and lower detectors. ζ represents the geometrical and instrumental efficienies for the counters.

$$R_{\text{off}} = \frac{N_u}{N_d} = \zeta \frac{1+AP}{1-AP} \tag{3-28}$$

where N_u and N_d are the β-ray counts for the upper counter and the lower counter, respectively. ζ is the asymmetry factor which represents the ratio of the geometrical and instrumental efficiencies for the counters. The polarization is totally destroyed after the spin manipulation. Therefore, one can obtain the counting rate ratio after the spin manipulation by putting zero into P as

$$R_{\text{on}} = \zeta \tag{3-29}$$

By defining the asymmetry change between R_{on} and R_{off} as

$$\Delta = \frac{R_{\text{on}}}{R_{\text{off}}} - 1, \tag{3-30}$$

then Δ can be written as

$$\Delta = \frac{\zeta}{\zeta \frac{1+AP}{1-AP}} - 1 \sim 2AP \qquad (AP \ll 1), \tag{3-31}$$

or, more actually,

$$AP = \frac{1-X}{1+X}, \qquad \text{where } X = \frac{R_{\text{on}}}{R_{\text{off}}}. \tag{3-32}$$

(b) 4AP method:a simple application of AFP technique

In the AFP method, the initial polarization is totally reversed when the RF is swept over the resonance position with the proper RF condition with external

field kept constant. The typical time sequence of this method is shown in Fig. 3-11. In this case, the counting rate ratio after the spin manipulation is written as follows

$$R_{on} = \zeta \frac{1 - AP}{1 + AP}. \qquad (3\text{-}33)$$

Then the asymmetry change can be obtained as follows;

$$\Delta \equiv \frac{R_{on}}{R_{off}} = \frac{\zeta \dfrac{1 - AP}{1 + AP}}{\zeta \dfrac{1 + AP}{1 - AP}} - 1 \sim 4AP, \qquad (AP \ll 1) \qquad (3\text{-}34)$$

or, more explicitly as

$$AP = \frac{1 - \sqrt{X}}{1 + \sqrt{X}}, \qquad \text{where } X = \frac{R_{on}}{R_{off}}. \qquad (3\text{-}35)$$

Notice that the NMR effects is doubled compared with the depolarization method and therefore the counting statistics is improved four times.

(c) 8AP method:an advanced application of AFP technique

Since the counting rate ratios with the polarization is manipulated and with its polarization as it is produced are observed in the different beam count cycles in the above two methods, beam fluctuation can induce small, but finite, spurious asymmetry change. To eliminate this effect, another AFP process is inserted into the β-ray counting section in the present method. Typical time sequence is shown in Fig. 3-12. Here, the counting ratios can be written as follows;

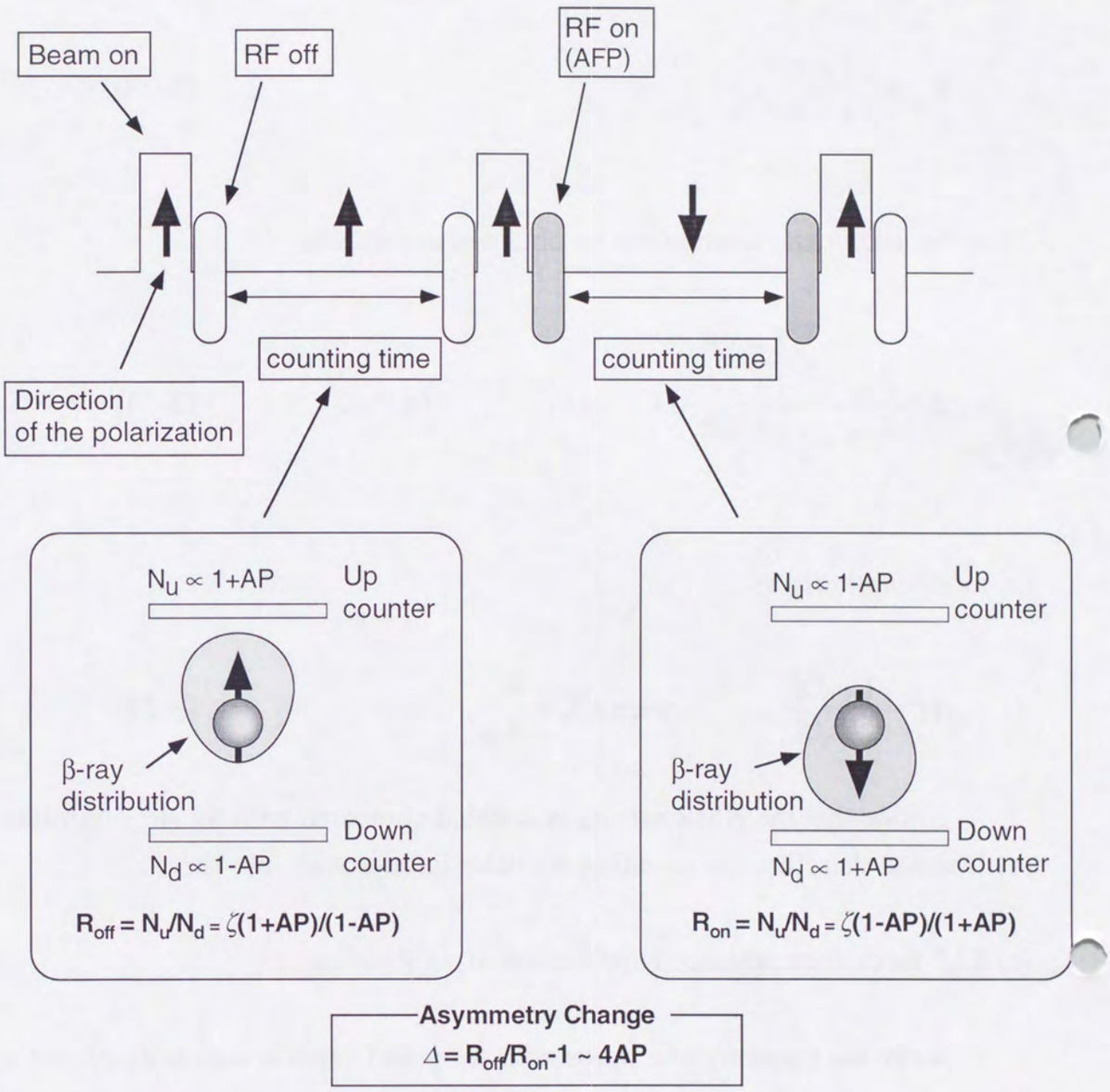

Fig. 3-11. Sequence for β-NMR with AFP. β-ray asymmetry change on resonance is detected by asymmetry of β-ray counts at upper and lower detectors. ζ represents the geometrical and instrumental efficienies for the counters.

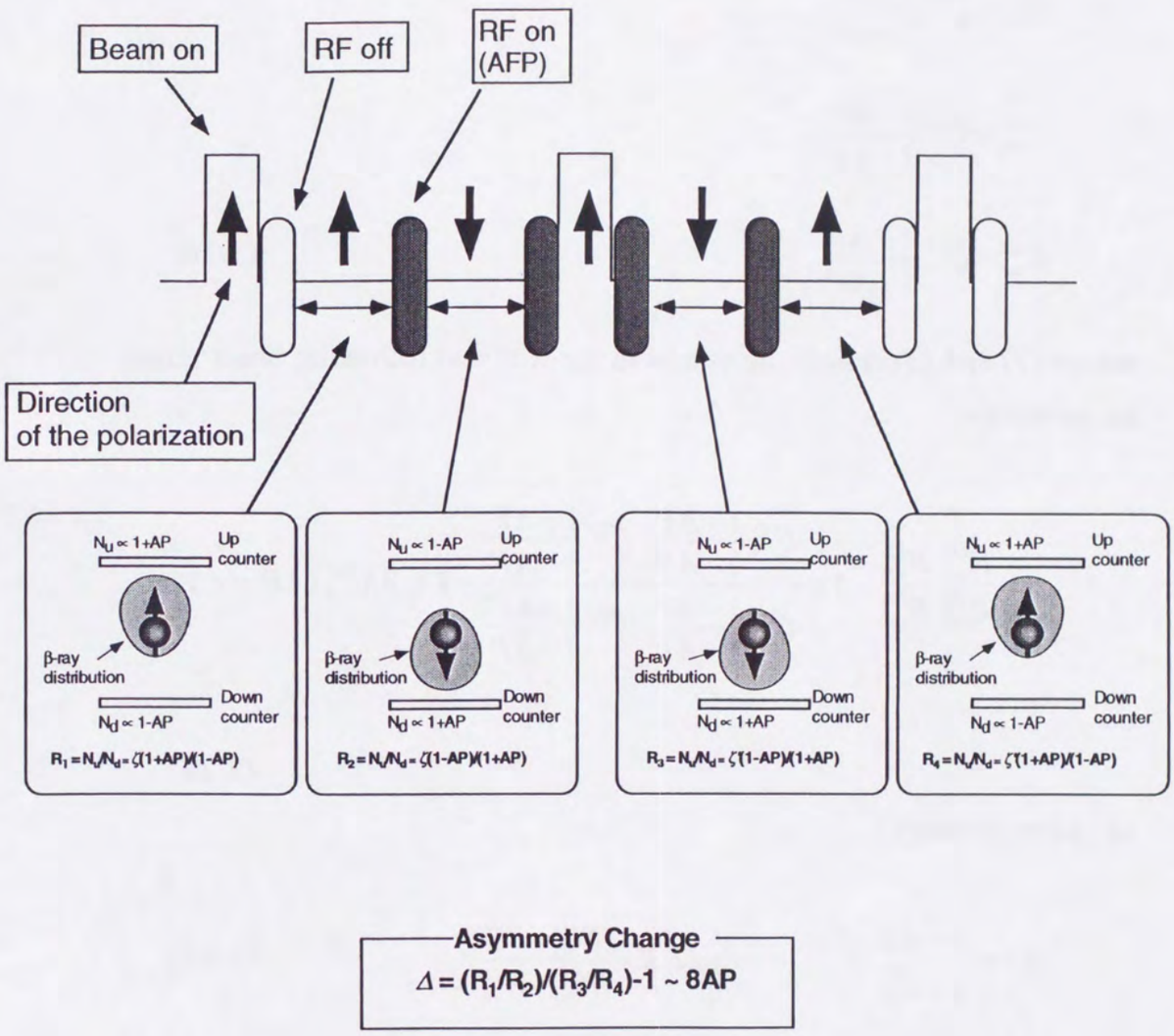

Fig. 3-12. Sequence for 8AP method. β-ray asymmetry change on resonance is detected by taking the ratio of β-ray counts at upper and lower detectors. ζ and ζ' represents the geometrical and instrumental asymmetries for the counters of each beam pulse.

$$R_{\mathrm{off}}^{(1)}=\zeta^{(1)}\frac{1+AP}{1-AP}$$

$$R_{\mathrm{off}}^{(2)}=\zeta^{(2)}\frac{1-AP}{1+AP}$$

$$R_{\mathrm{on}}^{(1)}=\zeta^{(1)}\frac{1-AP}{1+AP}$$

$$R_{\mathrm{on}}^{(2)}=\zeta^{(2)}\frac{1+AP}{1-AP}, \qquad (3\text{-}36)$$

where (1) and (2) denote the values in the first and following beam pulse, respectively.

$$\Delta\equiv\frac{R_{\mathrm{on}}^{(1)}}{R_{\mathrm{off}}^{(1)}}\frac{R_{\mathrm{off}}^{(2)}}{R_{\mathrm{on}}^{(2)}}-1=\frac{\zeta^{(1)}\dfrac{1+AP}{1-AP}\;\zeta^{(2)}\dfrac{1+AP}{1-AP}}{\zeta^{(1)}\dfrac{1-AP}{1+AP}\;\zeta^{(2)}\dfrac{1-AP}{1+AP}}-1\sim 8AP,\ (AP<<1) \qquad (3\text{-}37)$$

or, more actually,

$$AP=\frac{1-\sqrt{X}}{1+\sqrt{X}}, \qquad \text{where } X=\frac{R_{\mathrm{on}}^{(1)}}{R_{\mathrm{off}}^{(1)}}\cdot\frac{R_{\mathrm{off}}^{(2)}}{R_{\mathrm{on}}^{(2)}} \qquad (3\text{-}38)$$

Notice that the advantages of this technique is in excluding the effects of beam spot fluctuation, not in the improvement of figure of merit.

3.6. β-NQR:new nuclear quadrupole resonance

$2I$ lines are observed by conventional NMR under the existence of quadrupole interactions as discussed in the previous section. The larger the nuclear spin I

becomes, the more difficult the detection becomes. This is because the difference of the populations of neighboring states becomes smaller as I increases.

For simplicity, the population of each magnetic substate is assumed to be written by the linear function of magnetic quantum number m as

$$p(m)=a+bm, \qquad \sum_m p(m)=1.$$

$$\therefore P_{\text{initial}}=\sum_m mp(m)=\frac{bI(I+1)(2I+1)}{3} \tag{3-39}$$

If an RF is applied to the transition frequency between m and $m+1$, populations of these two levels are equalized. Then the polarization change induced by this spin manipulation can be deduced as

$$\begin{aligned}\Delta P &= P_{\text{final}}-P_{\text{intial}} \\ &= \frac{\sum mp_{\text{final}}(m)}{I}-\frac{\sum mp_{\text{initial}}(m)}{I} \\ &= -\frac{b}{2I} = -\frac{3}{2}\cdot\frac{P_{\text{initial}}}{I(I+1)(2I+1)}.\end{aligned} \tag{3-40}$$

From this result, it is shown that the polarization change is equal to $(3/2)\times\{I(I+1)(2I+1)\}^{-1}$ of the incident polarization. So, the polarization change ΔP decreases as the nuclear spin I increase.

So called β-NQR method with AFP spin manipulation give us more efficient detection of the resonance by multi RF application. For simplicity, the spin-lattice relaxation of polarization is neglected. By applying the single AFP RF sweep at the transition frequency between $m = m_0 \leftrightarrow m_0+1$, the population of these substates can be exchanged. Therefore, the initial polarization can be totally inverted by applying RFs in an appropriate sequence. Fig. 3-13 shows the principle of β-NQR method with the AFP technique in the case of $I = 3/2$ nuclei. In this case, to complete the polarization inversion, a sequence of 6 RFs, selected from the 3 resonance frequencies is applied. The maximum polarization change

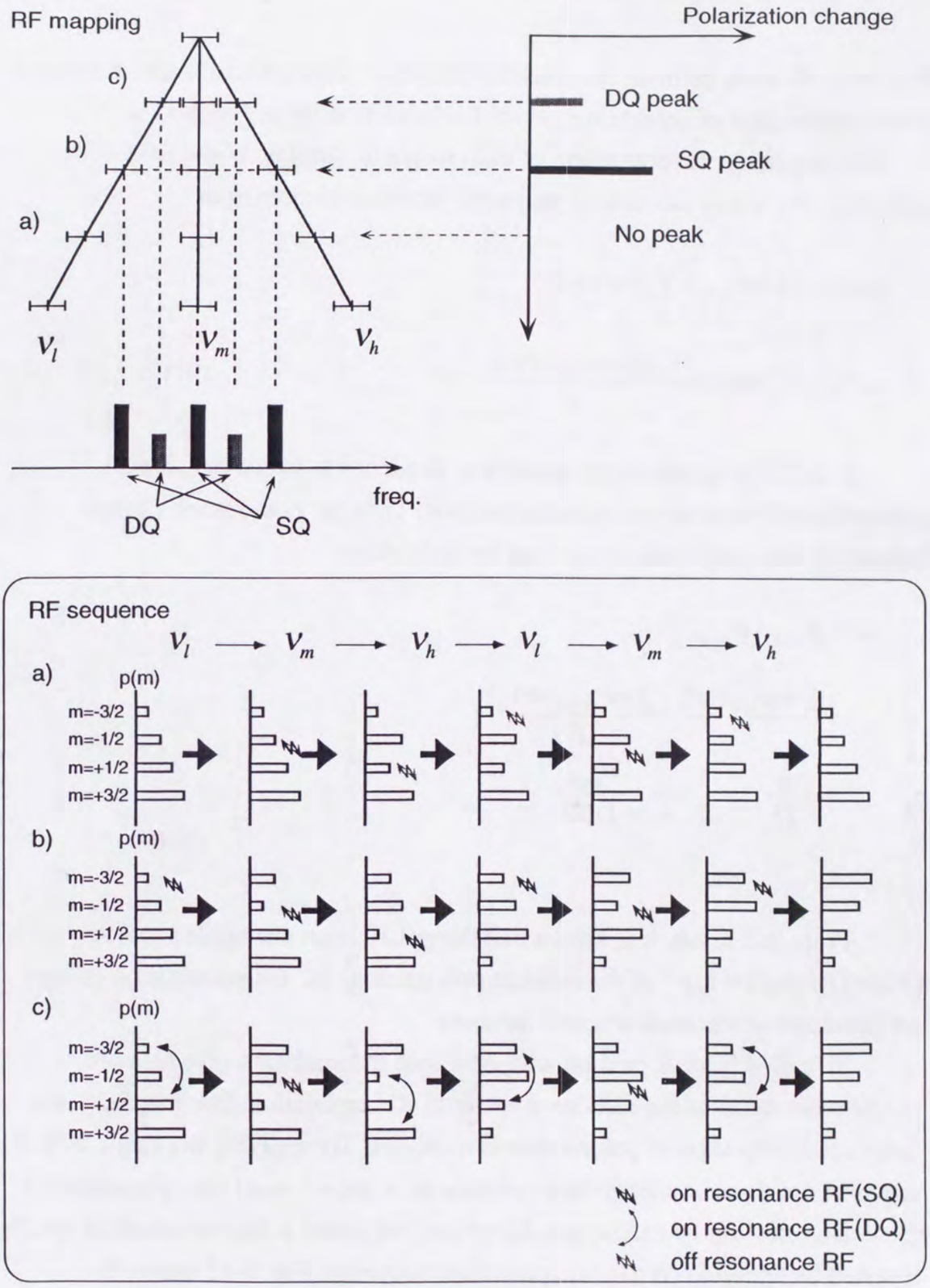

Fig. 3-13. β-NQR with AFP technique for $I = 3/2$ nuclei. 6 RFs are applied sequencially for the complete inversion of the initial polarization. If all RFs are on the resonance frequency of SQ, the initial polarization will be inversed as in a). b) is the case for off resonance. In the case that ν_l and ν_h are on DQ resoanace frequencies and that their intensity are enough high, the spin is also inversed as in c).

can be obtained when all RFs are applied on the exact resonance frequencies. On the other hand, no polarization change is observed if the frequencies of applied RFs are not on the resonance for half integer spin nuclei such as $I = 3/2$.

Since the resonance frequencies for spin I are calculated using the known Larmor frequency, the asymmetry parameter η and the orientation of H_0 relative to the crystal frame, the coupling constant can be obtained from the frequencies of the RF set on resonance if the other parameters are given for an electric quadrupole coupling constant eqQ/h.

3.7. Causes of the resonance shift and line broadening of a NMR spectrum

Generally, observed NMR spectra give us various information, e.g., the interactions between surrounding electrons and host nuclei, and interactions of nuclear moments with the applied RF. In this section, the main reasons for the line broadening and the resonance shift are summarized.

3.7.1. Chemical shifts

In diamagnetic substances such as ionic crystals, an applied magnetic field H_0 induces a small electronic magnetization by polarizing the electronic shells of ions or atoms. This polarized shells produce a small magnetic field proportional to H_0 at the position of the nucleus. Therefore, the NMR frequency of the nucleus is shifted by a small amount also proportional to H_0. This shift is called chemical shift. The chemical shift is the sum of the diamagnetic field and the paramagnetic filed. The diamagnetic field at the site of a nucleus is produced by the orbital motions of the electron in the external magnetic field. The paramagnetic field comes from the admixture with the excited orbital states. These values reflect the electronic structure of the surroundings of the nucleus, such as chemical bonding. Chemical shifts have been studied well for many nuclei in a variety of substances.

Usually, the chemical shift is measured as the frequency shift from the reference substance defined as,

$$\sigma_X = \frac{f_{ref.} - f_X}{f_{ref.}}, \qquad (3\text{-}41)$$

where the $f_{ref.}$ and f_X represent the resonance frequencies of nuclei in the reference substance and in a material under the same external magnetic field.

In the case of oxygen, ^{17}O in H_2O is chosen as the reference substance. Especially in the case of O, the absolute chemical shift is studied experimentally [27] and theoretically [28] and both are in good agreement. From their result, the absolute chemical shift can be determined for oxygen compounds, which is inevitable for the determination of the magnetic moment of ^{13}O. The relations of chemical shifts among some oxygen compounds are shown in Fig. 3-14.

In a metallic sample a local field due to Fermi contact interaction is induced at the nuclear site and the resonance frequency shift is observed. This shift is called Knight shift. The magnitude of the induced field is proportional to the external magnetic field. This shift is caused by the hyperfine interaction between the nuclear moment and the moments of conduction electrons in s-states, this is much in common with the Fermi contact interaction for the hyperfine splitting of an ESR line.

The contribution of each electron depends on how much of its time is spent at the nucleus, i.e., the wave function of electron at nuclear position.

If only the Fermi contact interaction is considered, the Knight shift K is given as,

$$K = \frac{\Delta H}{H_0} = \frac{8\pi}{3}\mu_B^2 \int \{\rho_\uparrow(E) - \rho_\downarrow(E)\} dE, \qquad (3\text{-}42)$$

where $\rho_\uparrow(E)$ and $\rho_\downarrow(E)$ are the local density of up spin and down spin electrons at the energy E and μ_B is the Bohr magneton, respectively.

The conduction electrons are responsible for the spin-lattice relaxation of nuclear spins. If only the Fermi contact interaction is considered, the nuclear polarization is reduced through a simultaneous spin flip with the conduction electron at the nucleus position. Therefore, by neglecting the energy change of electrons after the spin flip, the probability of the simultaneous spin flip is given

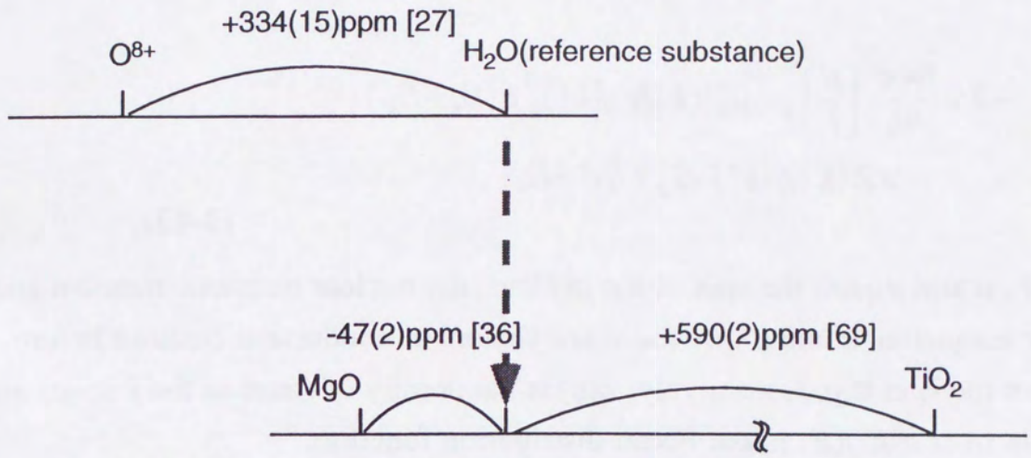

Fig. 3-14. Chemical shifts of Oxygen for some substances. Diamagnetic corrections(the shift to lower frequency for the same H_0, or the shift to higher H_0 for the same RF frequency) is taken to be positive sign. H_2O is usually used as the reference substance and chemical shifts of most subsatances are measured relative to H_2O.

as

$$\frac{1}{T_1}=2\times\frac{64\pi^4}{9h}\left(\frac{\mu}{I}\right)^2\mu_N^2\mu_B^2|\langle k|\delta r_N|k'\rangle|^2\delta(E_k-E_{k'})$$
$$\times Z(k)Z(k')f(E_k)(1-f(E_k))$$

$$\simeq 2\times\frac{64\pi^4}{9h}\left(\frac{\mu}{I}\right)^2\mu_N^2\mu_B^2|\langle k|\delta r_N|k'\rangle|^2\delta(E_k-E_{k'})$$
$$\times Z(k)Z(k')\times k_BT\delta(E-E_F)\ , \qquad (3\text{-}43)$$

where I, μ and μ_N are the spin of the nucleus, the nuclear magnetic moment and nuclear magneton, $\boldsymbol{k}$ and $\boldsymbol{k'}$ are the wave vectors of conduction electron before and after the spin flip, respectively. $Z(\boldsymbol{k})$ is the density of states in the k space and integrate over d^3k. $f(E)$ is the Fermi distribution function.

Electrons at the Fermi energy are the most important ones since all the electrons of lower energy are in paired states. Thus, the Knight shift depends on the density of states at the Fermi energy in the first order and the integral of electron densities replaced with those at Fermi level. Then Eq. 3-42 is rewritten as,

$$K=\frac{\Delta H}{H_0}=\frac{8\pi}{3}\mu_B^2\rho(E_F). \qquad (3\text{-}44)$$

Assuming that the Fermi surface has the spherical shape and $\rho(E)dE$ is the number of states between E and $E+dE$ around the Fermi energy, Eq. 3-43 is rewritten as

$$(T_1T)^{-1}=\frac{128\pi^4k_B}{9h}\left(\frac{\mu}{I}\right)^2\mu_N^2\mu_B^2\{\rho(E_F)\}^2. \qquad (3\text{-}45)$$

Since both T_1 and K are the functions of $\rho(E_F)$, one obtains the following relation from these equations,

$$(T_1T)K^2=\frac{h}{8\pi^2 k_B(\gamma_e\gamma_n)^2}. \qquad (3\text{-}46)$$

This is called Korringa relation.

3.7.2. Dipolar broadening

The nucleus in solid is surrounded by host nuclei. If these nuclei have magnetic moments, they cause dynamic magnetic field at the nucleus. The Hamiltonian of this dipole-dipole interaction between two nuclei is given as,

$$W_{12}=\frac{\gamma_1\gamma_2}{r_{12}^3}\left\{\vec{I}_1\cdot\vec{I}_2-3\frac{(\vec{I}_1\cdot\vec{r}_{12})(\vec{I}_2\cdot\vec{r}_{12})}{r_{12}^3}\right\}, \qquad (3\text{-}47)$$

where r_{12} is the distance between these two nuclei, γ_1 and γ_2 are the gyromagnetic ratios of the probe and the host nuclei. Because of the motion of the host nuclei, a dynamic magnetic field is caused at the site for the probe nucleus and the resonance line is broadened due to this contribution.

Using the method of moments, any line broadening due to a dipole-dipole interaction can be deduced. The *n*th moment M_n is defined as

$$M_n=\int(\omega-\omega_0)^n f(\omega)d\omega, \qquad (3\text{-}48)$$

where $f(\omega)$ is normalized shape function. For example, a normalized Gaussian function is described by

$$f(\omega)=\frac{1}{\Delta\sqrt{2\pi}}e^{\left(-\frac{(\omega-\omega_0)}{2\Delta^2}\right)}, \qquad (3\text{-}49)$$

from which a relation between the *n*th moments and the line width can be derived as

$$M_2 = \Delta^2,\ M_4 = 3\Delta^4,\ \ldots\ldots,\ M_{2n} = 1\cdot 3\cdot 5\cdots(2n-1)\Delta^{2n}, \qquad (3\text{-}50)$$

in which the odd moments vanish. The half width at half maximum of the line width can be written as

$$\delta = \Delta\sqrt{2\log 2} = 1.18\Delta. \qquad (3\text{-}51)$$

In the β-NMR experiments, the probe nuclei is different from the host nuclei. In other words, the host spins and that of probe are unlike spins. In this case, the second moment can be written as

$$M_2 = \frac{1}{3}\gamma_1^2\gamma_2^2 I_2(I_2+1)\sum_k \frac{\left(1-3\cos^2\beta_k\right)^2}{r_k^6} \qquad (3\text{-}52)$$

where β_k is the angle between the external field and the vector $\vec{r}_k$, which describes the relative position of host nucleus k from the probe nuclei as shown in Fig. 3-15.

3.7.3. Spread in the electric field gradients

Many defects are introduced in the catcher sample following the ion implantation. However, the final sites of the implanted nuclei can be considered to be far away from the sea of damages. If there is a defect near to the final site, implanted nuclei are perturbed by a strong field gradient, and the line will be spread out. The contributions from defects on the electric field gradient at an implanted nucleus are added to the intrinsic one. The electric field gradients are then distributed around an intrinsic value. This was observed in many cases, for example ^{17}F in MgF_2 or ^{41}Sc in TiO_2. In these studies, it was shown that the distribution of the field gradient was $\Delta q/q$ = 5 ~10 % at HWHM.

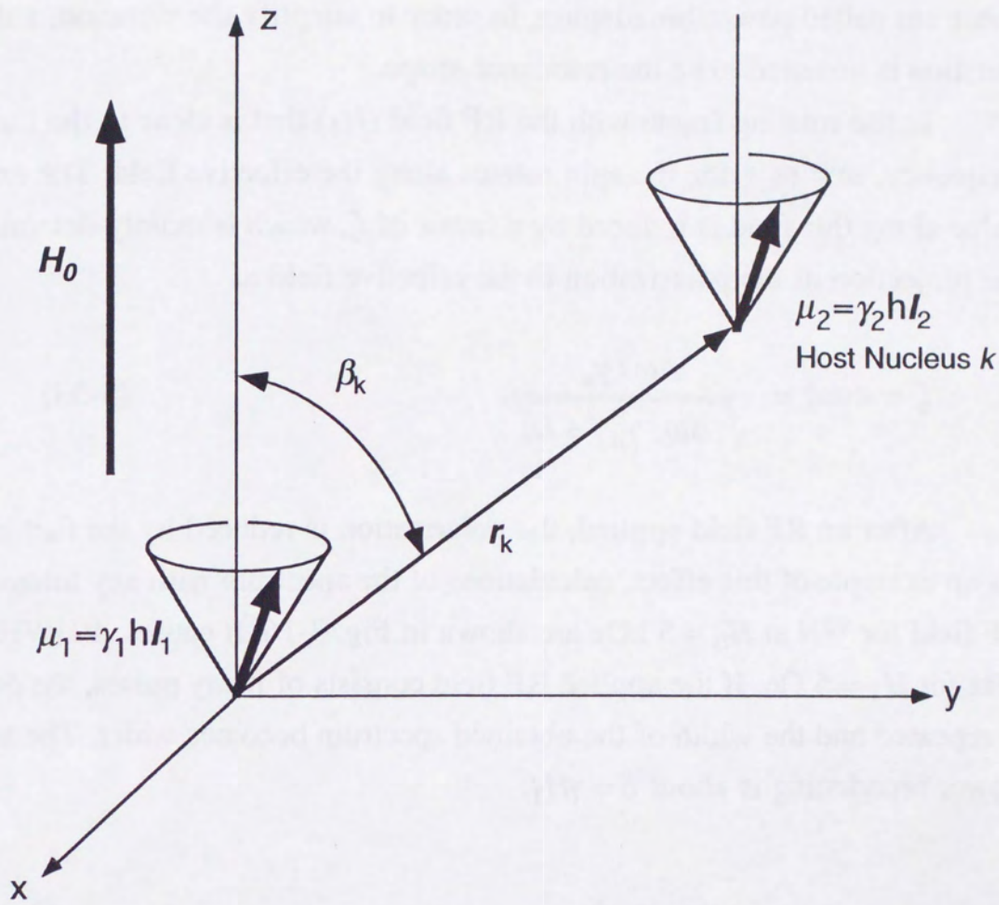

Fig. 3-15. Dipole-dipole interaction.

3.7.4. Effect of the RF field to the resonance width

The finite intensity of an rf field causes a broadening on the resonance spectrum called power broadening. In order to simplify the situation, a delta function is assumed to be the resonance shape.

In the rotating frame with the RF field (H_1) that is close to the Larmor frequency, $\omega = \omega_L + \Delta\omega$, the spin rotates along the effective field. The expectation value along this field is reduced by a factor of ζ, which is mainly determined by the projection of the polarization to the effective field as

$$\zeta = \cos\xi = \frac{\Delta\omega / \gamma_N}{\sqrt{(\Delta\omega / \gamma_N)^2 + H_1^2}}. \qquad (3\text{-}53)$$

After an RF field applied, the polarization is reduced by the factor of ζ^2. As an example of this effect, calculations of the spectrum with any intensity of the RF field for ^{12}N at $H_0 = 5$ kOe are shown in Fig. 3-16. It causes Δ(HWHM) = 1.8 kHz for $H_1 = 5$ Oe. If the applied RF field consists of many pulses, the destruction is repeated and the width of the obtained spectrum becomes wider. The size of the power broadening is about $\delta = \gamma H_1$.

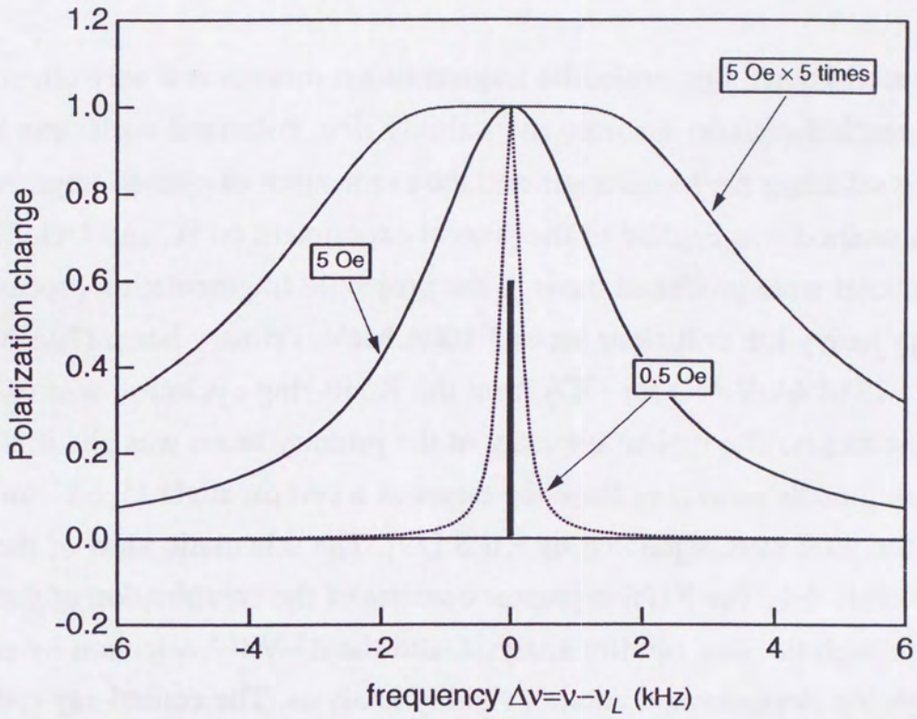

Fig. 3-16. Effect of the applied RF field on the resonance shape of ^{12}N at H_0 = 5 kOe. The shape of the inherent resonance line is supposed to be the delta function. The strong RF and the multiple RF cause some line broadening.

4. Experimental apparatus

4.1. Production of polarized radioactive beam

It is well known that projectile fragmentation process is a very effective method to reach the nuclei far from the stability line. Polarized nuclei can be obtained by selecting the recoil angle and the momentum of ejected fragments.

This method was applied to the present experiment on ^{9}C and ^{13}O. The polarized nuclei were produced through the projectile fragmentation process in a high-energy heavy-ion collisions around 100*A* MeV. Primary beam (70*A* MeV ^{12}C for ^{9}C, 135*A* MeV ^{16}O for ^{13}O) from the K540-ring cyclotron was used to bombard the target. The typical intensity of the primary beam was about 200 pnA. The fragments emerging from the target at a certain angle ($5 \pm 1^{\circ}$ for ^{9}C, $1.5 \pm 1.0^{\circ}$ for ^{13}O) were separated by RIPS [29]. The schematic view of the RIPS is shown in Fig. 4-1. The RIPS separator consists of the combination of the A/Z selection through the first rigidity analysis, and the $A^{2.5}/Z^{1.5}$ selection by energy loss through the degrader and another rigidity analysis. The central-ray radius and the bending angle of the dipole magnet for the first rigidity analysis were 3.6 m and 45°, respectively. The momentum selection to obtain the polarization was performed by a slit placed at the exit of the magnet. The momentum windows were opened at $+5 \pm 1$ % and $+2.0 \pm 0.5$ % relative to the beam for ^{9}C and ^{13}O, respectively. For example, the magnet was set to 7.59 kOe and the slit was opened at ±12 mm, which corresponds to $+2.0 \pm 0.5$ % momentum width window for ^{13}O. The Fig. 4-2 shows the momentum dependence of the polarization of ^{12}N produced through the projectile fragmentation process in the ^{16}O on Be and Au collisions. As clearly seen in this result, a large polarization can be obtained by the appropriate momentum selection. The degrader for $A^{2.5}/Z^{1.5}$ selection was made of aluminum. The thickness of the degraders were 1.59 mm (429 mg/cm^2) for ^{9}C and 3.03 mm (816 mg/cm^2) for ^{13}O, respectively. The specification of the dipole magnet for the second rigidity analysis were the same as those for the first rigidity analysis. The isotope separation was employed here combined with the slit at the exit of this magnet. For example, the magnetic filed was set at 6.92 kOe and

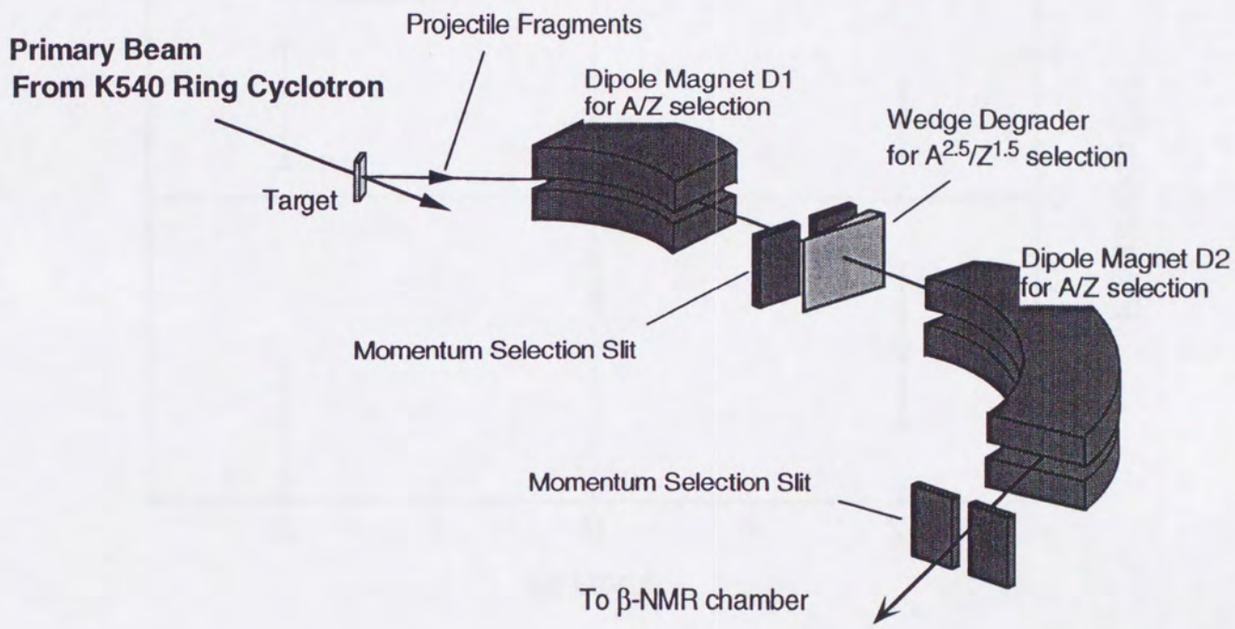

Fig. 4-1. Schematic view of the Riken Projectile Fragment Separator (RIPS). The objective nuclei is produced through the projectile fragmentation process. Then the nuclei selection is achieved by the combination of dipole magnet (A/Z selection) - wedge energy degrader ($A^{2.5}/Z^{1.5}$) - dipole magnet (A/Z selection).

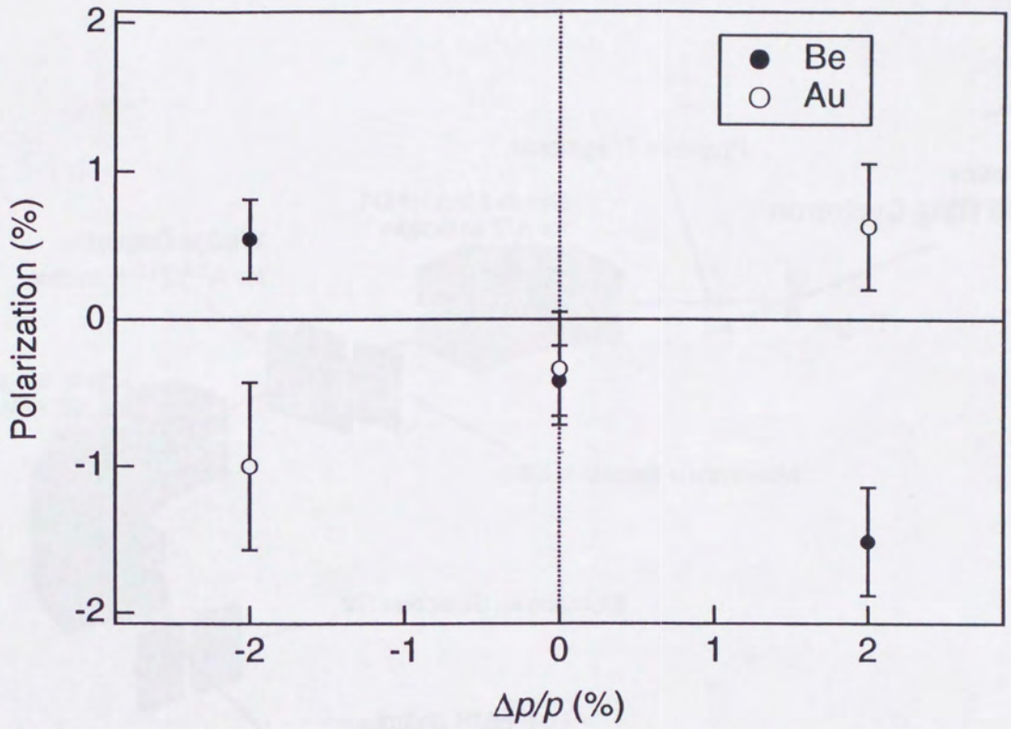

Fig. 4-2. Momentum dependence of the polarization of ^{12}N measured by β-NMR. Incident beam was ^{16}O at 135 *A* MeV.

the slit was opened at ±5 mm in the case of ^{13}O. This configuration gives the resolution less than 1/10 of the difference of rigidity between ^{13}O and ^{12}N, thus enough to separate ^{13}O from ^{12}N which was the main background for ^{13}O measurement. The intensities of the obtained secondary beams were monitored by the 0.5 mm thick ΔE detector at the entrance of the NMR chamber as ~4 kcps and ~2 kcps for ^{9}C and ^{13}O, respectively.

To observe the purity of the obtained secondary beam, the TOF spectrum was measured by detecting the signals from the ΔE detector and RF signal of

Table 4-1. Parameters for the production of polarized ^{9}C and ^{13}O.

	^{9}C	^{13}O
Primary Beam	^{12}C	^{16}O
Beam Energy	70*A* MeV	135*A* MeV
Beam Intensity	~200 pnA	~200 pnA
Target	205 mg/cm^2 C	481 mg/cm^2 Be
Energy Loss at the Target	6*A* MeV	10*A* MeV
Selection Angle	5 ± 1°	1.5 ± 1.0°
Bρ for D1	1.744 Tm	2.730 Tm
Momentum Slit Width	±14 mm	±12 mm
Momentum Selection	+5 ± 1 %	+2.0 ± 0.5 %
Thickness of the Degrader	429 mg/cm^2 (1.59 mm)	816 mg/cm^2 (3.03 mm)
Energy Loss at the Degrader	8*A* MeV	17*A* MeV
Bρ for D2	1.504 Tm	2.487 Tm
Slit after D2	±10 mm	±5 mm
Secondary Beam Inetnsity	~4 kcps	~2 kcps
β-ray Counting Rate at the Catcher	~300 cps	~150 cps
Typical Polarization	-3.4 %	-2.3 %

K540 ring cyclotron accelerator. Fig. 4-3 is the typical TOF spectrum of the obtained beam from RIPS for ^{13}O setup.

The parameters for the production of ^{9}C and ^{13}O are summarized in the Table 4-1.

4.2. β-NMR chamber

The experimental setup is shown in Fig. 4-4 and Fig. 4-5. The polarized unstable nuclear beam from RIPS were slowed down by an energy degrader and were collimated to the size of the catcher by the collimator made of Pb before. The collimation size was 32 × 16 mm. A 7.75-mm thick absorber made of lucite was also mounted just behind this collimator in ^{13}O measurement. Finally, the beam was implanted into a catcher under a strong magnetic field H_0 for maintaining the polarization and the NMR. Applied H_0 was always monitored by a proton NMR probe placed 60 mm away from the catcher. At the monitor point the magnetic field was about 0.2 % less than the center. Deviations from the intensity of H_0 at the magnet center, where the catcher was placed, were at most ~-0.02 % at 20 mm away from the center, at most ~-0.3 % at 60 mm away from the center.

The wedge thickness was optimized for the maximum β-ray counts. Typical thickness dependence of β-ray counts are shown in Fig. 4-6.

The catcher was mounted in a RF coil placed between a pair of pole piece. The size of the catcher was typically 3 cm × 2 cm. RF magnetic field was applied perpendicular to the external magnetic field. In the case of ^{9}C, the Pt catcher was cooled down to about 30 K for maintaining the polarization in it. A Pt foil was placed at the end of the cold finger of the cryostat with the mechanical refrigerator system. The temperature was monitored by thermocouples attached on the cold finger and the catcher holder. The deviation from the preset temperature was confirmed to be within ±2 degrees. For the ^{13}O experiment, catchers were placed at room temperature since the life time was expected to be shorter than the relaxation time of the polarization.

1) ^{9}C

2) ^{13}O

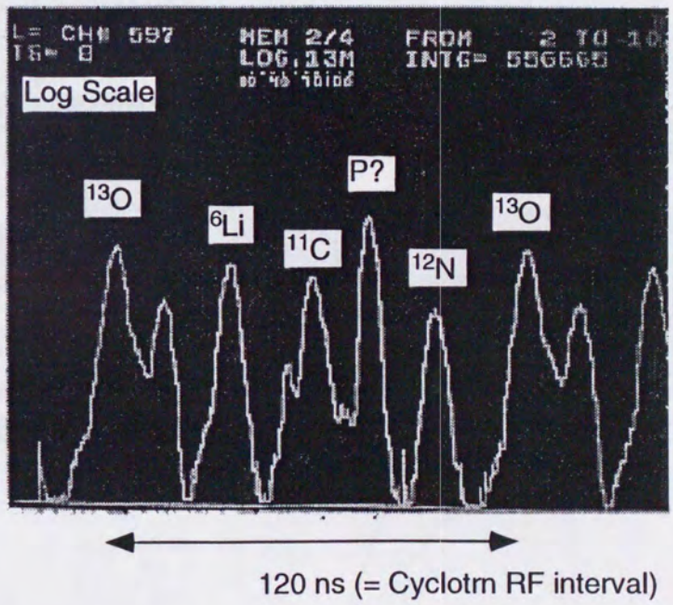

Fig. 4-3. Typical TOF spectra of 1) ^{9}C beam and 2) ^{13}O beam from RIPS.

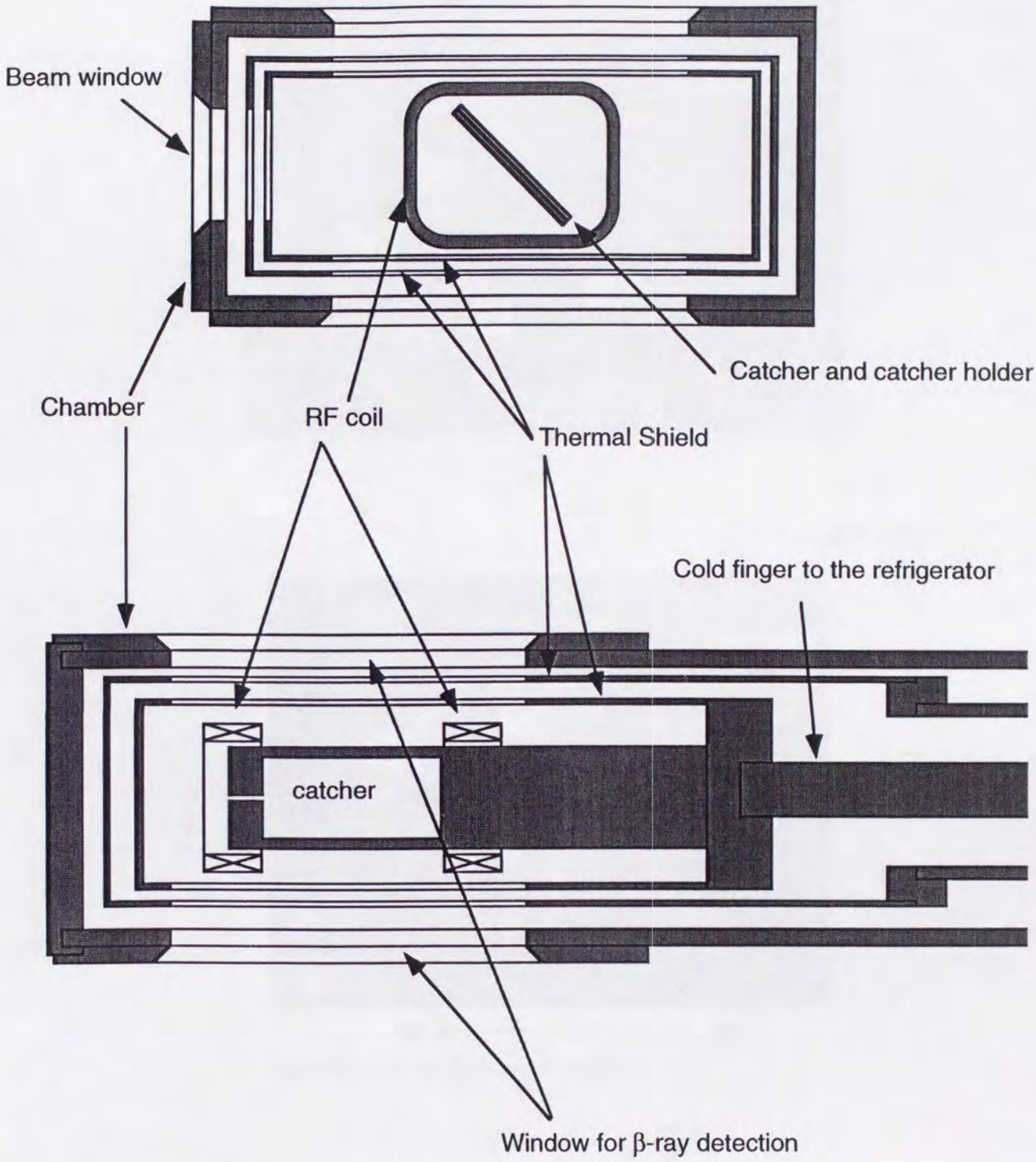

Fig. 4-4.(1) Cold chamber for ^{9}C measurement. The catcher is mounted at the end of the cold finger and cooled down to 30 K by the refrigerator. This drawing is the exact size of the chamber.

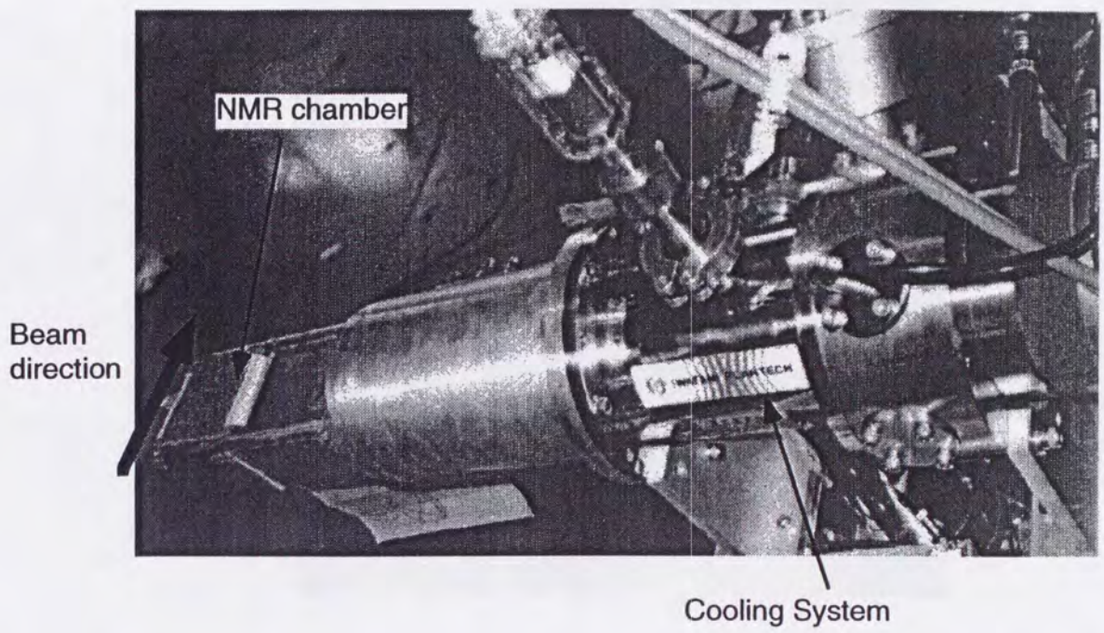

Fig. 4-4.(2) Overview of the NMR chamber for a low temperature measurement.

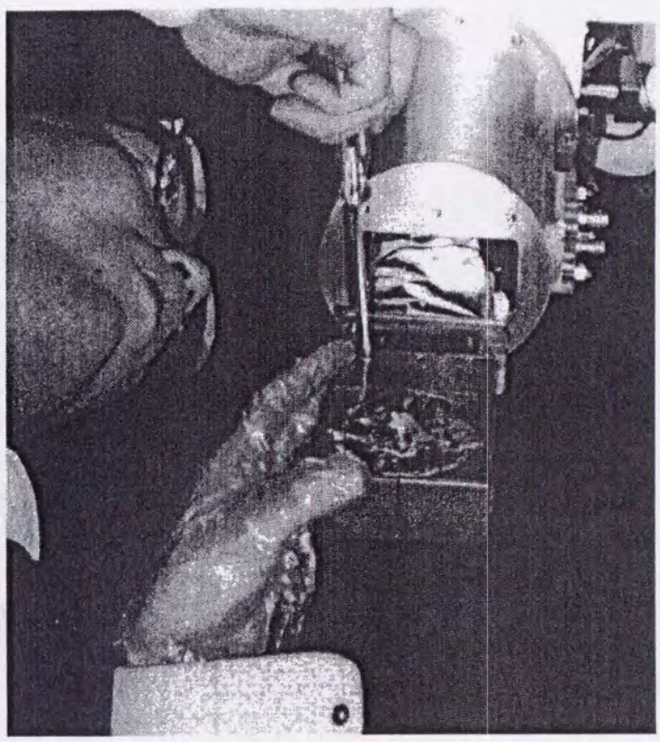

Fig. 4-4.(3) Close up view of the inner side of the cold chamber. RF coil and the catcher are mounted inside the cupper box.

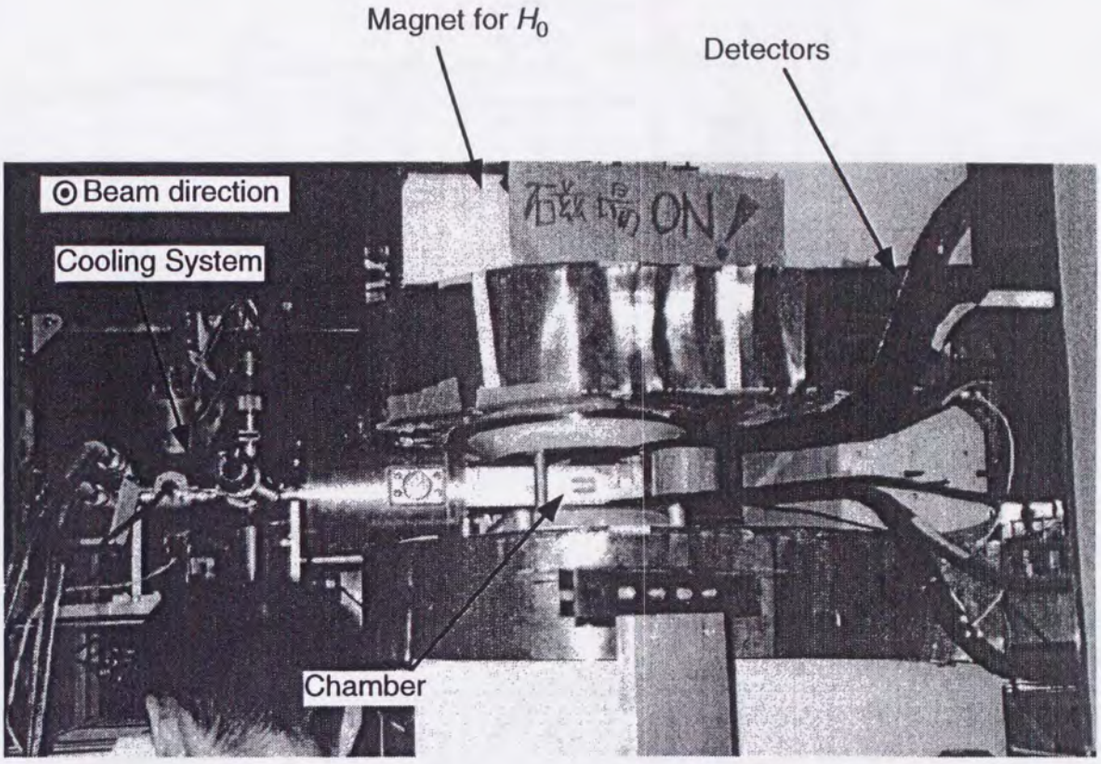

Fig. 4-4.(4) Setup of the NMR chamber for a low temperature.

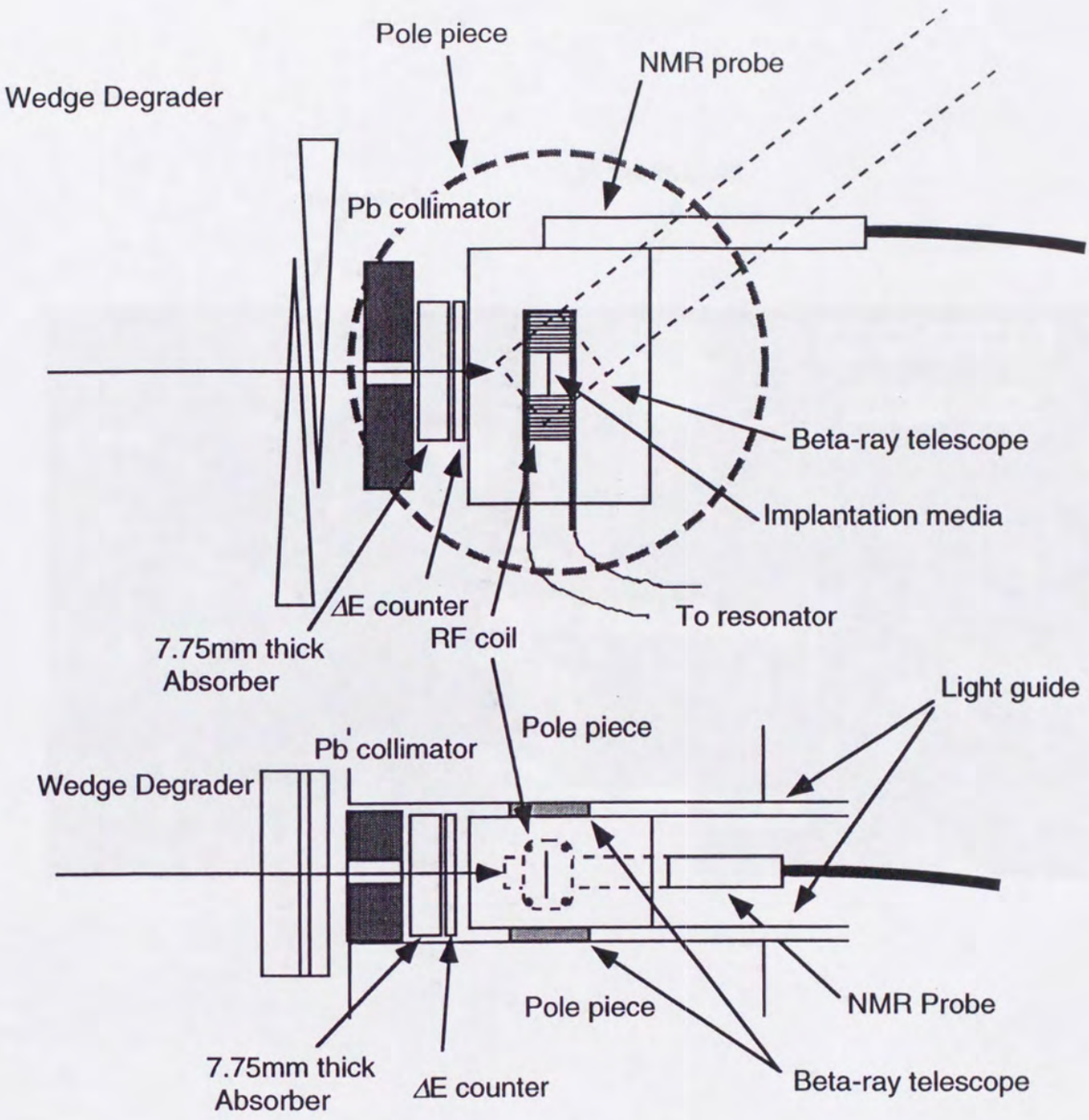

Fig. 4-5.(1) Set up of the chamber for room temperature. All systems were placed in atomosphere.

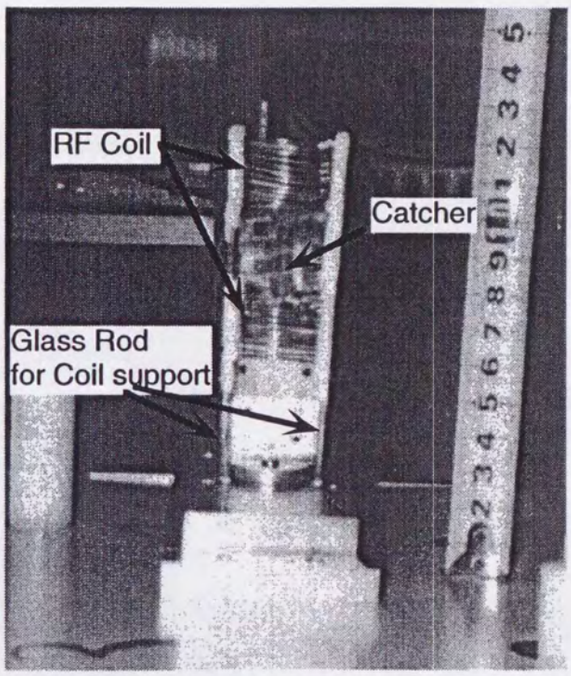

Fig. 4-5.(2) Close up view of the setup of RF coil and catcher.

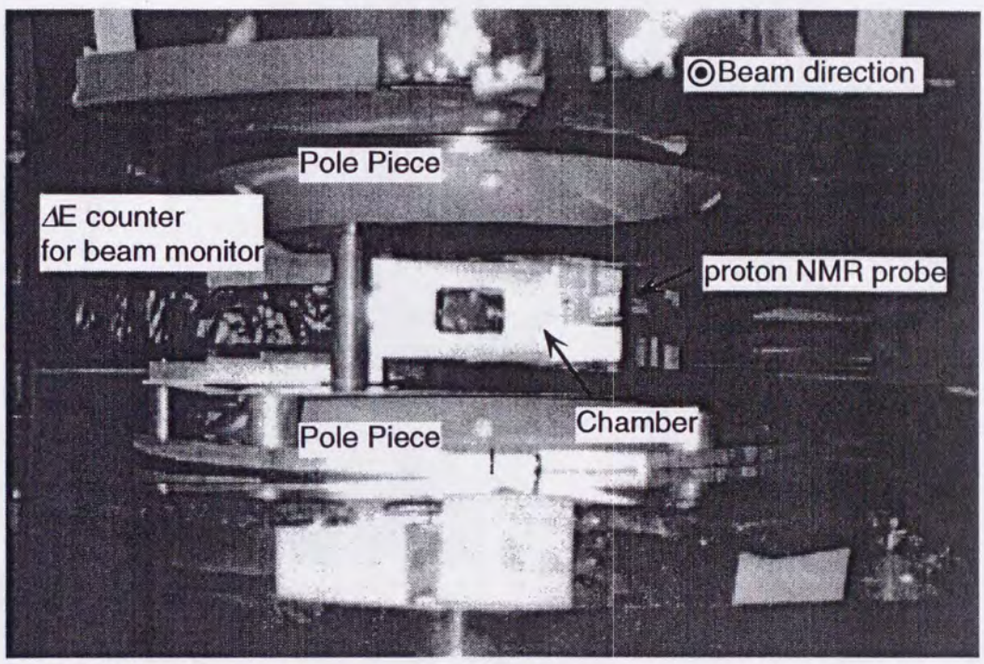

Fig. 4-5.(3) Setup of the NMR chamber for a room-temperature experiment.

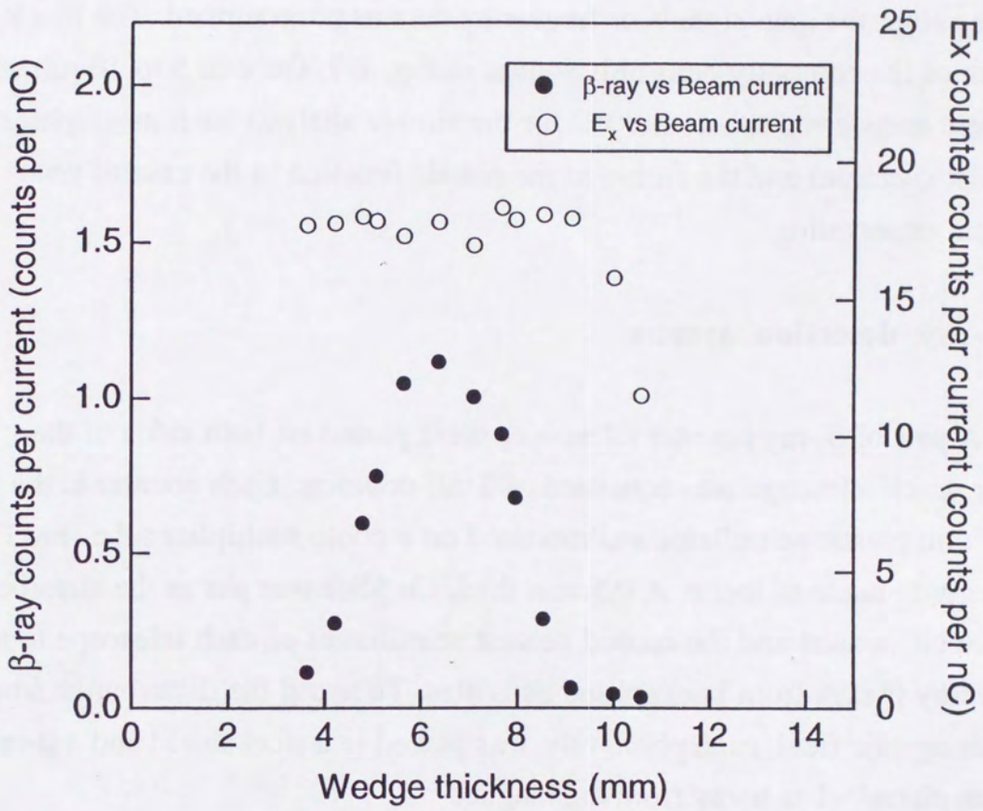

Fig. 4-6. β-ray counts versus wedge thickness for ^{9}C. The wedge thickness was optimized for the maximum β-ray counts.

4.3. System control by a computer

The beam control, the RF and the data taking equipments were supervised by a personal computer (NEC PC-9801VX21) system. The computer gives the start, the stop, the gate signals or frequency data as programmed. The block diagram of the computer control is shown in Fig. 4-7. Once in 5 to 10 minutes the data were transferred to another PC for the simple analysis such as graphics for the NMR spectrum and the fitting to the simple function in the case of time spectrum observation.

4.4. β-ray detection system

A pair of β–ray counter telescopes were placed on both sides of the catcher. Each telescope was consisted of 3 ΔE-counters. Each counter is the 50 × 50 × 1 mm plastic scintillator and mounted on a photo multiplier tube (PMT) with a light guide made of lucite. A 0.5 mm thick Cu plate was put as the absorber between the nearest and the second nearest scintillators of each telescope to reduce low energy β-rays from background activities. To avoid the disturbance from the strong magnetic field, each photo tube was placed in a steel shield and a μ-metal and was placed ~1 m away from the magnet.

Then obtained β-ray signals were analyzed by the electronic circuit system as is shown in the block diagram Fig. 4-8. The timings of three pulses from the counters of a telescope, which were typically -1 ~ -2 V_p, were adjusted by cable delay modules. Electric noises from the counters are rejected by selecting signals larger than a certain discrimination level by discriminators, typically -50 mV. Just the events where the signals from all the three counters were coincide were selected as a true events by coincidence module. The stretched true signals were converted to TTL signal (~ 10 ms) by the gate generators, and were counted by a scaler and interface board installed in the microcomputer. The data for each run were summed up and transferred to a floppy disk every 5 to 10 minutes.

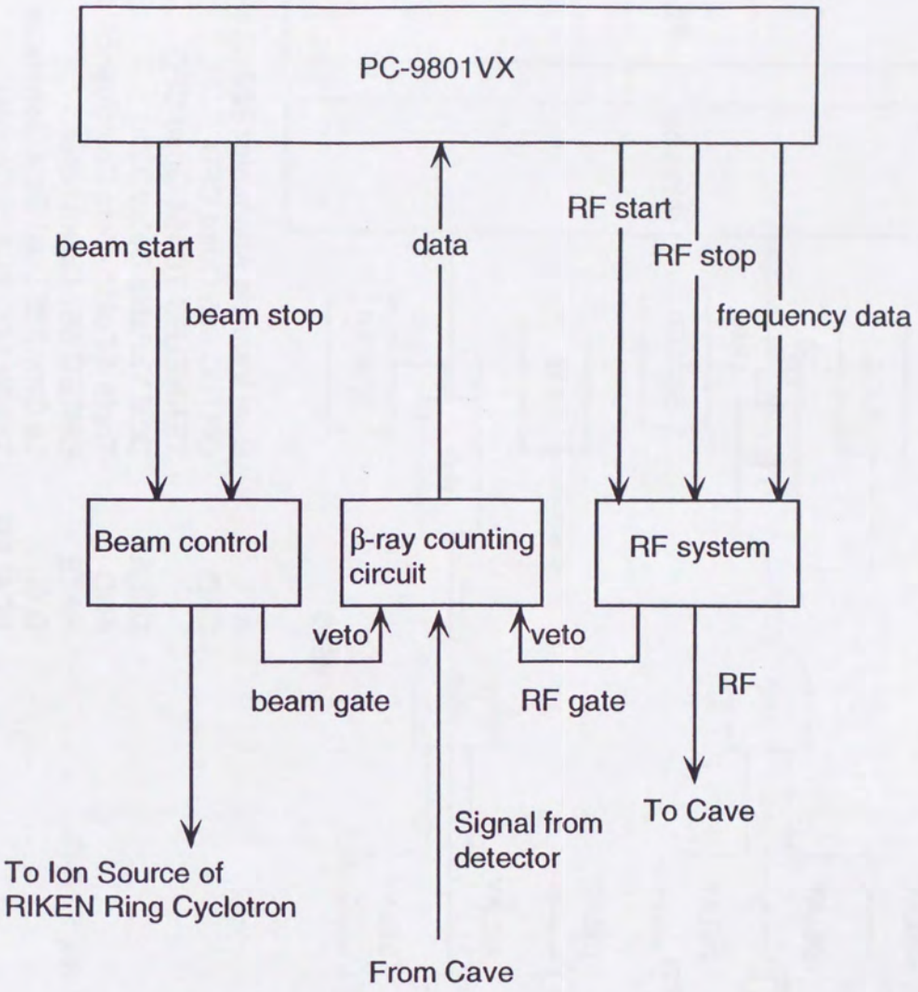

Fig. 4-7. Block diagram of the control system. Whole system is controlled by a personal computer PC9801-VX. While the beam or RF is on, the β-ray counting system was stopped by the veto signals sent from each block.

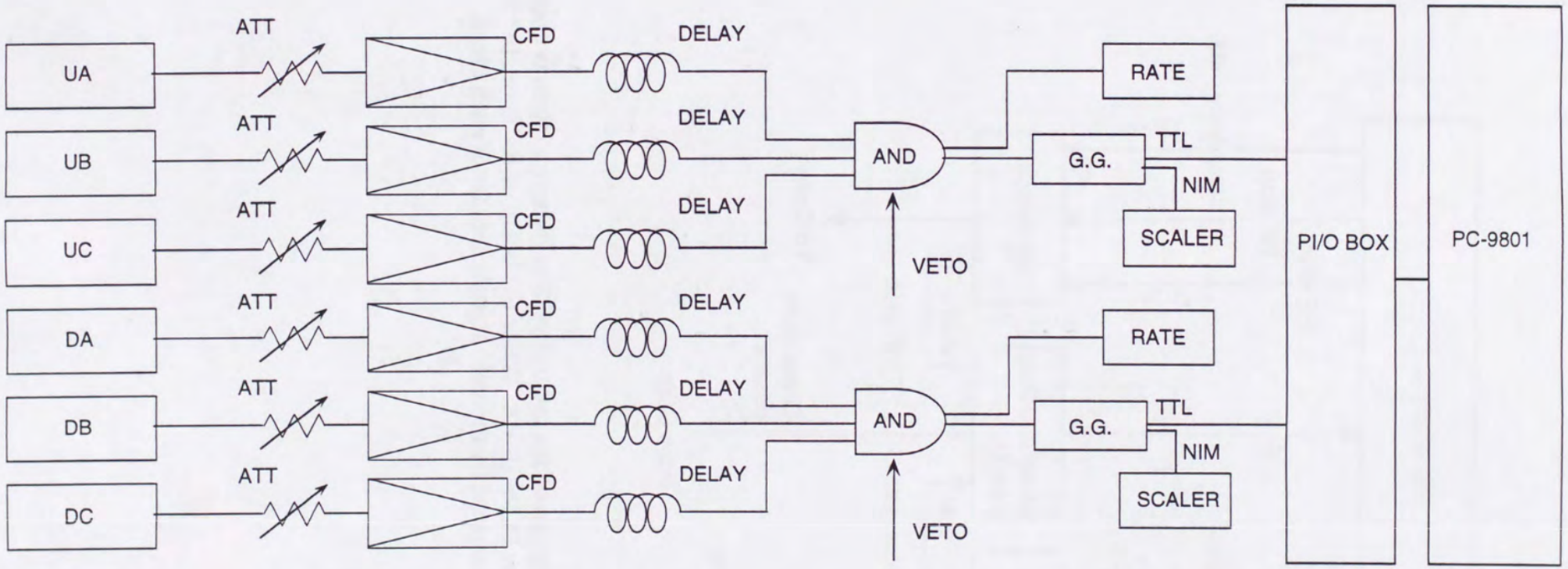

ATT	Dual Variable Attenuator 320
CFD	ORTEC 935 Quad CFD
	TENNELEC TC454 Quad CFD
DELAY	Dual Variable Delay 330
AND	Triple 4-Fold 1-Veto Coincidence 470
RATE	ORTEC 661 Countmeter
G.G.	Le Croy 222 Dual Gate Generator
SCALER	TENNELEC TC532 Counter

Fig. 4-8.(1) Block diagram of Beta-ray counting system.

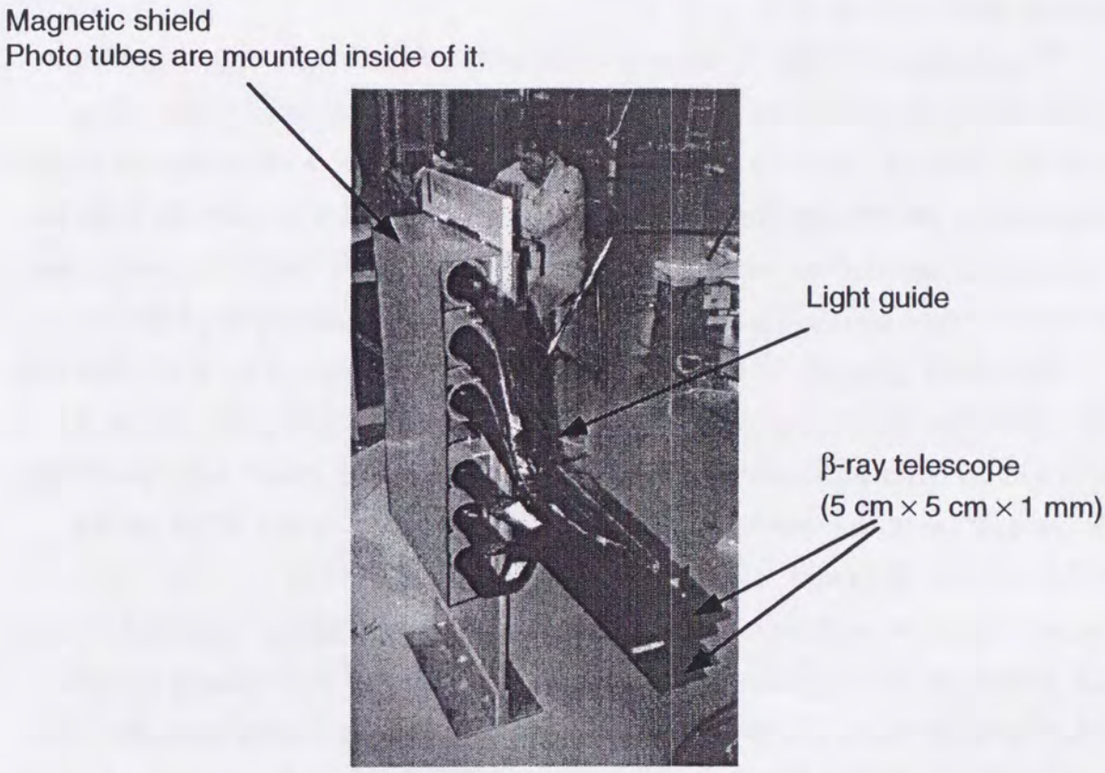

Fig. 4-8.(2) β-ray counter telescope. NMR chamber is mounted between the telescope. Each telescope is consisted of three ΔE plastic scintillators.

4.5. RF system

The RF system consists of two parts: one for the logic control of the RF and the other for synthesizing the RF for the NMR. The block diagram of the RF system is shown in Fig. 4-9.

The logic part of this system is explained as follows. A trigger pulse for each RF was given from the micro computer, the same one used for the data taking. This trigger pulse was stretched to the time duration necessary for the RF application by an interval generator (IG). This gate signal was used for both the RF gating and for the saw tooth waves processing in Ramp generator which was fed to the voltage controlled oscillator (VCO) for the frequency modulation.

The block diagram of RF-synthesizing part is shown in Fig. 4-10. The saw tooth wave from the Ramp generator were fed to VCO which generates an RF of which was 20 MHz modulated in frequency. The width of which is proportional to the amplitude of the input saw tooth waves. To realize such a VCO, an RF signal generator (FG) which generates an RF of 10 MHz with frequency-modulation which is proportional to the Ramp signal obtained from the Ramp generator. The signal was converted to 20 MHz by a frequency doubler. For the RF with wider FM width more than ± 50 kHz, the signal from the VCO was mixed with mother RF from a frequency synthesizer to generate the desired RF frequency with the desired modulation width in the low frequency side band. The higher frequency side band was rejected by a Low Pass Filter. A different system was attached for the FM width less than ± 50 kHz since the present VCO didn't have enough stability for generating signals with small FM width. The RF with 10 times wider FM width than required was produced at first, then converted to the necessary width by counting it down to 1/10 and mixed with 18MHz. For the precise measurement of the resonance frequency, RF without FM was used. In this case, the signal directory generated from the frequency synthesizer was used (Fig. 4-11).

The synthesized RF signal was amplified by a linear wideband power amplifier. The serial resonance circuit (Fig. 4-12) and the transformer was used for the impedance matching. The vacuum capacitor which had a wide capacity

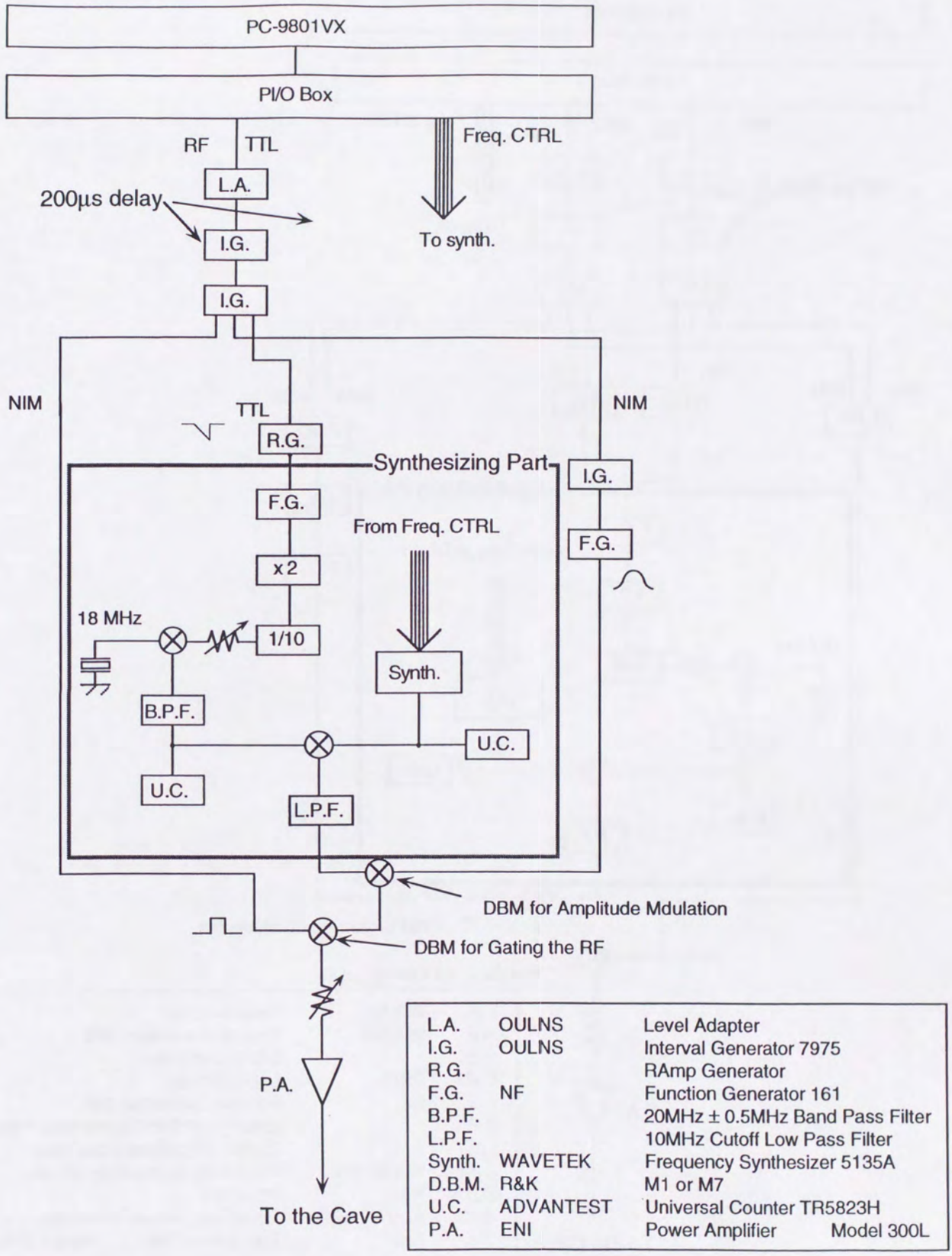

Fig. 4-9.(1) Block diagram of the RF system for signals with frequency modulations.

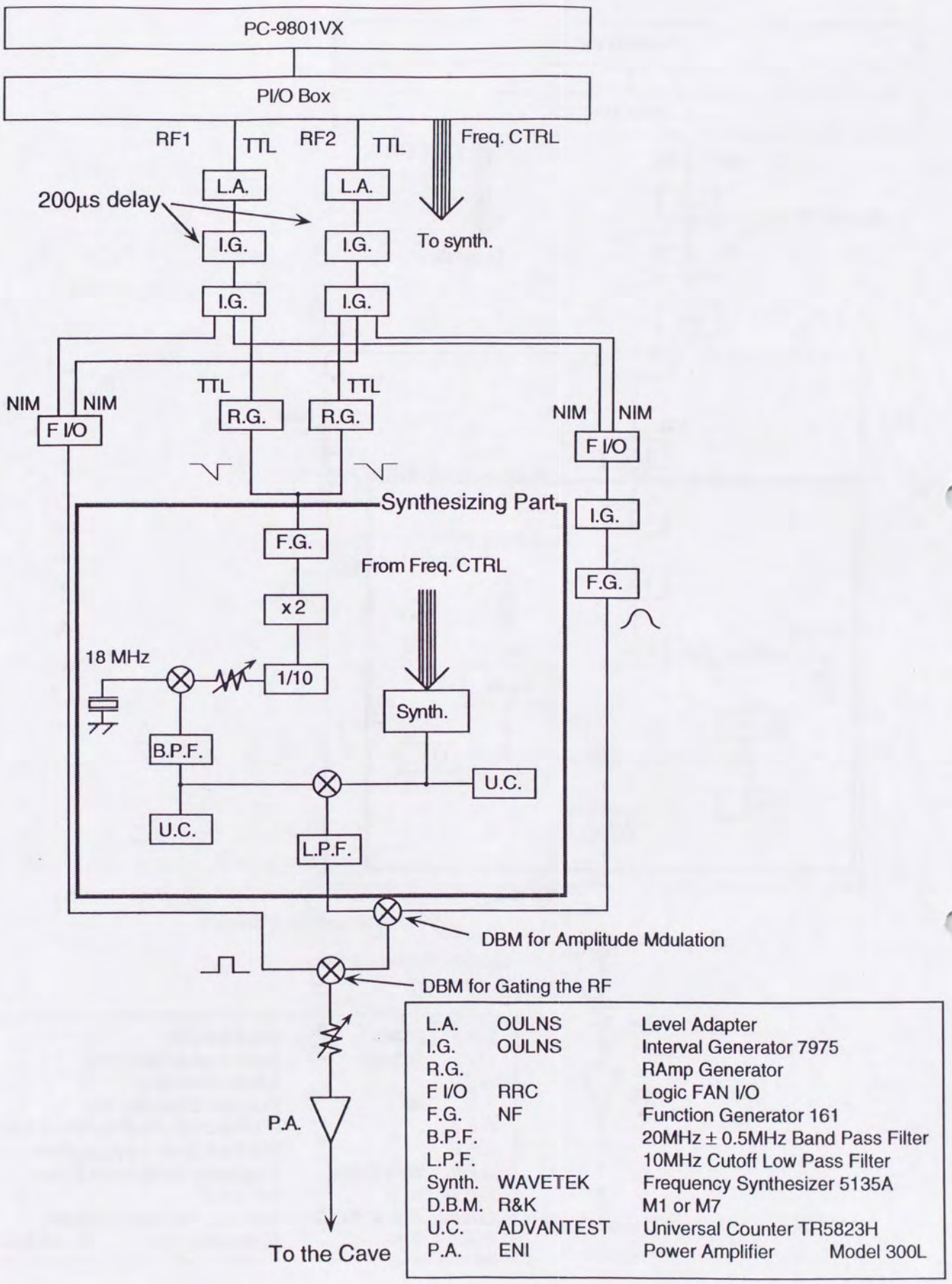

L.A.	OULNS	Level Adapter
I.G.	OULNS	Interval Generator 7975
R.G.		RAmp Generator
F I/O	RRC	Logic FAN I/O
F.G.	NF	Function Generator 161
B.P.F.		20MHz ± 0.5MHz Band Pass Filter
L.P.F.		10MHz Cutoff Low Pass Filter
Synth.	WAVETEK	Frequency Synthesizer 5135A
D.B.M.	R&K	M1 or M7
U.C.	ADVANTEST	Universal Counter TR5823H
P.A.	ENI	Power Amplifier Model 300L

Fig. 4-9.(2) Block diagram of the RF system for the NNQR with the AFP.

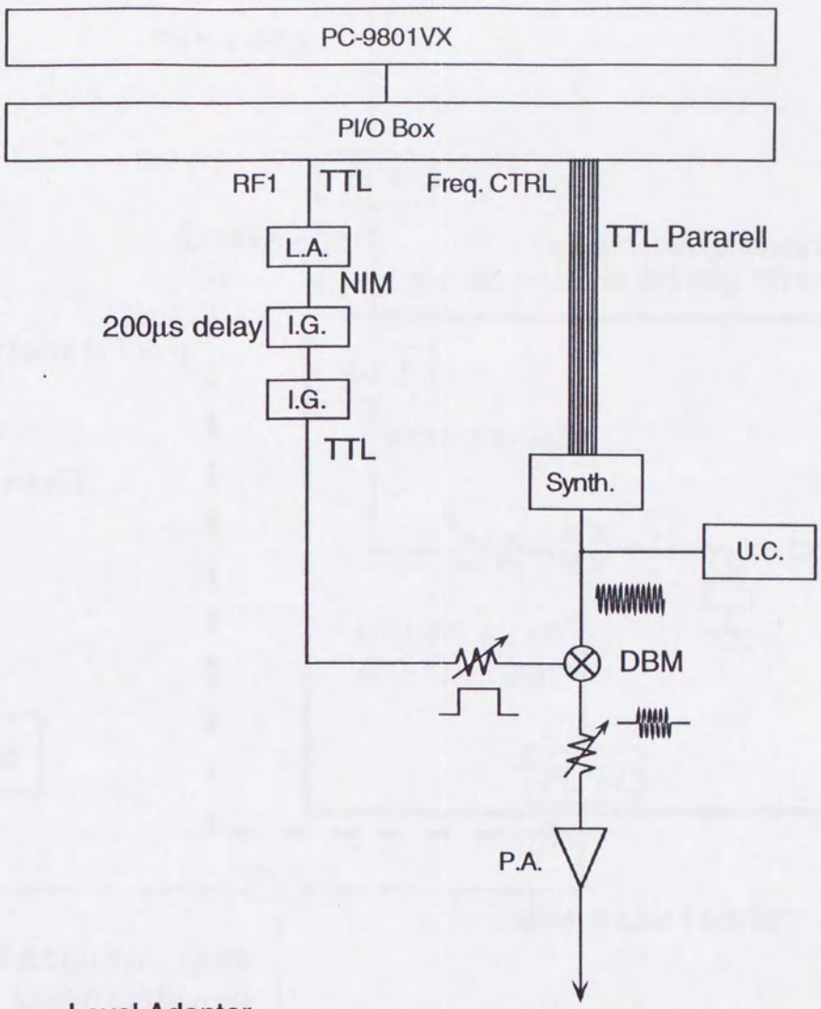

L.A.	OULNS	Level Adapter
I.G.	OULNS	Interval Generator 7975
Synth.	WAVETEK	Frequency Synthesizer 5135A
DBM	R&K	M1 or M7
U.C.	ADVANTEST	Universal Counter TR5823H
P.A.	ENI	Power Amplifier Model 300L

Fig. 4-9.(3) Block diagram of the synthesizing system of monochromatic RF. Continuous RF from the frequency synthesizer is shaped by the gate signal with the RF time length at DBM.

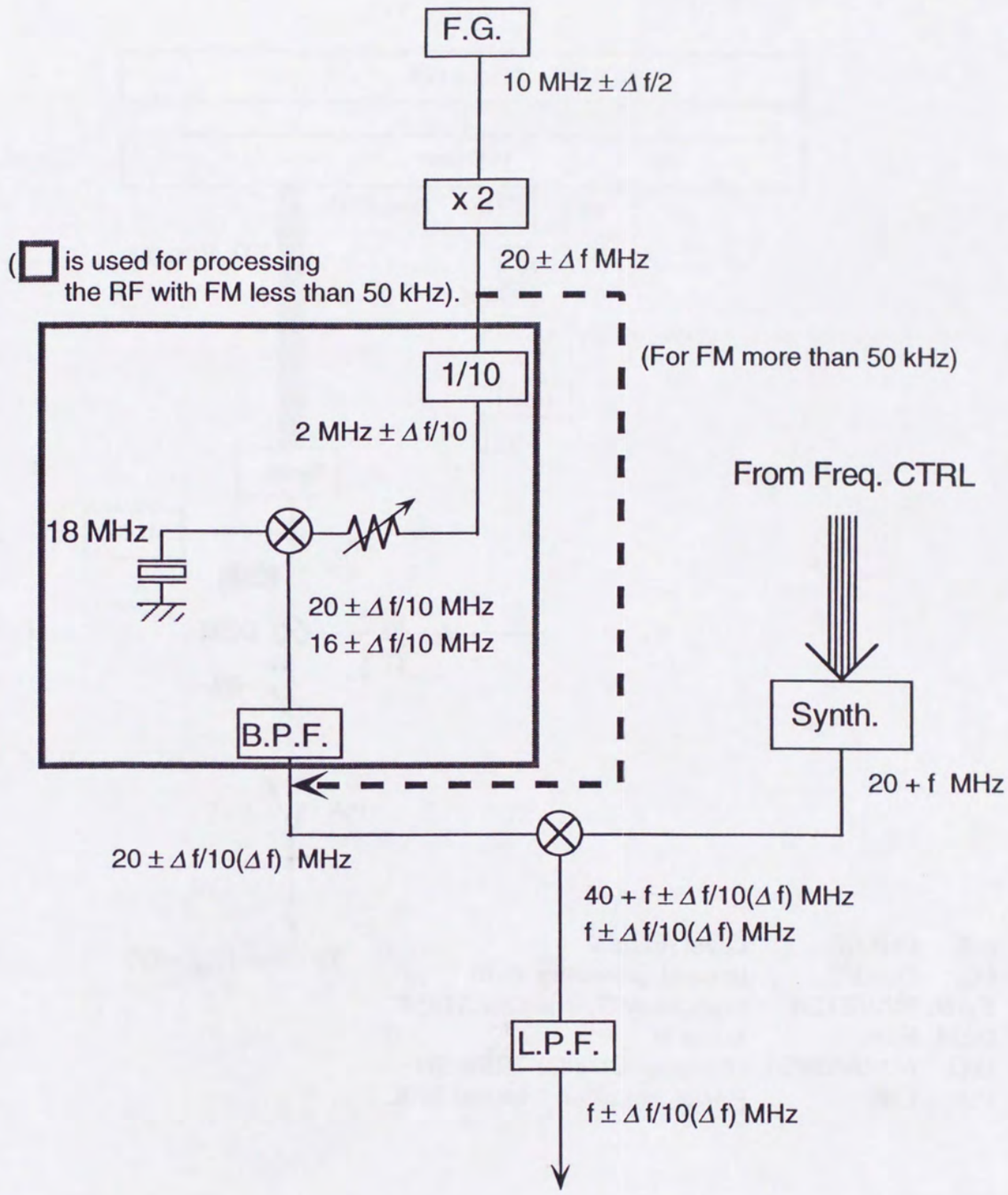

Fig. 4-10. Synthesizing system of the frequency-modulated RF.

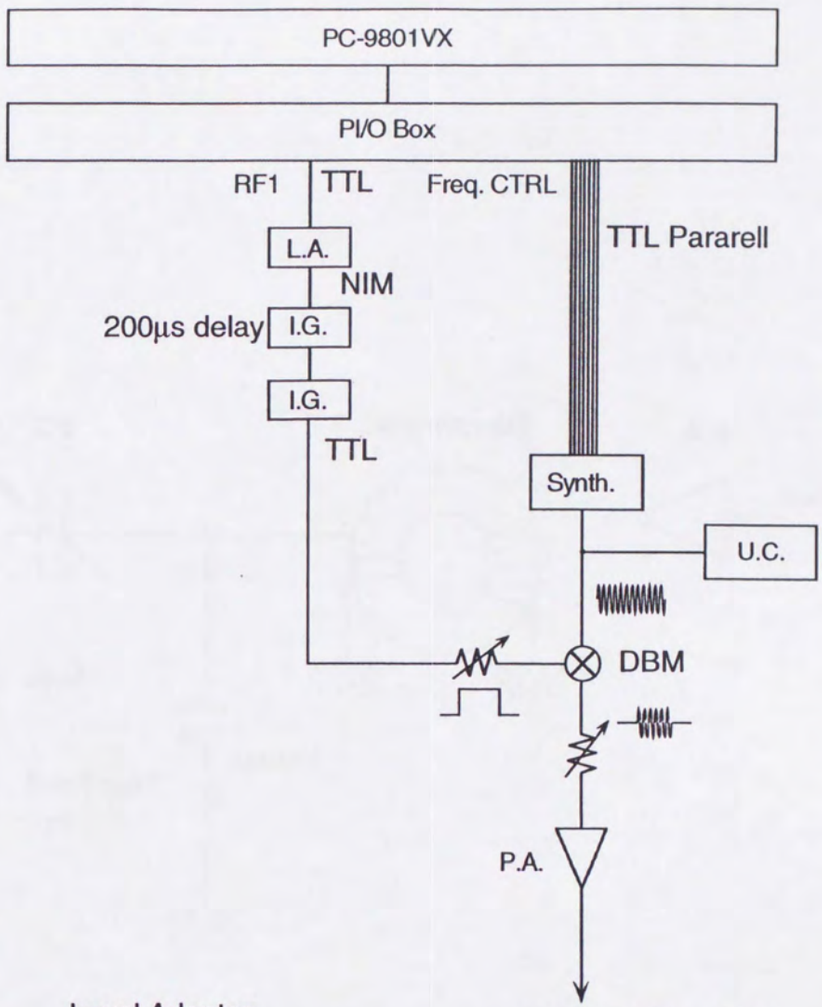

L.A.	OULNS	Level Adapter
I.G.	OULNS	Interval Generator 7975
Synth.	WAVETEK	Frequency Synthesizer 5135A
DBM	R&K	M1 or M7
U.C.	ADVANTEST	Universal Counter TR5823H
P.A.	ENI	Power Amplifier Model 300L

Fig. 4-11. Block diagram of the synthesizing system for a monochromatic RF. A continuous RF from the frequency synthesizer is gated (amplitude modulated) by the gate signal with the RF time length at the DBM.

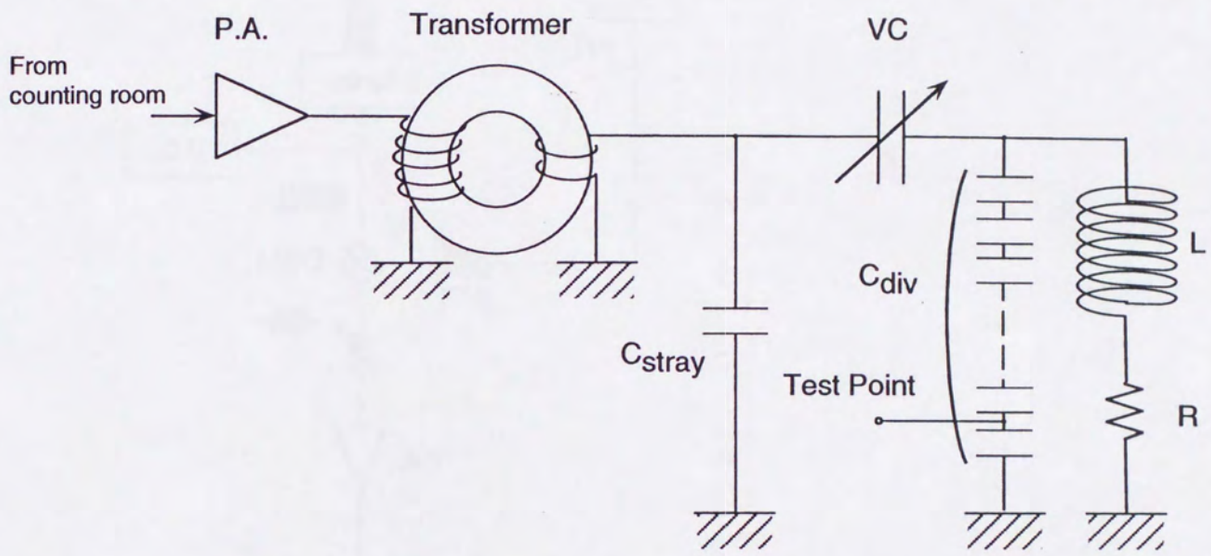

Fig. 4-12. Schematic diagram of the matching system for the H_1 feeding. The C_{stray} is the equivalent capacitance to the stray capacitance. The C_{stray} is estimated to be ~50 pF. The RF voltage in the coil is monitored at the test point in the C_{div}. The quality Q of this circuit is optimized by choosing an appropriate value of R.

range of 50 pF ~ 1500 pF was used as the capacitor (C) component in the resonance circuit. This vacuum capacitor is good for high voltage up to 10 kV. The resistor R was chosen so that the Q of the resonance circuit was appropriate for the applied RF frequency range. The reactance of the resisters was small enough up to ~30 MHz.

The turn number ratio of the transformer was selected so that the impedance matching at the resonance frequency was achieved. In this experiment, N_{in} / N_{out} = 5 / 2 was chosen, since the expected impedance ratio 5^2 / 2^2 is close enough to the impedance, 50 ohms / 10 ohm at the resonance frequency.

The typical parameters for this impedance matching system is summarized in Table 4-2.

Table 4-2. Resonator circuit parameters.

Frequency	~ 2.8 MHz
Inductance of H_1 coil	~ 9 μH
N_{in} / N_{out}	5 / 2
Resister	12.5 Ω
Q of the circuit	~ 10

4.6. Implantation media

Once the polarized ^{9}C or ^{13}O nuclei are produced, the polarization has to be kept during their lifetimes. It has been well known that the polarization can be maintained by implanting the nuclei into suitable crystals under a strong magnetic field. The selection of crystals is also important for obtaining well defined electric field gradients in them, which are too strong to produce artificially. In the present experiment, the energy of the nuclei are much higher than the energy loss given by the thickness of the implantation medium, the nuclei are implanted all depth equally. The crystals used as implantation media in this experiment are as follows.

4.6.1. Pt (Platinum)

A Pt film was used for measuring the magnetic moments of ^{9}C and ^{13}O. The crystal structure of the Pt metal has a face-centered cubic structure (fcc) as shown in Fig. 4-13. The lattice constant of this crystal is 3.92 Å at 25 C°. Since the structure of Pt crystal is cubic, no electric field gradients exist at the octahedral site, the body center of a unit cell, where light impurities are mainly implanted. Therefore, the Pt foil is suitable for the measurement of the magnetic moment. A Pt metal has another specific character that the spin-lattice relaxation times of the light impurities are very long. The local electron density is quenched because the Fermi level lies at anti-resonance dip in s-states occurring due to the s-d hybridization (Fano effect) [30, 31].

The sample foil from Fuchikawa Kinzoku co. ltd. was used in this experiment. This foil was annealed in vacuum around 1800 K, which is near the melting point of Pt, for two hours to remove the damages and/or cracks. Then the temperature was kept around 1500 K for 10 hours to decrease the defects inside the Pt crystal. At last the sample temperature was gradually down to the room temperature. This treatment is known to diminish the broad resonance component observed for the case of ^{12}B implanted into Pt without this treatment [32]. After this treatment, large grains of 2~3 mmϕ were observed on the surface of the foil.

4.6.2. MgO (Magnesium oxide)

A plate of MgO was used for the measurement of the magnetic moment of ^{13}O. The structure of this crystal is NaCl like with the lattice constant of 4.21 Å at 25 C° (Fig. 4-14). Since MgO is a cubic crystal, no static electric fields gradient exist at the substitutional site of O, where ^{13}O is expected to be settled in.

To obtain a perfect crystal, the sample was cleft by a thin knife from a large single crystal just before the experiment.

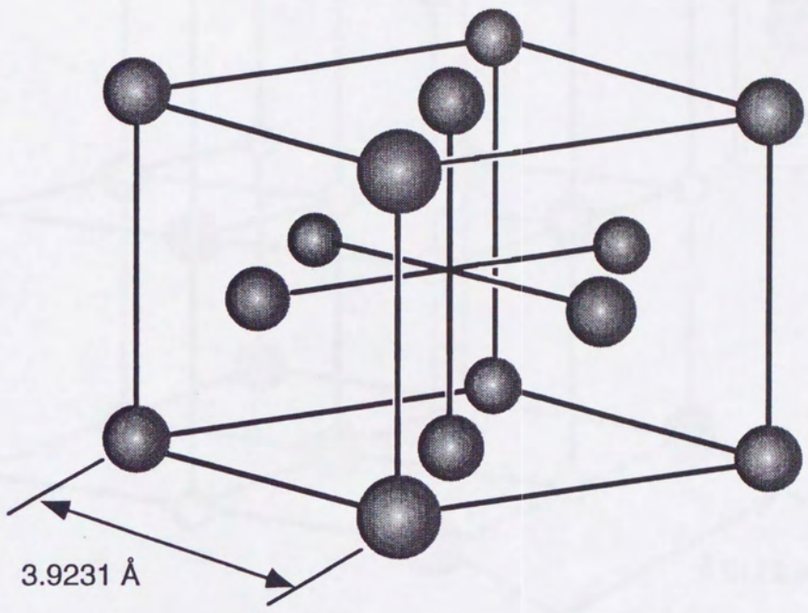

Fig. 4-13. Crystal structure of the Pt metal, fcc.

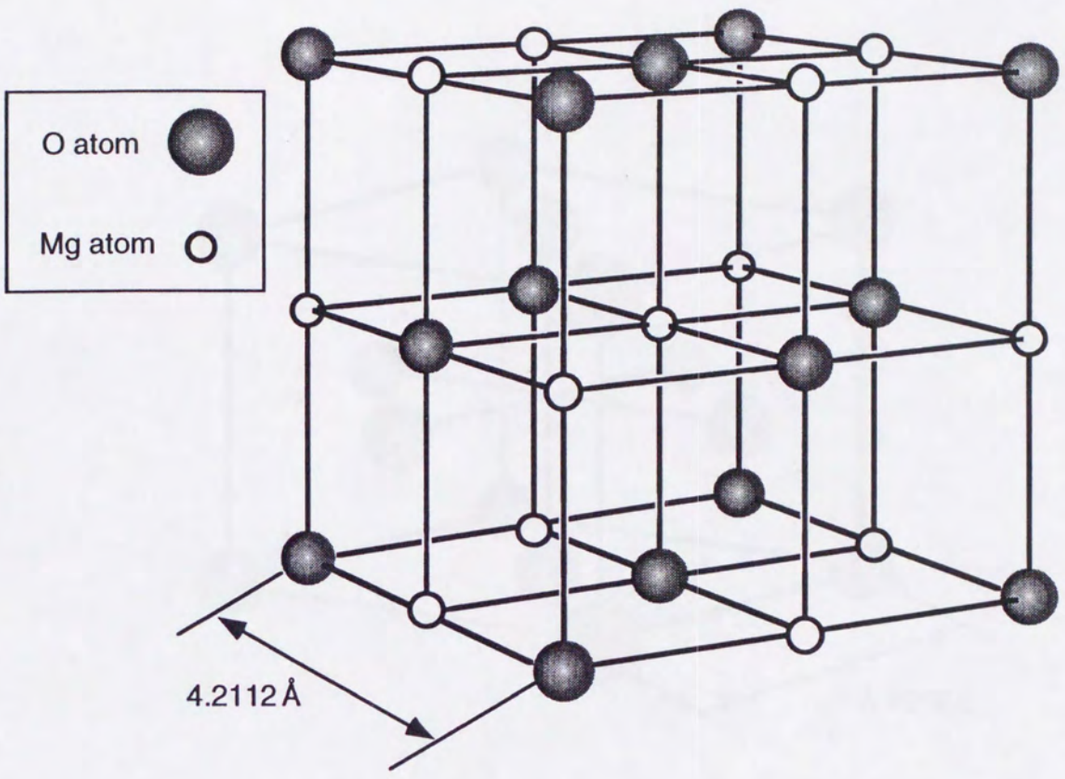

Fig. 4-14. Crystal strucuture of MgO. The structure of the MgO crystal is that of NaCl.

4.6.3. TiO_2 (Titanium dioxicide)

This sample was used for the measurement of the quadrupole moment of ^{13}O. This crystal has rutile structure as shown in Fig. 4-15 and is known as a ferroelectric material. The electric field gradient at O sites in a middle plane of a unit cell has a direction vertical to the one for O at the top and bottom plane. Both are included in the $\langle 110 \rangle$ plane. A single plate of 15 mm $\times$ 25 mm $\times$ 0.5 mm thick TiO_2 was used for Q measurement of ^{13}O. The present TiO_2 plate with well polished to optical flat were purchased from Earth Jewelry. The X-ray pattern for this crystal is shown in Fig. 4-16.

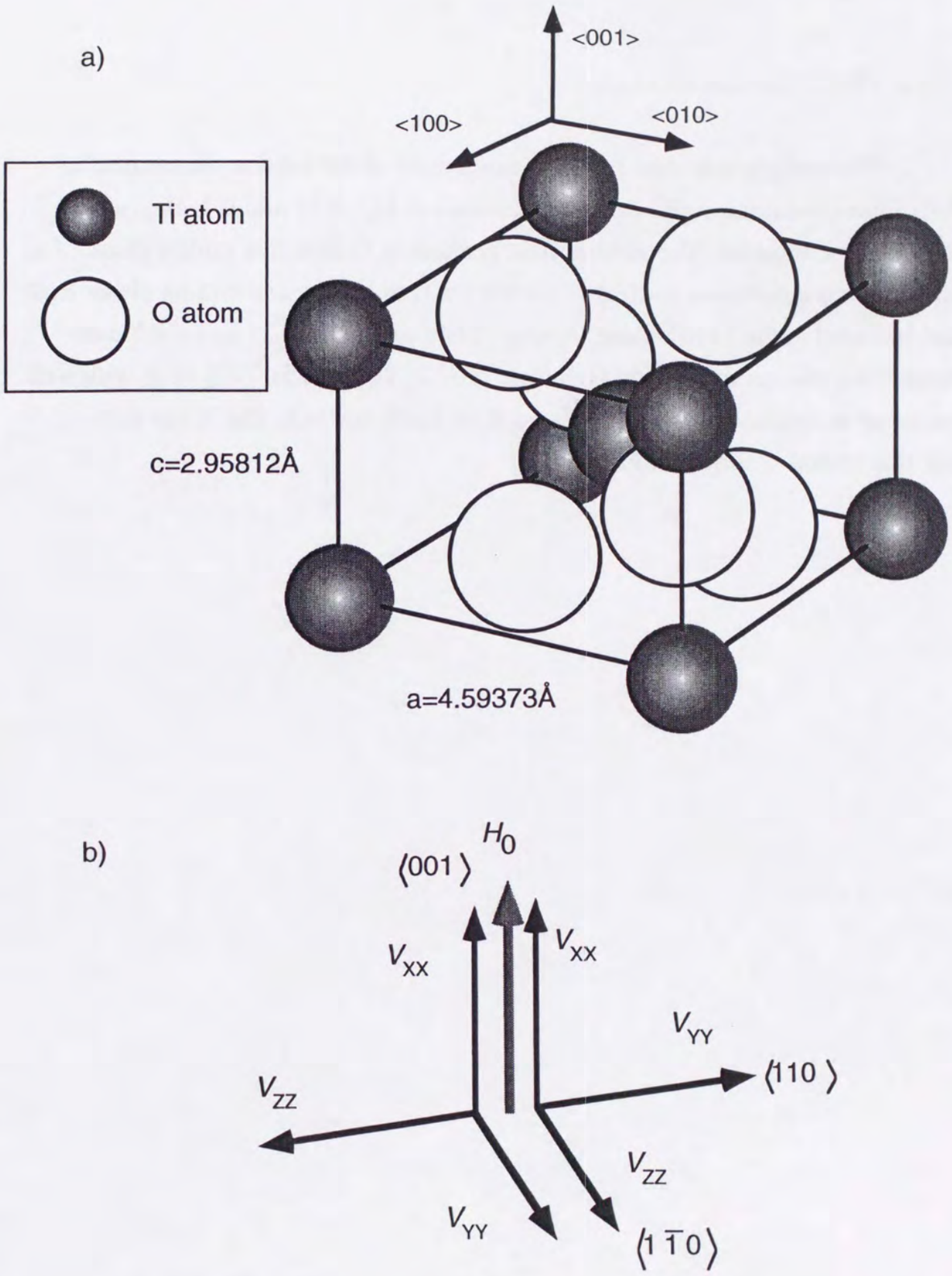

Fig. 4-15. a) Crystal structure of TiO_2(rutile). b) Orientation of the electric field gradient(EFG). Two equivalent field gradients exist at O site.

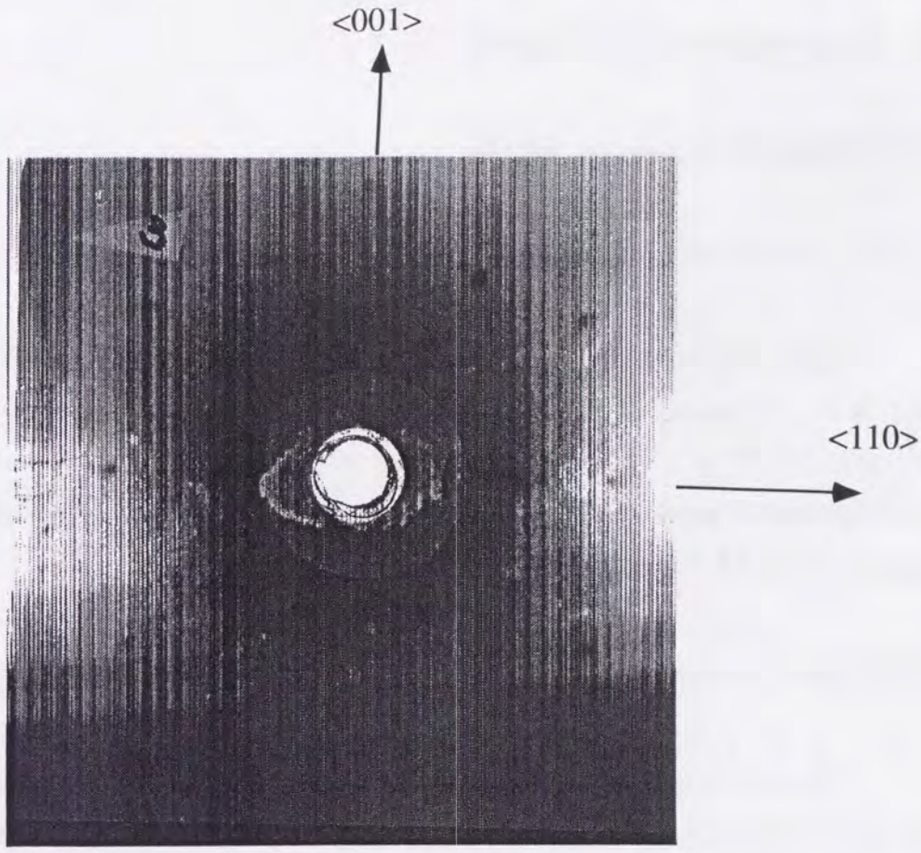

Fig. 4-16. Typical X-ray photograph of TiO_2 crystal for the NNQR measurement of ^{13}O in TiO_2. This photo was taken from the direction perpendicular to c-axis direction. Two-fold rotation symmetrical pattern was observed.

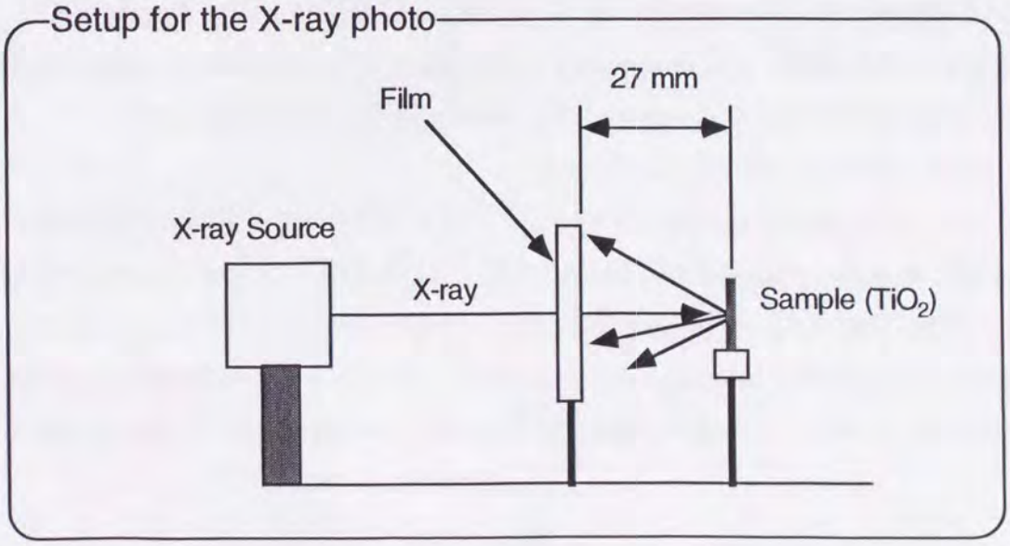

5. Experimental Result

5.1. Magnetic moment of ^{9}C

5.1.1. Confirmation of the production of ^{9}C

The production of ^{9}C ($T_{1/2}$ = 127 ms) was confirmed by the β-ray time spectrum. As shown in the typical time spectrum in Fig. 5-1, main component was ^{9}C, and ^{8}B ($T_{1/2}$ = 769 ms), which was the main impurity in the secondary beam, was contained as little as one tenth of the ^{9}C. That was pure enough for the present β-NMR detection.

5.1.2. NMR detection of ^{9}C

The NMR resonance frequency was searched for ^{9}C implanted in a polycrystalline Pt foil, which was cooled down to 30 K to maintain the polarization during the life time of ^{9}C. The size of this Pt foil was 16 mm × 30 mm × 50 μm. This foil was placed at the end of the cold finger extended from the refrigerator with a tilted angle of 45 degrees relative to ^{9}C beam direction.

The NMR detection of ^{8}B was employed for the check of the whole system, especially whether spin manipulations could be performed. The ^{8}B nuclei were easily obtained by slightly changing the tuning of RIPS because the ^{8}B nuclei were also produced through the ^{12}C + C collision. The β-ray asymmetry change was observed by 4AP detection method as a function of RF intensity. Applied RF frequency was 3.1 MHz with frequency modulation of ±200 kHz. A large static magnetic field of ~8 kOe was applied. As shown in Fig. 5-2, the NMR manipulation was successfully employed.

As the first step, a resonance search with a wide range was carried out. The width of RF frequency modulation was ±100 kHz and the applied magnetic field H_0 was 4 kOe. The AFP technique was used for the detection of a large β-ray asymmetry change. The intensity of applied H_1 was 4 ~ 8 Oe depending on the FM width, which was enough for the AFP technique. The time length of the

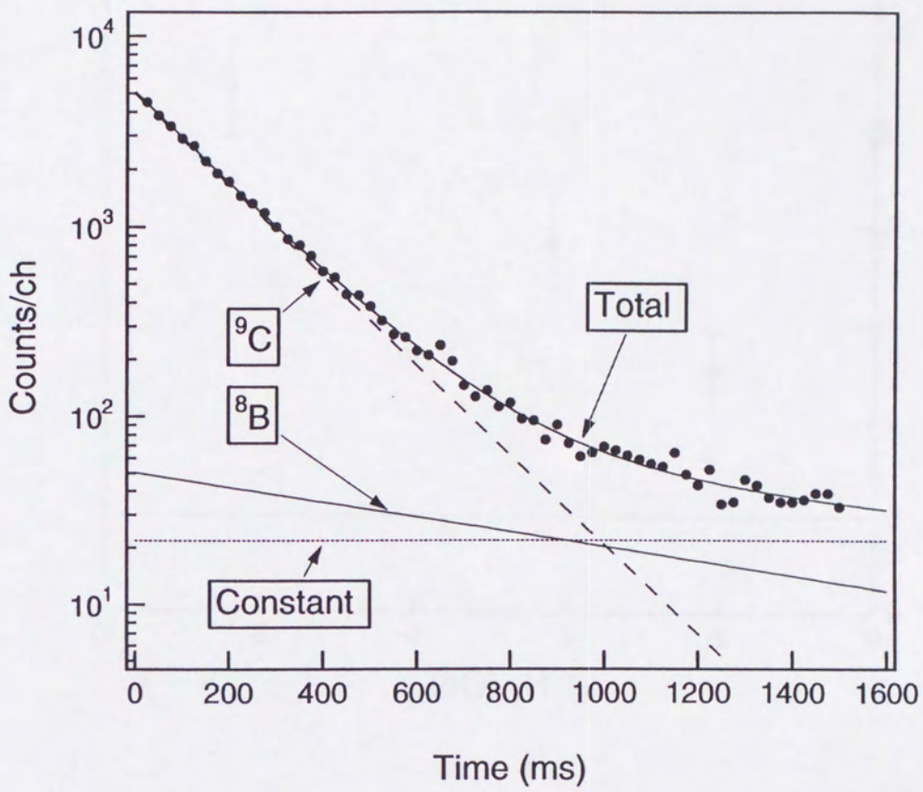

Fig. 5-1. Typical time spectrum of ^{9}C. The ^{8}B component, which is the main back ground of the present experiment, is less than 1/10 of ^{9}C.

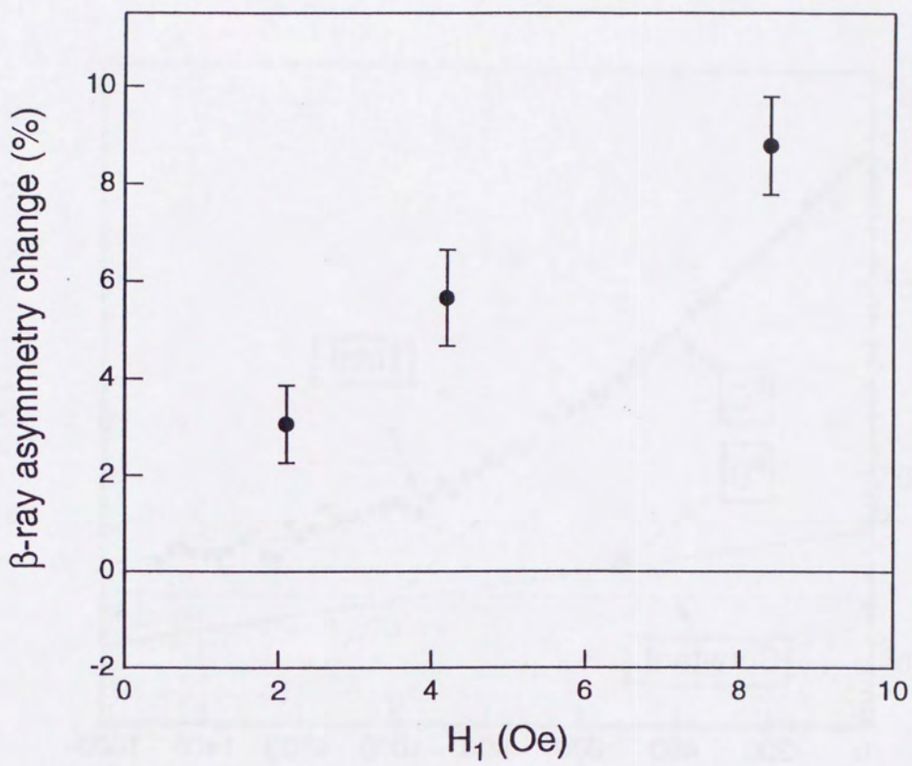

Fig. 5-2. Typical H_1 dependence of the β-ray asymmetry change of ^{8}B in Pt.

applied RF was 20 ms. A single resonant polarization reversal was found at ~ 2.8 MHz (Fig. 5-3). Then the precise resonance search was continued with a narrower frequency modulation around 2.8 MHz. A typical spectrum of this search is shown in Fig. 5-4. Finally, the precise resonance condition was determined by use of the depolarization method without frequency modulation. The static magnetic field H_0 ~4 kOe was monitored with a proton NMR at the monitor point near the catcher, 6 cm away from the center of the NMR magnet. The stability of the applied H_0 was kept within the order of 10^{-6}. The time length of the applied RF was 20 ms. A typical β-NMR spectrum of ^{9}C is shown in Fig. 5-5. Observed β-ray asymmetry change was up to ~ 3 %. The resonance frequency was obtained by fitting Lorentzian to the data. Obtained results are summarized in Table 5-1.

Table 5-1. Results of the NMR measurement of ^{9}C in Pt.

Resonance Frequency (kHz)	2827.3 ± 0.3
H_0 at the monitor point (Oe)	3991.40 ± 0.02

5.1.3. H_0 calibration

For the determination of a magnetic moment by the NMR technique, the exact external field H_0 at the catcher has to be determined. In the case of $\mu(^{9}C)$, β-NMR on ^{8}B in Pt was also employed for this purpose because the resonance condition of ^{8}B in Pt was precisely determined by Minamisono [24] et al. During the measurement, H_0 was monitored by a proton NMR at the same position as that for the ^{9}C measurement.

A typical spectrum of ^{8}B in Pt is given in Fig. 5-6. The resonance frequency of ^{8}B in Pt was obtained by fitting Lorentzian to the data. Obtained results are summarized in Table 5-2.

Table 5-2. Results of the NMR measurement of ^{8}B in Pt.

^{8}B in Pt (kHz)	1578.27 ± 0.08
H_0 at the monitor point (Oe)	3991.35 ± 0.02

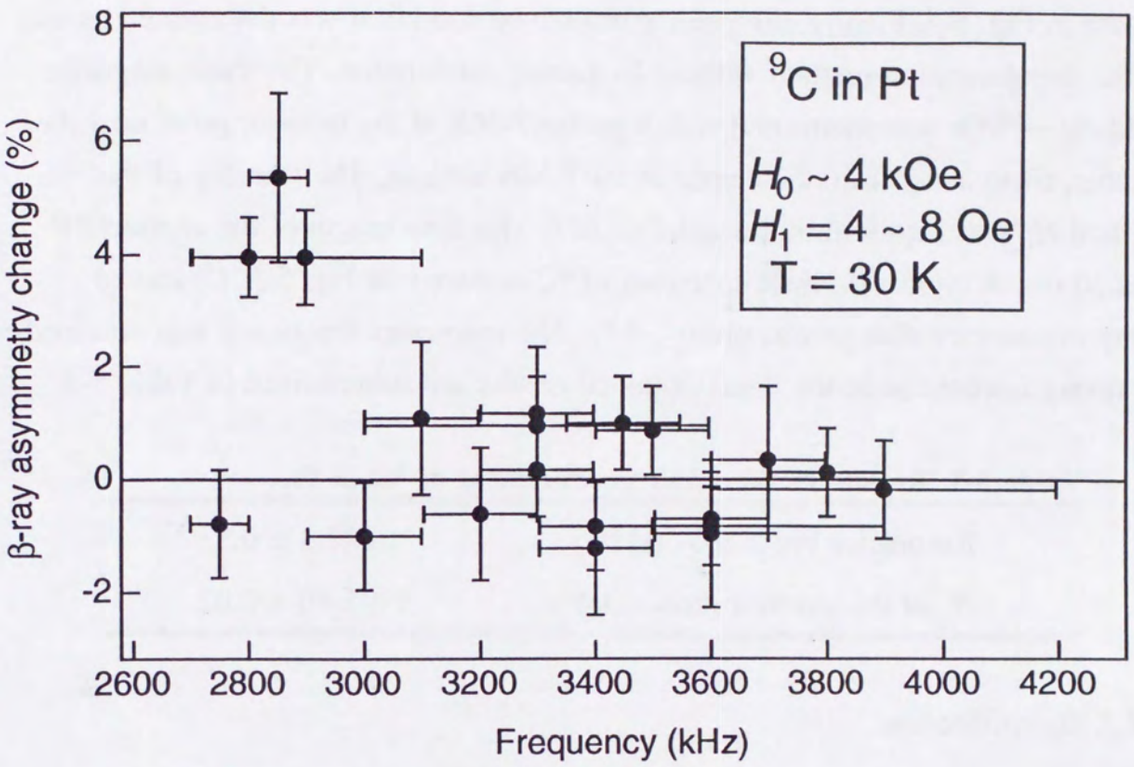

Fig. 5-3. NMR search for ^{9}C in Pt at T = 30 K. The intensity of the applied H_1 for the AFP measurement was from 4 to 8 Oe depending on the FM width.

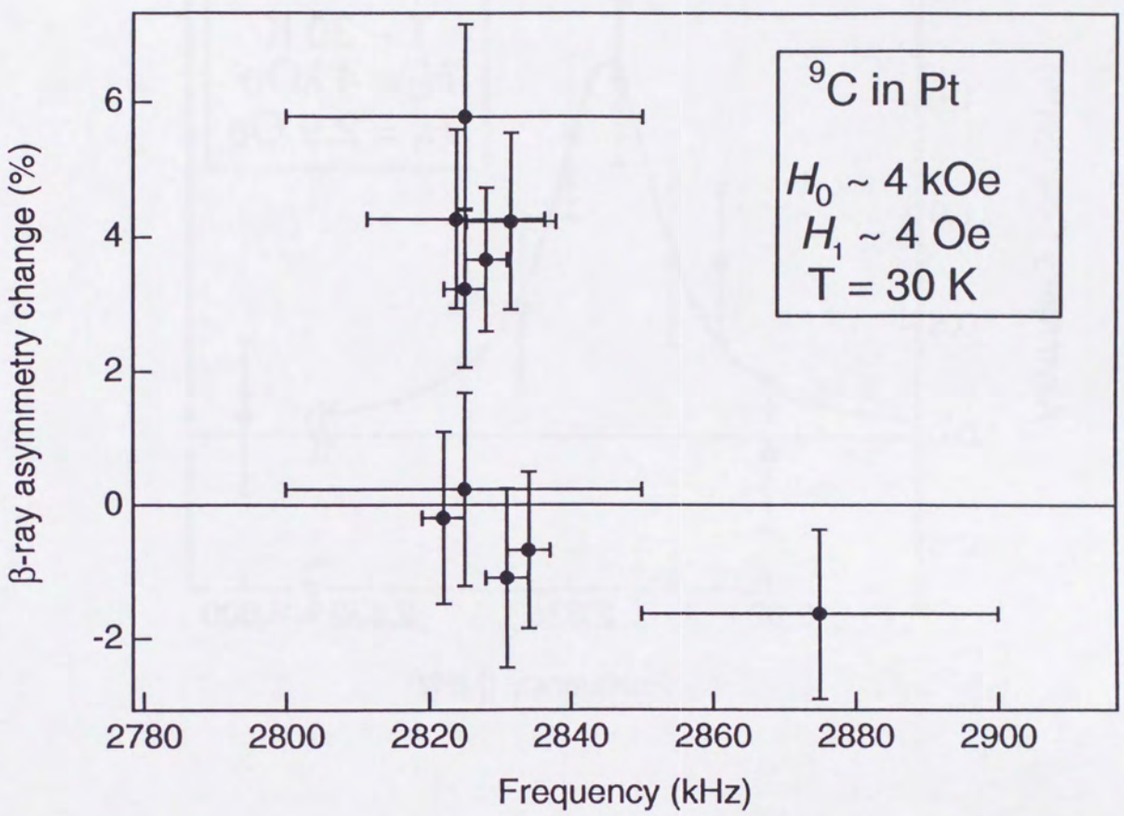

Fig. 5-4. NMR search for ^{9}C implanted in Pt around $f \sim 2.8$ MHz. The applied H_1 for the AFP measurement was about 4 Oe.

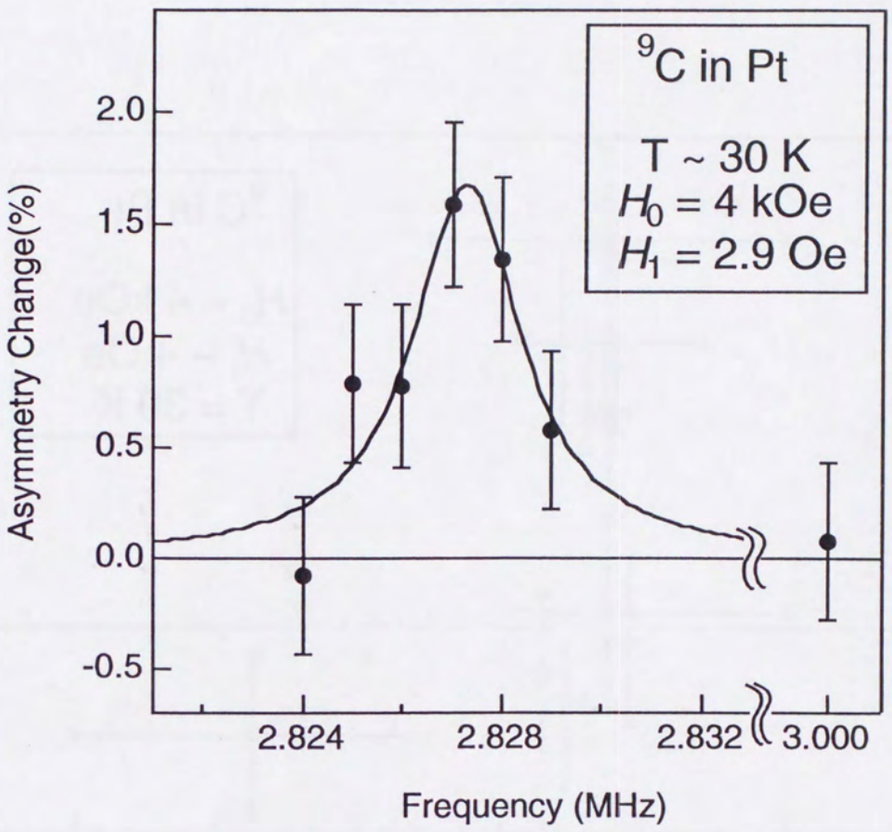

Fig. 5-5. Typical NMR spectrum of ^{9}C implanted in Pt. Pt was cooled down to ~30 K to maintain the polarization.

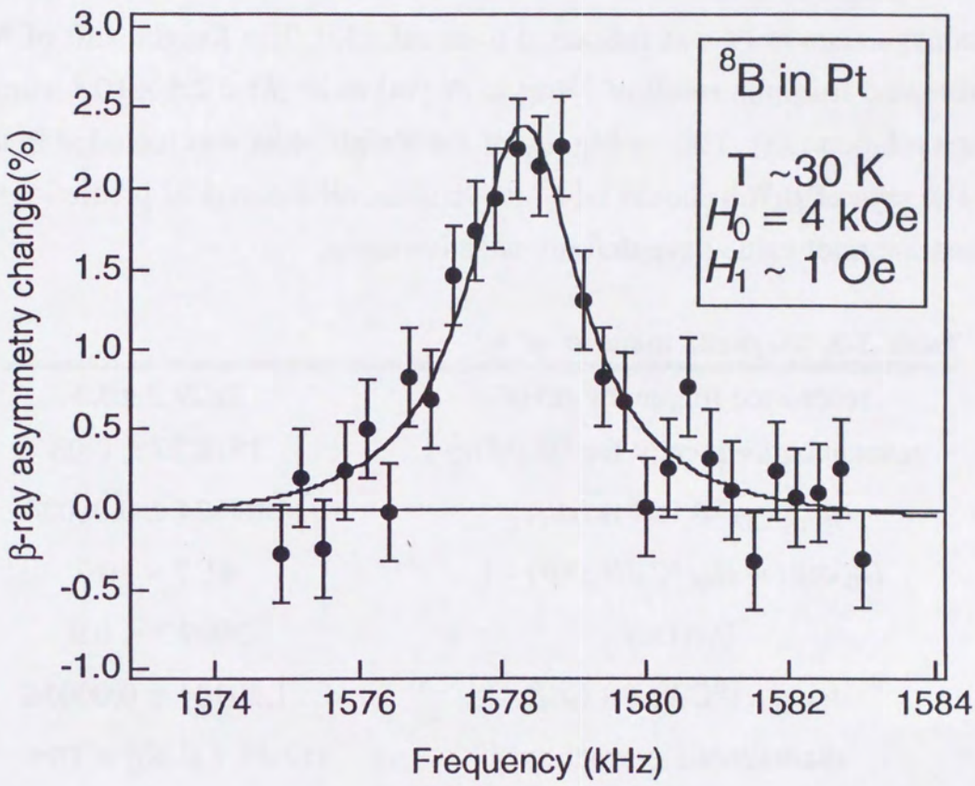

Fig. 5-6. Typical NMR spectrum of ^{8}B in Pt at T ~30 K. The strength of the external field H_0 was pecisely measured.

5.1.4. Magnetic moment of ^{9}C

The magnetic moment of ^{9}C was determined as summarized in Table 5-3. The diamagnetism in Pt was estimated from ref. [33]. The Knight shift of ^{9}C in Pt was estimated from the result of ^{23}Mg in Pt [34] to be $|K| < 2.5 \times 10^{-4}$ using the Korringa relation [23]. This ambiguity of the Knight shift was included in the error. The sign of $\mu(^{9}C)$ should be negative since all theoretical predictions including Schmidt value have definite negative signs.

Table 5-3. Magnetic moment of ^{9}C.

resonance frequency (kHz)	2827.3 ±0.3
resonance frequency for ^{8}B (kHz)	1578.27 ± 0.08
$\mu_{uncorr.}(^{8}B$ in Pt) (μ_N)	1.03534 ± 0.00024
H_0 drift = $H_0(^{9}C)/H_0(^{8}B)$ - 1	$+1.3 \times 10^{-5}$
H_0 (Oe)	3999.7 ± 0.9
$\mu_{uncorr.}(^{9}C$ in Pt) (μ_N)	1.39101 ± 0.00036
diamagnetic correction	$+(2.43 \pm 0.40) \times 10^{-4}$
Knight shift	$\|K\| < 2.5 \times 10^{-4}$
μ (^{9}C) (μ_N)	(-)1.3914 ± 0.0005

5.2. Magnetic moment of ^{13}O

5.2.1. Confirmation of the production of ^{13}O

The implanted nuclei were confirmed to be ^{13}O by measuring the β-ray time spectrum. A typical time spectrum is shown in Fig. 5-7. As shown in the figure, the main component was ^{13}O ($T_{1/2}$ = 8.6 ms) and a small fraction of ^{12}N ($T_{1/2}$ = 11 ms), which was the main impurity in the secondary beam, was as small as one tenth of ^{13}O. This was pure enough for the β-NMR detection of ^{13}O.

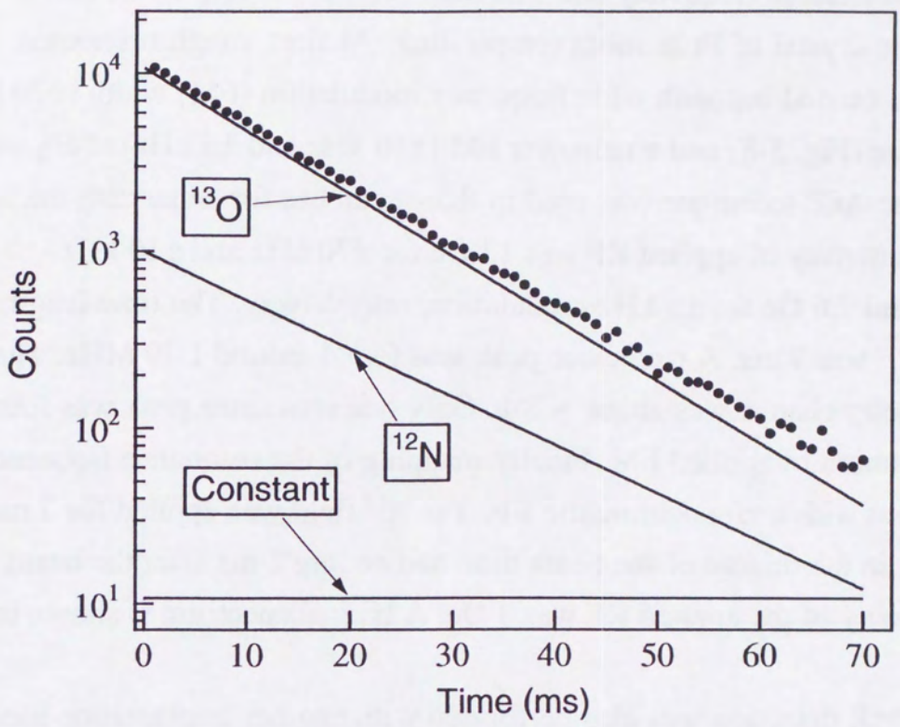

Fig. 5-7. Typical spectrum of ^{13}O. The main back ground is ^{12}N for the present measurement.

5.2.2. NMR detection of ^{13}O

NMR resonance frequency was searched for the ^{13}O implanted into a polycrystalline crystal of Pt at room temperature. At first, rough resonance searches were carried out with wide frequency modulation (FM) width (±70 kHz) at H_0 ~2.5 kOe (Fig. 5-8) and a narrower FM (±10 kHz and ±5 kHz) at H_0 ~4 kOe (Fig. 5-9). The AFP technique was used in these searches for enhancing the NMR signals. The intensity of applied RF was 12 Oe for ±70 kHz and ±10 kHz modulation and 7.6 Oe for ±5 kHz modulation, respectively. The time length of the applied RF was 7 ms. A resonance peak was found around 1.79 MHz. The net β-ray asymmetry change was about ~ 3%. Only one resonance peak was found with the resolution of applied FM. Finally mapping of the resonance frequency was carried out with a monochromatic RF. The RF field was applied for 7 ms in total, starting in the middle of the beam time and ending 2 ms after the beam was off. The intensity of the applied RF was 3 Oe. A typical spectrum is shown in Fig. 5-10.

The NMR detection was also performed with another implantation medium, MgO. The procedure of the measurement was basically the same as that in the case of Pt. Applied H_0 was 4 kOe. At first, the resonance search was employed with AFP method. The time length of the applied RF was 7 ms. The intensity and modulation width of the applied RF was 12 Oe and ±10 kHz, respectively. A typical spectrum is shown in Fig. 5-11. Then the precise mapping of the resonance with the monochromatic RF was employed. The intensity of applied RF for this precise mapping was H_1 = 1.5 Oe. The time length of the RF field was 7 ms in total, starting in the middle of the beam time and ending 2 ms after the beam was off. A typical spectrum is shown in Fig. 5-12. The resonance was found at 10 kHz below the frequency observed in Pt. This large shift in the resonance frequency for ^{13}O in Pt was consistent with the estimation from a fast relaxation time T_1 observed in Pt via Korringa relation. Obtained results were fit to the theoretical function. Results are summarized in Table 5-4.

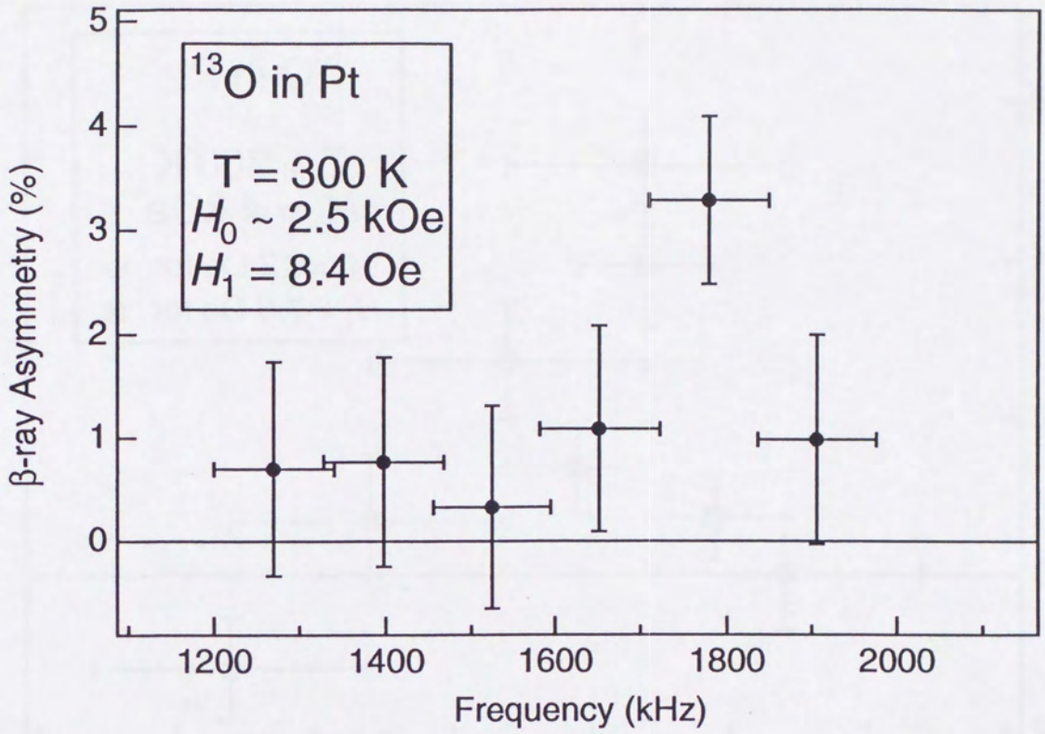

Fig. 5-8. Typical NMR spectrum of ^{13}O implanted in Pt at H_0 ~2.5 kOe.

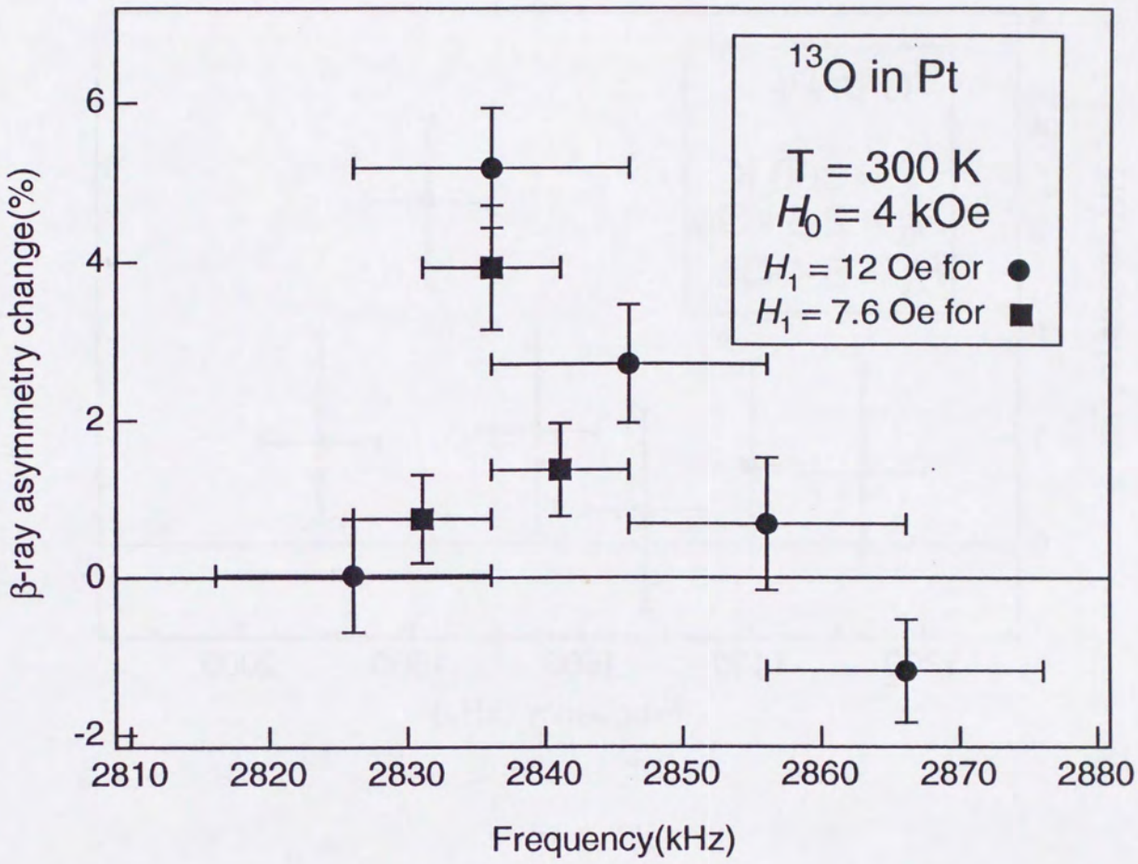

Fig. 5-9. Typical NMR spectrum of ^{13}O implanted in Pt with FM modulation.

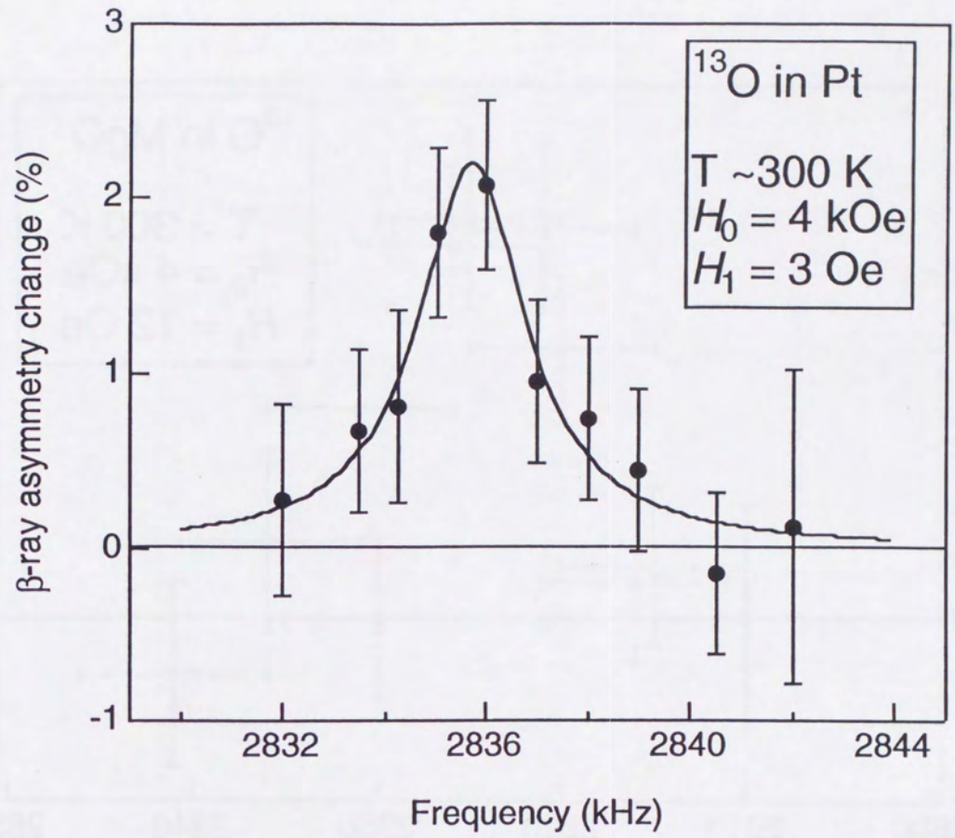

Fig. 5-10. Typical NMR spectrum of ^{13}O implanted in Pt at room temperature.

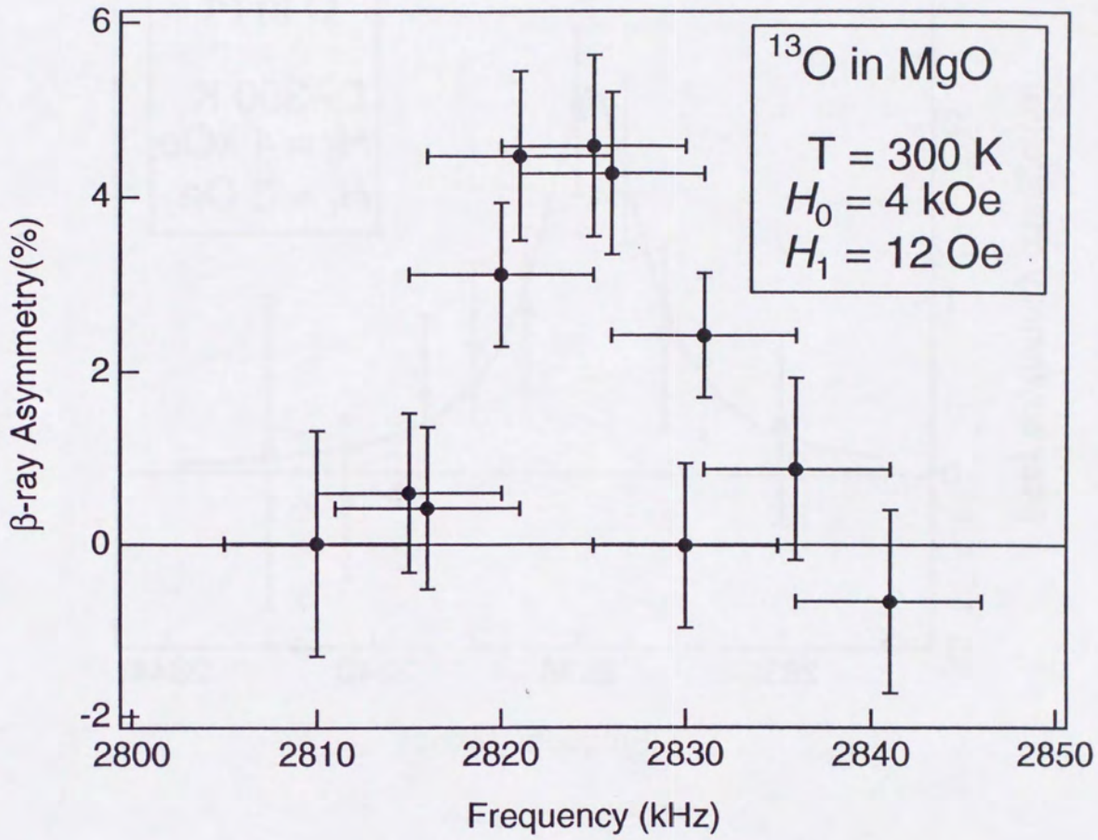

Fig. 5-11. NMR search of ^{13}O in MgO. The AFP technique was used.

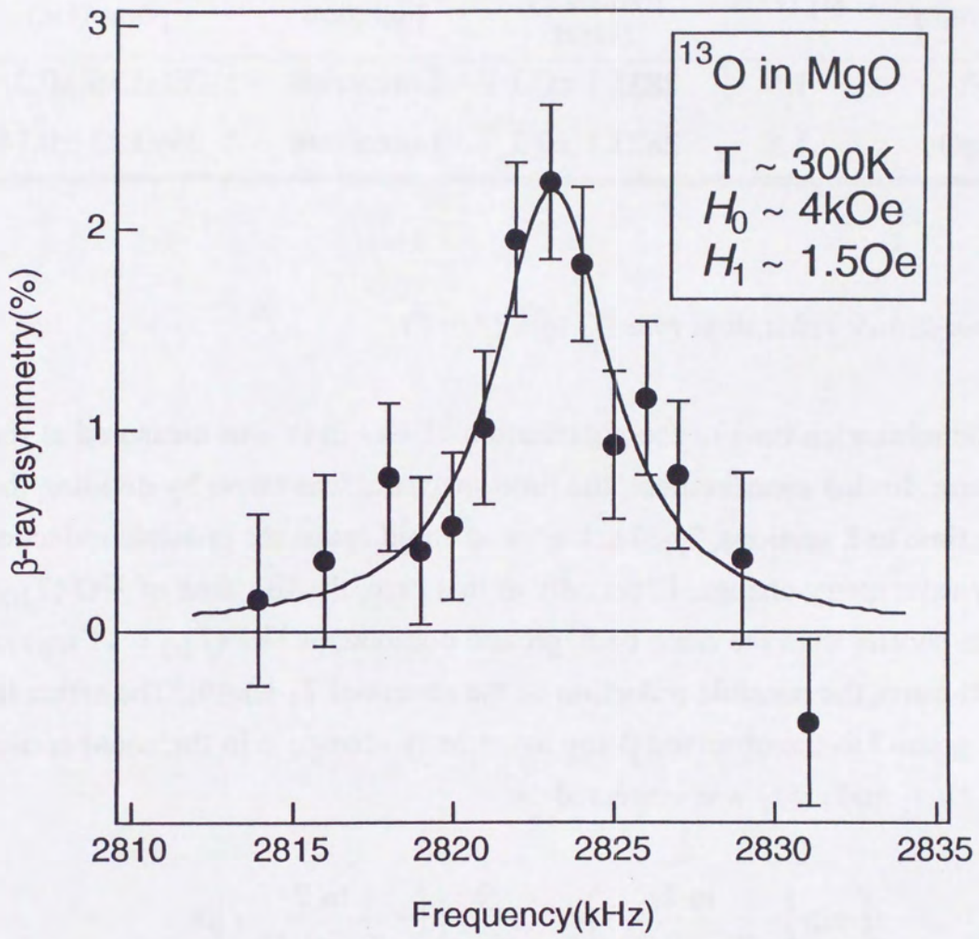

Fig. 5-12. Typical NMR spectrum of ^{13}O in MgO. The monochromatic RF was used.

Table 5-4. Experimental results for measurements of ^{13}O resonances.

Implantation medium	H_1 (Oe)	Center frequency (kHz)	Fitting Function	H_0 at the monitor point (Oe)
Pt	1.5	2835.1 ±0.3	Lorentzian	3993.36 ±0.21
MgO	1.5	2823.1 ±0.3	Lorentzian	3993.13 ±0.14

5.2.3. Spin-lattice relaxation time T_1 of ^{13}O in Pt

The relaxation time of the polarization of ^{13}O in Pt was measured at room temperature. In this measurement, the time spectrum was taken by dividing the counting time to 8 sections. The back ground could cause the possible reduction of the β-ray asymmetry change. Especially in this case, the life time of ^{13}O ($T_{1/2}$ = 8.6 ms) is shorter than the main back ground component ^{12}N ($T_{1/2}$ = 11 ms) and this could cause the possible reduction of the observed T_1 length. The effect from the back ground to the observed β-ray asymmetry change Δ in the count section between $t = t_1$ and $t = t_2$ was corrected as,

$$\Delta_{\text{corrected}} = \frac{\int_{t_1}^{t_2} \exp\left(-\frac{\ln 2}{T_{1/2}(^{13}\text{O})}t\right)dt + R\int_{t_1}^{t_2} \exp\left(-\frac{\ln 2}{T_{1/2}(^{12}\text{N})}t\right)dt}{\int_{t_1}^{t_2} \exp\left(-\frac{\ln 2}{T_{1/2}(^{13}\text{O})}t\right)dt} \times \Delta \qquad (5\text{-}1)$$

where R is the ratio of the initial counting rate ratio of the ^{12}N to that of ^{13}O. In the present case, the reduction due to the back ground contamination was estimated to be at most 15% even in the last counting section. A very fast relaxation of $T_1 = 9.7^{+2.6}_{-1.7}$ ms was observed as shown in Fig. 5-13. Knight shift of ^{13}O in Pt was estimated from the Korringa relation to be $K_s \sim 2 \times 10^{-3}$. This estimation was consistent with the deviation observed in the resonance frequency between ^{13}O in Pt and in MgO. Detailed discussion will be given in the appendix A.

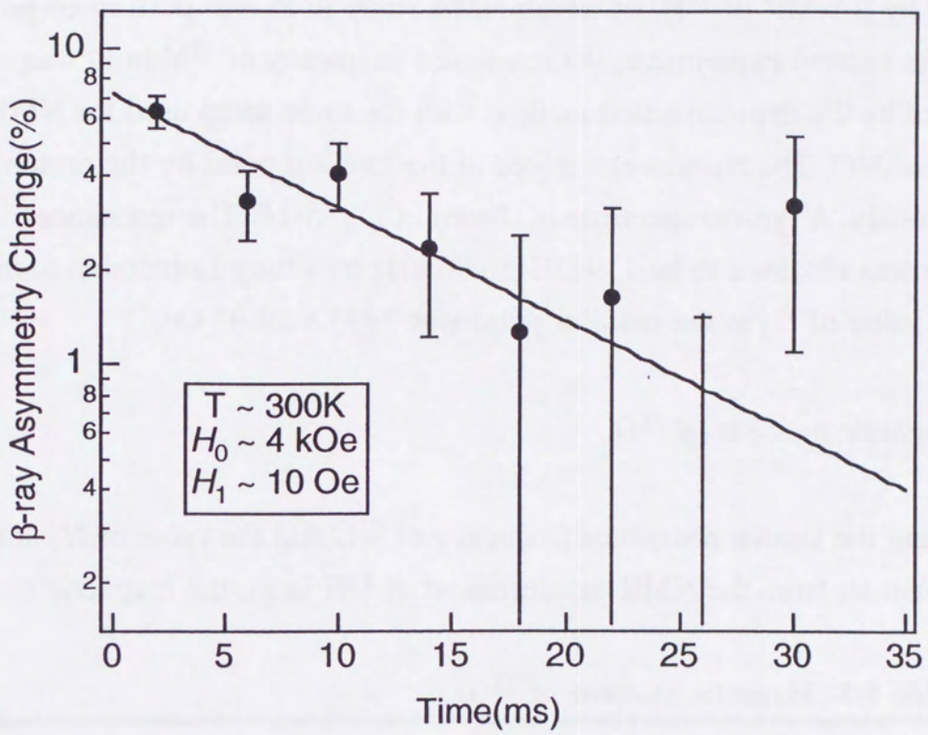

Fig. 5-13. Typical time spectrum of spin-lattice relaxation of ^{13}O in Pt at room temperature.

5.2.4. H_0 calibration

The external field H_0 at the position of the implantation media was measured by β-NMR of ^{12}N, of which NMR study in Pt was performed precisely [35]. In the present experiment, the resonance frequency of ^{12}N in Pt was determined by the depolarization method with the same setup used for NMR detection of ^{13}O. The H_0 was monitored at the monitor point by the proton NMR simultaneously. A typical spectrum is shown in Fig. 5-14. The resonance frequency was obtained to be 1394.01 ±0.06 kHz by fitting Lorentzian to the data, while the value of H_0 at the monitor point was 3993.5 ±0.03 Oe.

5.2.5. Magnetic moment of ^{13}O

Using the known resonance frequency of ^{13}O and the value of H_0 at the catcher position from the NMR measurement of ^{12}N in Pt, the magnetic moment

Table 5-5. Magnetic moment of ^{13}O.

res. frequency (kHz)	2823.1 ±0.3
res. freq. for ^{12}N (kHz)	1394.01 ±0.06
$\mu_{\text{uncorr.}}$ (^{12}N in Pt)	0.45709 ±0.00007
H_0 drift = $H_0(^{13}O)/H_0(^{12}N)$ - 1	-1.05×10^{-4}
H_0 (Oe)	4000.5 ±0.6
$\mu_{\text{uncorr.}}$	1.38867 ±0.00025
Chemical shifts (diamagnetic correction is taken to be positive)	
MgO (ref. H_2O)[a)]	$-(4.7 \pm 0.2) \times 10^{-5}$
H_2O (ref. O^{8+})[b)]	$+(3.34 \pm 0.15) \times 10^{-4}$
MgO (ref. O^{8+})	$+(2.87 \pm 0.15) \times 10^{-4}$
$\lvert\mu(^{13}O)\rvert$ (μ_N)	1.3891 ±0.0003

a) [36], b) [27]

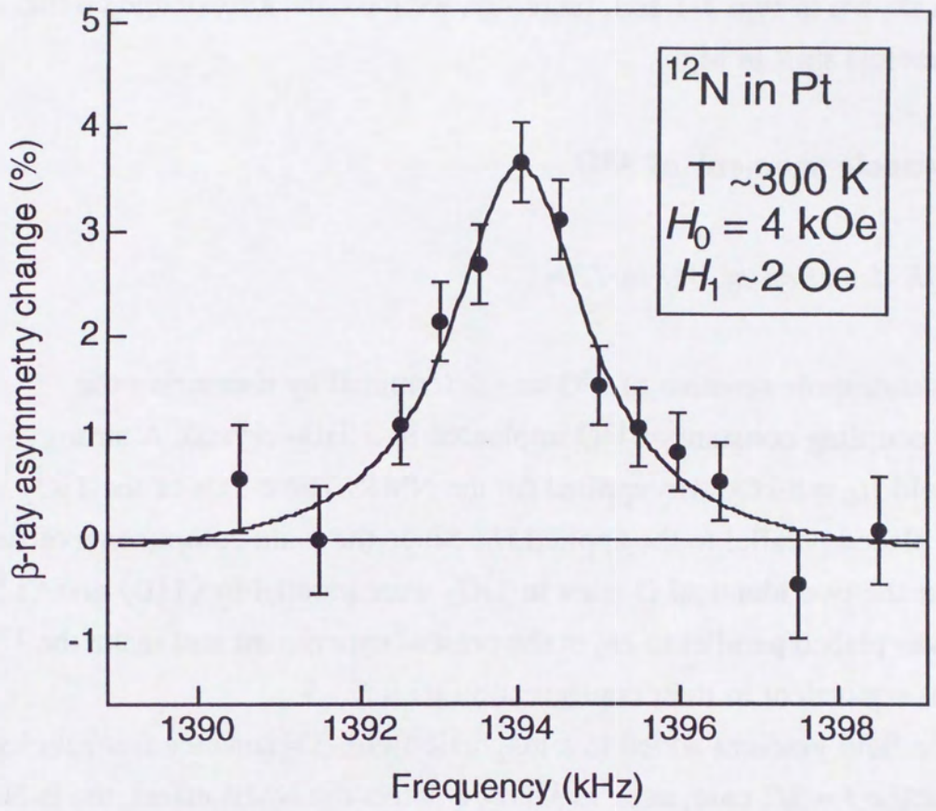

Fig. 5-14. Typical NMR spectrum of the short lived ^{12}N implanted in Pt.

of ^{17}O in MgO from H_2O [36] and ^{17}O in H_2O from O^{8+} [27] of ^{13}O can be derived as is given in Table 5-5. The resonance frequency of ^{13}O in MgO is used for the derivation of the magnetic moment since the chemical shifts have been available as shown in Fig. 3-1 and, therefore, we have the knowledge on the absolute chemical shift in MgO.

5.3. Quadrupole moment of ^{13}O

5.3.1. β-NQR detection of ^{13}O in TiO_2

The quadrupole moment of ^{13}O was determined by measuring the quadrupole coupling constant of ^{13}O implanted in a TiO_2 crystal. A strong magnetic field H_0 = 8 kOe was applied for the NMR. The c-axis of the TiO_2 crystal was placed parallel to the applied H_0. Since the main components of field gradients for the two identical O-sites in TiO_2 were parallel to $\langle 110 \rangle$ and $\langle 1\bar{1}0 \rangle$, the c-axis was placed parallel to H_0 in the present experiment and make the ^{13}O in the two sites equivalent in their configuration with $H_0 \perp q$.
In an electric field gradient added to a magnetic field, 3 resonance frequencies are observed for the I = 3/2 case, such as ^{13}O. To detect the NMR effect, the β-NQR method was employed, where the polarization was inverted by use of the AFP technique. In this technique, 6 RFs were applied sequentially in the present I = 3/2 case to invert the polarization at the on-resonance condition. The intensity and the duration of the applied RF field was about 12 Oe and 1 ms, respectively, which satisfies the AFP condition.

An β-NQR spectrum was measured as a function of Δf which is defined as a half of the quadrupole spitting or the deviation from the Larmor frequency with a frequency sweep width of ±15 kHz. The Larmor frequency was calculated as 5464 kHz from the magnetic moment of ^{13}O, the chemical shift of O in TiO_2 and the intensity of the applied H_0. A typical spectrum is shown in Fig. 5-15. Two peaks were found in the present β-NQR spectrum. Unfortunately, the lower Δf side of the spectrum was not completed. The quadrupole split Δf was determined for the outer peak as 64 ±3 kHz by fitting a theoretical function to the spectrum

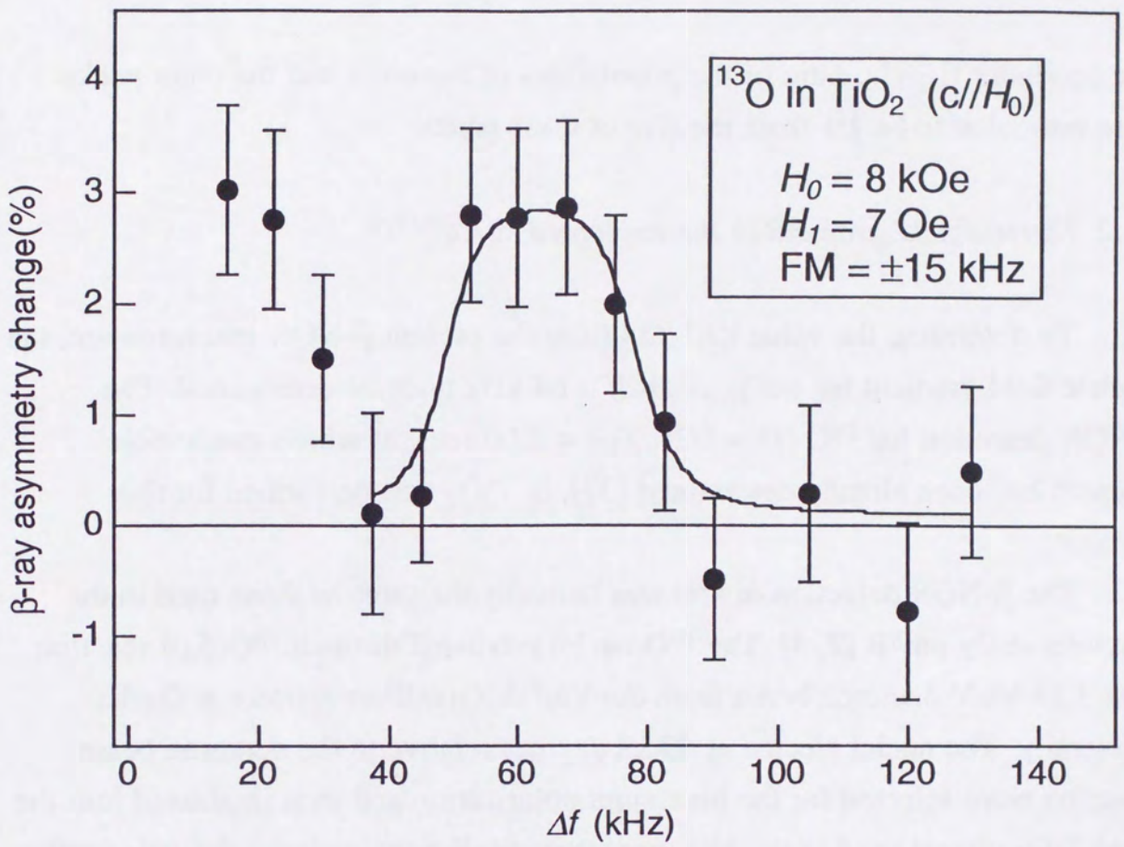

Fig. 5-15. Typical NNQR spectrum of the ^{13}O implanted in a TiO_2 crystal. The separation Δf is the distance of the ($\pm 1/2 \leftrightarrow \pm 3/2$) transition frequency from the ($-1/2 \leftrightarrow +1/2$) transition.

Table 5-6. β-NQR of ^{13}O in TiO_2.

Δf (kHz)	64 ±3
Population ratio of the inner and the outer peak	1:1

(see appendix E). The ratio of the populations of the inner and the outer peaks were estimated to be 1:1 from the size of these peaks.

5.3.2. Electric field gradient at the implanted site of ^{13}O

To determine the value $|Q(^{13}O)|$ from the present β-NQR measurement, the electric field gradient for the peak at $\Delta f = 64$ kHz must be determined. The β-NQR detection for ^{19}O ($I^{\pi} = 5/2^{+}$, $T_{1/2} = 27.0$ sec), of which quadrupole moment has been already determined [37], in TiO_2 was performed for this purpose.

The β-NQR detection of ^{19}O was basically the same as those used in the previous study on ^{8}B [2, 3]. The ^{19}O nuclei produced through ^{18}O(d,p) reaction with 3.25 MeV deuteron beam from the Van de Graaff accelerator at Osaka University. The nuclei ejected at 40 ±8 degrees relative to the deuteron beam direction were selected for the maximum polarization and then implanted into the same TiO_2 crystal used in the ^{13}O measurement. For maintaining the polarization, a large static magnetic field of H_0 ~8 kOe was applied to the target, the flight path of ^{19}O and the implantation medium.

At first, an β-NQR spectrum of ^{19}O in TiO_2 with the orientation of c // H_0 was measured by the depolarization method. The monochromatic RF whose intensity of 0.3 Oe and the duration time of 30 ms were used for the precise mapping. Typical β-NQR spectrum is shown in Fig. 5-16. The double peaks observed in the ^{13}O measurement were reproduced in the ^{19}O measurement with the orientation of c // H_0. The quadrupole split Δf were determined to be 2.64 ±0.19 kHz and 6.31 ±0.12 kHz for the inner and outer peaks, respectively. The line shapes of these resonances were assumed to be the Gaussian shape. The ratio of the populations of the inner and outer peaks were estimated as 6:4 from the size of these peaks.

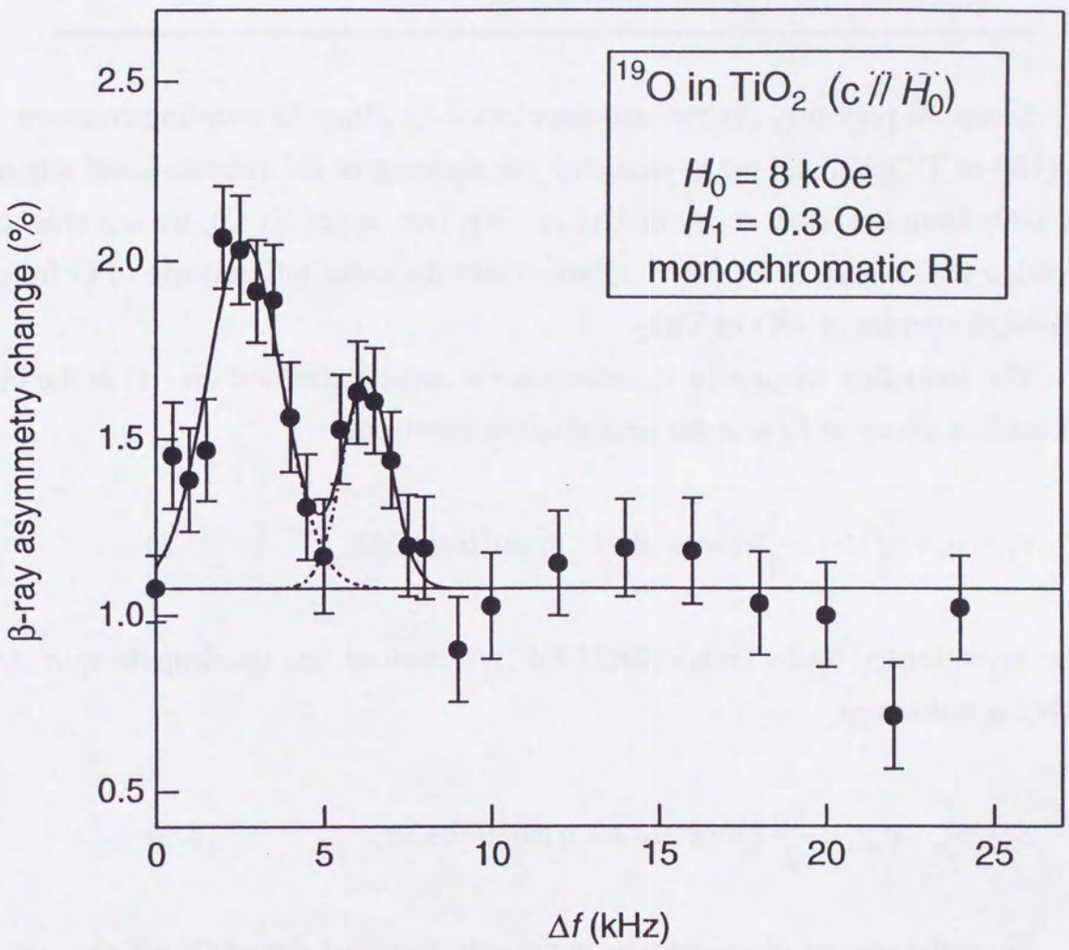

Fig. 5-16. Typical β-NQR spectrum of ^{19}O in TiO_2 (c // H_0). Double peaks observed in ^{13}O in TiO_2 were also found in the present spectrum.

Table 5-7. β-NQR of ^{19}O in TiO_2 (c // H_0).

Δf for the inner peak (kHz)	2.64 ±0.19
Δf for the outer peak (kHz)	6.31 ±0.12
Population ratio of the inner and outer peak	6:4

Since we presently determined the electric quadrupole coupling constant $|eqQ(^{17}O \text{ in } TiO_2)/h|$ and the asymmetry parameter η of the substitutional site of O in TiO_2 from the NMR study of ^{17}O in TiO_2 (see appendix C), we are able to determine which peak is for ^{13}O implanted into the substitutional site of O from the β-NQR spectra of ^{19}O in TiO_2.

The transition frequency ν_m between the substates m and $(m - 1)$ at the high field limit is given in first-order perturbation theory as

$$\nu_m = \nu_L + \frac{\nu_Q}{2}(m - \frac{1}{2})(3\cos^2\theta - 1 + \eta \sin^2\theta \cos 2\phi), \qquad (5\text{-}2)$$

where $\nu_Q = 3eqQ(^{13}O \text{ in } TiO_2)/\{2I(2I\text{-}1)h\}$. Therefore, the quadrupole split Δf for ^{19}O is written as

$$\Delta f \equiv \nu_m - \nu_{m-1} = \frac{\nu_Q}{2}\left(3\cos^2\theta - 1 + \eta \sin^2\theta \cos 2\phi\right). \qquad (5\text{-}3)$$

Since the present discussion is on the substitutional site of O in TiO_2, q is either in $\langle 110 \rangle$ or $\langle 1\bar{1}0 \rangle$. In the case of c // H_0, the orientation of H_0 can be described as $\theta = 90°$ and $\phi = 0°$ in polar angles (Fig. 5-17). Here, Δf is related to ν_Q as

$$\Delta f_{xx} = \frac{\nu_Q}{2}(1 - \eta), \qquad (5\text{-}4)$$

In the case of $\langle 110 \rangle$ // H_0, the orientation of H_0 can be described as $\theta = 0°$ in polar angles (Fig. 5-18). Therefore, Δf is related to ν_Q as

$$\Delta f_{zz} = \nu_Q. \qquad (5\text{-}5)$$

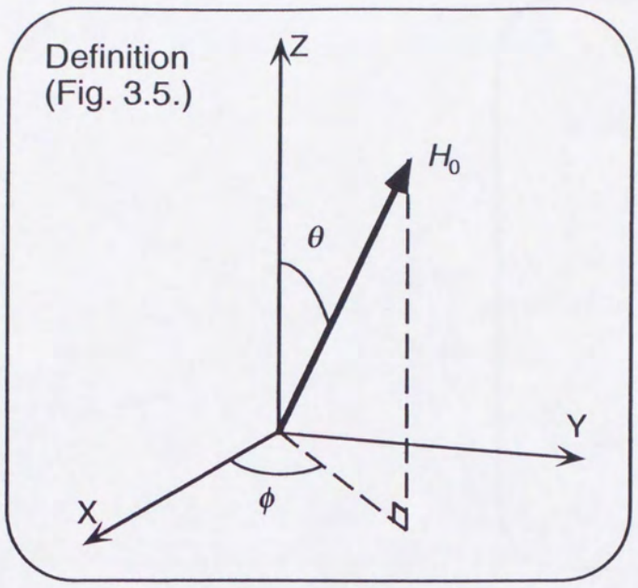

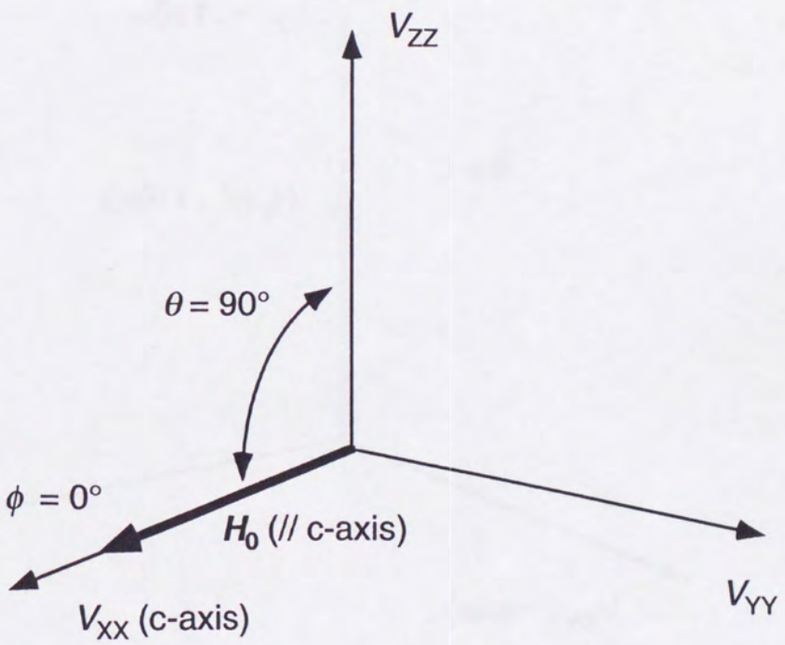

Fig. 5-17. Orientation of H_0 in polar angle. Since H_0 was applied paralell to c-axis (V_{XX}) of TiO_2, θ, the angle between H_0 and V_{ZZ}, becomes 90 degrees and ϕ, the angle between H_0 and V_{XX} becomes 0 degrees.

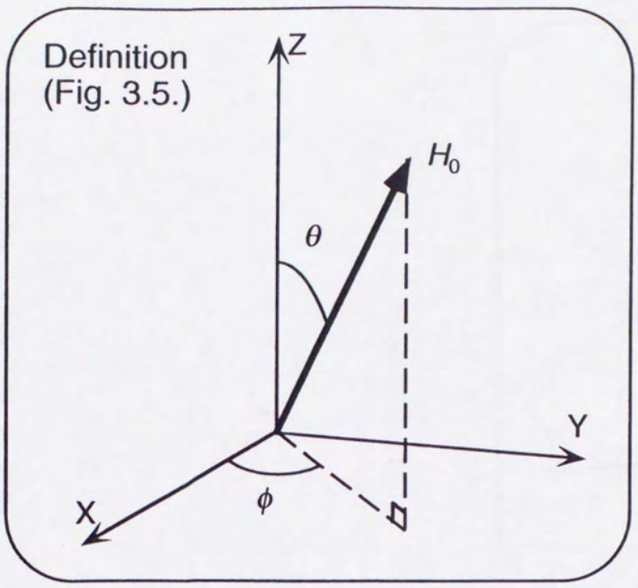

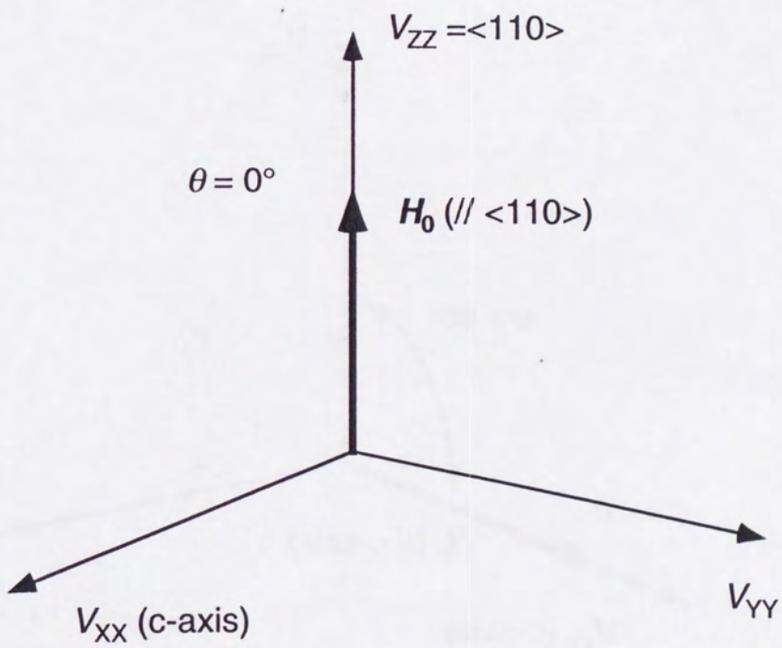

Fig. 5-18. Orientation of H_0 in the polar angle. Since H_0 was applied paralell to the <110> axis (V_{ZZ}) of TiO_2, θ, the angle between H_0 and V_{ZZ}, becomes 0 degree.

In this case, the orientation of $\langle 1\bar{1}0 \rangle$, which is the equivalent direction of $\langle 110 \rangle$, is described as $\theta = 90^\circ$ and $\phi = 90^\circ$ in polar angles. Therefore, Δf becomes

$$\Delta f_{YY} = \frac{\nu_Q}{2}(1+\eta). \qquad (5\text{-}6)$$

From Eq. 5-4, 5-5 and 5-6, the Δf_{ZZ} is equal to ν_Q and the difference of Δf_{ZZ} and Δf_{YY} is equal to Δf_{XX}.

If the peak at $\Delta f = 6.3$ kHz in the c // H_0 spectrum is for the substitutional site, two peaks should be observed at $\Delta f_{ZZ} = 75$ kHz and $\Delta f_{YY} = 69$ kHz in the $\langle 110 \rangle$ // H_0 spectrum from Eq. 5-5. On the other hand, if the peak at $\Delta f = 2.6$ kHz in the c // H_0 spectrum is for the substitutional site, the corresponding peaks should be observed at $\Delta f_{ZZ} = 31$ kHz and $\Delta f_{YY} = 28$ kHz.

To assign the resonance for the substitutional site in the spectrum of c // H_0, β-NQR measurement for $\langle 110 \rangle$ // H_0 was performed. We employed the AFP technique for this measurement. The intensity, the duration and the frequency modulation width of RFs were 3 Oe, 100 ms and ±10 kHz, respectively. As shown in Fig. 5-19, the peak at $\Delta f \sim 30$ kHz was observed in the β-NQR spectrum for $\langle 110 \rangle$ // H_0 and no peak was found around $\Delta f \sim 75$ kHz. The resonances of 31 kHz and 28 kHz could not be resolved due to the frequency modulation width of applied RF. So, we concluded that the inner peak in the c // H_0 spectrum corresponded to that of the substitutional site of O and that the outer peak was from Oxygen in the unidentified site in TiO_2. Therefore, the peak at $\Delta f = 64$ kHz in the β-NQR spectrum of ^{13}O in TiO_2 is not for the substitutional site of O.

The ν_Q for the substitutional site was determined to be 31.9 ±0.5 kHz by fitting of the two Gaussians whose frequency difference were fixed to $\Delta f_{XX} = 2.6$ kHz. From this ν_Q and the orientation of the crystal, the $|eqQ/h|$ and η for ^{19}O in the substitutional site of O in TiO_2 were determined to be 213 ±2 kHz and 0.836 ±0.008, respectively. The presently obtained η showed a good agreement with that from the FT-NMR of ^{17}O in TiO_2, $\eta = 0.831$ ±0.007 (see appendix C).

As shown in Fig. 5-19, a small peak corresponding to the unidentified site was observed at $\Delta f \sim 50$ kHz. Taking the symmetry of the crystal structure and the relation among V_{XX}, V_{YY} and V_{ZZ}, the resonance observed in Fig. 5-16 is for

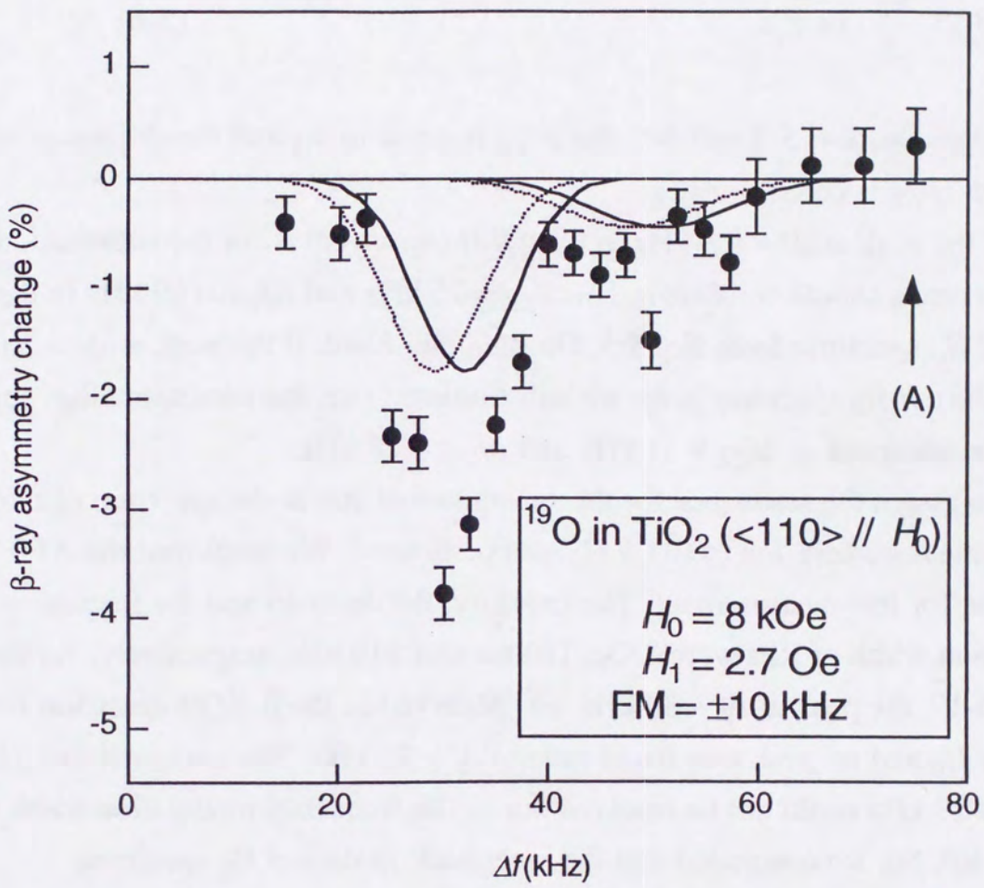

Fig. 5-19. Typical NNQR spectrum of ^{19}O in TiO_2 (<110> // H_0). (A) is the expected position if the outer peak observed in Fig. 5-16 were of the ^{19}O in the substitutional site of O in TiO_2. The split of each peak due to the large η were not resolved because the FM width of applied RF was wider than the split.

V_{XX} // H_0 and that observed in Fig. 5-19 is the unresolved peaks for V_{YY} // H_0 and V_{ZZ} // H_0 due to the frequency modulation width. Therefore, the ν_Q for the unidentified site was determined to be 31.9 ±0.5 kHz from the fitting by the two gaussian whose frequency difference was fixed to Δf_{XX} = 6.3 kHz. From the result of this fitting, the $|eqQ/h|$ and η for the ^{19}O in the unidentified site were determined to be 350 ±9 kHz and 0.760 ±0.009, respectively.

Table 5-8. Electric field gradients at O sites in TiO_2.

Substitutional site	$\|eqQ(^{19}O \text{ in } TiO_2)/h\|$	213 ±2 kHz
	η	0.836 ±0.008
Unidentified site	$\|eqQ(^{19}O \text{ in } TiO_2)/h\|$	350 ±9 kHz
	η	0.760 ±0.009

5.3.3. Derivation of the quadrupole moments of ^{19}O and ^{13}O

Once the sites for the peaks in the present β-NQR spectrum of ^{13}O in TiO_2 are assigned, the $Q(^{13}O)$ is extracted as follows.

Although the electric field gradient and the asymmetry parameter are not known for the unidentified site in the present case, the $Q(^{13}O)$ can be determined from the present measurements because the $Q(^{19}O)$ and Δfs of ^{13}O and ^{19}O in the unidentified site of TiO_2 under the orientation of c // H_0 are available.

In [37], they determined $|eqQ(^{19}O \text{ in } TiO_2)/h|$ by averaging the resonance frequency because they could not resolve the peaks from the two equivalent site in the β-NQR spectrum. Now we know the peak at Δf = 2.6 kHz observed in the c // H_0 spectrum (Fig. 5-16) is for the substitutional site of O, $|eqQ(^{19}O \text{ in } TiO_2)|$ for the substitutional site was determined as 208 ±17 kHz from the fitting result of this peak, Δf = 2.64 ±0.19 kHz, with the asymmetry parameter η = 0.831 ±0.007 determined from the FT-NMR measurement of ^{17}O in TiO_2 (see appendix C). Then the value of $Q(^{19}O)$ can be extracted as $|Q(^{19}O)|$ = 3.6 ±0.5 mb from the following equation

$$|Q(^{19}\mathrm{O})| = \frac{|eqQ(^{19}\mathrm{O}\text{ in }\mathrm{TiO_2}\text{:substitutional})/h|}{|eqQ(^{17}\mathrm{O}\text{ in }\mathrm{TiO_2}\text{:substitutional})/h|} \times |Q(^{17}\mathrm{O})|, \quad (5\text{-}7)$$

using $Q(^{17}\mathrm{O})$ = -26 ±3 mb and $|eqQ(^{17}\mathrm{O}\text{ in }\mathrm{TiO_2})|$ = 1512 ±4 kHz (see appendix C).

Once the value of $Q(^{19}\mathrm{O})$ has been determined, the quadrupole moment of $^{13}\mathrm{O}$ can be determined from the peaks for the unidentified site in β-NQR spectra of c // H_0 for $^{19}\mathrm{O}$ and $^{13}\mathrm{O}$. The $|eqQ/h|$s for $^{19}\mathrm{O}$ and $^{13}\mathrm{O}$ in the unidentified site were obtained to be 350 ±9 kHz and 1070 ±60 kHz, respectively. Then the value $|Q(^{13}\mathrm{O})|$ can be determined from the relation

$$|Q(^{13}\mathrm{O})| = \frac{|eqQ(^{13}\mathrm{O}\text{ in }\mathrm{TiO_2}\text{:unknown})/h|}{|eqQ(^{19}\mathrm{O}\text{ in }\mathrm{TiO_2}\text{:unknown})/h|} \times |Q(^{19}\mathrm{O})|. \quad (5\text{-}8)$$

Using the available values, 11.0 ±1.6 mb was obtained as $|Q(^{13}\mathrm{O})|$. The values used here are summarized in Table 5-9.

Table 5-9. Quadrupole moment of $^{13}\mathrm{O}$.

Substitutional site		
Δf for $^{19}\mathrm{O}$ (c // H_0; kHz)	2.64 ±0.19	Present
$\lvert eqQ(^{17}\mathrm{O})/h\rvert$ (kHz)	1512 ±4	Present[a)]
η	0.831 ±0.007	Present[a)]
Unidentified site		
Δf for $^{13}\mathrm{O}$ (c // H_0; kHz)	64 ±3	Present
$\lvert eqQ(^{13}\mathrm{O})/h\rvert$ (kHz)	1070 ±60	Present
Δf for $^{19}\mathrm{O}$ (c // H_0; kHz)	6.31 ±0.12	Present
$\lvert eqQ(^{19}\mathrm{O})/h\rvert$ (kHz)	350 ±9	Present
$Q(^{17}\mathrm{O})$ (mb)	-26 ±3	[38]
$\lvert Q(^{19}\mathrm{O})\rvert$ (mb)	3.6 ±0.5	Present
$\lvert Q(^{13}\mathrm{O})\rvert$ (mb)	11.0 ±1.6	Present

a) See appendix C.

6. Discussion

6.1. Magnetic moment of ^{9}C and effective g-factors

6.1.1. Comparison with the theoretical predictions

Several theoretical predictions are available on the magnetic moment of ^{9}C and its mirror nuclei ^{9}Li. The experimental values of ^{9}C and ^{9}Li [39], and theoretical predictions based on the shell model [40, 41] and the cluster model [42] for these nuclei are summarized in Table 6-1. As shown, the magnetic moment of ^{9}C is much different from those calculated with shell model or cluster model, while theoretical calculations seem to be in good agreement with the experimental result in ^{9}Li.

The spin expectation values for both experimental and theoretical results were also extracted. Because of the good charge symmetry of the nuclear force, the structures of mirror nuclei are identical. Therefore, the sum moment of a mirror pair can be written as follows;

$$\mu^{(0)} \equiv \frac{1}{2}\left(\mu(T_z=+T)+\mu(T_z=-T)\right)=g_l^{(0)}\langle l_z\rangle+g_s^{(0)}\langle s_z\rangle$$

$$=g_l^{(0)}\langle l_z\rangle+\frac{1}{2}g_s^{(0)}\langle\sigma\rangle, \qquad (6\text{-}1)$$

where $\mu(T_z = \pm T)$ is the magnetic moment of the nucleus with $T_z = \pm T$, $g_s^{(0)}$, $g_l^{(0)}$ are the spin and orbital isoscalar g-factors and $\langle l_z\rangle$, $\langle s_z\rangle$ and $\langle\sigma\rangle$ are the expectation values of angular momentum and spin of the valence nucleon. Since the spin of a nucleus, I, is a good quantum number, the following relation is satisfied among I, $\langle l_z\rangle$ and $\langle s_z\rangle$ or $\langle\sigma\rangle$.

$$I=\langle l_z\rangle+\langle s_z\rangle=\langle l_z\rangle+\frac{1}{2}\langle\sigma\rangle$$

$$\therefore \langle l_z\rangle=I-\frac{1}{2}\langle\sigma\rangle \qquad (6\text{-}2)$$

From the spin expectation value $\langle\sigma\rangle$ can be obtained as

$$\langle\sigma\rangle=\frac{2\mu^{(0)}-2g_l^{(0)}I}{g_s^{(0)}-g_l^{(0)}}. \qquad (6\text{-}3)$$

If g-factors inside the nucleus are the same as those in the free space, $g_s^{(0)}$ and $g_l^{(0)}$ are 0.880 and 0.500, respectively. The relation Eq. 6-3 can be rewritten as follows by putting these values,

$$\langle\sigma\rangle=\frac{2\mu^{(0)}-I}{0.380}. \qquad (6\text{-}4)$$

The spin expectation value thus obtained from the present experimental results was $\langle\sigma\rangle$ = 1.44, which was far larger than $\langle\sigma\rangle$ = 1.03 given from the shell model calculation or $\langle\sigma\rangle$ = 1.13 given from the cluster model.

Table 6-1. Comparison of the experimental magnetic moments and theoretical predictions.
Magnetic moments are in the unit of μ_N.

Nuclei	exp.	Simple[b]	Shell[c]	Cluster[d]
^{9}C	(-)1.3914 ±0.005[a]	-1.62	-1.59	-1.50
^{9}Li	+3.4391 ±0.0006[e]	-	+3.48	+3.43
$\langle\sigma\rangle$	1.44	0.84	1.03	1.13

a) Present result. b) [40] c)[41] d)[42] e)[39]

6.1.2. Mesonic renormalization effects on ^{9}C-^{9}Li pair

Magnetic moments of LS doubly closed shell ±1 nucleon nuclei have been determined precisely [43-45] owing to the technical development and also the development of the hyperfine interaction studies of the nuclei in various implantation media. The isoscalar moments of these nuclei show slight, but clear deviations from the Schmidt values. These deviations cannot be well reproduced

Table 6-2. Effective g-factors obtained from LS doubly closed shell ±1 nucleon nuclei (see Appendix B or [46]).

	Arima et al.[a)]		Towner and Khana[b)]		free space
	mass-16	mass-40	mass-16	mass-40	
$g_l^{(0)}$	0.505	0.514	0.513	0.520	0.500
$g_s^{(0)}$	1.003	1.013	0.914	0.899	0.880

These values were extracted with the matrix given by a) [18] and b) [47]

by any theoretical calculations [48] in which the effects from the higher order configuration mixing, relativistic corrections and the spin tensor term are taken into account. The remaining deviations strongly suggests the possible renormalization of g-factors of the nucleon in these nuclei. Relying on the nuclear matrices provided from theories, the degrees of the renormalization are estimated (see Appendix B) as large as several percent of free g-factors.

It is reasonable to expect some renormalization for the ^{9}C-^{9}Li pair. If we use the effective g-factors extracted from the magnetic moments of the mirror doublets around $A \sim 16$ by combining the moments with the nuclear matrices by obtained by Arima et al. [18] and the relativistic correction obtained by Ohtsubo et al. [21], the spin expectation value thus extracted drastically reduces to 1.07. The experimental spin expectation value becomes closer to the shell model prediction. In the case of other nuclei, the agreement between $\langle\sigma\rangle$s extracted from the experimental magnetic moments with the effective g-factors and those from theoretical calculations become worse (Fig. 6-1). The consistency can be recovered by introducing the relativistic correction calculated by Ohtsubo et al [21]. The $\langle\sigma\rangle$ value including the relativistic correction is extracted as follows

$$\langle\sigma\rangle_{\text{rel.}} = \frac{2\left(\mu^{(0)} - \delta\mu_{\text{rel.}}^{(0)} - g_{leff}^{(0)} I\right)}{g_{seff}^{(0)} - g_{leff}^{(0)}}, \qquad (6\text{-}5)$$

where $\delta\mu_{\text{rel.}}^{(0)}$ is the sum of relativistic corrections for proton-odd and neutron-odd mirror pair. For the ^{9}C - ^{9}Li pair, their calculation is not available. As they mentioned in their paper, the relativistic correction depends on the total spin I,

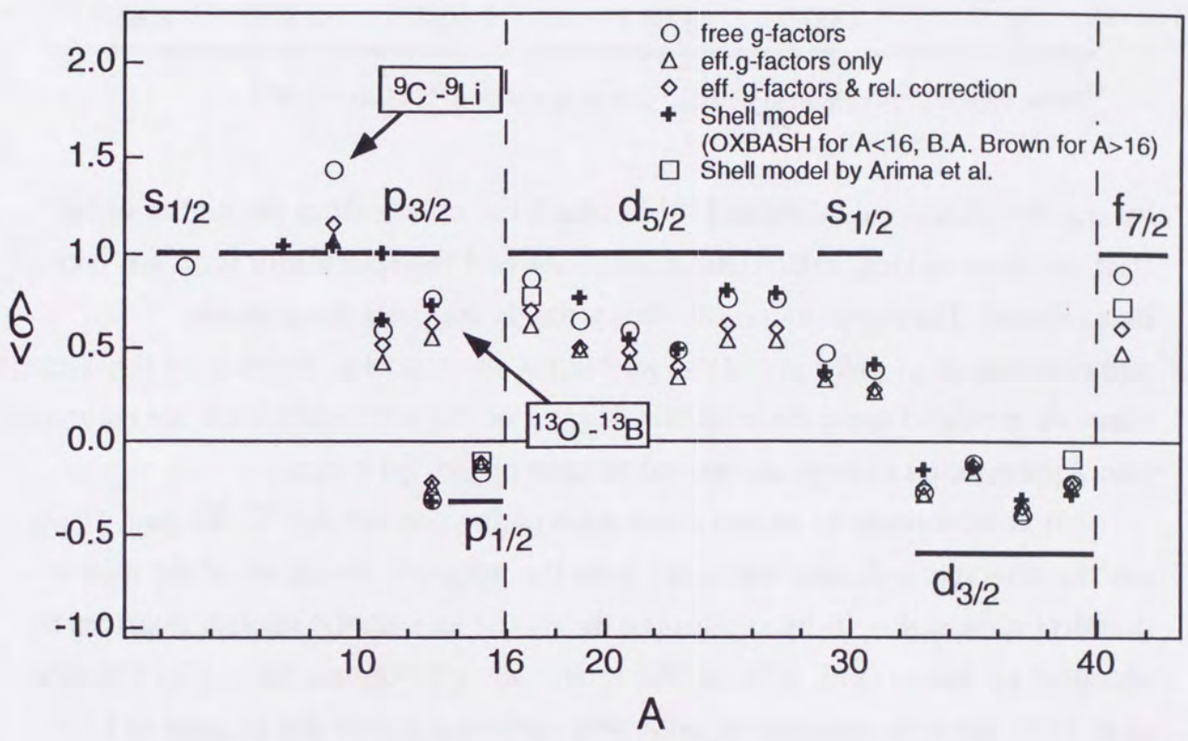

Fig. 6-1. Spin Expectation values extracted from the magnetic moments of mirror pairs up to $A = 41$. Open triangles denote the value extracted from experiment with effective g-factors (see appendix B or [46]). Open diamonds denote the value with effective g-factors and relativistic corrections [21]. Solid lines are Schmidt values. Spin expectation values for LS doubly closed shell ± 1 nucleon nuclei ($A = 15, 17, 39, 41$) are results of Arima et al. In their calculation, the second order configration mixing with higher excitation energies was taken into account.

but not on the orbital angular momentum. Hence, from the results of other $I = 3/2$ nuclei, the relativistic corrections to ^{9}C and ^{9}Li are assumed to be ~ $+0.01\mu_N$ and ~ $-0.05\mu_N$, respectively. Although the presently assumed relativistic corrections push up $\langle\sigma\rangle$ to ~1.15, the drastic reduction of $\langle\sigma\rangle$ caused by the effective g-factors is still obvious. The agreement can be easily recovered by just assuming the 3% renormalization of the nucleon mass, i.e., the valence nucleon becomes lighter 3%. The $\langle\sigma\rangle$ including this mass renormalization effect is easily obtained by just replacing the g-factors in Eq. 6-5 to those multiplied by M/M_{eff} times, where M_{eff} is the renormalized mass of the nucleon, because the mass renormalization effect changes the M in the nuclear magneton, $\mu_N = \frac{e\hbar}{2M}$.

Table 6-3. Comparison of spin expectation values of ^{9}C-^{9}Li pair.
The value for "OXBASH" is extracted from the calculated magnetic moments by OXBASH with Cohen-Kurath model and CKPOT as the two-body effective interaction parameters. "Free", "Eff.", "Eff. + rel." and "Eff. + rel. + mass" are the values extracted with free g-factors, effective g-factors, effective g-factors + relativistic correction and effective g-factors + relativistic correction + 3% mass renormalization of the valence nucleon, respectively.

	Theory	Experiment			
	OXBASH	Free	Eff.	Eff. + rel.	Eff. + rel. + mass
$\langle\sigma\rangle$	1.03	1.44	1.07	1.15	1.02
$\delta\langle\sigma\rangle$(%)	-	+39.8	+3.9	+11.7	-0.9

This fact strongly suggests the necessity for considering the renormalization effects to understand the anomaly of the present spin expectation value.

Arima et al. estimated the one boson exchange current contributions to the isoscalar g-factors in the Fermi gas model [18]. They mentioned that the degree of this effect was very sensitive to the Fermi momentum of nucleon. Generally speaking, the valence nucleon of drip line nuclei is in a loosely bound state and this should be reflected on its momentum. Their matter distribution or the Fermi level should also reflect their configurations and the p_F of such nuclei should be different from those of near stable line. This difference might cause the present renormalization of g-factors of nucleons. But it should be noted that they also

Table 6-4. Contributions of the exchange current processes to the isoscalar *g*-factors in the Fermi gas model.
c is the cutoff range of one pion exchange potential and p_F is the Fermi momentum of nucleons. The meson masses and coupling constants by Holinde and Horen are used. The last column (total) contain contributions due to δ and ϕ meson exchange.

c (fm)	p_F (MeV)	σ		ω		ρ		$\rho\pi$		Total	
		$\delta g_s^{(0)}$	$\delta g_l^{(0)}$	$\delta g_s^{(0)}$	$\delta g_l^{(0)}$	$\delta g_s^{(0)}$	$\delta g_l^{(0)}$	$\delta g_s^{(0)}$	$\delta g_l^{(0)}$	$\delta g_s^{(0)}$	$\delta g_l^{(0)}$
0	260	0.204	0.131	-0.147	-0.093	0.099	0.004	-0.025	0	0.081	0.025
0.7	260	0.101	0.064	-0.087	-0.027	0.016	0.000	-0.001	0	0.023	0.036
0.7	206	0.046	0.031	-0.040	-0.013	0.009	0.000	0.002	0	0.012	0.018

mentioned the contribution from the second order configuration mixing overwhelmed this effect in usual nuclei.

Recently, Saito et al. calculated the effective mass of hadrons in closed shell nuclei based on the quark-meson coupling model [49]. According to their results, the nucleon mass in ^{40}Ca core shows a drastically change from 0.8*M* to ~0.99*M* (*M* is the nucleon mass in free space) around the nuclear surface. Minamisono et al. investigated the effective mass of the valence nucleon inside the nucleus in the case of LS doubly closed shell ±1 nucleon nuclei from their nuclear magnetic moments [43-45, 46]. Their results are summarized in Table 6-5 and these are consistent with the theoretical result obtained by Saito if the valence nucleon moves round at the very surface of the nucleus (see Fig. 6-2). From this result, one would easily expect the halo structure affects on the valence nucleon mass and cause finite *g*-factor renormalization. It is noted that Yamazaki found a larger mass reduction of about 8 % in the nucleon bound in nuclide around Pb region [50].

Table 6-5. Renormalization degrees around *A* = 16 and 40 region.
The values for the experiment and the theory are from [46] and [49], respectively.

	Experiment		Theory
	mass-16	mass-40	mass-40
from g_l	-(1.7 ±0.9) %	-(3.4 ±0.6) %	-1 ~ -20 %.
from g_s	-(8.2 ±4.4) %	-(7.6 ±4.4) %	

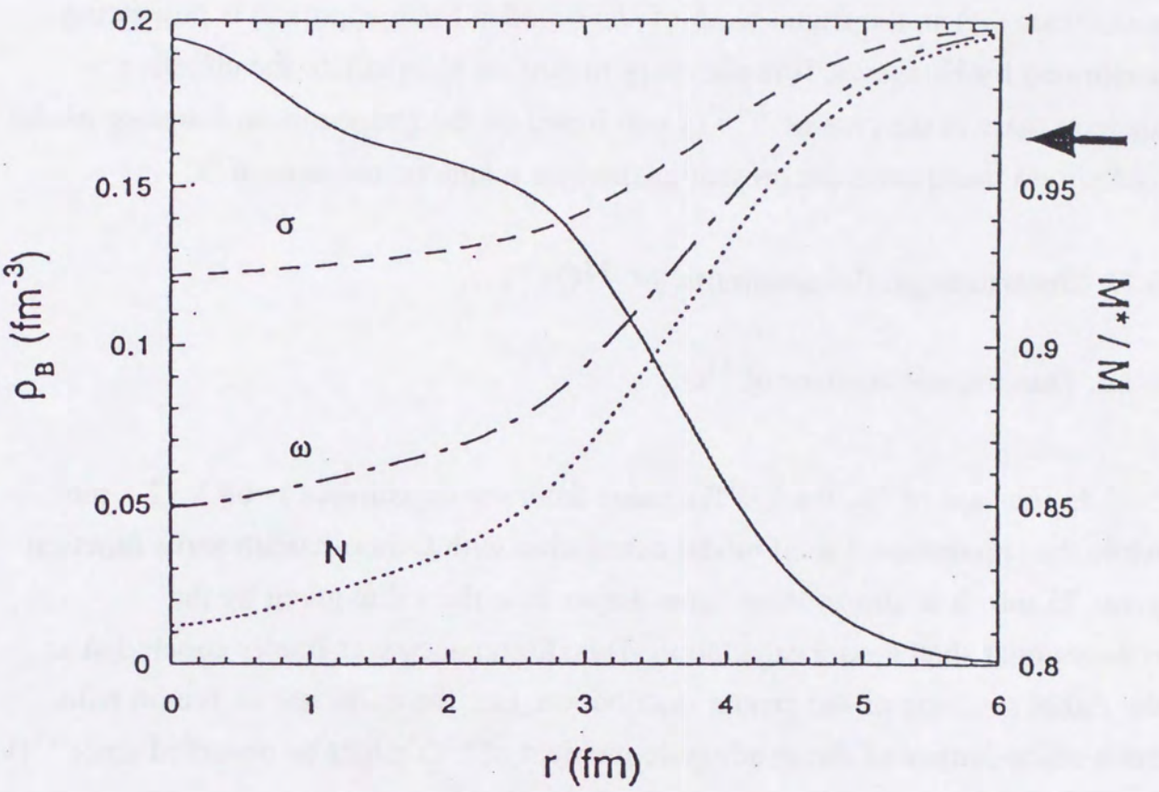

Fig. 6-2. Mass of nucleon (N), σ meson and ω meson in ^{40}Ca [49]. The arrow shows the effective mass of nucleon in the nucleus around $A = 40$ LS doubly closed shell deduced from the magnetic moments by Minamisono (See appendix B or [46]).

Advanced theoretical calculations for drip-line nuclei including the proper treatment of meson exchange currents and higher order configuration mixing under the realistic potential is required for the understanding of present anomalous $\langle\sigma\rangle$ in the frame work of shell model. Such approach is now being performed by Kitagawa. It is also very important to calculate the effective nucleon mass in the case of ^{9}C-^{9}Li pair based on the quark-meson coupling model by Saito to understand the present anomalous magnetic moment of ^{9}C.

6.2. Electromagnetic moments of ^{13}O

6.2.1. Quadrupole moment of ^{13}O

In the case of ^{8}B, the $|Q(^{8}B)|$ value from the experiment is 68.3 ±2.1 mb while the conventional shell model calculation with Cohen-Kurath wave function gives 25 mb. It is almost three times larger than the value given by the conventional shell model calculation. This discrepancy was finally concluded as the radial swelling of the proton distribution, i.e., the existence of proton halo. Such enhancement of the quadrupole moment of ^{13}O might be observed since ^{13}O is another proton drip-line nuclei with rather small one proton separation energy E_{sp} = 1.56 MeV.

The comparison of the experimental and that of the conventional shell model calculation for ^{13}O and ^{13}B, which is the mirror nucleus of ^{13}O, are summarized in Table 6-6.

As Sagawa and Kitagawa showed in the case of ^{8}B [51], the proper treatment of the small separation energy is very important especially for the proton drip-line nuclei which have relatively small binding energies compared with those around the stable line. They showed that adjusting depth of the potential in order to reproduce the separation energy of the shell model configuration was crucial to explain the discrepancy between the experimental result and the conventional shell model calculation.

To examine the effect of the binding energy to the quadrupole moments, Kitagawa performed the shell model calculations for A = 8, 11, 12 and 13 mirror

Table 6-6. Comparison of quadrupole moments of ^{13}O and ^{13}B from experimental results and the conventional shell model calculation.

OXBASH was used as the code for the conventional shell model calculation. OXBASH calculation was performed with in the p-shell with Cohen-Kurath wave function and effective charges $e_p^{eff} = 1.3e$ and $e_n^{eff} = 0.5e$. The signs of the experimental results are expected to be positive from their nuclear structure.

	Experiment	OXBASH
$Q(^{13}O)$ (mb)	(+)11.0 ±1.6[a)]	+15.7
$Q(^{13}B)$ (mb)	(+)37.4 ±4.0[b)]	+40.7

a) Present result. b) The value is taken from [52].

nuclei including the binding energy [53]. In his calculations,

1) the Cohen-Kurath wave functions were solved in Harmonic Oscillator potential (H.O.),
2) the wave functions were solved in the Skyrme Hartree-Fock with SG2-interaction (H.F.),
3) the core of the nuclide was solved by H.O. and the valence nucleon is solved by use of the Skyrme Hartree-Fock (H.O. + halo), and
4) both the core and the valence nucleon are solved by use of the Skyrme Hartree-Fock (H.F. + halo).

In H.O. + halo and H.F + halo models, the potential depth was adjusted to reproduce the one proton (neutron) separation energy for each nucleus. In all cases, the effective charges of $e_p = 1.3e$ and $e_n = 0.5e$ for proton and neutron were used, respectively. All calculations are performed in p-space. The results of his calculation are summarized in Table 6-7. As shown in this table, not only that the results from the calculation considering the binding energy gives good agreement with the experimental values on typical halo nuclei such as ^{8}Li and ^{8}B, but also showed overall agreements with the experimental values better than the conventional shell model calculation did. In the case of ^{13}O, the finite reduction of the quadrupole moment was caused by considering the binding energy, regardless of its core wave function. Therefore, it is reasonable to understand

Table 6-7. Comparison of quadrupole moments of A = 8, 11, 12 and 13 nuclei calculated by Kitagawa [53].
The quadrupole moments of A=8, 11, 12 and 13 nuclide calculated by the OXBASH code in p-space are shown. Effective charges of proton and neutron were 1.3e and 0.5e, respectively. H.O. and H.F. are harmonic oscillator potential and the Hartree-Fock potential. "+halo" means the calculation in which the potential depth were adjusted to reproduce the experimental separation energy of the last valence nucleon. All are in the unit of mb.

	H.O.	H.F.	H.O. + halo	H.F. + halo	Exp.
^{8}Li	22.2	26.7	27.3	29.9	32.8 ±0.6
^{8}B	34.7	45.9	54.7	60.4	68.3 ±2.1
^{11}B	44.4	45.6	44.4	45.6	40.59 ±0.10
^{11}C	31.9	33.9	30.8	33.4	33.27 ±0.24
^{12}B	19.0	18.9	18.2	18.3	13.4 ±1.4
^{12}N	9.8	10.0	4.8	5.7	9.8 ±0.9
^{13}B	40.7	39.7	38.5	38.0	37.4 ±4.0
^{13}O	15.7	15.1	7.4	9.0	11.0 ±1.6

that the discrepancy observed between the conventional shell model calculation and the experimental result for ^{13}O is due to its relatively low binding energy.

A quadrupole moment can be written as the sum of the two matrix elements as follows,

$$Q(N_p,N_n)=e_p^{eff}Q(N_p)+e_n^{eff}Q(N_n), \qquad (6\text{-}6)$$

where N_p and N_n are proton and neutron numbers in the nucleus, respectively. Effective charges $e_p^{eff}=1.3e$ and $e_n^{eff}=0.5e$ are used which are given by Sagawa et al. [54]

By assuming the charge independence of the nuclear force, the quadrupole moments of ^{13}O and ^{13}B can be written as follows,

$$\begin{cases} Q(^{13}\mathrm{O})=e_p^{eff}Q(8)+e_n^{eff}Q(5) \\ Q(^{13}\mathrm{B})=e_p^{eff}Q(5)+e_n^{eff}Q(8) \end{cases}. \qquad (6\text{-}7)$$

Then $Q_{exp}(8)$ = -3.0 ±2.0 mb and $Q_{exp}(5)$ = +29.9 ±3.2 mb are extracted from Eq. 6-7 and experimentally determined $Q(^{13}O)$ and $Q(^{13}B)$. The errors in these results are the experimental uncertainty only. From the OXBASH calculation with Cohen-Kurath wave function and harmonic oscillator potential, the $Q(8)$ and $Q(5)$ are given as $Q_{OX}(8)$ = 0.0 mb and $Q_{OX}(5)$ = +31.3 mb. $Q_{OX}(8)$ can be easily understood as the shell effect of N = 8. In the same manner, the $Q_{HF}(8)$ = -5.1 mb and $Q_{HF}(5)$ = +31.8 mb are also obtained from the Hartree-Fock calculation including the binding energy effect, which was performed by Kitagawa. These results are summarized in Table 6-8. The five neutrons(protons) are expected to be deeply bound inside the $^{13}O(^{13}B)$ since $Q_{OX}(5)$, which is from the calculation with Harmonic Oscillator potential, $Q_{HF}(5)$ and $Q_{exp}(5)$ are in agreement within the error. Therefore, the five neutrons are expected to be deeply bound in ^{13}O.

Table 6-8. Comparison of quadrupole moments from experiments and the conventional shell model calculation.
OXBASH calculation was performed in the p-shell with Cohen-Kurath wave function. "H.F.+ halo" calculation is the same as "H.F. +halo" in Table 6-7. Effective charges used in both calculations are $e_p^{eff} = 1.3e$ and $e_n^{eff} = 0.5e$. The errors in the experimental results are experimental uncertainty only.

	$Q(^{13}O)$	$Q(^{13}B)$	$Q(8)$	$Q(5)$
Exp. (mb)	(+)11.0 ±1.6[a)]	(+)37.4 ±4.0[b)]	-3.0 ±2.0	+29.9 ±3.2
OXBASH (mb)	+15.7	+40.7	0.0	+31.3
H.F. + halo (mb)	+9.0	+38.0	-5.1	+31.8

a) Present result. b) The value is taken from [52].

To avoid the uncertainty of the experimental result of $Q(^{13}B)$, the contribution of protons to the quadrupole moment of ^{13}O is estimated from the following relation,

$$Q_p(^{13}O) = Q_{exp}(^{13}O) - e_n^{eff} Q_{HF}(5). \qquad (6\text{-}8)$$

$Q_{HF}(5)$ is used as the contribution of neutrons to the quadrupole moment. Then $Q_p(^{13}O)$ is deduced to be -4.9 ±1.6 mb. From the conventional shell model

calculation, $Q_p(^{13}O)$ should be 0 mb because the protons form the $N = 8$ closed shell.

Assuming the five protons are deeply bound in ^{13}B, the contribution of neutrons to the quadrupole moments of ^{13}B can be also extracted following the same procedure as,

$$Q_n(^{13}B) = Q_{exp}(^{13}B) - e_p^{eff} Q_{HF}(5). \qquad (6\text{-}9)$$

$Q_n(^{13}B)$ is obtained to be -3.9 ±4.0 mb from Eq. 6-9. In this case, the deviation is not obvious due to a large experimental error and the small effective charge of neutron compared with that of proton. These results are summarized in Table 6-9.

Table 6-9. Contribution of the closed shell to the quadrupole moments. The values in OXBASH and H.F+halo are from the same shell model calculation in Table 6-8.

	experiment	OXBASH	H.F. + halo
$Q_p(^{13}O)$ (mb)	-4.9 ±1.6[a)]	0.0	-6.6
$Q_n(^{13}B)$(mb)	-3.9 ±4.0[b)]	0.0	-2.6

a) Present result. b) The value is taken from [52].

From these results, it is possible that some deformation of the closed shell of protons inside ^{13}O causes the discrepancy between the conventional shell model calculation and the experimental result; a small deformation of $\varepsilon = 1.3 \pm 0.5\%$ satisfactory reproduces the small discrepancy between the experimental and the conventional shell model results.

The root mean square (RMS) radii for proton, neutron and matter distribution from the present calculation and those from the experiments are compared in Table 6-10. The present calculation is successful in the qualitative reproduction of the deviation from the harmonic oscillator potential which are observed in the RMS radius of the proton of ^{8}B and the neutron of ^{8}Li, while the almost equal values to the harmonic oscillator potential are given for the RMS

radii of tightly bound proton such as ^{12}B or ^{8}Li. It should be noted that the values given in [55] and [56] were obtained from the interaction cross sections at high energy, 800*A* MeV. The proton and neutron RMS radii of ^{8}Li obtained by Litard [57] from the interaction measurement at far low energy (25 ~60*A* MeV) showed good agreements with the calculations including the binding energy effect. Therefore, the energy dependence of the interaction cross section is important for the discussion on the RMS radii. The contribution of proton halo to the interaction cross section is expected to be enhanced because of the larger nucleon-nucleon interaction cross section at low energy region around several tens *A* MeV. The present calculation gives the enhancement of the proton RMS radius not only for the ^{8}B, but also for ^{13}O. The enhancement of the proton RMS radius becomes much clear if it is compared with that of ^{13}N, which is closer to the stable line. This indicates that the halo-like structure of proton found in ^{8}B is

Table 6-10. Root mean square radii for *A* = 8, 11, 12, 13 nuclide calculated by Kitagawa and those from the experiments.
"p", "n" and "total" denote the root mean square radii for the proton, neutron and nucleon distributions, respectively. Experimental results are taken from [55, 56], except for ^{8}Li from [55] and [57], and ^{8}B from [55] and [58]. All are in fm.

	H.O.	H.O. + halo			H.F. + halo			Exp.		
		p	n	total	p	n	total	p	n	total
^{8}Li	2.26	2.16	2.59	2.44	2.19	2.69	2.51	2.26	2.44	2.37
		(from the interaction cross section at 25 ~60*A* MeV)						2.17	2.80	-
^{8}B	2.26	2.75	2.16	2.54	2.86	2.18	2.63	2.45	2.27	2.38
		(from the reaction cross section at 40 ~60*A* MeV)						2.53	2.31	2.45
^{11}B	2.42	2.40	2.43	2.42	2.40	2.47	2.43	-	-	-
^{11}C	2.42	2.47	2.40	2.44	2.51	2.38	2.45	-	-	-
^{12}B	2.46	2.42	2.59	2.52	2.39	2.61	2.52	2.35	2.42	2.39
^{12}N	2.46	2.69	2.42	2.58	2.73	2.38	2.59	-	-	-
^{13}C	2.49	2.48	2.46	2.55	2.61	2.60	2.53	-	-	-
^{13}N	2.49	2.64	2.64	2.57	2.48	2.44	2.55	-	-	-
^{13}B	2.49	2.44	2.58	2.53	2.40	2.65	2.55	2.41	2.50	2.46
^{13}O	2.49	2.73	2.44	2.62	2.77	2.39	2.63	2.56	2.48	2.53

also expected in ^{13}O. In the present calculation, the enhancement of the RMS radius of proton in ^{13}O is mainly from the spatial expansion of $1p_{1/2}$, as shown in Table 6-11. The density distribution for ^{13}O obtained from the present calculation shows the spatial extension of the matter distributions in the cases of H.O. + halo and H.F. + halo calculations (Fig. 6-3). Relying on the present calculation, it is highly expected that the protons in ^{13}O form the halo-like structure. Although the proton RMS radius of ^{13}O from the interaction cross section at 800*A* MeV does not show the clear enhancement as in ^{8}B, the interaction cross section of ^{13}O must be measured at low energy region around several tens *A* MeV, where the sensitivity for the halo structure is improved.

Table 6-11. The proton RMS radii for each orbit from the calculation by Kitagawa [53].
All are in fm.

		$1s_{1/2}$	$1p_{3/2}$	$1p_{1/2}$	total
^{13}O	H.O.	2.06	2.66	2.66	2.49
	H.O. + halo	2.06	2.74	3.25	2.73
	H.F. + halo	2.04	2.81	3.30	2.77
^{13}N	H.O.	2.06	2.66	2.66	2.49
	H.O. + halo	2.06	2.75	3.12	2.64
	H.F. + halo	2.01	2.76	3.17	2.64

6.2.2. Magnetic moment of ^{13}O

In the previous section, it becomes clear that the low binding energy is the main reason of the possible reduction of the quadrupole moment of ^{13}O. The magnetic moments of A = 8, 11, 12 and 13 nuclei calculated by Kitagawa from the same wave functions used in the discussion on the quadrupole moments are compared with the conventional shell model calculations as in Table 6-12. No discrepancies are found in the results of the conventional shell model calculations.

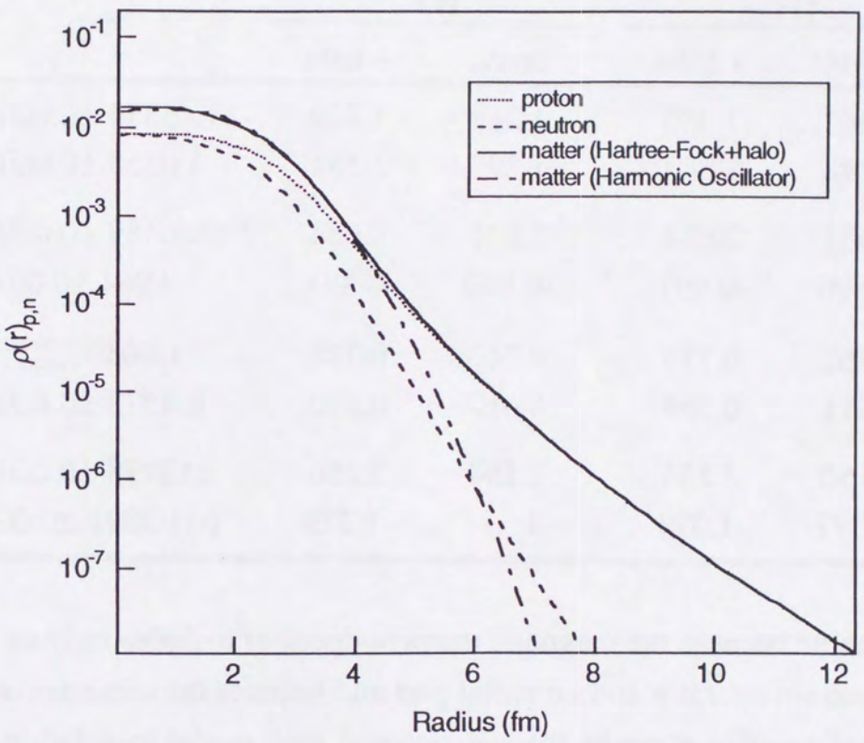

Fig. 6-3. Matter density distribution of ^{13}O calculated by Kitagawa [53]. The densities of proton, neutron and matter are from Hartree-Fock considering the binding energy. The matter density distribution from the conventional Harmonic Oscillator is also shown for comparison.

Table 6-12. Binding energy contributions to the magnetic moments of A = 8, 11, 12 and 13 nuclei.
H.O. and H.F. are the harmonic oscillator potential and the Hartree-Fock potential, respectively. "conv." means the conventional calculation and "+halo" are the calculation in which the potential depth were adjusted to reproduce the experimental separation energy of the last valence nucleon. All are given in μ_N. Experimental results except for ^{13}O are from [52].

	H.O.		H.F.		Exp.
	conv.	+ halo	conv.	+ halo	
^{8}Li	1.367	1.356	1.368	1.340	1.65356 ±0.00018
^{8}B	1.298	1.303	1.297	1.331	1.0355 ±0.0003
^{11}B	2.631	2.634	2.631	2.634	2.6886489 ±0.0000010
^{11}C	-0.890	-0.891	-0.890	-0.894	-0.964 ±0.001
^{12}B	0.762	0.773	0.762	0.765	$1.0030\ ^{+0.00015}_{-0.00014}$
^{12}N	0.611	0.599	0.612	0.610	0.4573 ±0.0005
^{13}B	3.150	3.153	3.150	3.156	3.17778 ±0.00051
^{13}O	-1.377	-1.379	-1.377	-1.379	(-)1.3891 ±0.0003

This is reasonable because the magnetic moment operator includes only an angular momentum operator and no radial part and because the same set of theoretical configuration given by the conventional shell model calculation is used in the frame work of the present calculations.

The experimental magnetic moment of ^{13}O and the theoretical predictions are summarized in Table 6-13. As shown in the table, the experimental result is consistent with the shell model calculation [14] with g-factors of free nucleon. The magnetic moments and $\langle\sigma\rangle$ extracted from the experimental results of ^{13}O and ^{13}B [59] also show good agreements with those from the shell model calculations. These results are consistent with other T = 1/2 mirror pairs as shown in Fig. 6-1.

Since the valence neutron of ^{13}O is in $p_{3/2}$ orbit, $\langle\sigma\rangle$ is expected to be 1 from the single particle model. On the contrary to the case of ^{9}C-^{9}Li pair, the quenching of the spin expectation value is found and reproduced well by theoretical calculations.

By applying the same procedure as used in the case of ^{9}C-^{9}Li pair, $\langle\sigma\rangle$ was extracted with effective g-factors and the relativistic corrections. In the present

Table 6-13. Comparison of the present result of $\mu(^{13}O)$ with the theories. "Effective + rel." is the value extracted with effective g-factors + relativistic correction. The value for "OXBASH" is extracted from the calculated magnetic moments by OXBASH with Cohen-Kurath model and CKPOT as the two-body effective interaction parameters. "H.F. + halo" is the Skyrme Hartree-Fock with SG2-interaction in which the potential depth is adjusted to reproduce the proton (neutron) separation energy. "Single" is the value from the single particle model. Magnetic moments are in the unit of μ_N.

	Exp.	Eff. + rel.	OXBASH	H.F. + halo	Single
^{13}O	(-)1.3891 ±0.0003[a)]	-	-1.38	-1.38	-1.91
^{13}B	+3.17778(51)[b)]	-	3.15	3.15	+3.79
$\langle\sigma\rangle$	0.76	0.55	0.72	0.72	1

a) Present result. b) [59]

$\langle\sigma\rangle$ extraction, the effective g-factors and the relativistic corrections are the same as used for ^{9}C-^{9}Li pair. Although the agreement with the values from theories becomes worse, obtained $\langle\sigma\rangle$ still shows the same trend, the quench of the spin expectation value. Therefore, this quenching can be basically understood as the effect of the configuration mixing. The discrepancy observed in $\langle\sigma\rangle$ derived with the effective g-factors should be understood as the result of the neglect of the higher order configuration mixing in the shell model, the limitation of the phase space to p-shell in the Hartree-Fock and that the degrees of the mass renormalization of nucleons in ^{13}O and ^{13}B pair are different from that obtained for $A = 16$ LS doubly closed shell. Here again, advanced theoretical calculations for drip-line nuclei including the proper treatment of meson exchange currents, in-medium renormalization of nucleons, and higher order configuration mixing under the realistic potential is required for the understanding of present $\langle\sigma\rangle$ in the frame work of shell model and for the discussions on the mass renormalization of the nucleons.

7. Summary

The magnetic moments of ^{9}C and ^{13}O, and the quadrupole moment of ^{13}O were measured by use of the β-NMR and the β-NQR methods which were combined with the radioactive beam technique. The results are $|\mu(^{9}C)| = 1.3914 \pm 0.005\mu_N$, $|\mu(^{13}O)| = 1.3891 \pm 0.0003\ \mu_N$ and $|Q(^{13}O)| = 11.0 \pm 1.6$ mb, respectively. The magnetic moment of ^{9}C and the unexpectedly large spin expectation value obtained from the magnetic moments of ^{9}C and ^{9}Li pair are not reproduced successfully by any theoretical calculations. The present large spin expectation value strongly suggests the large mass renormalization of the nucleons embedded in the pair. Systematic studies are continued for other nuclides around the nucleon drip-lines.

The magnetic moment of ^{13}O and the spin expectation value derived with the magnetic moment of mirror nucleus ^{13}B and the g-factors of the free nucleons show comparatively good agreement with the elaborate shell-model calculations with and without the effect of the small single nucleon separation energy. More reliable nuclear matrices and the understanding of the effective g-factors of nucleons inside the nuclide are required for the understanding of the small discrepancy between the experimental values and those from the theories.

The quadrupole moment of ^{13}O is successfully reproduced by the theoretical calculations including the effect of the small binding energy. The matter distribution obtained from the theoretical analyses of the quadrupole moment shows the halo-like structure in the ^{13}O nuclide.

8. Future prospect

Since an unexpectedly large spin expectation value obtained from ^{9}C and ^{9}Li pair strongly suggests the large renormalization of the nucleon mass in the drip-line nuclei, and since, on the other hand, the spin expectation value obtained from ^{13}O and ^{13}B pair shows the good agreements with the conventional theories, the degrees of in-medium renormalization of nucleons in the nucleus may largely depend on the orbit of the valence nucleons in the nuclides and/or on the small nucleon separation energies from the nuclides. Therefore, systematic studies on the degrees of in-medium renormalization in light nuclei is urged and also for this purposes the theoretical studies of reliable nuclear matrices including the proper treatment of meson exchange currents and higher order configuration mixing under the realistic potential are required mainly for the drip-line nuclei. For this aim, the knowledge of nucleon densities (nuclear matter distributions) in nuclides, where the valence nucleons reside is imperative.

It is also very important to calculate theoretically, in parallel to the experimental studies, the effective nucleon mass of the valence nucleons in the drip-line nuclei based on the quark-meson coupling model, especially for the understanding of the anomalous magnetic moments of unstable nuclei, and also, of the giant mesonic effects of more than 50 % of the axial charge matrices detected in the axial charges of weak nucleon currents [60]. A possible enhancement is suggested for the RMS radius of protons from the theoretical analyses of the experimental data in the present study. Therefore, in order to confirm the matter-density distributions and the RMS radii in the nuclides, interaction cross sections must be measured not only at high energy, but also at low energy region around several tens *A* MeV where the cross sections are more sensitive to the halo structure than those at higher energies.

References

1 I. Tanihata, H. Hamagaki, O. Hashimoto, *et al.*, Phys. Rev. Lett. **55**, 2676 (1985).

2 T. Minamisono, Phys. Rev. Lett. **69**, 2058 (1992).

3 T. Minamisono, Hyp. Int. **78-80**, 165 (1993).

4 T. Minamisono, Hyp. Int. **78-80**, 169 (1993).

5 K. Sugimoto, J. Phys. Soc. Japan **34**, 197 (1973).

6 T. Minamisono, Hyp. Int. **35**, 979 (1987).

7 Y. Nojiri, K. Matsuta, T. Minamisono, *et al.*, Hyp. Int. **35**, 1019 (1987).

8 K. Matsuta, A. Ozawa, Y. Nojiri, *et al.*, Phys. Lett. **B281**, 214 (1992).

9 K. Asahi, M. Ishihara, N. Inabe, *et al.*, Phys. Lett. **B251**, 488 (1990).

10 K. Sugimoto, J. Phys. Soc. Japan **21**, 213 (1966).

11 T. Minamisono, Doctral Thesis (1970).

12 T. Minamisono, Hyp. Int. **78-80**, 1315 (1993).

13 A. Bohr and B. R. Mottelson, *Nuclear Structure Volume 1*, New York, (1969).

14 B. A. Brown, A. Etchegoyen, and W. D. M. Rae, MSUCL Report **524** (1988).

15 S. Cohen and D. Kurath, Nucl. Phys. **73**, 1 (1965).

16 B. A. Brown and B. H. Wildenthal, Phys. Rev. **C28**, 2397 (1983).

17 H. Miyazawa, Prog. Theor. Phys. **6**, 801 (1951).

18 A. Arima, K. Shimizu, W. Bentz, *et al.*, Adv. Nucl. Phys. **18**, 1 (1988).

19 H. A. Mavromatis, L. Zamick, and G. E. Brown, Nucl. Phys. **80**, 545 (1966).

20 M. Ichimura and K. Yazaki, Nucl. Phys. **63**, 401 (1965).

21 H. Ohtsubo, M. Sano, and M. Morita, J. Phys. Soc. Japan **34**, 509 (1973).

22 A. Abragam and M. Goldman, *Nuclear Magnetism:order and disorder* (1982).

23 A. Abragam, *Principles of Nuclear Magnetism*, Oxford Science Publications (1961).

24 T. Minamisono, Y. Nojiri, A. Mizobuchi, *et al.*, J. Phys. Soc. Jpn. Suppl. **34**, 156 (1973).
25 N. Takahashi, T. Shimoda, H. Miyatake, *et al.*, Hyp. Int. **97/98**, 469-477 (1996).
26 M. Morita, *Beta Decay and Muon Capture* (1973).
27 B. R. Appleman, J. Chem. Phys. **60**, 2574 (1974).
28 C. J. Janeson, Nucl. Mag. Res. **12** (1980).
29 T. Kubo, M. Ishihara, N. Inabe, *et al.*, Nucl. Inst. Methods **B70**, 309-319 (1992).
30 K. Terakura and J. Kanamori, J. Phys. Soc. Jpn. **34**, 1520 (1973).
31 N. Yokoyama, Y. Yamada, S. Kohzuki, *et al.*, J. Phys. Soc. Jpn. **37**, 73 (1974).
32 T. Ohtsubo, K. Matsuda, T. Araki, *et al.*, Hyp. Int. **78**, 439-443 (1993).
33 F. D. Feicock and W. R. Johnson, Phys. Rev. **187**, 39 (1969).
34 K. Matsuta, M. Fukuda, T. Izumikawa, *et al.*, Hyp. Int. **97/98**, 501-508 (1996).
35 K. Sugimoto, K. Nakai, K. Matsuda, *et al.*, J. Phys. Soc. Jpn. **25**, 1258 (1968).
36 C. L. Turner, S. E. Chung, and E. Oldfield, J. Magn. Res. **64**, 316 (1985).
37 Y. Matsumoto, Master thesis (1996).
38 R. A. Kamper, K. R. Lea, and C. D. Lustig, Proc. Phys. Soc. London **70B**, 897 (1957).
39 F. D. Correl, Phys. Rev. **C28**, 862 (1983).
40 B. Buck and S. M. Perez, Phys. Rev. Lett. **50**, 1975 (1983).
41 H. Sagawa and H. Kitagawa, private communication.
42 K. Valga, Y. Suzuki, and I. Tanihata, Phys. Rev. C **52**, 3013 (1995).
43 T. Minamisono, T. Ohtsubo, Y. Nakayama, *et al.*, Hyp. Int. **73**, 347-356 (1992).
44 T. Minamisono, Y. Nojiri, K. Matsuta, *et al.*, Nucl. Phys. **A516**, 365 (1990).
45 M. Tanigaki, M. Matsui, M. Mihara, *et al.*, Hyp. Int. **78**, 105 (1993).

46 M. Tanigaki, T. Minamisono, Y. Nojiri, *et al.*, *Proceedings of the International Symposium on Non-Nucleonic Degrees of Freedom Detected in Nucleus Osaka, Japan, Sept. 2-5, 1996* , 365 (1996).
47 I. S. Towner and F. C. Khana, Nucl. Phys. **A399**, 334 (1983).
48 I. S. Towner and F. C. Khana, Phys. Rep. **155**, 264 (1987).
49 K. Saito, K. Tsushima, and A. W. Thomas, Phys. Rev. **C55**, 2637 (1997).
50 T. Yamazaki, Phys. Lett. **B160**, 227 (1985).
51 H. Kitagawa and H. Sagawa, Hyp. Int. **78**, 175 (1993).
52 P. Raghavan, Atomic Data and Nuclear Data Tables **42**, 189 (1989).
53 H. Kitagawa and H. Sagawa, private communication.
54 H. Sagawa and B. A. Brown, Nucl. Phys. **A430**, 84 (1984).
55 I. Tanihata, T. Kobayashi, O. Yamakawa, *et al.*, Phys. Lett. **B206**, 592-596 (1988).
56 A. Ozawa, I. Tanihata, T. Kobayashi, *et al.*, Nuclear Physics **A608**, 63-76 (1996).
57 E. Litard and e. al, Europhys. Lett. **13**, 401 (1990).
58 M. Mihara, private communication.
59 R. L. W. Jr. and L. Madansky, Phys. Rev. **C3**, 2149 (1971).
60 T. Minamisono and *et al.*, Phys. Rev. Lett. **80**, 4132-4135 (1998).
61 J. C. B. Jr. and *et al.*, Phys. Rev. **116**, 87 (1959).
62 F. Alder and *et al.*, Phis. Rev. **116**, 87 (1951).
63 W. Sahm and *et al.*, Nature **A29**, 1754;1763 (1974).
64 T. Minamisono and *et al.*, Phys. Lett. **B61**, 155 (1976).
65 E. Brun and *et al.*, Phys. Rev. Lett. **9**, 166 (1962).
66 C. Gabathuler, Proc. of 17th. Congress Ampere, Turku(North - Holland, Amsterdam, 1973) , 499 - 501 (1973).
67 S. Fukuda, Doctral thesis (1995).
68 K. Sato, private communication.
69 T. J. Bastow and S. N. Stuart, Chem. Phys. **143**, 459 (1990)

Appendix A. HFI of ^{13}O in Pt:anomalous knight shift

As discussed in chapter 5, a large Knight shift was observed in the case of ^{13}O in Pt. The Knight Shift K and the spin relaxation time T_1 for interstitial impurities implanted in metals are important clues to investigate the electronic structure of the metals. Because Pt has very low local electron density around the Fermi level for interstitial impurities, Pt is known as the unique implantation medium in which the implanted nuclei show small K and large T_1. In this appendix, the results of β-NMR of $^{13}O(I^{\pi} = 3/2^{-}, T_{1/2} = 8.6$ ms) and $^{12}N(I^{\pi} = 1^{+}, T_{1/2} = 11.0$ ms) implanted into polycrystalline Pt (fcc) are compared with the theoretical calculations for the systematic study of the electric structures of interstitial impurities.

A.1. Knight shift of ^{13}O in Pt

The Knight shift was obtained to be $K = +(4.23 \pm 0.14) \times 10^{-3}$ by correcting the chemical shift for ^{13}O in MgO. The polarization was measured as a function of time at the room temperature as shown in Fig. 5-13. $T_1T = 2.90 \pm 0.65$ Ks is obtained. The result is summarized in Table A-1.

Table A-1. Knight shift of O in Pt.

	^{13}O in MgO	^{13}O in Pt, $T = 300$ K
Observed Frequency (kHz)	2823.1 ±0.2	2835.1 ±0.3
H_0 drift=$H_0(^{13}O$ in Pt)/$H_0(^{13}O$ in MgO) -1	-	$+5.8 \times 10^{-5}$
Frequency Shift(MgO ref.)	-	$+(4.19 \pm 0.13) \times 10^{-3}$
Chemical Shift	$-(2.87 \pm 0.15) \times 10^{-4}$	-
Diamagnetism		-3.3×10^{-4}
Knight Shift (K)	-	$+(4.23 \pm 0.14) \times 10^{-3}$

Table A-2. Spin-Lattice relaxation of O in Pt.

	^{13}O in Pt (T = 300 K)
T(K)	300
T_1(ms)	$9.7^{+2.6}_{-1.7}$
T_1T(Ks)	2.90 ±0.65

Comparing with other interstitial impurities in Pt, T_1T for ^{13}O is unusually fast and K for ^{13}O is unusually large (Fig. A-1). The Knight shift K_c calculated from the observed T_1T with Korringa relation is $|K_c| = (1.8 \pm 0.3) \times 10^{-3}$. This fairly good agreement implies that the main cause of both the spin-lattice relaxation and the Knight shift is Fermi contact interaction. The present results, the large K and the short T_1, strongly suggest the electronic structure around ^{13}O in Pt is unusual compared with other light impurities and the local electron density at Fermi level must be huge. In order to explain the present results, the electronic structure was calculated for the second period main group elements in Pt in the framework of the local spin density approximation of the density functional theory using the super-cell method in the Korringa-Kohn-Rostoker (KKR) band-structure calculation. In this calculation, impurities are assumed to settle in the octahedral interstitial site under an external fields corresponding to the electron Zeeman energy of 10^{-3} Ry with the 10 % local lattice relaxation as is experimentally determined for ^{12}B and ^{12}N in fcc Cu.

The calculation result is well reproduced the present large K for ^{13}O. From this calculation, the Knight shift of N in Pt is expected large, $+5 \times 10^{-3}$.

A.2. ^{12}N in Pt

For the systematic study of the electronic structure of light impurity in Pt and to see the validity of the KKR calculation, the measurement of K and T_1T of N in Pt was employed. The procedure was essentially the same as that in the case of ^{13}O, except for the production of probe nuclei. ^{12}N was produced through ^{10}B(^{3}He, n)^{12}N reaction with 3.0 MeV ^{3}He beam from Van de Graaff accelerator

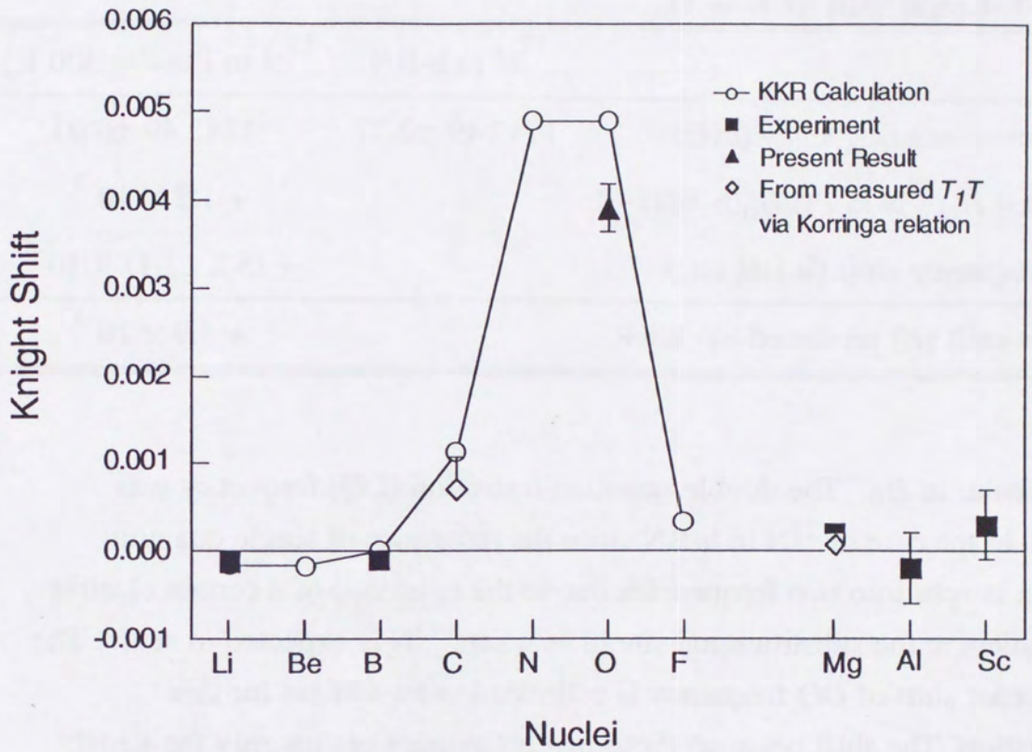

Fig. A-1. Knight shifts in Pt obtained from experiments including the result of ^{13}O and the KKR calculation.

at Osaka University. The polarization was obtained by selecting the recoil angle of ^{12}N to $\theta_L = 20 \pm 7$ degrees in the laboratory frame. Applied H_0 was 5 kOe in this case. The Knight shift was measured as the frequency shift between the resonance of ^{12}N in h-BN(hexagonal) and that in Pt. The c-axis of h-BN was placed

Table A-3. Knight shift of N in Pt.

	^{12}N in h-BN	^{12}N in Pt (T = 300 K)
Resonance frequency (kHz)	1742.49 ±0.37	1743.49 ±0.01
H_0 drift = H_0(^{12}N in Pt)/H_0(h-BN) - 1	-	$+ 1.2 \times 10^{-5}$
Frequency shift (h-BN ref.)	-	$+ (5.8 \pm 2.1) \times 10^{-4}$
Knight shift (K) predicted by KKR		$+ 4.9 \times 10^{-3}$

perpendicular to H_0. The double quantum transition (DQ) frequency was observed in the case of ^{12}N in h-BN since the resonance of single quantum transition is split into two frequencies due to the existence of a certain electric field gradient at the substitutional site of N where ^{12}N is expected to settle. The second order shift of DQ frequency is estimated to be +84 Hz for this configuration. The shift between these two resonances are roughly the Knight shift of N in Pt because the chemical shift of N in h-BN is expected to be about 1/10 of the predicted Knight shift, from the systematics of chemical shifts in nitrogen compounds. Typical NMR spectra are shown in Fig. A-2. The observed Knight shift $K = (5.8 \pm 2.1) \times 10^{-4}$ is as small as 1/10 of that expected from the KKR calculation. The results are summarized in Table A-3.

The spin relaxation time was also measured at room temperature. A typical spectrum is shown in Fig. A-3. T_1 for N in Pt was also obtained to be $T_1 = 66\ ^{+9}_{-7}$ ms. The calculated Knight shift from obtained T_1 with the Korringa relation is $|K_c| = (1.4 \pm 0.1) \times 10^{-4}$, which shows good agreement with the measured Knight shift. The results are summarized in Table A-4.

Knight shifts obtained from experiments including the present results and the KKR calculation are shown in Fig. A-4. A large discrepancy between

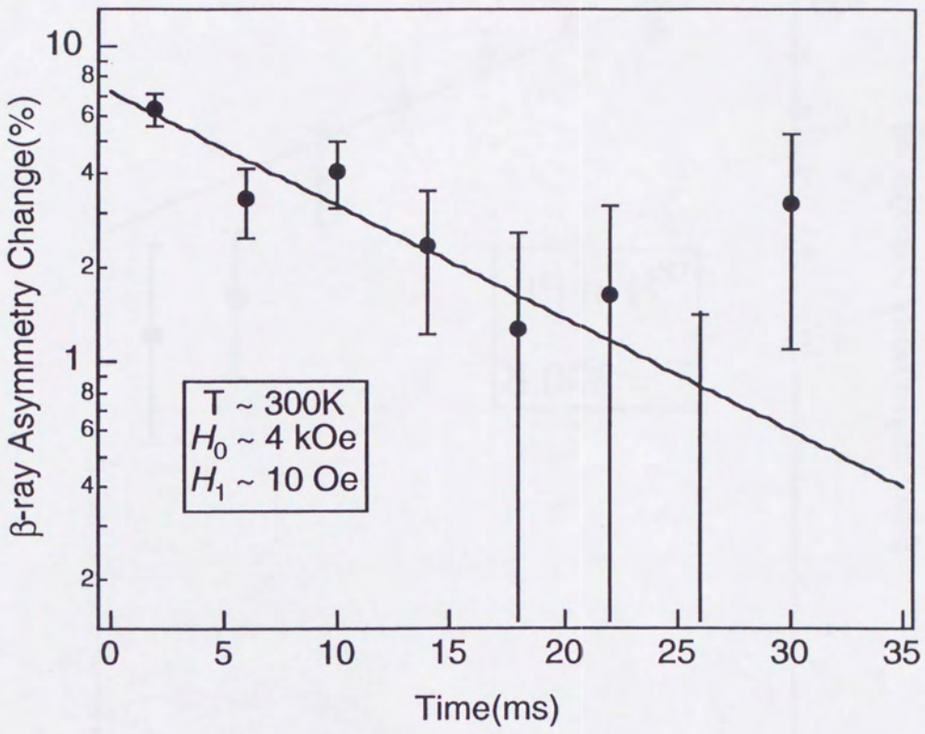

Fig. A-2. Typical time spectrum of spin-lattice relaxation of ^{13}O in Pt at room temperature.

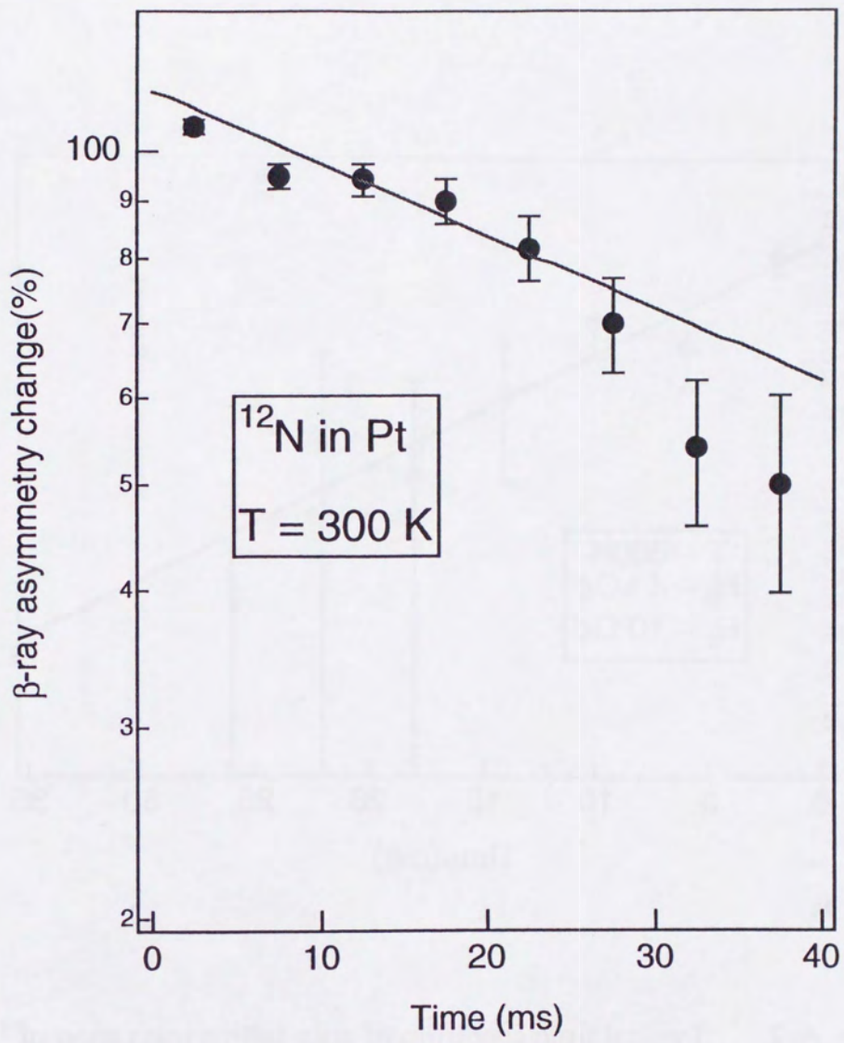

Fig. A-3. Typical time spectrum of polarization of ^{12}N observed in Pt.

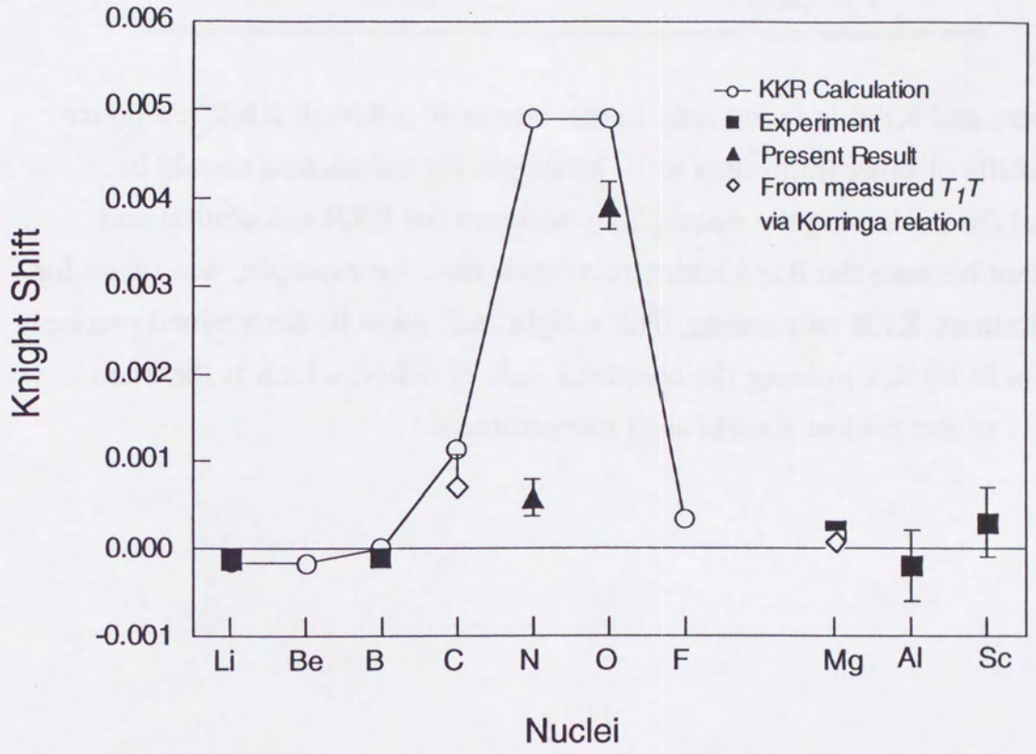

Fig. A-4. Knight shifts obtained from experiments including the present results and the KKR calculation.

Table A-4. Spin-Lattice relaxation of N in Pt.

	^{12}N in Pt (T = 300 K)
T (K)	300
T_1	66^{+9}_{-7} (ms)
T_1T (Ks)	20 ±2

experiment and KKR is found only in the case of N although KKR reproduce Knight shifts of other impurities well. More precise calculation should be employed for explaining the discrepancy between the KKR calculation and experiment because the fixed lattice relaxation rate, for example, was taken for the preliminary KKR calculation. The Knight shift must be determined precisely for ^{12}N in Pt by determining the chemical shift of h-BN, which is the main ambiguity of the present Knight shift measurement.

Appendix B. Effective g-factors for doubly closed shell ± 1 nucleon nuclei

Because of the good isospin symmetries, the magnetic moments of mirror nuclei give us useful information on nuclear structure and non-nucleonic degrees of freedom in nucleus. For investigating such effects, LS doubly closed shell ± 1 nucleon nuclei are especially the good cases since these nuclei have no first order configuration mixing.

Theoretical approaches for understanding these magnetic moments have been performed by Arima et al. [18], and Tower and Khana [48, 49]. They included the mixing of highly excited configurations up to $12\hbar\omega$ and tensor correlations into their calculations and successfully explained the deviations from the Schmidt value fairly well. Recent technical developments and the accumulation of the knowledge on the hyperfine interactions of the nucleus inside the implantation media to evaluate the magnetic shielding (chemical shift or Knight shift) enabled us to improve the precision of the magnetic moments of ^{15}O, ^{17}F, ^{41}Sc [43-45].

Here, we discuss non-nucleonic effects observed in LS doubly closed shell ± 1 nucleon nuclei based on these recent theoretical and experimental improvements in magnetic moments.

B.1. Magnetic moments of LS doubly closed shell ± 1 nucleon nuclei

In Table B-1., the experimental magnetic moments are shown with the Schmidt value and the theoretical calculations by Arima et al., and Towner and Khana. The theoretical results give essentially similar values and agreements between the theoretical predictions and experimental values are fairly well. Still though, there remain open problems in reproducing the known magnetic moments, i.e., a few percent of deviations are left unexplained systematically.

The mesonic exchange correction to the isoscalar magnetic moment predicted from the non-relativistic framework [18, 48, 49] was as small as $\delta\mu^{(0)}_{exc} / \mu^{(0)}_{S} \cong +0.3$ %. Although Arima et al. give rather large mesonic corrections

Table B-1. Magnetic moments of the LS doubly closed shell ±1 nucleon nuclei.

A		I^π	μ_S [a] [μ_N]	μ_{exp} [μ_N]	$\delta\mu_{exp}^{(0)}$ [b] [μ_N]	$\delta\mu^{(0)}_{exp}/\mu^{(0)}_S$ (%)	$\mu^{(0)}_{conf}/\mu^{(0)}_S$ [c] Arima et al. [d]	T&K [e]
1	^{15}N	1/2$^-$	-0.26248	-0.283188842(45) [f]				
	^{15}O	1/2$^-$	-0.63773	(-)0.71951(12) [g]				
	$\mu^{(0)}$		+0.18673	+0.21816(6)	+0.003143	+16.85(3)	+22.85	+18.2
1	^{17}O	5	-1.91315	-1.89379(9) [h]				
	^{17}F	5	+4.79274	(+)4.72130(25) [i]				
	$\mu^{(0)}$		+1.43980	+1.41376(13)		-1.82(1)	-2.95	-2.1
39	^{39}K	3	+0.12435	+0.3915063(2) [j]				
	^{39}Ca	3	+1.14789	(+)1.0216(2) [k]				
	$\mu^{(0)}$		+0.63612	+0.70659(6)	+0.0705	+11.08(2)	12.49	+9.7
41	^{41}Ca	7/2$^-$	-1.91315	-1.594780(9) [l]				
	^{41}Sc	7/2$^-$	+5.79274	(+)5.4305(18) [m]				
	$\mu^{(0)}$		+1.93980	+1.91785(9)	-0.0221(9)	-1.14(5)	-2.70	-2.0

a) Schmidt value.

b) $\delta\mu_{exp}^{(0)} = \{\mu_{exp}^{(0)} - \mu_S^{(0)}\}$, where the isoscalar magnetic moment is defined as $\mu^{(0)} = \frac{1}{2}\{\mu(T_z=+\frac{1}{2}) + \mu(T_z=-\frac{1}{2})\}$.

c) $\mu^{(0)}_{conf}/\mu^{(0)}_S$ is the configuration mixing correction to the isoscalar magnetic moment given by Arima et al. [18] divided by $\mu_s^{(0)}$.

d) Theoretical value given by Arima et al. [18]

e) Theoretical values given by Towner and Khana [47, 48].

f) Ref. [61]. g) Ref. [45]. h) Ref. [62]. i) Ref. [43].
j) Ref. [63]. k) Ref. [64]. l) Ref. [65]. m) Ref. [44].

obtained from $\sigma\omega$ model which include relativistic treatment, they claim that these values are very much model dependent and it is too early to compare the values directly with the experimental ones.

B.2. Effective *g*-factors of nucleon in nucleus

A possible explanation for the observed discrepancies is that the effective mass of the valence nucleon is changed inside the nucleus. Here we deduce the effective *g*-factors and mass renormalization of the nucleon under the following assumptions.

1) The mesonic effects affect spin and orbital g-factors only, in another word, motion of the renormalized nucleon in a nucleus affects the nuclear magneton $\mu_N^{eff} = \mu_N(1+\kappa) = (e\hbar/2M_p)(1+\kappa)$ only.
2) The nuclear matrices including corrections due to spin tensor term, cross term, core deformation and relativistic effects [21] are given theoretically.
3) Effective g-factors are the same for nuclei around the same core.

Then the relations between the experimental isoscalar magnetic moment and the effective g-factors can be written as,

$$\mu_{exp.}^{(0)} - \left\{\delta\mu_P^{(0)} + \delta\mu_{cross}^{(0)} + \delta\mu_{def}^{(0)} + \delta\mu_{rel}^{(0)}\right\} = \left[(I - \langle S_z\rangle_{eff})g_l^{(0)} + \langle S_z\rangle_{eff} g_s^{(0)}\right]\mu_N. \quad \text{(B-1)}$$

This equation gives four solid lines on the g_l-g_s plane corresponding to the four mirror pairs of interest as shown in Fig. B-1. Effective g-factors are obtained as the crossing point of two of the four solid lines. For example, effective g-factors around A = 16 are given by the crossing point of lines for mass-17 and 15. Obtained effective g-factors are listed in Table B-2. They are clearly different from the g-factors in free space.

Table B-2. Effective isoscalar g-factors and the renormalization factor κ deduced from effective isoscalar g-factors.
Nuclear matrices were obtained from Arima et al., and Towner and Khana (T.K.). Relativistic corrections were obtained from Ohtsubo.

	Matrix from Arima *et al.*		Matrix from T.K.	
	mass-16	mass-40	mass-16	mass-40
$g_l^{(0)}$(experiment)	0.504	0.514	0.513	0.520
$g_s^{(0)}$(experiment)	1.007	1.015	0.914	0.899
κ from $g_l^{(0)}$(%)	0.8	2.8	2.5	4.1
κ from $g_s^{(0)}$(%)	14.1(1)	15.2(2)	3.9(1)	2.2(2)

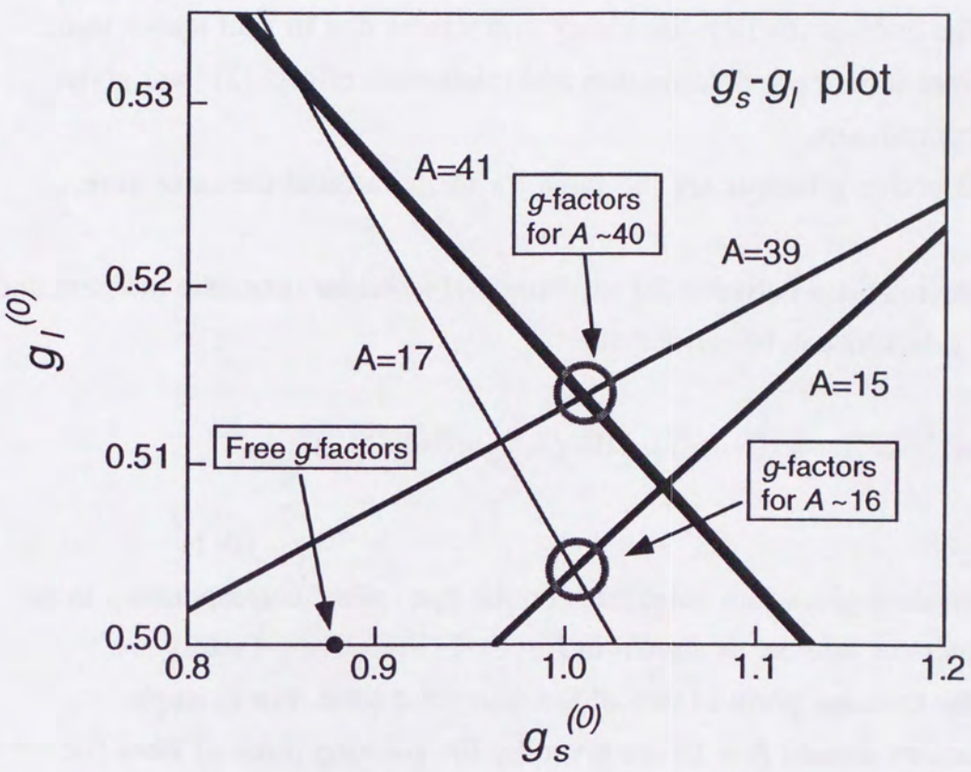

Fig. B-1. $g_l^{(0)}$-$g_s^{(0)}$ graph. Isoscalar magnetic moments are plotted using the nuclear matrics given by Arima et al. From the assumption 3), the cross points of the lines for closed shell ±1 nucei give the effective g-factors. The width shown for each line indicates each experimental error only.

Isoscalar moments are relatively independent of various corrections, especially independent of the mesonic effects as is expected from Sach's Theorem. The degrees of mass renormalization were estimated from the obtained effective isoscalar g-factors as

$$\kappa = \{ g_l^{(0)}(\text{experiment}) - g_l^{(0)} \} / g_l^{(0)} \text{ , and/or}$$
$$\kappa = \{ g_s^{(0)}(\text{experiment}) - g_s^{(0)} \} / g_s^{(0)}. \qquad \text{(B-2)}$$

The obtained κ are also listed in Table B-2. Although the degree of the renormalization depends on the nuclear matrices, both results show the same tendency. Therefore, we assume that the true κ is in between the value from Arima's matrices and that from Towner's matrices. Thus the degrees of mass renormalization deduced from the orbital and spin g-factors as shown in Table B-3.

Therefore, the existence of about 3 % of nucleon mass renormalization is strongly suggested in the present lighter mass region. The present result still depends on the nuclear model. More precise calculation including appropriate relativistic treatment is urged.

Table B-3. Renormalization degrees around A = 16 and 40 region.

	mass-16	mass-40
κ(from g_l)	+(1.7 ±0.9) %	+(3.5 ±0.6) %.
κ(from g_s)	+(9.1 ±5.2) %	+(8.5 ±6.3) %.

Appendix C. Electric field gradient at O site in TiO_2

C.1. Introduction

One has to know the electric field gradient (EFG) at the site where the nucleus is implanted to determine its quadrupole moment. In the case of the implantation of ^{13}O into TiO_2, ^{13}O is expected to settle at the O site in TiO_2. Therefore, the quadrupole coupling constant of ^{17}O in TiO_2 is required. Although ^{17}O is the only stable isotope of O which has a finite quadrupole moment, the signal of ^{17}O in TiO_2 is almost undetectable by the conventional NMR detection because of its low natural abundance ratio (as low as 0.04 %). The EFG for O sites have already been studied by Gabathuler et al. with Cr doped TiO_2. The coupling constant of ^{17}O at O site in TiO_2 has already determined to be $|eqQ(^{17}O)/h| = 1.497 \pm 0.004$ MHz and $\eta = 0.868 \pm 0.005$ by Gabathuler et al [66]. They doped Cr into TiO_2 for the enhancement of NMR signal and it is reasonable to expect that some lattice relaxation must be caused by the doped Cr in the crystal. Therefore, the EFG must be measured again with TiO_2 free from such lattice relaxation for the determination of Q of ^{13}O.

In this appendix, the synthesis of ^{17}O enriched TiO_2 crystal which is free from the lattice relaxations caused by impurities such as Cr is introduced, and the FT-NMR measurement of ^{17}O in TiO_2 is discussed.

C.2. Principle of FT-NMR measurement

FT-NMR is an advanced technique of NMR for stable nuclei. If RF field H_1, the frequency nearly equal to the resonance frequency, is applied Δt with $(\gamma H_1 \Delta t) \sim \pi/2$ (90° pulse), the direction of the spin is tipped, and the direction of the spin is changed as shown in Fig. C-1. As a result of this operation, the spin ensemble is tilted from its equilibrium position along H_0 and precesses around the external magnetic field. The tilted angle of the ensemble depends on the deviation between the rotating frequency of the spin ensemble and that of the applied RF signal. The motion of the spin is monitored by a surrounding pickup coil through

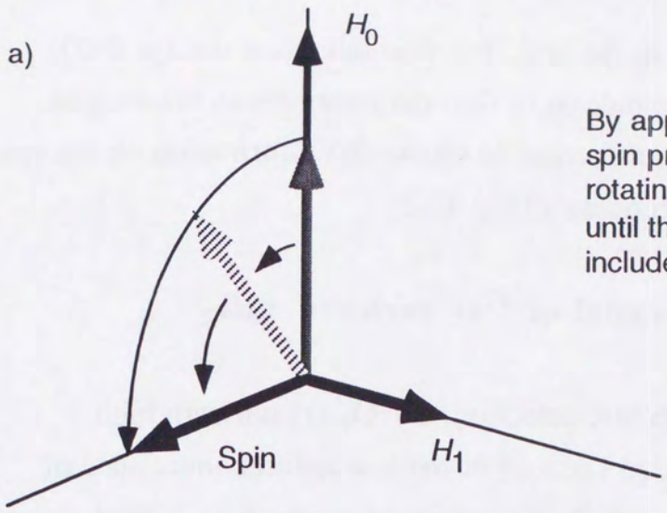

By applying a pulsed, high intensity RF, the spin precesses around effective z-axis in the rotating frame fixed to H_1 field. RF is applied until the spin is lay down in the plane which includes H_1.

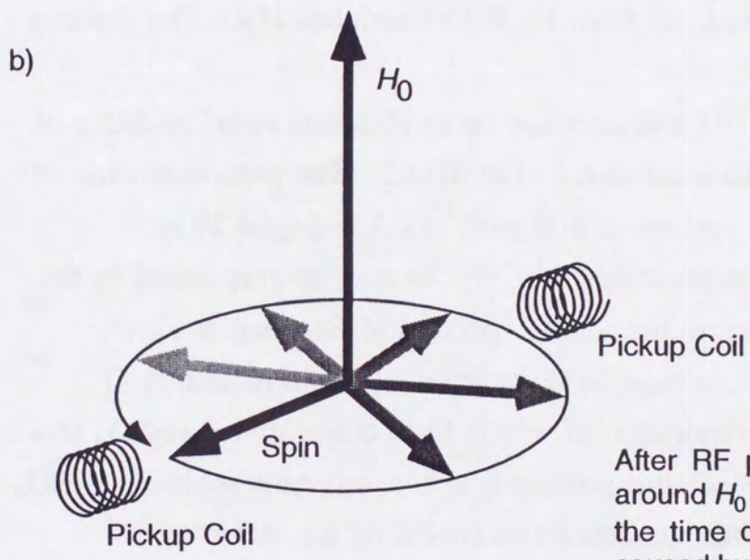

After RF pulse, the spin starts precessing around H_0 again. A pair of pickup coil detect the time dependence of the magnetization caused by this precession.

Fig. C-1. Principle of Pulsed NMR.

a weak residual RF field flowing in the coil. The free induction decays (FID) which contains information on the motion of the spin ensemble in the sample. This FID signal is then Fourier transformed to obtain the information on the spin ensemble such as the resonance frequency (Fig. C-2).

C.3. Synthesis of the single crystal of ^{17}O enriched TiO_2

To employ the defect-free NMR detection, a TiO_2 crystal with high concentration rate of ^{17}O is required because of the low natural abundance of ^{17}O. Required concentration rate of ^{17}O was estimated as much as several percent from the NMR detection of ^{45}Sc in TiO_2 [67]. ^{17}O doped TiO_2 crystal was synthesized at Earth Chemical co ltd. from 10 % ^{17}O enriched H_2O. The process of the synthesis was as follows.

62.5g of H_2O in which ^{17}O was enriched up to 10% was acted on 325 g of $TiCl_4$ to produce the intermediate substance, $Ti(OH)_nCl_x$. The present amount of these materials was enough to synthesize 100 g of ^{17}O 5 % doped TiO_2 theoretically. Since this is exothermic reaction, $H_2{}^{17}O$ may be evaporated by the heat during the reaction. Therefore the adding speed of H_2O was kept slow enough and was cooled down less than 20 C° by ice made from natural H_2O during the addition to avoid evaporation of water. Then concentrated H_2SO_4 was added to obtain $Ti(OH)_nCl_x$. Since this process is also exothermic reaction, H_2SO_4 was added slowly enough and the substance was cooled by ice. After the $(NH_4)_2SO_4$ was added to $TiOSO_4$ to obtain $TiOSO_4(NH_4)_2SO_42H_2O$, which was then heated to be resolved to TiO_2, NH_3 and H_2SO_4.

Obtained TiO_2 of powder form was then crystallized by the Vernueil method. Powder TiO_2 was melted at 1900 C° in the oxygen and hydrogen atmosphere, then crystallized on the kernel rod at the rate of 10 mm/hour. After the crystallization, the obtained TiO_2 was annealed at 1300 C° to 500 C° in the atmosphere to remove the defects in the crystal. Finally three 15 mm$\phi \times$ 25 mm long crystals were obtained.

The concentration of ^{17}O in finally obtained TiO_2 was 5 % theoretically, but the true ratio may be less because of the difficulty to estimate the substitution

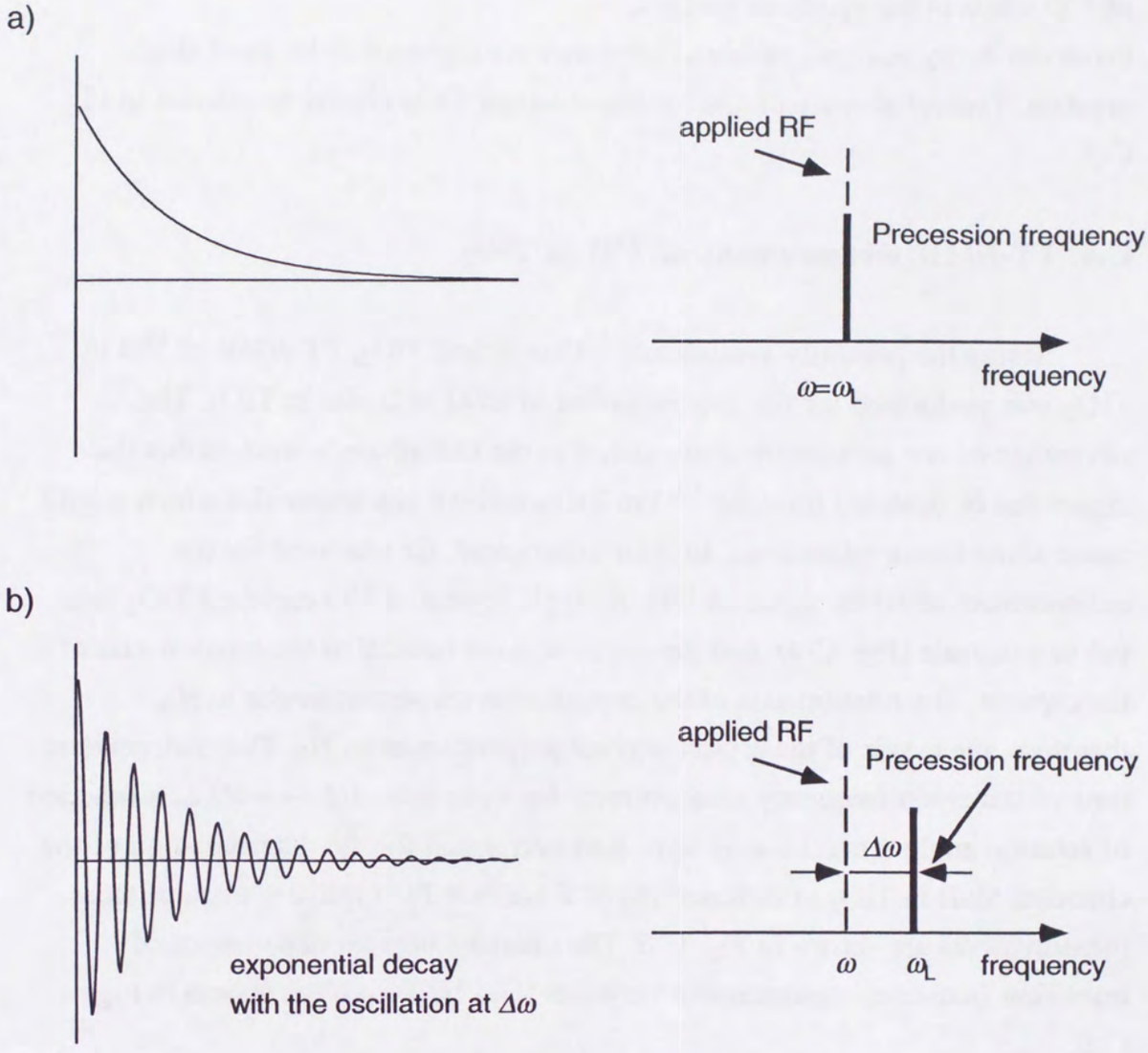

Fig. C-2. FID signal of the spin under a strong static magnetic field after the pulsed RF at the frequency of ω is applied. If the applied RF frequency is equal to the precession frequency of the spin(ω_L), The exponential decay signal is observed as FID (a). Otherwise, the exponential decay oscillated at the frequency of differential from applied RF($\Delta\omega$) is observed as FID (b).

of ^{17}O while in the synthesis process.
From the X-ray analysis, obtained crystals were expected to be good single crystals. Typical X-ray patterns for the obtained TiO_2 crystal are shown in Fig. C-3.

C.4. FT-NMR measurement of ^{17}O in TiO_2

Using the presently synthesized ^{17}O enriched TiO_2, FT-NMR of ^{17}O in TiO_2 was performed for the determination of EFG at O site in TiO_2. The advantage of our measurement compared to the Gabathuler's work is that the signal can be detected from the ^{17}O in TiO_2 without any impurities which would cause some lattice relaxations. In their experiment, Cr was used for the enhancement of NMR signal of ^{17}O. A single crystal of ^{17}O enriched TiO_2 was put in a capsule (Fig. C-4) and the c-axis was set parallel to the rotation axis of the capsule. The rotation axis of the capsule was set perpendicular to H_0, therefore, the c-axis of the crystal was set perpendicular to H_0. Two independent runs of transition frequency measurement between $m = -1/2 \leftrightarrow +1/2$ as a function of rotation angle around c-axis were also performed for the determination of the chemical shift in TiO_2 at different H_0 (7 T and 9.4 T). Typical spectra of these measurements are shown in Fig. C-5. The obtained angular dependence of transition frequency measurement between $m = -1/2 \leftrightarrow +1/2$ is shown in Fig. C-6.

The angular dependence of the chemical shift is described as, ignoring the off-diagonal terms,

$$\sigma = \sigma_X \cos^2\phi \sin^2\theta + \sigma_Y \sin^2\phi \sin^2\theta + \sigma_Z \cos^2\theta, \qquad \text{(C-1)}$$

using the polar angle shown in Fig. C-7. The X, Y and Z axis taken in the present measurement are shown in Fig. C-8. The notable contribution from the electric quadrupole interaction to the observed frequency shift of $m = -1/2 \leftrightarrow +1/2$ is the second order perturbation term, thus this term is included in the fitting function. As discussed in chapter 3, this second order shift term is described as follows Eq.

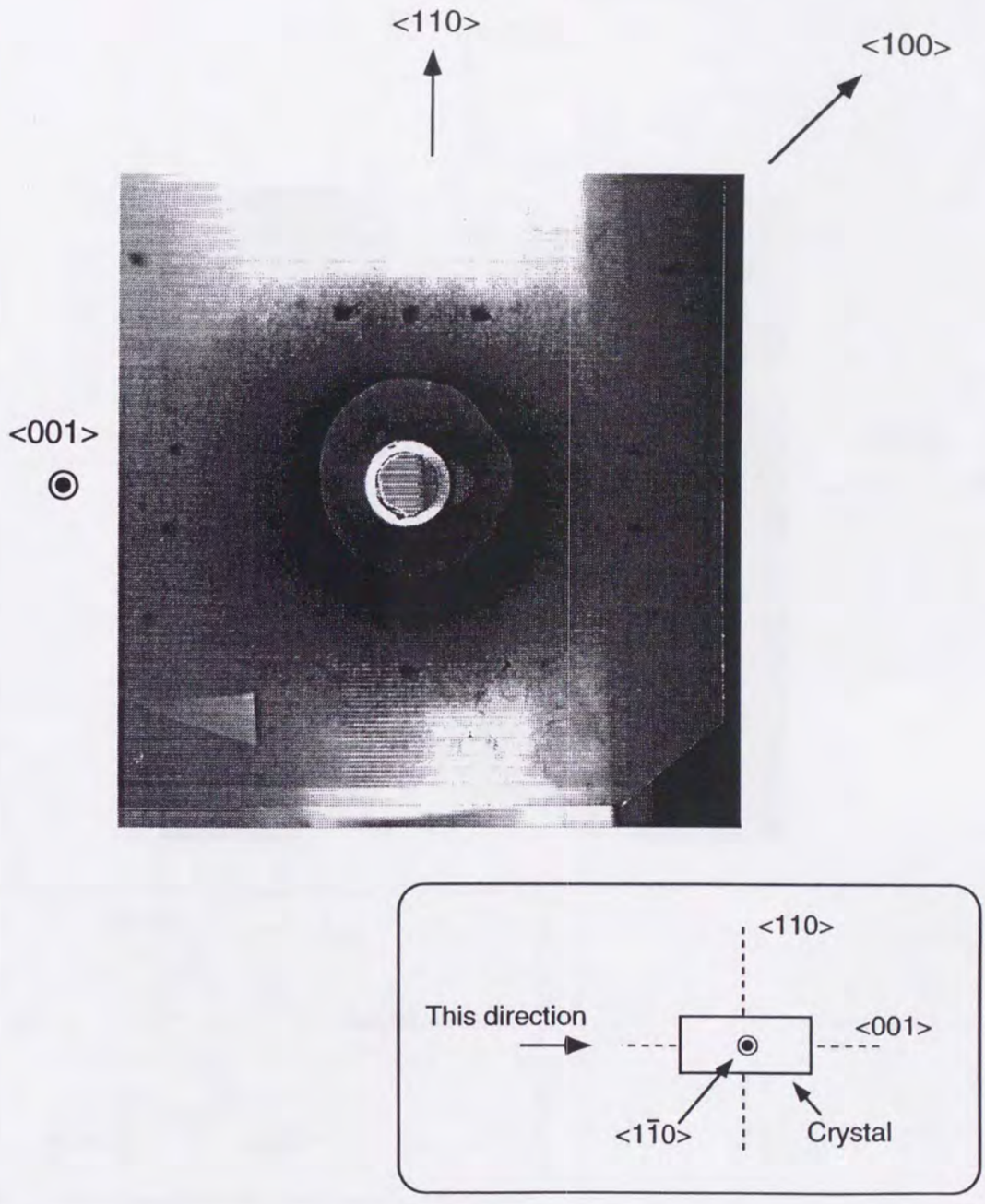

Fig. C-3.(1) Typical X-ray photo of synthesized TiO_2 crystal for FT-NMR measurement. This photo was taken from the direction of crystal growth, which is expected to be c-axis direction. As is expected, the c-axis is in this direction since four-fold rotation symmetrical pattern is observed.

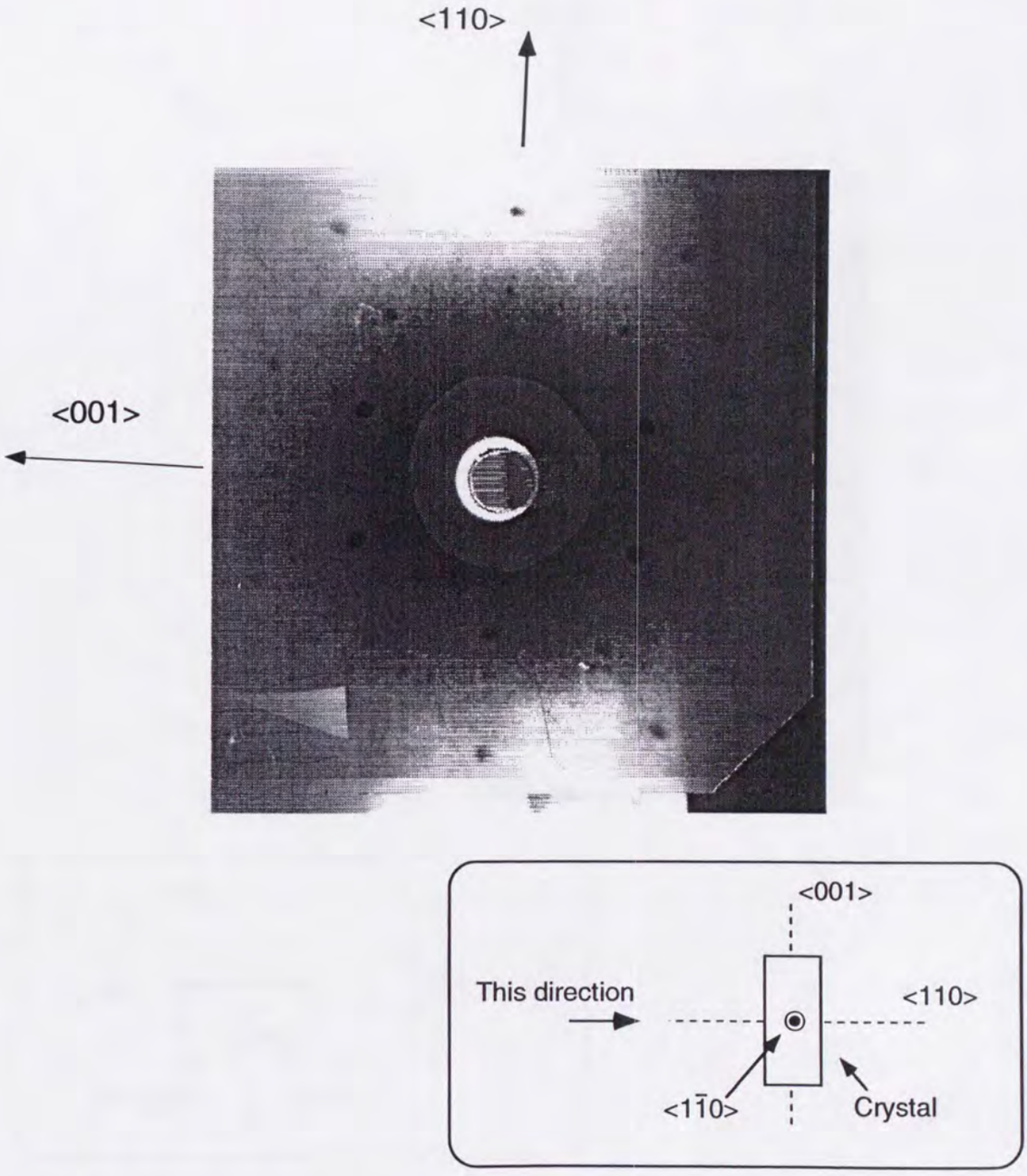

Fig. C-3.(2) Typical X-ray photo of synthesized TiO_2 crystal for FT-NMR measurement taken from the direction perpendicular to the crystal growth direction. Two-fold symmetrical pattern is observed, this direction corresponds to <110> of the crystal.

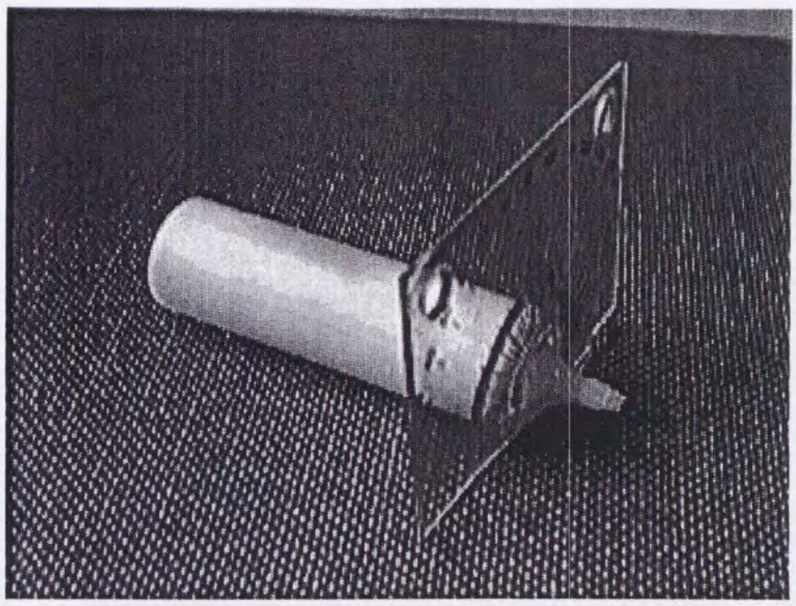

Fig. C-4.(1) The capsule which ^{17}O enriched TiO_2 for FT-NMR measurement was placed in. Three grains were inside the cupsule and their c-axis were pararell to the rotation axis. The transparent plate is the gauge for the rotation angle.

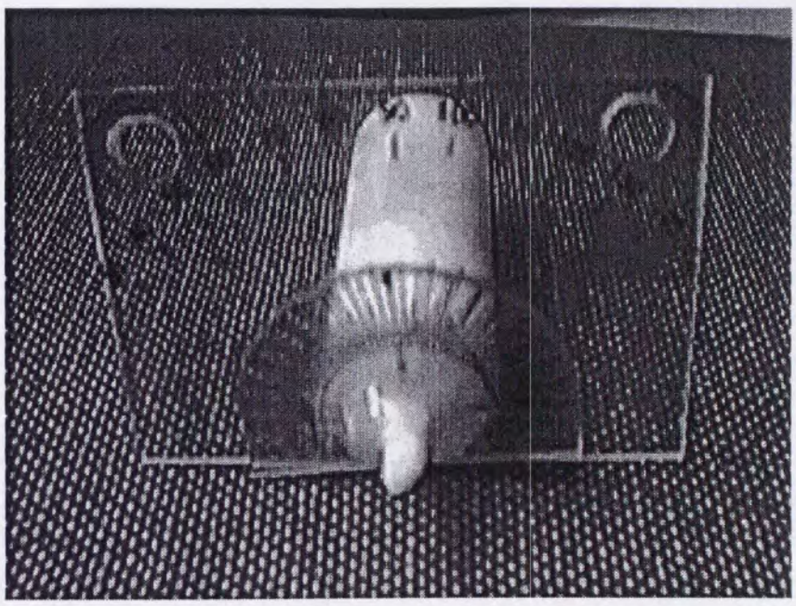

Fig. C-4.(2) Front view of the capsule

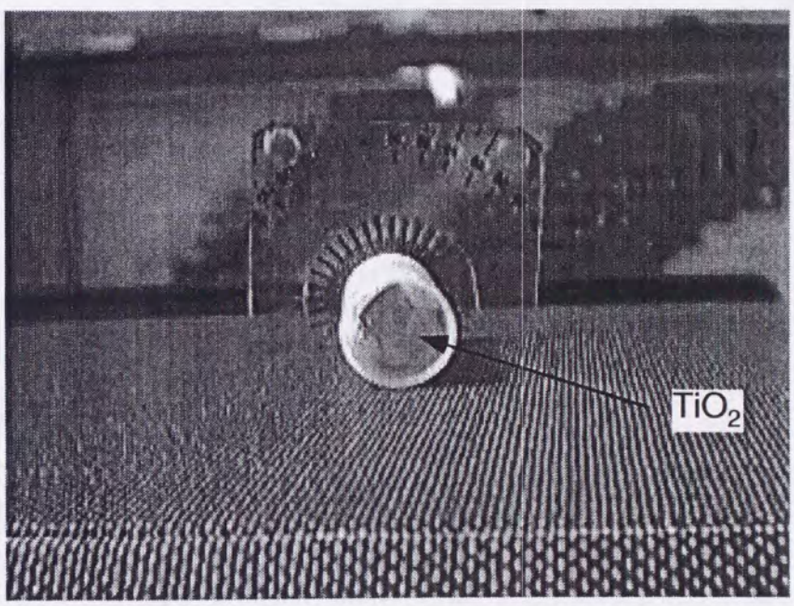

Fig. C-4.(3). The capsule for ^{17}O enriched TiO_2 from behind.

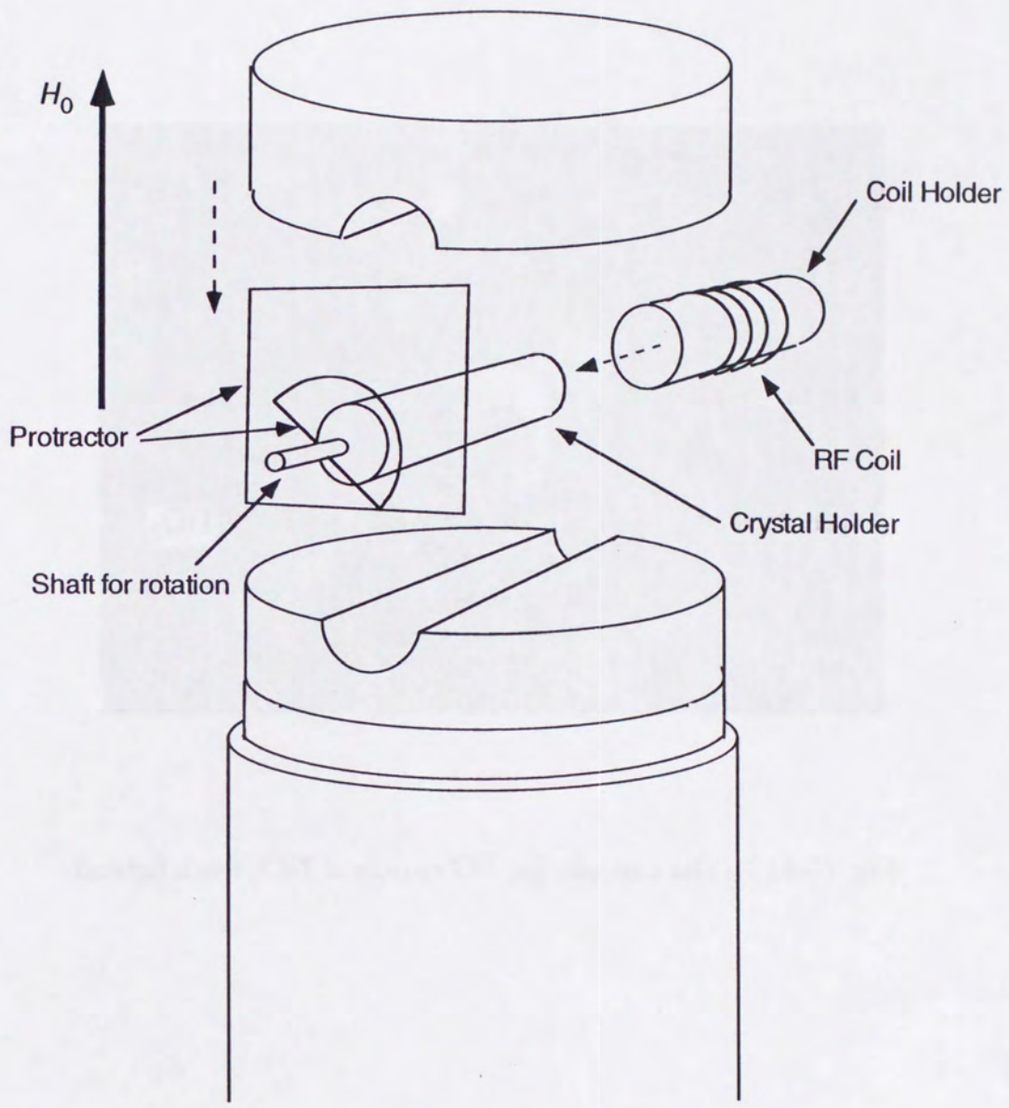

Fig. C-4.(4). Setup for the FT-NMR head. The radius of the head is about 5 cm. This head is mounted in a superconduction magnet.

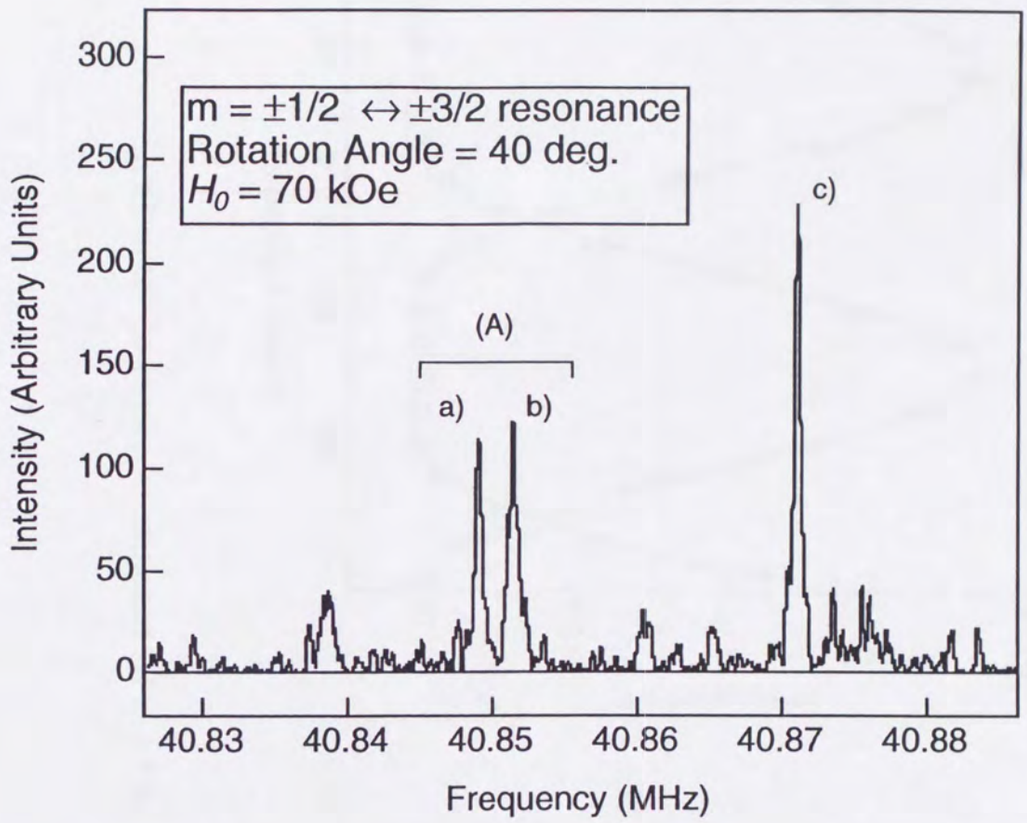

Fig. C-5. Typical FT-NMR spectrum of $m = \pm 1/2 \leftrightarrow \pm 3/2$ transition of ^{17}O in TiO_2. Since the present TiO_2 crystal is consisted from three grains and the two equivalent q exist at O site, several resonance peaks are observed. a) and b) are the peaks of the same q in different grains and their deviation was understood as the misallignment of the grains. From this split, the misallignment was estimated less than ~ 0.5 degrees. c) is the peaks of the other q, which rotates 90 degrees forward the q for a) and b). The present misallignment did not cause the resonance split at the present rotation angle. The deviation between (A) and c) was mainly due to the existence of η.

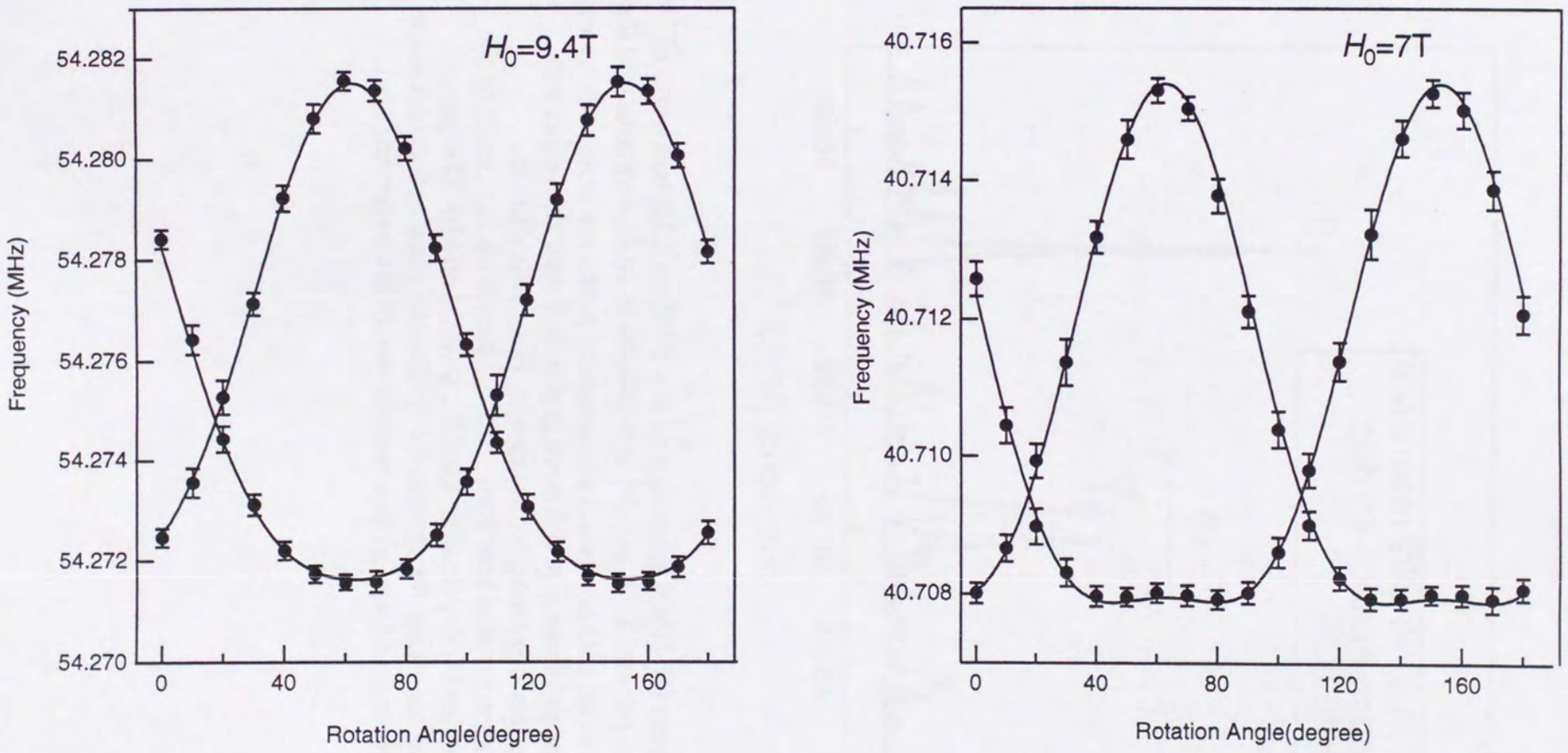

Fig. C-6. Angular dependence of the -1/2 ↔ +1/2 transition frequency of ^{17}O in TiO_2.

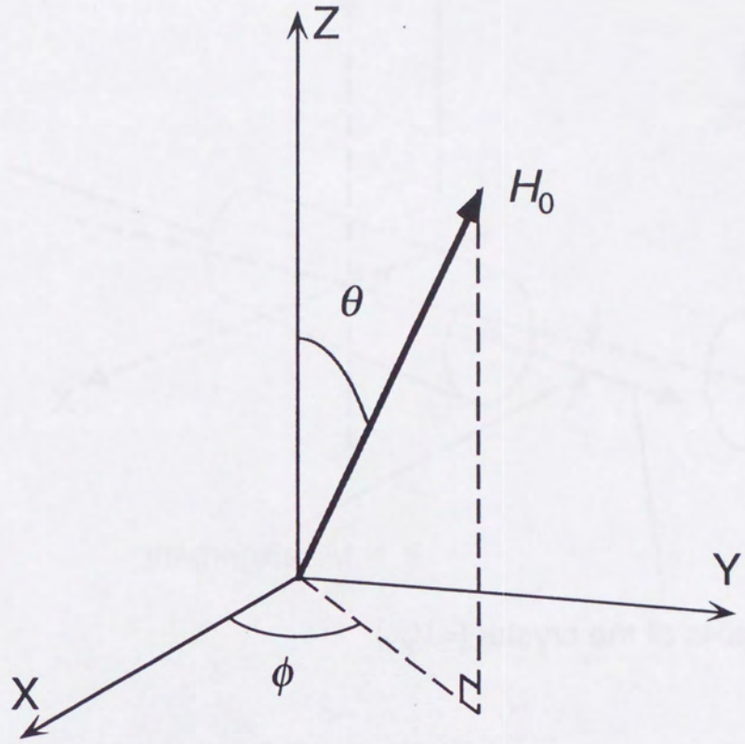

Fig. C-7. Definition of the polar angle.

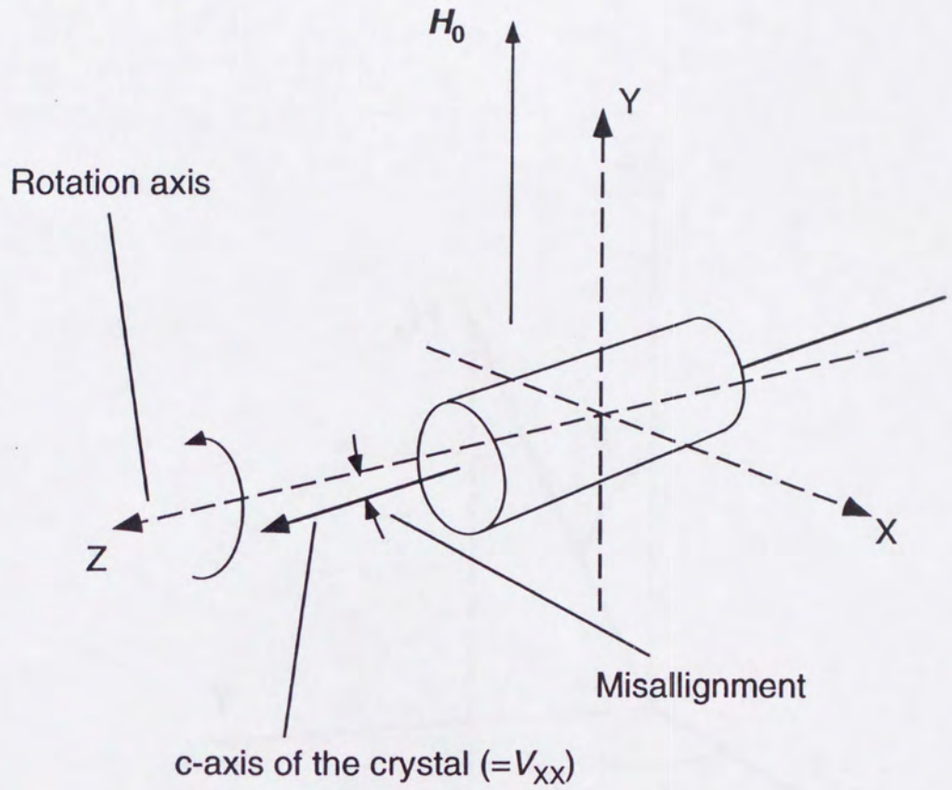

Fig. C-8. Orientation of the crystal. The rotation axis is not parallel to the c-axis of the crystal in the holder. The angle between the rotation axis and c-axis was taken as a free parameter in the present fitting. From the angular dependence of the resonance frequency of ^{17}O in TiO_2, the degree of misallignment is esitimated as ~5 degrees. This is consistent with the esitimation from the accuracy of mounting the crystal into the holder.

C-2,

$$\nu^{(2)}_{\frac{1}{2}} = -\left(\frac{h\nu_Q^2}{12\nu_L}\right)\{[3\sin 2\theta - \eta(\sin 2\theta\cos 2\phi + 2i\sin\theta\sin 2\phi)]$$
$$\times[3\sin 2\theta - \eta(\sin 2\theta\cos 2\phi - 2i\sin\theta\sin 2\phi)]\left[\frac{1}{8} - \frac{I(I+1)}{6}\right]$$
$$-\{3\sin^2\theta + \eta[(1+\cos^2\theta)\cos 2\phi + 2i\cos\theta\sin 2\phi]\}$$
$$\times\{3\sin^2\theta + \eta[(1+\cos^2\theta)\cos 2\phi - 2i\cos\theta\sin 2\phi]\}\left[\frac{3}{16} - \frac{I(I+1)}{12}\right]\Bigg\}. \quad \text{(C-2)}$$

For the determination of the present chemical shift anisotropy, the accuracy of eqQ/h and η are not required because the contribution of the electric quadrupole interaction to the observed frequency shift of m = -1/2 ↔ +1/2 is at most ~20% of that from chemical shift and the chemical shift anisotropy is expected to be at most ~1/50 of the first order shift, which is used for the determination of eqQ/h and η. Therefore, eqQ/h and η by Gabathuler were used for the determination of the chemical shift anisotropy. The fitting result is summarized in Table C-1.

The angular dependence of the transition frequencies between $m = \pm 1/2 \leftrightarrow \pm 3/2$ at H_0 = 7T was measured for the determination of eqQ/h and η. Fig. C-9 is the result and the best fit by the theoretical function for $m = \pm 1/2 \leftrightarrow \pm 3/2$ transition. Several peaks resulting from the two equivalent qs at O sites and the existence of three large grains in the present crystal were observed. These peaks were classified into two groups each of which corresponds to one q at O sites. This angular dependence, one peak group follow 90° after the other, was understood as the rotation around V_{XX} , i.e., two equivalent V_{ZZ} were in the plane perpendicular to rotation axis. From the angular dependence of the peaks in each group, the all axes of three grains in the present crystal were aligned within the precision of ±0.5°. The angular dependence of $m = \pm 1/2 \leftrightarrow \pm 3/2$ resonances was fitted by the function summing up the Larmor frequency term $\nu_m^{(0)}$, the first order perturbation term $\nu_m^{(1)}$, the second order perturbation term $\nu_m^{(2)}$ and the obtained chemical shift from m = -1/2 ↔ +1/2 measurements. As

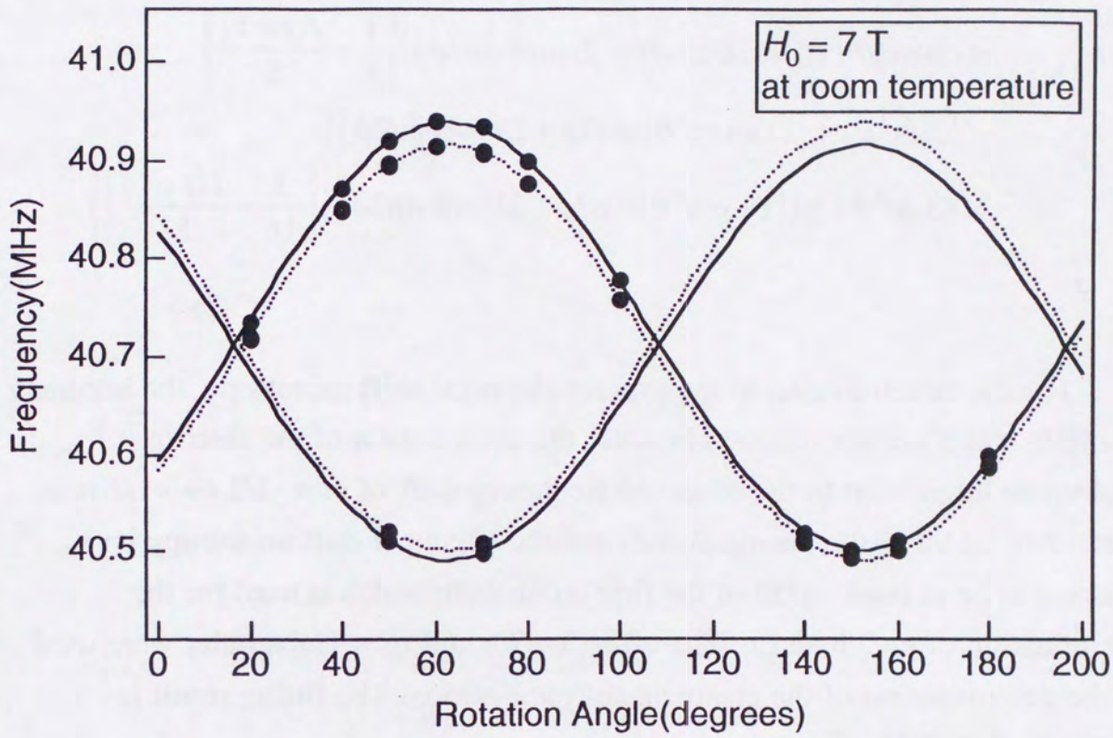

Fig. C-9. Angular dependence of $m = \pm 3/2 \leftrightarrow \pm 1/2$ transition frequency for ^{17}O in TiO_2. Rotation axis was set perpendiculart to H_0.

discussed in chapter 3, $\nu_m^{(0)} \sim \nu_m^{(2)}$ are written as,

$$\nu_m^{(0)} = \nu_L,$$

$$\nu_m^{(1)} = -\frac{\nu_Q}{2}\left(3\cos^2\theta - 1 + \eta\sin^2\theta\cos 2\phi\right),$$

$$\begin{aligned}\nu_m^{(2)} = -\left(\frac{h\nu_Q^2}{12\nu_L}\right)\{&[3\sin 2\theta - \eta(\sin 2\theta\cos 2\phi + 2i\sin\theta\sin 2\phi)] \\ &\times[3\sin 2\theta - \eta(\sin 2\theta\cos 2\phi - 2i\sin\theta\sin 2\phi)]\left[m(m-1) - \frac{I(I+1)}{6} + \frac{3}{8}\right] \\ &-\{3\sin^2\theta + \eta[(1+\cos^2\theta)\cos 2\phi + 2i\cos\theta\sin 2\phi]\} \\ &\times\{3\sin^2\theta + \eta[(1+\cos^2\theta)\cos 2\phi - 2i\cos\theta\sin 2\phi]\}\left[\frac{m(m-1)}{4} - \frac{I(I+1)}{12} + \frac{1}{8}\right]\}.\end{aligned}$$

(C-3)

where θ and ϕ are defined as in Fig. C-7, m = +3/2 for m = +1/2 ↔ +3/2 transition and m = -1/2 for m = -1/2 ↔ -3/2 transition, respectively. In the present analysis, the misalignment of V_{XX} relative to the rotation axis is also included in the fitting parameter. This misalignment from the fitting result is ~5 degrees, which is consistent with the expected accuracy of mounting the crystal into the capsule, at most ~10 degrees. The results are also summarized in Table C-1.

Table C-1. FT-NMR of ^{17}O in TiO_2.
Assigned axes of the chemical shift are defined as in Eq. C-1.

Chemical shift from m = -1/2 ↔ +1/2 transitions	
σ_x (ppm)	67 ±1
σ_y (ppm)	(1.3 ±0.9) × 10^3
σ_z (ppm)	233 ±6
Electric quadrupole coupling constants from m= ±3/2 ↔ ±1/2 transitions	
$\lvert eqQ(^{17}O \text{ in } TiO_2)/h\rvert$ (kHz)	1512 ±4
η	0.831 ±0.007

C.5. Discussion

Comparison with the previous result and theoretical calculation is shown in Table C-2. Theoretical calculation was performed in the framework of the local spin density approximation of the density functional theory in the KKR band structure calculation. The error for eqQ/h from KKR calculation is due to the error of quadrupole moment of ^{17}O, which is used for the conversion from the calculated EFG to eqQ/h. Both experimental results are well consistent with the result of the KKR calculation. A relatively large discrepancy between the present and previous is observed on η, compared to eqQ/h. Since η reflects the symmetry of the location, this discrepancy strongly suggests a finite lattice relaxation or deformation occurred in Cr doped TiO_2 which is used in the previous experiment.

Table C-2. Comparison of present results with the previous measurement and theoretical calculation.

	Present result	Gabathuler et al.	KKR[a)]
eqQ/h(MHz)	1.512 ±0.004	1.497 ±0.004	+1.34 ±0.16
η	0.831 ±0.007	0.868 ±0.005	0.944

a) Calculation was performed by K. Sato [68].

Appendix D. Fitting function for the β-NQR with AFP spectrum of ^{13}O in TiO_2

D.1. Treatment of the population of substates in β-NQR with AFP

In the simple AFP process, the polarization is projected to uniquely defined H_{eff}. Because the resonance of the nuclei spin I are split into $2I$ frequencies under a finite EFG, the effective magnetic field $\vec{H}_{eff}$ for each resonance varies (Fig. D-1). The populations of all sublevels are projected simultaneously to corresponding $\vec{H}_{eff}$ at the beginning and the end of the RF sweep and the each projection must be treated properly in the fitting function.

As the simplest case, the projection of two sublevels is considered. After the first projection of polarization to $\vec{H}_{eff}$, the populations of these states are written as,

$$p'(m)=\frac{1}{2}\left(1+\cos\alpha_{init}\right)p(m)+\frac{1}{2}\left(1-\cos\alpha_{init}\right)p(m+1)$$
$$p'(m+1)=\frac{1}{2}\left(1+\cos\alpha_{init}\right)p(m+1)+\frac{1}{2}\left(1-\cos\alpha_{init}\right)p(m) \quad \text{(D-1)}$$

where $p(k)$ is the initial population of magnetic substate k, $p'(k)$ is the population after the projection and α_{init} is the projection angle as already defined in Eq. 3-12. Assuming that applied RF satisfies AFP condition, $p'(m)$ and $p'(m+1)$ are held during the RF sweep. At the end of the RF sweep, the polarization is projected from $\vec{H}_{eff}$ to $\vec{H}_0$. After the final projection, the populations are written as,

$$p''(m)=\frac{1}{2}\left(1+\cos\alpha_{end}\right)p'(m)+\frac{1}{2}\left(1-\cos\alpha_{end}\right)p'(m+1)$$
$$p''(m+1)=\frac{1}{2}\left(1+\cos\alpha_{end}\right)p'(m+1)+\frac{1}{2}\left(1-\cos\alpha_{end}\right)p'(m) \quad \text{(D-2)}$$

where $p''(k)$ is the population after the final projection and α_{end} is the angle

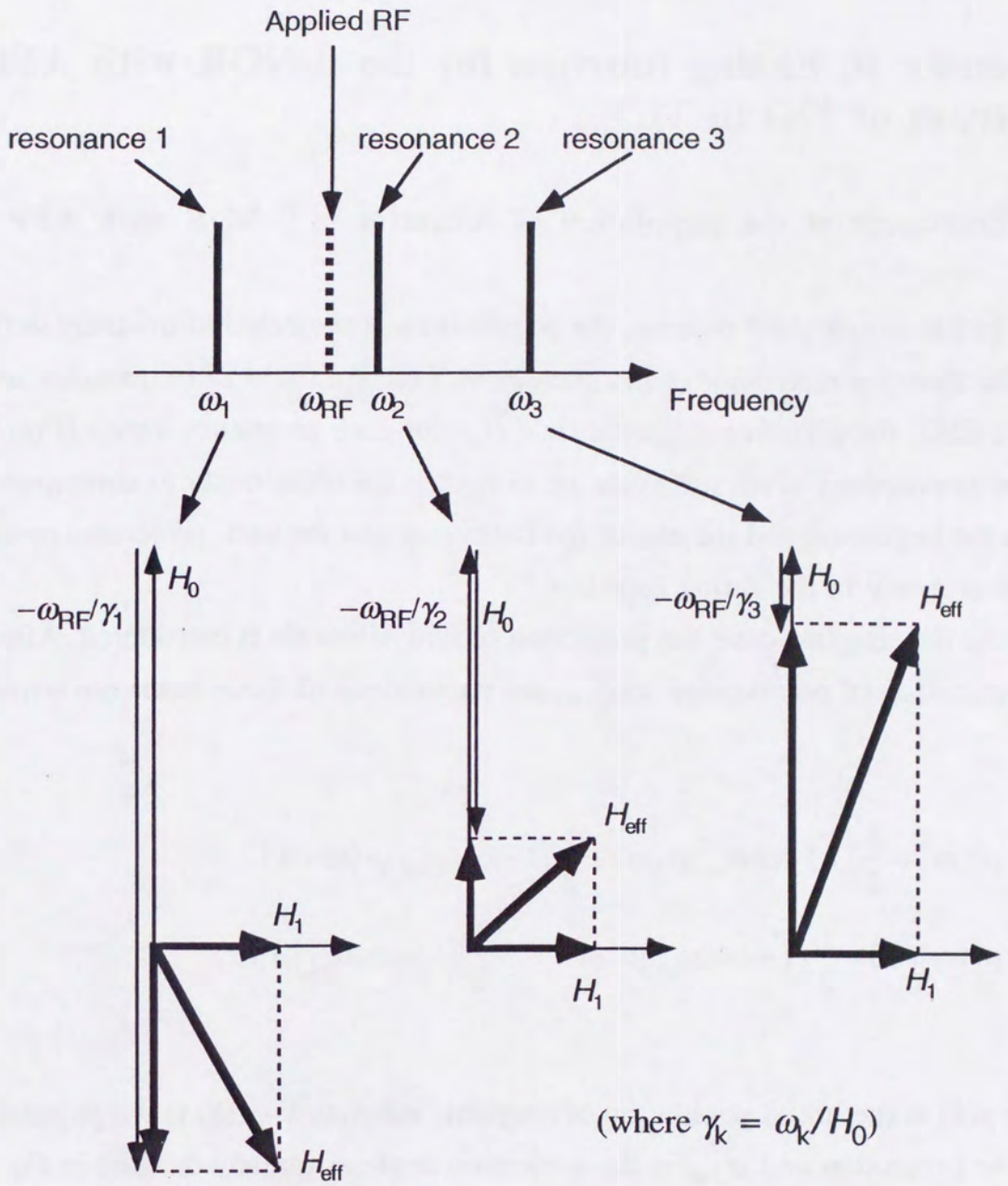

Fig. D-1. H_{eff} under a finite EFG. The effective gyromagnetic ratio, which includes the resonance shift due to EFG, is defined as $\gamma_k = \omega_k/H_0$. The effective megnetic fields H_{eff} for the magnetic sublevels depend on their resonance frequencies.

between $\vec{H}_0$ and $\vec{H}_{eff}$, which is already defined as in Eq. 3-13.

For example, the projection angle become $\pi/4$ where the frequency difference $\delta\omega = \omega - \omega_{res}$ is equal to H_1/γ. The populations are changed drastically if $\delta\omega$ becomes comparable to H_1/γ(Fig. D-2). In the case of $\delta\omega = H_1/\gamma$, the populations after the projection are obtained from Eq. D-2 as

$$\begin{aligned} p'(m) &\sim 0.85p(m) + 0.15p(m+1) \\ p'(m+1) &\sim 0.85p(m+1) + 0.15p(m). \end{aligned} \qquad \text{(D-3)}$$

If $\delta\omega = 2H_1/\gamma$, the populations after the projection become,

$$\begin{aligned} p'(m) &= 0.95p(m) + 0.05p(m+1) \\ p'(m+1) &= 0.95p(m+1) + 0.05p(m). \end{aligned} \qquad \text{(D-4)}$$

If $\delta\omega = 0$, the populations after the projection become,

$$\begin{aligned} p'(m) &= 0.5p(m) + 0.5p(m+1) \\ p'(m+1) &= 0.5p(m+1) + 0.5p(m). \end{aligned} \qquad \text{(D-5)}$$

From these results, as long as the split width between the resonances is larger than H_1/γ, the manipulation is eventually limited only on the sublevels which have the resonance within the sweep range of applied RF frequency. Therefore, as long as the width of resonance split is larger than H_1/γ, AFP process of each resonance can be treated separately. The matrics of the projection of m and m+1 states is written as,

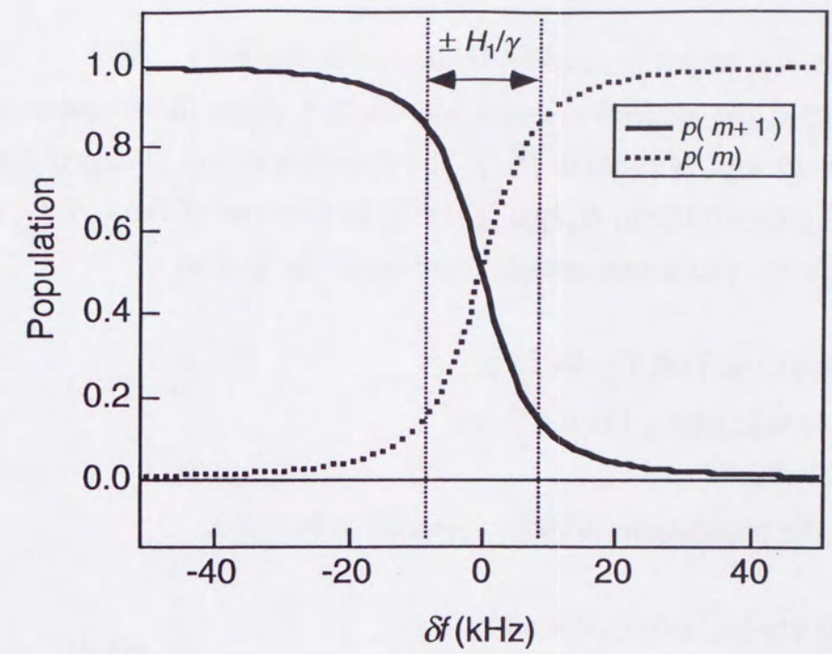

a) $\delta f < 0$

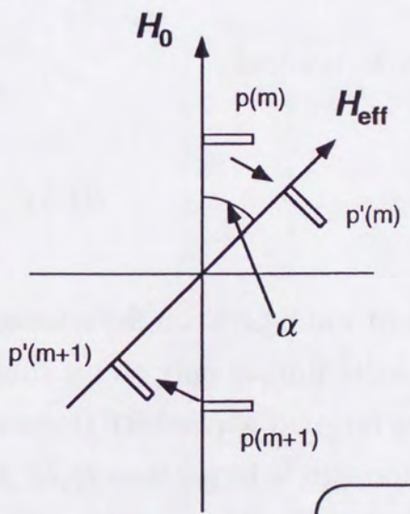

b) $\delta f > 0$

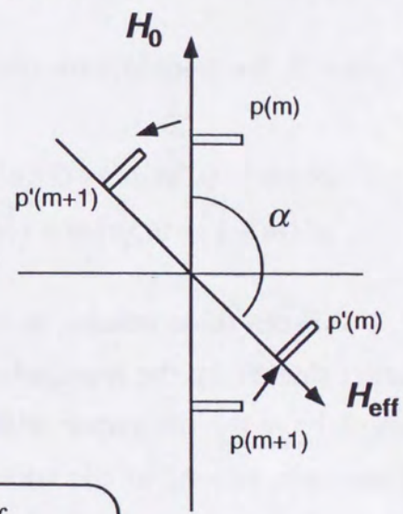

$$\alpha \equiv \frac{H_0 - \frac{2\pi f}{\gamma}}{\sqrt{\left(H_0 - \frac{2\pi f}{\gamma}\right)^2 + H_1^2}}$$

Fig. D-2. Population after the projection versus the applied RF frequency for ^{13}O at $H_0 = 8$ kOe. $\delta f \equiv f - \nu_{res}$ is the deviation of applied RF relative to resonance frequency. Initially, only the m+1 state is populated. As shown in the graph, the population change eventually occurs only if $\delta f < \pm H_1$.

$$\begin{pmatrix} p(-I) \\ \vdots \\ p'(m) \\ p'(m+1) \\ \vdots \\ p(+I) \end{pmatrix} = \begin{pmatrix} 1 & & & & 0 \\ & \ddots & & & \\ & & \frac{1}{2}(1+\cos\alpha_m) & \frac{1}{2}(1-\cos\alpha_m) & \\ & & \frac{1}{2}(1-\cos\alpha_m) & \frac{1}{2}(1+\cos\alpha_m) & \\ & & & & \ddots \\ 0 & & & & 1 \end{pmatrix} \begin{pmatrix} p(-I) \\ \vdots \\ p(m) \\ p(m+1) \\ \vdots \\ p(+I) \end{pmatrix}$$

$$= A(m,\alpha_m) \begin{pmatrix} p(-I) \\ \vdots \\ p(m) \\ p(m+1) \\ \vdots \\ p(+I) \end{pmatrix} \qquad \text{(D-6)}$$

where α_m is the projection angle of m and m+1 states. Then the populations of all substates after the projection can be written as

$$\begin{pmatrix} p'(-I) \\ \vdots \\ p'(+I) \end{pmatrix} = A\left(+(I-1),\alpha_{+(I-1)}\right)\cdots A\left(-I,\alpha_{-1}\right) \begin{pmatrix} p(-I) \\ \vdots \\ p(+I) \end{pmatrix}, \qquad \text{(D-7)}$$

under the present assumption.

More actually, the projection process of all substates should be treated simultaneously. But this treatment is difficult because the quantum axis for each transition in the rotating frame depends on its resonance frequency, which varies for each transition due to the existence of EFG.

In the present measurement of ^{13}O in TiO_2, the intensity of the applied RF was 12 Oe, i.e., $\delta\omega \sim 10$ kHz. As in Fig. 5-15, the split width between resonances

satisfies the present requirement. So, the projection process can be treated as Eq. D-7.

D.2. Fitting code for β-NQR with AFP

Following is the fitting program for the β-NQR with AFP spectrum. This code is written in macro language of Igor Pro 3.03. This code produces the theoretical function in the case of $\delta\omega > H_1/\gamma$.

This program calculates the achievement of 4AP method of β-NQR with AFP. In the present measurement, 6 AFP processes were applied for the spin inversion as shown in Fig. 3-12. The projection of each AFP process was calculated by Eq. D-7.

```
#pragma rtGlobals=1          // Use modern global access method.

function safp(w)          I initial projection angle calculation

        wave w;
        variable H0,H1,wm,wrf,dwrf,gamma

        H0=w[0]
        H1=w[1]
        wm=w[2]
        wrf=w[3]
        dwrf=w[4]
        gamma=wm/H0

        return (H0-(wrf+dwrf)/gamma)/sqrt((H0-(wrf+dwrf)/gamma)^2+H1^2)

end

function fafp(w)          I final projection angle calculation

        wave w;

        variable H0,H1,wm,wrf,dwrf,gamma
        H0=w[0]
        H1=w[1]
        wm=w[2]          wrf=w[3]
        dwrf=w[4]

        gamma=wm/H0
```

```
        return (H0-(wrf-dwrf)/gamma)/sqrt((H0-(wrf-dwrf)/gamma)^2+H1^2)

end

function afp(w,x)
        wave w;variable x
        variable H0,H1,wm,wrf,dwrf,gamma,initpol,finalpol,tmppol,A

        H0=w[0]
        H1=w[1]
        wm=w[2]
        wrf=x
        dwrf=w[3]

        A=0.2

        make /n=5 /d /O afppara
        make /n=2 /d /O apopul

        apopul[0]=w[4]
        apopul[1]=w[5]

        initpol=(apopul[0]-apopul[1])/(apopul[0]+apopul[1])

        variable tmppola,tmppolb,sachieve,fachieve
        afppara={H0,H1,wm,x,dwrf}
        sachieve=safp(afppara)

        tmppola=apopul[0]
        tmppolb=apopul[1]

        apopul[0]=0.5*(1+sachieve)*tmppola+0.5*(1-sachieve)*tmppolb
        apopul[1]=0.5*(1+sachieve)*tmppolb+0.5*(1-sachieve)*tmppola

        tmppol=(apopul[0]-apopul[1])/(apopul[0]+apopul[1])

        fachieve=fafp(afppara)

        tmppola=apopul[0]
        tmppolb=apopul[1]

        Variable up=0.5*(1+fachieve)*tmppola+0.5*(1-fachieve)*tmppolb
        Variable down=0.5*(1+fachieve)*tmppolb+0.5*(1-fachieve)*tmppola

end

function nnqr(w,x)
        wave w;variable x
        variable /G up,down

        variable
H0,H1,IS,ii,j,jj,jmax,achieve,vl,vm,dwrf,tmppa,tmppb,initial,final,A,gamma,k,initpol,tmppol,dwrf1,dwrf2,
ita,tm,vlr

        H0=w[0]
        H1=w[1]
        vl=w[2]
```

```
vm=w[3]
dwrf=w[4]
gamma=w[5]
A=w[6]

IS=1.5          ISpin
ita=0.831       lita
vlr=5646000     lvl in the case of pure magnetic interaction
ii=0
j=0
jmax=0
achieve=0

make /n=(2*IS+1) /d /O popul, tmppopul
make /n=6 /d /O afpinfo,dafpinfo
make /n=(2*IS) /d /O rffreq, resfreq
make /n=(2*IS-1) /d /O dqfreq
make /n=2 /d /O apopul

ii=0

popul[0]=1+100
popul[1]=2+100
popul[2]=3+100
popul[3]=4+100

tmppopul=popul

j=0

do
        rffreq[j]=vl-(j-(2*IS-1)/2)*x          | put rf frequency set for AFP
        resfreq[j]=vlr-(j-(2*IS-1)/2)*vm       | put resonance frequency set for AFP
        j=j+1

while (j<2*IS)

j=0

do
        tm=j-0.5

        resfreq[j]=resfreq[j]+((2*vm/(ita-1))^2/(12*vlr))*(3-ita)^2*((tm*(tm-1)/4)-(1.5*2.5/12)+1/8)    |
set 2nd shift on the resonance frequency for AFP
        j=j+1

while (j<2*IS)

j=0

do

        dqfreq[j]=(resfreq[j]+resfreq[j+1])/2       | put resonance frequency set for AFP
        j=j+1

while (j<2*IS-1)
```

```
jj=-1
jmax=2*IS

make /n=5 /d /O afppara,dafppara
make /n=2 /d /O apopul

do                      | β-NQR spin manupilation
        jmax=jmax-1

        do
                jj=jj+1

                        j=-1

                        do

                        j=j+1

                                afppara={H0,H1,resfreq[j],rffreq[jj],dwrf}

                                apopul[0]=popul[j]
                                apopul[1]=popul[j+1]

                                initpol=(apopul[0]-apopul[1])/(apopul[0]+apopul[1])

                                variable tmppola,tmppolb,sachieve,fachieve


                                sachieve=safp(afppara)
                                tmppola=apopul[0]
                                tmppolb=apopul[1]

                                apopul[0]=0.5*(1+sachieve)*tmppola+0.5*(1-sachieve)*tmppolb
                                apopul[1]=0.5*(1+sachieve)*tmppolb+0.5*(1-sachieve)*tmppola

                                tmppol=(apopul[0]-apopul[1])/(apopul[0]+apopul[1])

                                fachieve=fafp(afppara)

                                tmppola=apopul[0]
                                tmppolb=apopul[1]

                                popul[j]=0.5*(1+fachieve)*tmppola+0.5*(1-fachieve)*tmppolb
                                popul[j+1]=0.5*(1+fachieve)*tmppolb+0.5*(1-fachieve)*tmppola


                        while(j<jmax)

                while(jj<jmax)

        jj=-1

while(jmax>0)

initial=netpol(tmppopul,IS)
final=netpol(popul,IS)
return 100*(((1+A*initial)/(1-A*initial))/((1+A*final)/(1-A*final))-1)   |return 4AP effect
```

```
end

function netpol(popul,IS)          |calculating polarization from the population

        wave popul;variable IS

        variable j,tpop,tmpop

        tpop=0
        tmpop=0

        j=-IS-1

        do

                j=j+1
                tpop=tpop+popul[j+IS]
                tmpop=j*popul[j+IS]+tmpop

        while(j<IS)
        return (tmpop/(tpop*IS))
end
```

Appendix E. Tables of the experimental data

1) ^{9}C in Pt NMR search (Fig. 5-3)

Frequency (kHz)	FM (kHz)	Asymmetry Change (%)	Error (%)
3600	300	-0.8144	0.7199
3300	300	0.9798	0.8608
3900	300	-0.1566	0.8703
3600	100	-0.6695	0.8499
3300	100	0.1718	0.8098
3450	100	1.0174	0.8081
3400	100	-0.829	0.7943
3500	100	0.8808	0.8038
3800	100	0.1523	0.8027
3300	100	1.1994	1.1933
3100	100	1.124	1.3408
3600	100	-0.9327	1.2971
3400	100	-1.2311	1.1689
3200	100	-0.6103	1.1673
3700	100	0.3421	1.3176
2900	200	3.9272	0.8155
2800	100	3.9527	0.7081
3000	100	-1.0039	0.9671
2750	50	-0.7876	0.9652
2850	50	5.3471	1.469

2) ^{9}C in Pt NMR search (Fig. 5-4)

Frequency (kHz)	FM (kHz)	Asymmetry Change (%)	Error (%)
2875	25	-1.63	1.272
2825	25	5.7904	1.3566
2825	25	0.2331	1.4478
2823.75	12.5	4.2741	1.3232
2831.5	6.25	4.2406	1.3111
2828	3	3.674	1.0661
2834	3	-0.6729	1.1731
2825	3	3.2335	1.1704
2831	3	-1.0889	1.3384
2822	3	-0.1914	1.2877

3) ^{9}C in Pt (Fig. 5-5.)

Frequency (kHz)	Asymmetry Change (%)	Error (%)
2824	-0.0800811	0.357673
2825	0.786489	0.360103
2826	0.774247	0.360871
2827	1.587	0.363724
2828	1.34301	0.362502
2829	0.57831	0.359549
3000	0.0712645	0.358056

4) ^{8}B in Pt (Fig. 5-6.)

Frequency (kHz)	Asymmetry Change (%)	Error (%)
1574.9	-0.274956	0.311494
1575.2	0.193067	0.308546
1575.5	-0.24005	0.306671
1575.8	0.240439	0.308415
1576.1	0.501576	0.307404
1576.4	-0.0119949	0.308153
1576.7	0.83495	0.305942
1577	0.686228	0.307707
1577.3	1.4608	0.307269
1577.6	1.74194	0.3075
1577.9	1.93286	0.307101
1578.2	2.25359	0.30641
1578.5	2.13236	0.306905
1578.8	2.26183	0.306465
1579.1	1.31289	0.307174
1579.4	0.82781	0.306897
1579.7	0.673854	0.307866
1580	0.00854465	0.306759
1580.3	0.253934	0.30719
1580.6	0.772274	0.307774
1580.9	0.321936	0.307289
1581.2	0.128162	0.307656
1581.5	-0.326274	0.307932
1581.8	0.247878	0.307188
1582.1	0.0710807	0.306951
1582.4	0.101792	0.30774
1582.7	0.261274	0.307166
1583	-0.3055	0.3068
3000	0	0.125611

5) ^{13}O in Pt at H_0 ~2.5 kOe (Fig. 5-8.)

Frequency (kHz)	FM (kHz)	Asymmetry Change (%)	Error (%)
1525	70	0.3331	0.9838
1397.5	70	0.7695	1.0137
1270	70	0.70066	1.0362
1652	70	1.08892	0.9958
1779	70	3.2882	0.8028
1906	70	0.9849	1.0139

6) ^{13}O in Pt at H_0 ~4 kOe (Fig. 5-9.)

Frequency (kHz)	FM (kHz)	Asymmtery Change (%)	error (%)
2826	10	0.0385	0.7121
2836	10	5.1981	0.7517
2846	10	2.7036	0.7406
2866	10	-1.1949	0.6423
2856	10	0.6964	0.8562
2831	5	0.7381	0.5584
2836	5	3.9456	0.7919
2841	5	1.3685	0.5923

7) ^{13}O in MgO (Fig. 5-12.)

Frequency (kHz)	Asymmet ry Change (%)	Error (%)
2814	0.156781	0.425264
2816	0.356239	0.426003
2818	0.772204	0.373547
2819	0.405602	0.371819
2820	0.524391	0.372179
2821	1.00954	0.374059
2822	1.94333	0.377498
2823	2.22755	0.37868
2824	1.81814	0.377224
2825	0.928568	0.373905
2826	1.1563	0.374629
2827	0.774762	0.373452
2829	0.365535	0.425943
2831	-0.457248	0.422809

8) Spin Relaxation of ^{13}O in Pt (Fig. 5-13.)

Time (ms)	Asymmetry Change (%)	Error (%)
2	6.41555	0.731926
6	3.30928	0.832271
10	4.05753	0.979982
14	2.33751	1.12688
18	1.26618	1.30527
22	1.64056	1.5305
26	-0.325818	1.75488
30	3.20602	2.11102

9) ^{12}N in Pt (Fig. 5-14.)

Frequency (kHz)	Asymmetry Change (%)	Error (%)
1390.5	0.5932	0.5311
1391.5	-0.0026	0.5275
1392.5	1.13014	0.3822
1393	2.12744	0.386005
1393.5	2.68187	0.388075
1394	3.65282	0.391909
1394.5	3.11674	0.38949
1395	1.5004	0.383492
1395.5	1.11246	0.381918
1396	0.854211	0.380666
1396.5	0.58753	0.380278
1397.5	-0.434	0.5247
1398.5	0.1126	0.5284

10) ^{13}O in TiO_2 (Fig. 5-15.)

Frequency (kHz)	Asymmetry Change (%)	Error (%)
15	3.0284	0.7549
22.5	2.7632	0.8136
30	1.5214	0.7623
37.5	0.1077	0.91
45	0.271585	0.610695
52.5	2.8045	0.7702
60	2.7839	0.8032
67.5	2.8774	0.7839
75	1.9965	0.8093
82.5	0.9307	0.8035
90	-0.5014	0.7254
105	0.2838	0.812
120	-0.7806	0.8098
130	0.4813	0.7912

11) ^{19}O in TiO_2 with H_0 // c-axis (Fig. 5-16.)

Frequency (kHz)	Asymmetry Change (%)	Error (%)
0	1.07654	0.0937686
0.5	1.4524	0.1502
1	1.3845	0.1465
1.5	1.4686	0.1442
2	2.0658	0.143017
2.5	2.031	0.1515
3	1.9149	0.1445
3.5	1.8914	0.1543
4	1.56139	0.154477
4.5	1.3072	0.149
5	1.1679	0.161
5.5	1.5266	0.1545
6	1.63063	0.143777
6.5	1.6069	0.1483
7	1.4406	0.1364
7.5	1.1973	0.1442
8	1.19096	0.14622
9	0.9027	0.1489
10	1.02641	0.150678
12	1.14695	0.147995
14	1.19042	0.138743
16	1.1819	0.150119
18	1.03391	0.146328
20	1.00037	0.148208
22	0.714303	0.151387
24	1.02224	0.14739

12) ^{19}O in TiO_2 with H_0 // <110> (Fig. 5-19.)

Frequency (kHz)	Asymmetry Change (%)	error (%)
15	-0.406858	0.235379
20	-0.496657	0.234127
22.5	-0.368329	0.217987
25	-2.32766	0.23476
27.5	-2.39753	0.229232
30	-3.78401	0.23408
32.5	-3.13923	0.229698
35	-2.22933	0.237295
37.5	-1.66653	0.230717
40	-0.590841	0.203798
42.5	-0.667108	0.192995
45	-0.865015	0.205274
47.5	-0.690314	0.195044
50	-1.46038	0.255062
52.5	-0.33115	0.238417
55	-0.466832	0.246092
57.5	-0.747359	0.234647
60	-0.1661	0.3316
65	0.1142	0.3331
70	0.1133	0.3303
75	0.2961	0.3358

13) Angular dependence of $m = +1/2 \leftrightarrow -1/2$ transition frequency of ^{17}O in TiO_2 at 9.4 T (Fig. C-6.)

Rotation Angle (degrees)	Frequency (kHz)	Error (kHz)	Frequency (kHz)	Error (kHz)
0	54272.465	0.185431	54278.414	0.186232
10	54273.552	0.292086	54276.426	0.289189
20	54275.287	0.333847	54274.436	0.266311
30	54277.132	0.226207	54273.115	0.207889
40	54279.225	0.257017	54272.199	0.185132
50	54280.816	0.283529	54271.741	0.160534
60	54281.556	0.186037	54271.577	0.148357
70	54281.362	0.205428	54271.592	0.210078
80	54280.219	0.241469	54271.846	0.184644
90	54278.24	0.262677	54272.511	0.223218
100	54276.325	0.224737	54273.571	0.257389
110	54274.367	0.214642	54275.324	0.400044
120	54273.076	0.245415	54277.212	0.302611
130	54272.182	0.198199	54279.192	0.318008
140	54271.709	0.186759	54280.773	0.305035
150	54271.561	0.171337	54281.53	0.289512
160	54271.605	0.170512	54281.348	0.245733
170	54271.883	0.202864	54280.072	0.248219
180	54272.567	0.232624	54278.163	0.23794

14) Angular dependence of $m = +1/2 \leftrightarrow -1/2$ transition frequency of ^{17}O in TiO_2 at 7 T (Fig. C-6.)

Rotation Angle (degrees)	Frequency (kHz)	Error (kHz)	Frequency (kHz)	Error (kHz)
0	40708.011	0.147317	40712.577	0.248779
10	40708.654	0.194903	40710.456	0.265946
20	40709.929	0.254249	40708.975	0.260125
30	40711.367	0.333732	40708.305	0.194391
40	40713.18	0.23371	40707.969	0.145829
50	40714.599	0.282276	40707.957	0.129383
60	40715.308	0.177246	40708.019	0.137498
70	40715.046	0.173416	40707.985	0.148024
80	40713.776	0.244959	40707.925	0.138204
90	40712.11	0.229912	40708.026	0.161067
100	40710.403	0.270963	40708.606	0.215319
110	40709.004	0.203868	40709.798	0.249396
120	40708.237	0.162152	40711.389	0.278159
130	40707.94	0.159539	40713.229	0.355312
140	40707.943	0.147792	40714.62	0.265482
150	40708.002	0.135116	40715.275	0.198385
160	40708.002	0.153081	40715.032	0.258738
170	40707.939	0.192647	40713.868	0.281853
180	40708.084	0.165756	40712.076	0.268909

15) Angular dependence of $m = \pm 3/2 \leftrightarrow \pm 1/2$ transition frequency of ^{17}O in TiO_2 at 7 T (Fig. C-7.)

Rotation Angle (degrees)	Frequency (kHz)	Error (kHz)
20	40719.912	0.504392
40	40851.505	0.442848
50	40895.821	0.2592
60	40914.291	0.487877
70	40908.103	0.304152
80	40875.354	0.251733
100	40757.647	0.381595
140	40508.707	0.464509
150	40491.871	0.174497
160	40500.147	0.47772
180	40586.7	0.462167
20	40734.2	0.317993
40	40871.108	0.243338
50	40917.784	0.314834
60	40938.696	0.526711
70	40935.125	0.496443
80	40898.408	0.348636
100	40776.834	0.275181
140	40518.827	0.398373
150	40501.238	0.327708
160	40509.525	0.287916
180	40599.108	0.197586
20	40716.698	0.504392
40	40849.081	0.265107
50	40894.249	0.328891
60	40914.291	0.487877
70	40906.948	0.296931
80	40877.317	0.453513
140	40511.353	0.302689
150	40493.611	0.37201
160	40500.147	0.47772
180	40588.594	0.209776
50	40521.897	0.278736
70	40507.709	0.247965
50	40511.687	0.220179
70	40497.838	0.251905